Fritz Haber Research Center for Molecular Dynamics

Scientific Report 2019-2020

Institute of Chemistry

Faculty of Mathematics and Natural Sciences

The Hebrew University of Jerusalem

Edited by: Roi Baer, Veniamin Borin, Igor Schapiro

Contents

Chapter 1

The Fritz Haber Research Center for Molecular Dynamics

The Fritz Haber Research Center (FHRC) for Molecular Dynamics was established in 1981 by the Minerva Foundation of the Max Planck Society and by the Hebrew University of Jerusalem as part of the Chemistry Institute and the Faculty of Mathematics and Natural Sciences. The center's goal was twofold: to support theoretical chemical and physical research in Israel and foster German-Israeli scientific collaboration. Both of these goals form the focus of the center's activity even today, almost 40 years later. The founding director of the Fritz Haber Center was Professor Raphael D. Levine. Subsequently, the center was directed by Professors Robert B. Gerber, Ronnie Kosloff, Avinoam Ben Shaul, and Roi Baer (current director).

The center consists of fourteen independent research groups, each headed by a PI. Since the last report, four new PIs have joined the center: Snir Gazit, Eli Kraisler, Tamar Stein, and Raam Uzdin. Information for each group appears in Chapter 2. There are 90 researchers in the center at the time of reporting, including the 14 principal investigators, six non-faculty researchers, six long-term visitors, 18 postdoctoral researchers, 44 graduate, and six undergraduate students. A detailed account of the personnel in the center is given in Section 3.1.

The Beirat: The FHRC reports biennially to a Beirat, overseeing and guiding its operations in Jerusalem (last in 2018):

- Prof. Dr. Gerard J. M. Meijer, Chair (Fritz Haber Inst.; Pres. Radboud Univ.)
- Prof. Dr. Helmut Grubmüller (MPI Biophysical Chemistry).
- Prof. Dr. Frank Neese (MPI for Coal Research).
- Prof. Dr. Micha Asscher (Hebrew Univ).
- Prof. Dr. Leeor Kronik (Weizmann Institute).
- Prof. Dr. Nimrod Moiseyev (Technion).

The center reports biennially to the Beirat, headed by Professor Gerard J. M. Meijer from Fritz Haber Institute, Berlin. In 2020 Professor Frank Neese from the Max Planck Institute for Coal Research was elected as a Beirat member. See box for a list of the present Beirat members. The Beirat oversees the operations of the center, approves its budget, and advises the director. The long term support of the Beirat is gratefully acknowledged.

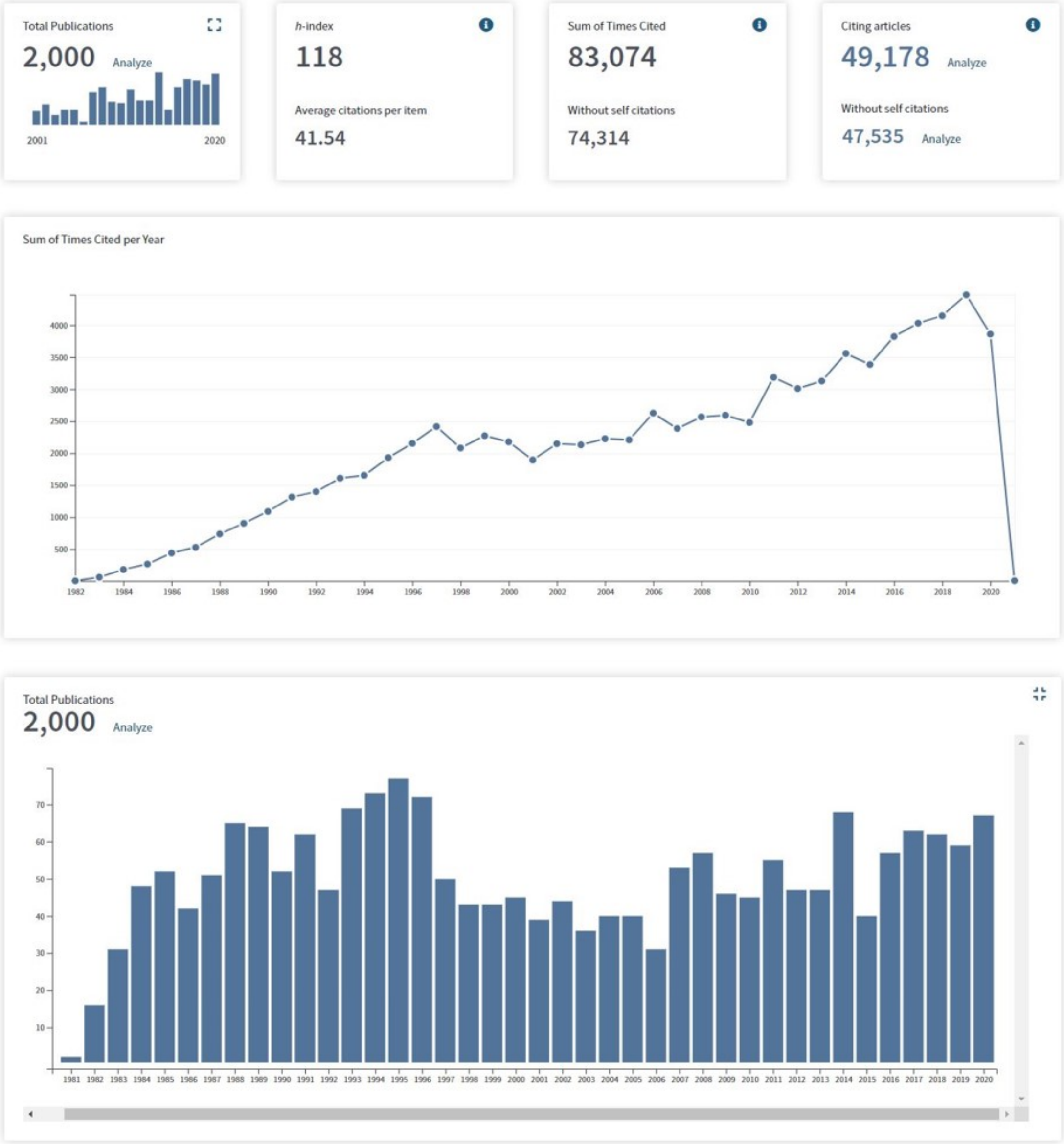

Total Publications
2,000 Analyze

h-index
118
Average citations per item
41.54

Sum of Times Cited
83,074
Without self citations
74,314

Citing articles
49,178 Analyze
Without self citations
47,535 Analyze

Sum of Times Cited per Year

Total Publications
2,000 Analyze

Figure 1.1. Web of Science Citation Report for the Fritz Haber Center till December 2020. The results were obtained by searching "Fritz Haber AND Jerusalem" in the Address field.

1.1 Scientific mission and impact

The Center's scientific goal lies in developing novel approaches for understanding and predicting complex phenomena in chemical, biological, and materials science systems. We aim to advance theoretical methods in the corresponding fields, collaborate with experimentalists, and develop new analytical and computational techniques. The purpose of our efforts is eventually to help discover new phenomena, to explain experimental findings while predicting new effects. The original field of research in the Center was the Theory of Molecular Dynamics. Since these first years, the focus of the center activities has evolved and broadened to the extent that it engulfs many aspects of the theory of chemistry, biochemistry, and materials science. Likewise, the research in the Center has evolved to embrace a variety of topics, including:

- Molecular dynamics (Schapiro, Gross, Baer, Kosloff, Levine, Gerber, Agmon),
- Molecular and nanocrystal-based solar-cells (Baer, Gross, Schapiro)
- Molecular electronics (Baer, Gross)
- Nonadiabatic dynamics (Gross, Schapiro, Kosloff, Levine, Baer)
- Photobiology and photochemistry (Schapiro, Gerber, Kosloff, Baer)
- Electronic structure and quantum chemistry (Gross, Schapiro, Baer, Stein, Kraisler)
- Optical/vibrational spectroscopy of large molecules (Gerber)
- Optimal coherent control (Kosloff, Gross)
- Cold chemistry in atomic condensates (Kosloff, Baer)
- Quantum thermodynamics (Kosloff, Uzdin)
- Attosecond electron dynamics (Kosloff, Levine and Baer),
- Proton transfer processes (Agmon, Gerber)
- Chemical catalysis on surfaces (Baer, Gerber, Kosloff)
- Ion hydration (Agmon, Gerber)
- Complex fluids (Ben Shaul, Harries)
- Peptide aggregation in crowded environments (Harries)
- Lipid interactions (Harries, Ben Shaul)
- Molecular recognition, chemical sensors (Niv)
- Sugars (Niv, Kosloff, Gerber, Harries)
- Bitter taste (Niv, Harries)
- Cell locomotion (Zemel)
- Elasticity (Zemel, Harries, Ben Shaul)
- Viral structure (Ben Shaul)
- RNA structure (Ben Shaul)
- Atmospheric chemistry (Gerber)
- Machine Learning in Quantum Chemistry (Stein)
- Astrochemistry (Stein)
- Strongly correlated systems (Gazit)

In Fig. 1.1, we show that the center's researchers have published 2000 papers, at an average rate of about 50 articles per year, and have accumulated over 83 thousand citations, with a current ratio of close to 4000 citations per year. A list of the publications in the reporting year is given in Appendix A.

Table 1.1: Academic Alumni of Fritz Haber Research Center

Name	Inst.	Name	Inst.	Name	Inst.
R Alimi	NRC, IL	E Geva	UMich, US	S May	N Dakota, US
N Aytemiz	Bandirma U, TR	D Harries	HUJI, IL	MI Mcarthy	PNNL, US
Z Bacic	NYU, US	J Harvey	U.Bristol, UK	L McCaslin	SNL, US
R Baer	HUJI, IL	B Hirshberg	Tel Aviv U, IL	AB McCoy	U of WA, US
A Baratz	BRC, IL	O Hod	Tel Aviv U, IL	Y Miller	BGU, IL
R Bisseling	Utrecht, NL	S Jørgensen	U.Copnhgen, DK	MY Niv	HUJI, IL
Y Bohbot	BRC, IL	P Jungwirth	Czch Acad, CZ	JP Palao	La Laguna, ES
E Brown	Loyola U, US	S Kais	Purdue U, US	E Rabani	UCB, US
V Buch	HUJI, IL	S Kallush	Brada Inst, IL	T Raz	JCE, IL
O Buchman	BRC, IL	M Khasin	NASA, US	B Schmidt	FU Berlin, DE
M Chaban	NASA, US	C Koch	FU Berlin, DE	T Stein	HUJI, IL
D Charutz	NRC, IL	V Kokouline	U Florida, US	I Szleifer	Purdue U, US
A Di Pizio	TUM, DE	AI Krylov	USC, US	N Tishby	HUJI, IL
R Elber	UT Austin, US	Y Kurzweil	NRC, IL	R Uzdin	HUJI, IL
E Fattal	BRC, IL	A Levi	Bar Ilan U, IL	J Valla	NU, IE
M Feldman	JCT, IL	D Lidar	USC, US	V Vlček	UCSB, US
E Fredj	JCT, IL	J Lundell	U.Jyväskylä, FI	B Whaley	UCB, US
A Gar-Vela	CSIC, ES	TJ Martinez	Stanford U, US	A Zemel	HUJI, IL

In light of the stated goal, our students and postdocs operate in a variety of fields in theoretical chemistry, biology, and physics and take part in explaining fascinating experiments and in developing some of the most advanced tools of computational chemistry. Indeed, dozens of our alumni are now leaders in world academia and Israel, as can be seen in Table 1.1.

1.2 German-Israeli Scientific Collaboration

Over the years, the Fritz Haber Research Center has been a cornerstone for German-Israeli scientific collaboration. Intensive, fruitful collaborations are evident in the ISI citation report given in Fig. 1.2, at a rate of 25 papers in the two years of the report and a total of 245 collaborative papers in the last 39 years (annual average of 6 articles). Furthermore, two of our faculty (Schapiro and Gross) are German scientists, and three German postdocs and a German graduate student are among our researchers.

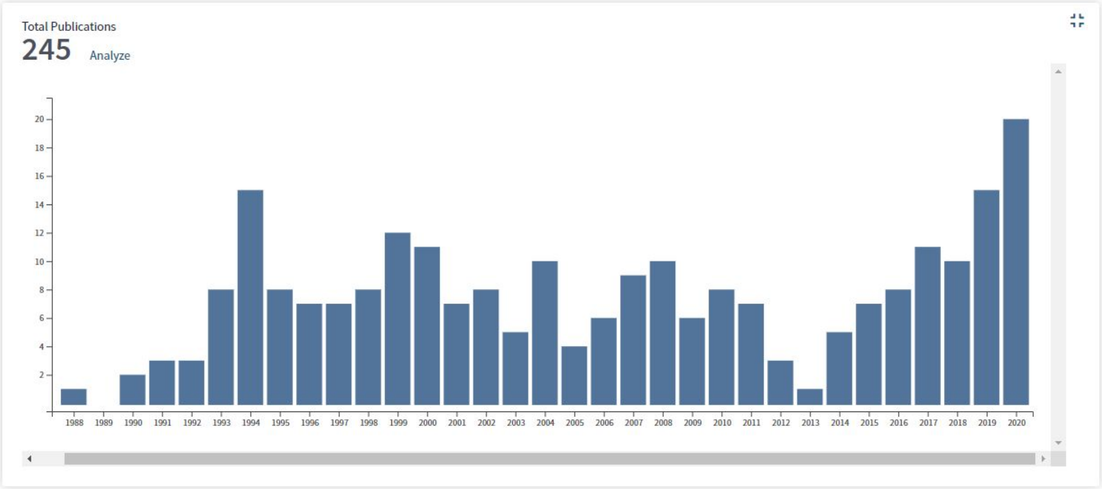

Figure 1.2. Web of Science Citation Report for joint publications with scientists from Germany. The results were obtained by searching "Fritz Haber AND Jerusalem AND Germany" in the Address field.

1.3 Operational principles of the center

One of the center's primary goals is to provide a bustling scientific atmosphere for intensive research activities. We achieve this by gathering the groups into a shared geographical location, where students and faculty socialize and interact scientifically. We also offer social activities, such as guest visits and seminars by scientists from outside of the university, mainly from abroad. In 2018-2020 we had over 50 visitors (see the list in Section B.1) and numerous lectures (see the list in Section B.2). Furthermore, the students and faculty organize and participate in scientific conferences and workshops (see Appendix B.3)

The second operational pillar is the computer administration services, provided by two staff scientists (Dr. Ester Livshits and Dr. Hadassah Elgavi). The services offered are (1) Maintenance of A/C, power, communications, IT, email, information storage, and backup infrastructure; (2) Planning, ordering, and installing new computer systems; (3) Maintenance of purchased computer systems; (4) Purchasing and updating dedicated computational chemistry and graphics/mathematics/physics software, including expertise in running and debugging such packages. (5) Participating in research, including guiding younger scientists. For more details concerning the computer center, see Appendix 3.2.

The center also provides its members with comprehensive administrative services, including managing budgets, salaries, tuition, travel reimbursements, guest services (hotel reimbursements), and seminar organization. Most of these services are provided by our administrator, Ms. Geula Levy.

Funding and expenditures

The Fritz Haber Research Center has three main types of funding sources available:

1. The funding due to the Minerva foundation: this is composed of the interest from Minerva

endowment plus a matching sum from the Hebrew University (a total $77,200$ Euros in 2019-20). A fiscal report for the Minerva funds is given in Section 3.3 and a proposed budget is given in Section 3.4

2. The Hebrew University further complements the income of the center to $200,000 as part of its commitment for developing the theoretical chemical physics field. The university also funds the PIs, the administrative assistant and the two staff scientists.
3. The Hebrew University further offered $800,000 as start up funds for the new faculty members in 2019.
4. The researchers of the center have raised in the two years of the reported period $5 million from external grants, mainly to cover the scholarships of students and postdoctoral researchers as well as to purchase computing equipment.

CoVid-19 impact on the center activities

During most of 2020 the center's operations, like activities of the university as a whole, shifted from a center-based activity to research mainly from home, relying on video conferencing software for meeting and collaborating. The travel of the center's scientists abroad or the arrival of guests has ceased this year almost completely. In the present semester we have renewed (online) seminar activity which grinded to a near halt during the previous (spring) semester. Just like research and academy in the rest of the world, we are waiting for the

Chapter 2

Research group reports

2.1 Noam Agmon

Research Activities

Our main research theme involves proton transport and spectroscopy in aqueous systems, from gas-phase clusters to the liquid state and biological systems. During the last two years, we have studied small gas-phase clusters of water and the hydrated sodium cation. Common to these systems are strong hydrogen-bonds (HBs) that determine the structure and dynamics.

Ionic Radii of Hydrated Sodium Cation from QTAIM

in collaboration with Jean Jules Fifen (Fifen, Jean Jules and Agmon, Noam 2019)

The sodium cation is ubiquitous in aqueous chemistry and biological systems. Yet, in spite of numerous studies, the (average) distance between the sodium cation and its water ligands, and the corresponding ionic radii, are still controversial. Recent experimental values in solution are notably smaller than those from previous X-ray studies and ab-initio molecular dynamics. (Galib et al. 2017) Using a “bottom-up” approach for constructing gas-phase $Na^+(H_2O)_n$ clusters (up to $n = 8$), the cation-water oxygen distances were obtained from quantum chemistry calculations (full MP2 with the 6-31++G(d,p) and cc-pVTZ basis-sets), as a function of the sodium cation coordination number ($CN \equiv m = 2$–6). The bulk limit was subsequently obtained with the polarizable continuum model (PCM) (Tomasi, Mennucci, and Cammi 2005). Finally, we utilized Bader’s quantum theory of atoms in molecules (QTAIM) (Bader, Anderson, and Duke 1979) to bisect the Na^+–O distances into Na^+ and water radii, for each value of n and m.

The conformers of size n were built from conformers of size n-1, by considering all possibilities for adding a water molecule. These clusters are denoted by mqr, where m, q and r represent the number of water molecules in the first, second, and third solvation shells, respectively, $m+q+r = n$, and m = CN. From these structures, we retain the most stable isomers for each n and m. Figure 2.1 shows the 10 smallest clusters out of the 23 considered here, with geometries and energies listed in our previous work (Fifen and Agmon 2016). For given m, the Na^+–O distance in the first hydration shell decreases with increasing n, due to enhanced electron donating strength of the water oxygen (water cooperativity). This effect seems to saturate around $n = 7$, but actually reverses for larger clusters (not studied here). Hence, to mimic the bulk limit we also apply a dielectric continuum theory (PCM) (Tomasi, Mennucci, and Cammi 2005).

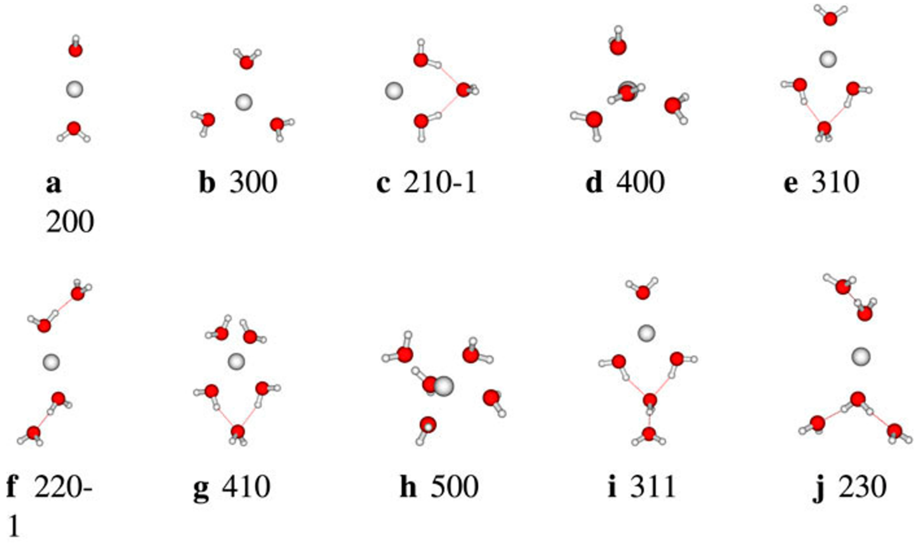

Figure 2.1. The first 10 (out of 23) clusters considered in this work. White sphere is Na^+.

The limiting (bulk) values of the Na^+–O distance (blue) are compared with crystal data (red) (Shannon 1976) in Figure 2.2. Due to the finiteness of the clusters, we only cover the behavior up to $m = 6$, whereas the crystal data span the range $4 - 12$. Our results, which are in agreement with the crystal data for $m = 4$, 5, & 6, show a notable effect of PCM only for the smallest clusters, when there is not enough water to solvate the cation. These data exhibit a double power law dependence: Small power for small m and large power for $m \geq 6$. At $m = 6$, the first solvation shell becomes critically crowded, accepting additional water ligands only after substantial increase in the solvation-shell radius.

Next, we use the electron density map to locate (via QTIM) (Bader, Anderson, and Duke 1979) the saddle points separating the electron density attributed to the sodium vs. the water oxygen. This bisects the Na^+–O distance into sodium (R_{Na}) and water (R_w) radii. One might expect R_{Na} to decrease with increasing n or decreasing m, as observed for the Na^+–O distance, with roughly constant R_w. We find that R_w is not at all constant, likely due to transfer of electron density from the water to the sodium cation: With increasing n and decreasing m, the water becomes a better electron donor (hence, R_w shrinks) and the water-sodium interaction resembles more a covalent bond. Ionic bonds occur in the opposite limit, of large CN.

Thermally Induced Hydrogen-Bond Rearrangements in Small Water Clusters and the Persistent Water Tetramer

in collaboration with Nagaprasad Reddy Samala (Samala, Nagaprasad Reddy and Agmon, Noam 2019)

Small water clusters absorb heat and catalyze pivotal atmospheric reactions. Yet, experiments produced conflicting results on water cluster size distribution under atmospheric conditions. Additionally, it is unclear which “phase transitions” such clusters exhibit, at what temperatures, and what are their underlying molecular mechanisms. We find that logarithmically small tails in the radial probability densities of $(H_2O)_n$ clusters ($n = 2 – 6$) provide direct testimony for such transitions.

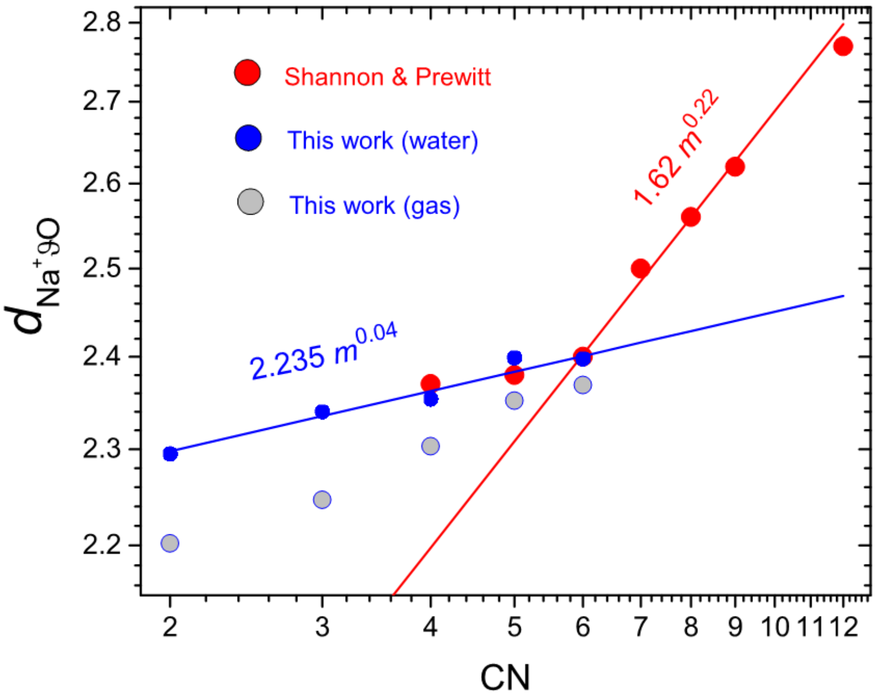

Figure 2.2. Coordination-number dependence of the sodium cation-water distance in “limiting” clusters (of $n = 7$). No PCM in gray, or with PCM in blue.Crystal data (red) collected by Shannon & Prewitt, see (Shannon, 1976).

Older classical molecular dynamics (MD) studies suggested that water clusters show a “melting” phase transition that can be observed as “jumps” in the average total (or kinetic) energies as a function of temperature, T (“caloric curves”). We have used the most up-to-date water potential, MB-pol (Reddy, Straight, et al. 2016), which is based on many-body interactions with parameters fitted to some 5000 quantum chemistry calculations at the CCSD(T) level. It is believed to give the best overall description of water across phase boundaries (excepting water dissociation). Our classical MB-pol simulations, over a wide temperature range, exhibit strictly linear caloric curves (Figure 2.4). There are no “jumps” that could be interpreted as abrupt changes in heat capacity (C_V) across phases.

As we are dealing with “equilibrium” structures (averages over a trajectory), we considered the familiar radial distribution function, $g(r)$, which is the particle density at distance, r, from a given observation point. It shows a wavy behavior indicative of solvation layers. In bulk liquids, it goes asymptotically to unity, where structure is no longer observable. In contrast, in the gas-phase $g(r) \to 0$, because there are no atoms at large distances from the molecule/cluster. Taking $(H_2O)_4$ as an example, Figure 2.5 shows $P(r) \equiv r^2 g(r)$ for the oxygen atoms of the water tetramer at two temperatures. On the linear scale (upper panels) there are no surprises: One observes two peaks corresponding to first- and second-neighboring O atoms. On a logarithmic scale and low T similar behavior is seen (not shown here). However, at higher temperatures a tail is visible. It is not a statistical error, but rather due to molecules occasionally undertaking long excursions. A notable tail first appears near 200 K, which is the “melting transition” of the cluster. However, it does not extend to long distances. This occurs near 240 K, the cluster “vaporization transition”, when monomers begin dissociating from the cluster.

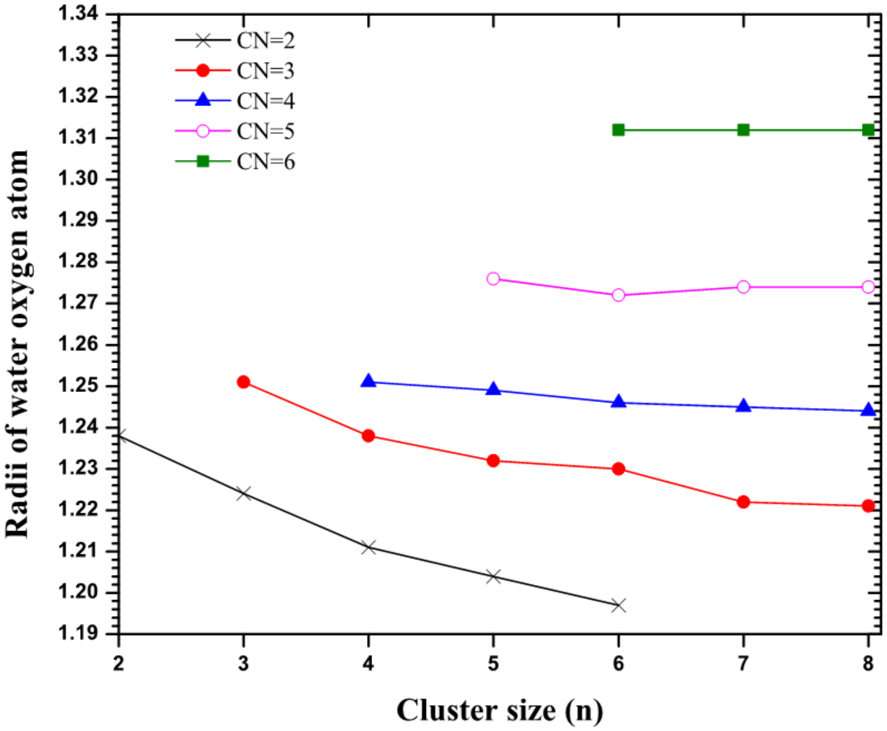

Figure 2.3. Dependence of the water radius on the CN of the central sodium cation and the overall number (n) of water ligands in the cluster.

Table 2.1: Transition temperatures (in K) for HB rearrangement events in small water clusters, using $\geq$ 3 ns MB-pol trajectories.

cluster/event	AS	B	melting	vaporization
dimer	30	50	110	140
trimer	20	75	140	213
tetramer	50	100	200	240
pentamer	10	85	125	210
hexamer			115	205

This interpretation is verified by considering the shift in the 2^{nd} peak of this distribution, $<r_2>$, as a function of T (Figure 2.6). Overall, $<r_2>$ increases, meaning that the cluster thermally expands. However, with sufficiently accurate data (trajectories longer than 3 ns) it becomes evident that this increase is piecewise linear. Discontinuities in the slope occur exactly at the transition temperatures identified in Figure 2.5. The growing tail seen in Figure 5 as T increases above a transition temperature leads to the faster increase in $<r_2>$.

The microscopic (molecular) events associated with these "phase" transitions are identified by visualizing trajectories near the transition temperatures (Figure 2.7). In stage A, one HB detaches, and the free H atom interacts with the next nearest O atom. This forms a trimeric ring, with the 4^{th} water molecule on its surface (B). This molecule reorients to become a HB acceptor (C). The free H again attacks the next nearest neighbor O atom (D), reforming the ring in a different order. The occasional residence of a water molecule outside the ring (B & C) leads to the small tail in Figure 2.5. Close to T_V, this lone water can move away from the trimer to very large distances (E). It

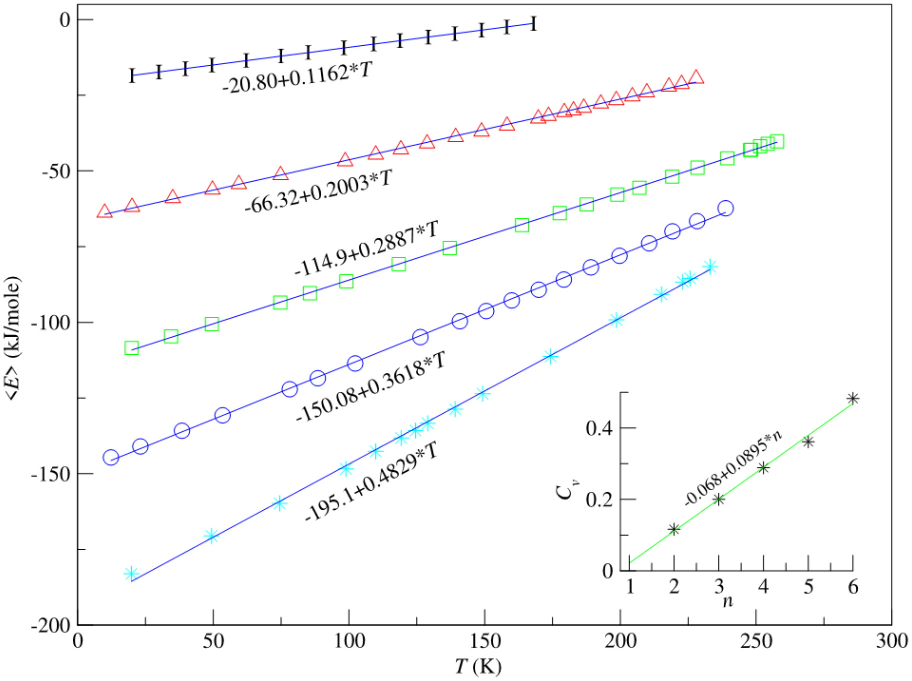

Figure 2.4. Average (over time) total energies of small water clusters from classical MB-pol NVT trajectories as a function of T. Bars – dimer, triangles – trimer, squares – tetramer, circles – pentamer and asterisks – hexamer. The temperature dependence is fitted to a linear function written under each respective line. The inset shows their slope (the “heat capacity”) as a function of the cluster size.

eventually returns, unless T is further increased and then it dissociates. Such “critical fluctuations” near T_V are the finite cluster manifestation of the analogous fluctuations in bulk water at the critical point (leading to the phenomenon of critical opalescence).

Results from all clusters studied are summarized in table 2.1 above. Remarkably, the water tetramer has the highest T_m and T_v of all clusters. This suggests a scenario in which large water clusters formed in humid regions at sea elevation fragment, elevate and cool until T_v of the tetramer is reached. Below T_v, it fragments no more, while the other clusters do, a process that enriches the atmosphere in water tetramers (Figure 2.8). Under favorable conditions, therefore, the tetramer may be a central player in atmospheric chemistry.

Temperature & Nuclear Quantum Effects on the Vibrational Spectra

1*in collaboration with Nagaprasad Reddy Samala (Samala and Agmon 2019; Samala, N. R. and Agmon, Noam 2020)*

From the classical MB-pol trajectories described above, we have also calculated the intramolecular vibrational spectra (OH stretch and HOH bend) for the $(H_2O)_n$ clusters ($n = 2 - 6$), and their temperature dependence. For the hexamer, we calculated the low T (10 K) spectra for the four lowest energy conformers (book, cage, prism and ring), but the temperature dependence only for the cage. This is because the other conformers convert to the cage isomer as T increases. The spectra were calculated from the Fourier transform of the velocity autocorrelation function (VACF), of either all atoms, or of the OH distances for the free vs HBed H atoms. We did not calculate the dipole-moment autocorrelation, because the dipole surface for MB-pol was not made

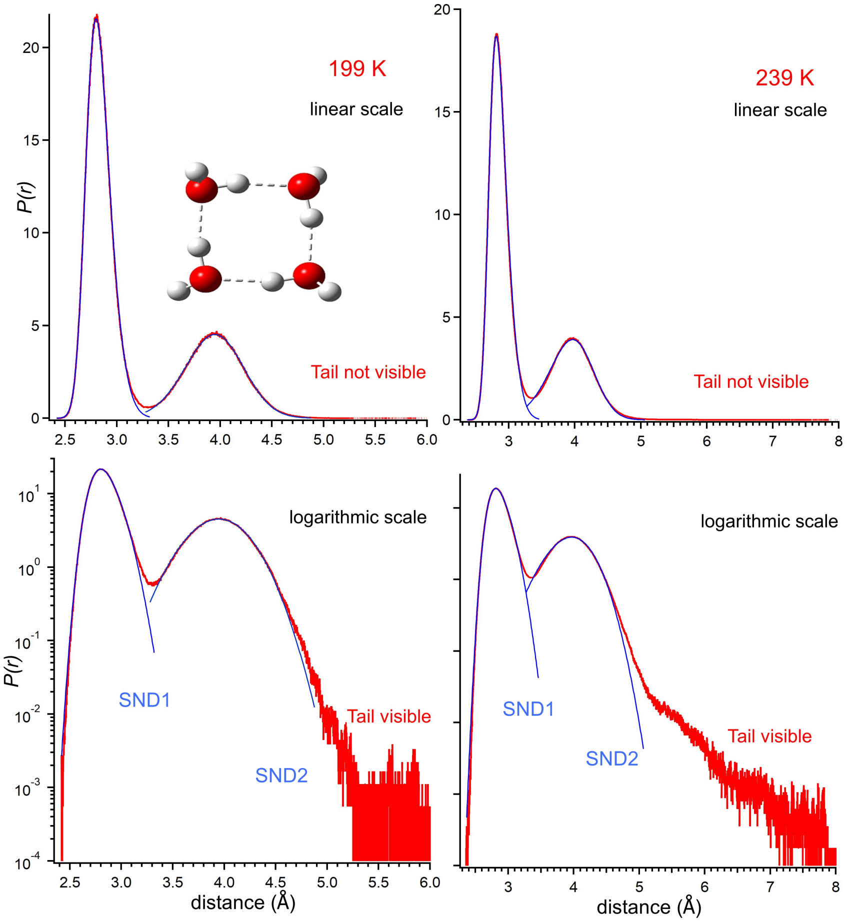

Figure 2.5. Averaged $r^2 g(r)$ for the oxygen atoms of the water tetramer. Upper panel – linear scale; lower-panel – logarithmic scale. Blue lines show a best fit to a skewed-normal distribution (SND) for each of the two peaks.

public. However, in our earlier *ab initio* molecular dynamics (AIMD) simulations we have found that the VACF and DACF spectra agree very well for the frequencies (to within $1-2$ cm^{-1}), and only the intensities differ.

Clearly, however, the frequencies do depend on the quantum nature of the H atoms. This nuclear quantum effect (NQE) red-shifts all frequencies, particularly the OH stretches. To get the spectra right, one should perform quantum (rather than classical) nuclear simulations, which can be done above say, 230 K. Unfortunately, for the low temperature regime studied here, methods based on Feynman-like path-integral molecular dynamics have very large errors. Instead, we take advantage of the recent observation that for bulk water and ice (above 230 K), the quantum and classical frequencies differ by a temperature-independent constant (Reddy, Moberg, et al. 2017). We have found that this holds also for water clusters at low *T*, allowing us to accurately correct the classical calculations for NQE. This leads to a first determination of NQE dependence on the cluster size ($n = 2-5$), and the $(H_2O)_6$ conformer.

Considering, again, the tetramer as an example, Figure 2.9 shows the simulated (MB-pol) spectrum in the OH-stretch region as a function of *T*. Black lines depict the spectra based on the all-H atom VACFs, whereas the colored lines are based on partial VACFs of free (blue) or HBed (red)

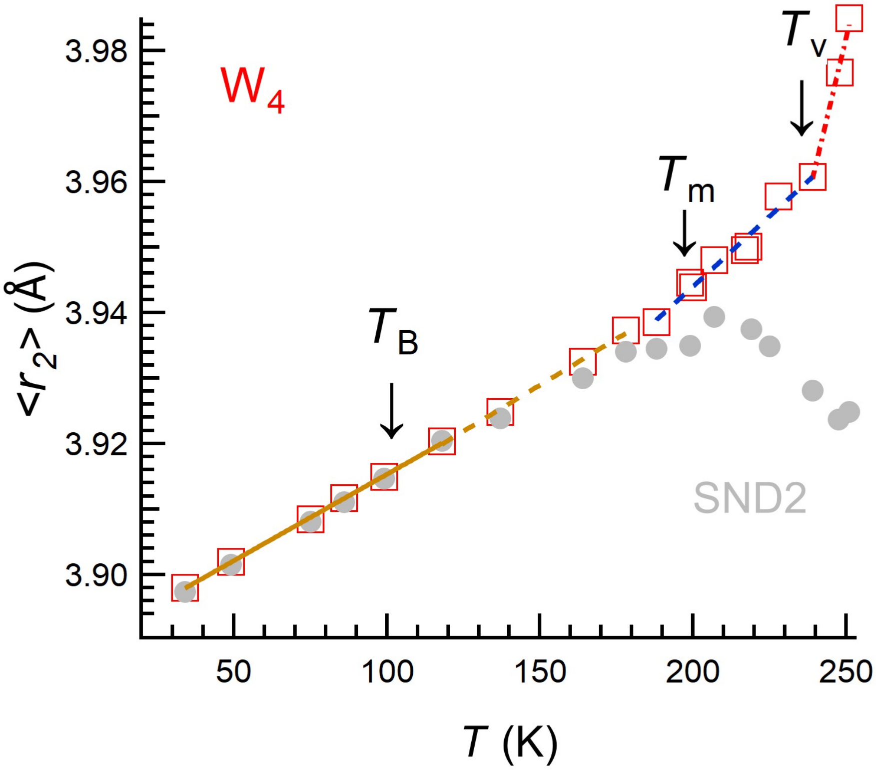

Figure 2.6. The O—O distance, averaged over the 2^{nd} peak in $P(r)$, shown for the water tetramer as a function of temperature. The marked transition temperatures are the onset of bifurcation, melting and vaporization events (see Table 2.1) .

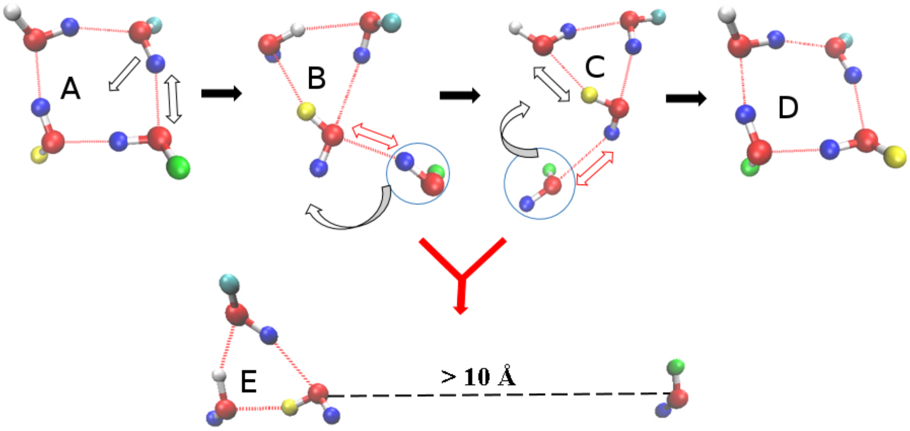

Figure 2.7. A schematic sequence of molecular events characterizing the "melting" and "vaporization" transitions in the water tetramer. The sequence ABCD leads to water molecule exchange within the ring, which is the onset of melting. In the "vaporization" transition, step E is added (dissociation onset). Oxygen atoms – red, hydrogen atoms – various colors to allow one to follow the sequence of events.

OH moieties. As T increases (99 K), these couple and the same spectrum is generated from all OH oscillators. The lone peak at high frequencies is assigned to the free OH, whereas the bands at low

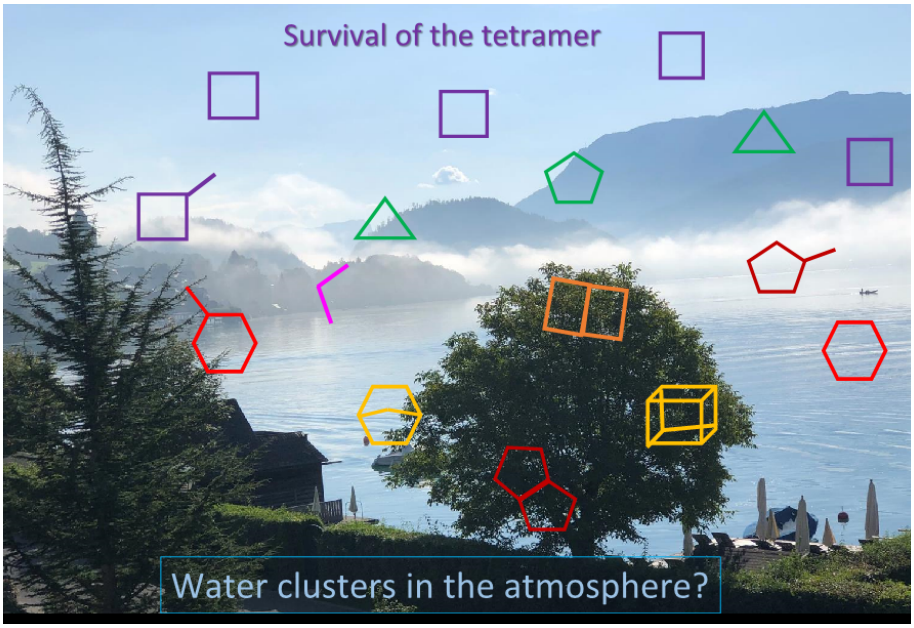

Figure 2.8. A possible mechanism for injecting water clusters into the atmosphere. Water vapor from the lake is rich in large water clusters that fragment and cool as they rise, until the vaporization temperature of the tetramer is reached. Supplementary cover of ACS Omega.

frequencies are assigned to the four HBed OH moieties. From the overall VACF, there seem to be only three such bands, but the partial VACF at 49 K (red line) shows that the middle band is split, so there are four bands as expected.

Qualitatively, one can understand the spectra with the aid of the schematic depiction in Figure 2.10 (a detailed theory is given in our papers). There are 4 coupled OH-bonds (harmonic oscillators) in a ring, leading to a spectrum analogous to the Hückel theory for cyclobutadiene. When all H-atoms move concertedly (Raman active A mode) there is minimal repulsion between them and hence this is the most red-shifted band. Conversely, for the antisymmetric B mode, all H atoms move in anti-phase, resulting in maximal repulsion. In between, there is the doubly-degenerate, IR-active E mode. In our simplified model, the Hamiltonian matrix for the system is written in terms of two force constants: The O—H bond is characterized by a force constant k, and the coupling between H atoms on the ring, by a force constant κ. With increasing T, k increases (due to weakening HBs) while κ decreases. This leads to blue-shifts in all the bands, but more so for the A mode, as seen indeed in Figure 2.9. The blue-shifted frequencies depend linearly on T(not shown), and no evidence for phase transitions is manifested in the IR spectra.

In order to compare with experimental data, we find the best NQE shifting constant, here 188 cm^{-1}. Subtracting this from the calculated frequencies gives the frequencies in Table 2.2 below. At low temperatures (20 K) we compare the E mode with the IR band of water in a Ne matrix. At 50 K, we compare with the only molecular beam measurement of the temperature effect (Zischang and Suhm 2014). The mean absolute deviation (MAD) is only $2-3$ cm^{-1}, attesting to the accuracy of both the MB-pol potential and the NQE shifting assumption. In comparison, 2nd order vibrational perturbation theory (VPT2), which calculates both anharmoicities and NQEs from first principles, shows a much larger deviation from experiment.

With this level of accuracy, we get a first determination of the NQE shifts for the water OH stretching bands. We find 174, 188, and 204 cm^{-1}, for n = 3, 4, and 5 water rings, respectively.

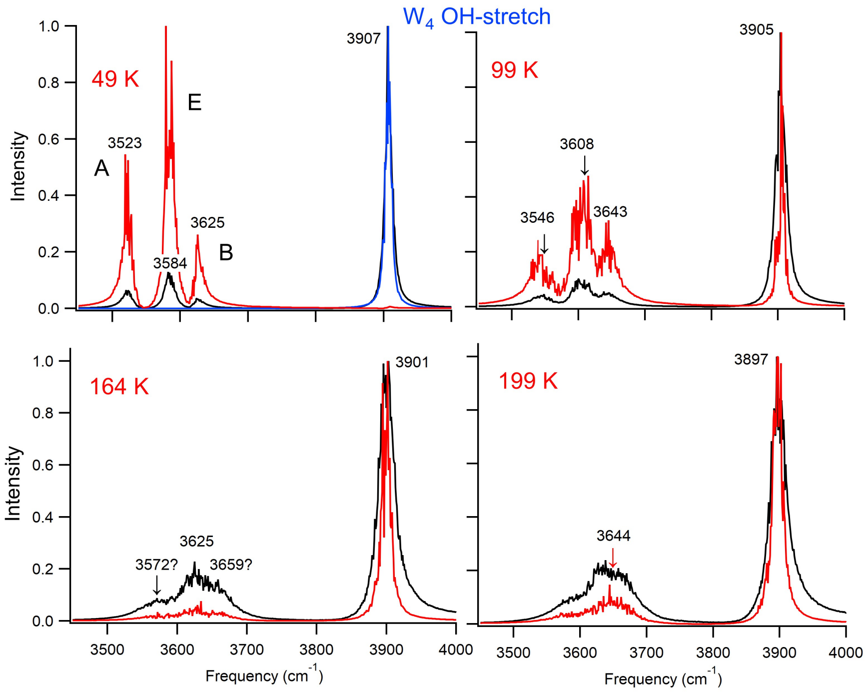

Figure 2.9. Vibrational VACF spectra for the water tetramer (ring isomer) at 4 temperatures, in the OH-stretch region of the spectrum. Black lines are the full VACF spectra, for all H atoms; blue line – only for the four free OH distances; red – only for the four HBed OH moieties. Note that the frequencies here have not yet been corrected for NQE.

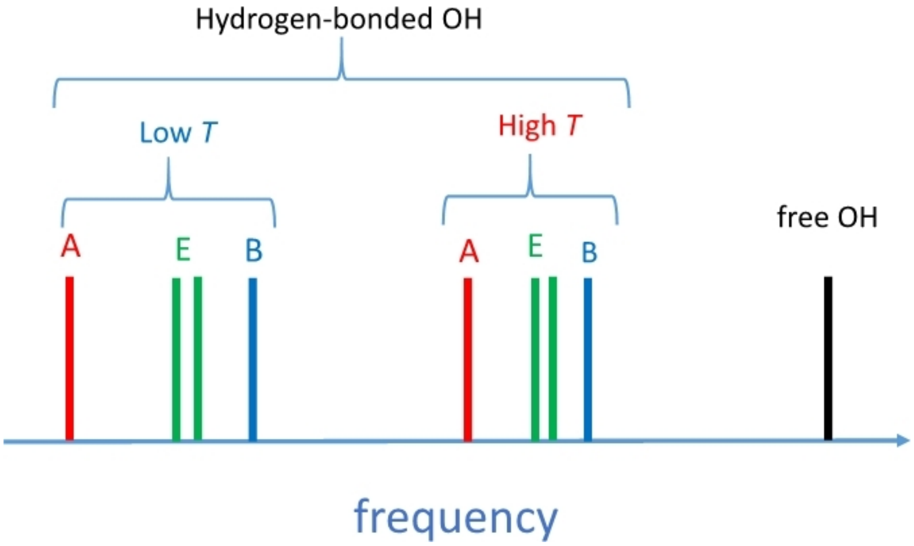

Figure 2.10. Schematic depiction of the temperature dependence of the HBed OH tetramer bands.

This nearly linear increase with cluster size, n, becomes more pronounced for $n = 6$. Here we distinguish between the different 4 conformers. The ring and the book conformers are nearly two dimensional, while the added HBs in the cage and prism renders them the smallest three-dimensional drops of water. Figure 2.11 shows these conformers next to their NQE shifts. The

Table 2.2: Computed vs. experimental intramolecular vibrational frequencies (in cm^{-1}) for the water tetramer

W_3, symmetry	VPT2 0 K	MB-pol 20 K	Ne matrix 3 K	MB-pol 49 K	gas-phase ≥50 K
HBed-OH					
A	3268	3323	-	3335	3334
E	3332	3387	3383	3396	3401
B	3363	3428	-	3437	-
free	3695	3722	3719	3719	3718
HOH bend					
E	1607	1625	-	1624	-
MAD	38	3	0	2	0

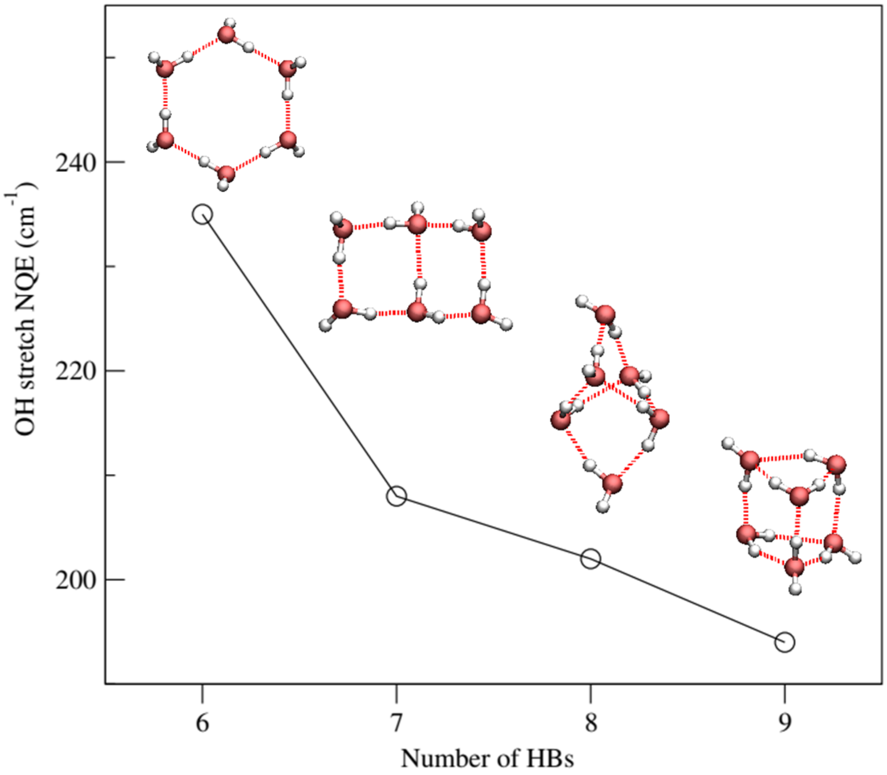

Figure 2.11. Red shift due to nuclear quantum effects on the OH stretching bands of the four lowest energy conformers of the water hexamer (top to bottom: ring, book, cage and prism). The NQE values shown (circles) were determined from the best agreement of shifted classical MB-pol VACF frequencies with those from low T experiments.

largest shift (larger than for hexagonal ice) is observed for the ring isomer. But as added HBs render the cluster more three dimensional, the NQE decreases, approaching the value (175 cm^{-1}) (Samala, Nagaprasad Reddy and Agmon, Noam 2019) for liquid water.

We tentatively ascribe the excess NQE (above that of liquid water) to water cooperativity and coupling between the OH oscillators, which is maximal for the A mode. This “resonance coupling”, maximal in the ring isomer, diminishes with added HBs as the rings (that can support concerted motions) become progressively smaller.

References

Bader, R. F.W., S. G. Anderson, and A. J. Duke (1979). “Quantum Topology of Molecular Charge Distributions”. In: *Journal of the American Chemical Society* 101, pp. 1389–1395. ISSN: 15205126. DOI: 10.1021/ja00500a006.

Fifen, Jean Jules and Noam Agmon (2016). “Structure and Spectroscopy of Hydrated Sodium Ions at Different Temperatures and the Cluster Stability Rules”. In: *Journal of Chemical Theory and Computation* 12.4, pp. 1656–1673. ISSN: 15499626. DOI: 10.1021/acs.jctc.6b00038.

Fifen, Jean Jules and Agmon, Noam (2019). “Ionic radii of hydrated sodium cation from QTAIM”. In: *Journal of Chemical Physics* 150.3, p. 034304. ISSN: 00219606. DOI: 10.1063/1.5020150.

Galib, M. et al. (2017). “Revisiting the hydration structure of aqueous Na+”. In: *Journal of Chemical Physics* 146, p. 084504. ISSN: 00219606. DOI: 10.1063/1.4975608.

Reddy, Sandeep K., Daniel R. Moberg, et al. (2017). “Temperature-Dependent Vibrational Spectra and Structure of Liquid Water from Classical and Quantum Simulations with the MB-pol Potential Energy Function”. In: *Journal of Chemical Physics* 147, p. 244504. ISSN: 00219606. DOI: 10.1063/1.5006480.

Reddy, Sandeep K., Shelby C. Straight, et al. (2016). “On the Accuracy of the MB-pol Many-Body Potential for Water”. In: *Journal of Chemical Physics* 145, p. 194504. ISSN: 00219606. DOI: 10.1063/1.4967719. arXiv: 1609.02884.

Samala, Nagaprasad Reddy and Noam Agmon (2019). “Temperature Dependence of Intramolecular Vibrational Bands in Small Water Clusters”. In: *Journal of Physical Chemistry B* 123, pp. 9428–9442. DOI: 10.1021/acs.jpcb.9b07777.

Samala, N. R. and Agmon, Noam (2020). “Temperature and Nuclear Quantum Effects on the Stretching Modes of the Water Hexamer”. In: *The Journal of Physical Chemistry A* 124, pp. 8201–8208. ISSN: 1089-5639. DOI: 10.1021/acs.jpca.0c05557.

Samala, Nagaprasad Reddy and Agmon, Noam (2019). “Thermally Induced Hydrogen-Bond Rearrangements in Small Water Clusters and the Persistent Water Tetramer”. In: *ACS Omega* 4, pp. 22581–22590. ISSN: 2470-1343. DOI: 10.1021/acsomega.9b03326.

Shannon, R D (1976). “Revised Effective Ionic Radii and Systematic Studies of Interatomic Distances in Halides and Chaleogenides”. In: *Acta Cryst. A* 32, pp. 751–767.

Tomasi, Jacopo, Benedetta Mennucci, and Roberto Cammi (2005). “Quantum mechanical continuum solvation models”. In: *Chemical Reviews* 105.8, pp. 2999–3093. ISSN: 00092665. DOI: 10.1021/cr9904009.

Zischang, Julia and Martin A. Suhm (2014). “The OH Stretching Spectrum of Warm Water Clusters”. In: *Journal of Chemical Physics* 140, p. 064312. ISSN: 00219606. DOI: 10.1063/1.4865130.

Scientific activities

Noam Agmon group members

Name	Project	Status	Period
Nagaprasad Reddy Samala	Water clusters	PostDoc	2016-2019
Satyaranjan Biswal	Proton transport in collagen	Ph.D student	2020-

Noam Agmon scientific collaborations

Name	Project	Institution
Peter Pohl	Proton transport on the hydration layers	Linz, Austria
Jochen Hub	Subject to be determined	Saarland University, Germany
Ana-Nicoleta Bondar	Mapping water wires within and on the surface of the green fluorescent protein	FU Berlin, Germany

Noam Agmon active grants

Project	Period	Foundation	Total grant in thousands
Proton Transport and Proton-coupled Transport	2019-2023	Horizon 2020 Innovative Training Network (ITN)	€263.5
Temperature Dependence of Cyclic Water Clusters in the Atmosphere and the Supercooled Liquid	2019-2023	ISF	₪880

2.2 Roi Baer

Research Activities

Transition to metallization in warm dense helium-hydrogen mixtures

in collaboration with Ronald Redmer of Rostock Univ Ref. Y Cytter Phy Rev B 100, 195101, 2019

The Kubo-Greenwood (KG) formula is often used in conjunction with Kohn-Sham (KS) density functional theory (DFT) to compute the optical conductivity, particularly for warm dense mater. For applying the KG formula, all KS eigenstates and eigenvalues up to an energy cutoff are required and thus the approach becomes expensive, especially for high temperatures and large systems, scaling cubically with both system size and temperature. Here, we develop an approach to calculate the KS conductivity within the stochastic DFT (sDFT) framework, which requires knowledge only of the KS Hamiltonian but not its eigenstates and values. We show that the computational effort associated with the method scales linearly with system size and reduces in proportion to the temperature unlike the cubic increase with traditional deterministic approaches. In addition, we find that the method allows an accurate description of the entire spectrum, including the high-frequency range, unlike the deterministic method which is compelled to introduce a high-frequency cut-off due to memory and computational time constraints. We apply the method to helium-hydrogen mixtures in the warm dense matter regime at temperatures of ~ 60kK and find that the system displays two conductivity phases, where a transition from non-metal to metal occurs when hydrogen atoms constitute ~ 0.3 of the total atoms in the system.

We study the conductivity and DOS of various hydrogen-helium mixtures at temperature of 57kK and constant volume. For each system, we obtained a set of thermally-distributed nuclear configurations using the electron force-field (eFF) dynamics as implemented in LAMMPS , which has been shown to give a good description of the pair correlation and equations of state of first-row materials under extreme conditions. For He_{128} at 57kK we generate a set of Boltzmann-distributed

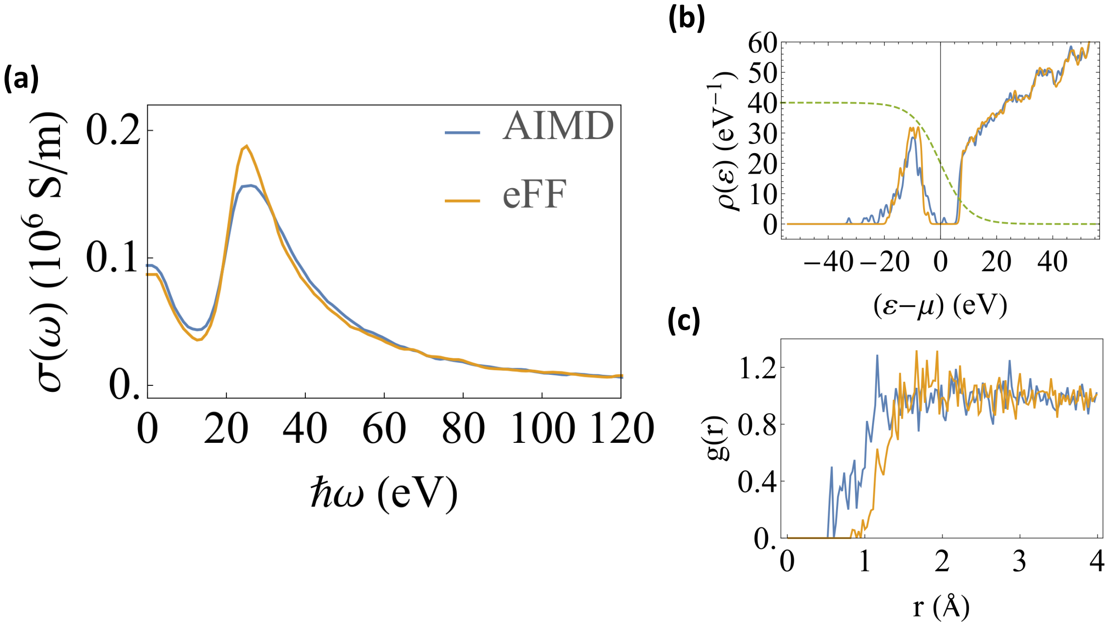

Figure 2.12. Comparison of the calculated conductivity $\sigma(\omega)$ (a), the DOS $\rho(\varepsilon)$ (b) and the radial pair correlation $g(r)$ (c) for He$_{128}$ at 57kK and density of $0.75\frac{\text{g}}{\text{cm}^3}$ based on configurations generated by AIMD (Presining2018) vs. eFF dynamics. The dashed line in panel (b) shows the Fermi-Dirac level occupation, transiting from a value of 1 at low energies ε to 0 at high energies .

configurations using both an empirical force field and an *ab inito* approach taken from Preising et al. The configurations where then used to average the results over the thermal fluctuations of the nuclei. In Fig. 2.12 we compare the two sets of results and show that while giving two visibly different spectra they share similar trends with peaks/troughs located at nearly identical frequencies. Comparing the two DOSs we see small differences in the occupied state energies while being nearly identical at the unoccupied state energies. Comparing the correlation functions $g(r)$, we find that AIMD gives significant weight to He pairs approaching as close as 0.5Å while the eFF does not. Both functions show a peak at 1.1Å, but it is more significant in AIMD. It is perhaps surprising that despite the rather large differences in the pair correlation between the two methods, the electronic properties, as mentioned above, are not very different.

We characterize the mixture by the hydrogen fraction in the system

$$X_{\mathrm{H}} = \frac{N_{\mathrm{H}}}{N_{\mathrm{H}} + N_{\mathrm{He}}} , \tag{2.1}$$

where N_{H} and N_{He} are the number of hydrogen and helium atoms, respectively. For practical purposes, this ratio is achieved by holding the total number of atoms $N_{\mathrm{H}} + N_{\mathrm{He}}$ in the simulation cell constant and equal to 1024.

We ran five molecular dynamics trajectories at fixed volume (minimum image periodic boundary conditions for $L = 39.4\,a_0$) and temperature (T = 57kK) with interactions between He and H described by the eFF force-field with a cutoff of 6.45a_0. Each trajectory started with the same ordered configuration, and a different velocity allocation, equilibrated, and then ran for a total of 3ps with time step of 10^{-3}fs, needed due to consideration of both electronic and nuclear time scales. The duration of the trajectories corresponded to the correlation time of 3ps estimated using the same data. The final nuclear configuration for each trajectory represented a set of five uncorrelated H-He mixtures. For each structure, a sDFT calculation determined the Hamiltonian $\hat{h}$ which

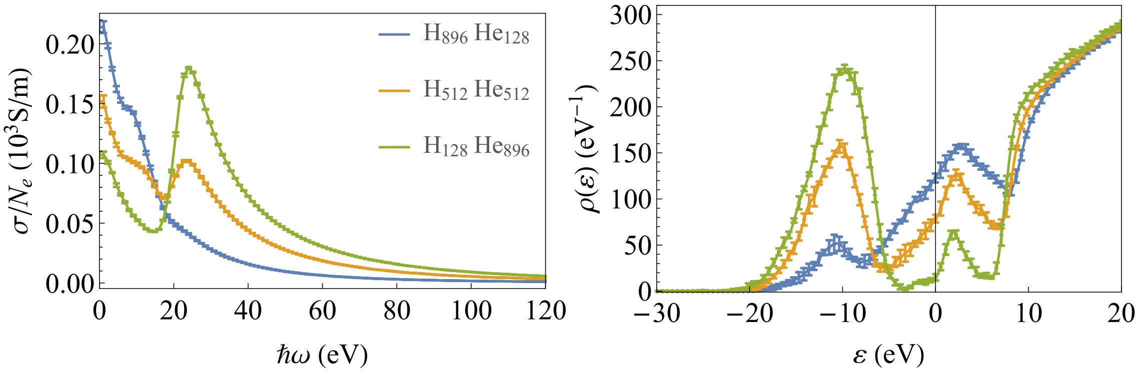

Figure 2.13. The Conductivity (upper panel) and the DOS (lower panel) of different H-He mixtures containing 1024 atoms with different hydrogen percentages at $T = 57$kK and an average atomic volume of $60\, a_0^3$ per atom. The conductivity was normalized according to the number of electrons in the system. The DOS is shifted so that the chemical potential is zero.

was used for the sKG calculation of the conductivity spectrum. For both sDFT and sKG an identical simulation box and grid of $N_g = 120^3$ points was used which correspond to a grid spacing of $\delta x = 0.33\ a_0$. The sDFT calculation was based on $I_H = 120$ sDFT-o's and the sKG calculation used a distinct set of $I_\sigma = 120$ sKG-o's.

In Fig. 2.13 the conductivity spectra and the density of states (DOS) for three different mixtures is displayed. These two characteristics are closely related and will therefore be discussed together. The statistical fluctuation in the DOS (lower panel), denoted as error bars, was determined by running sDFT calculations on the five distinct configuration snapshots as described above, each using a different set of sDFT-o's. These five Hamiltonians were then used for evaluating the conductivity (upper panel) employing a different set of sKG-o's to avoid additional bias. The resulting five conductance spectra and DOS were used for estimating the thermally-averaged curves and their associated statistical errors. It is seen in the upper panel of Fig. 2.13, that the statistical fluctuations are small compared to the difference between the curves and they do not seem to increase as a function of the hydrogen atomic fraction X_H and therefore, only one snapshot was used in all other calculations.

When a relatively small fraction of hydrogen atoms is present in the system, it gives rise to a small peak at 3eV inside the Helium energy gap in the DOS (see the lower panel of Fig. 2.13). As the hydrogen concentration increases the He gap fills with states until it is no longer visible and at the same time the DOS of the valence band (seen in the figure at around -10eV), decreases steadily. Both effects show a gradual transition to metallization as the hydrogen ratio grows. At high energies the DOS of all mixtures converges to the free electron limit.

The sKG conductivity follows the changes seen in the DOS. Consider first the DC conductivity, shown in the lower panel of Fig. 2.14, which remains relatively constant as the hydrogen fraction grows until $X_H^{crit} \sim 0.3$. Beyond this value of the hydrogen fraction the DC conductivity increases near-linearly with χ_{H} as a result of the energy gap filling in the DOS, allowing more transitions at low energies. Due to the finite temperature and therefore partial occupation there exists zero frequency transitions even at helium dominated systems causing the DC conductivity to change only by a factor of 2.5 when moving from pure helium to pure hydrogen systems. The peak in the He dominated spectrum, as seen in the upper panel of Fig. 2.13, appears at around 25eV and corresponds to the transition from the highest density in the occupied band to the non-occupied band threshold levels (as seen in the DOS at 10eV). Furthermore, at higher He concentrations due to the energy gap, transitions in 15eV become less probable, resulting in a local minimum in the conductivity at this frequency.

Next, we consider the frequency ω_{max} for which the conductivity is maximal, plotted as a

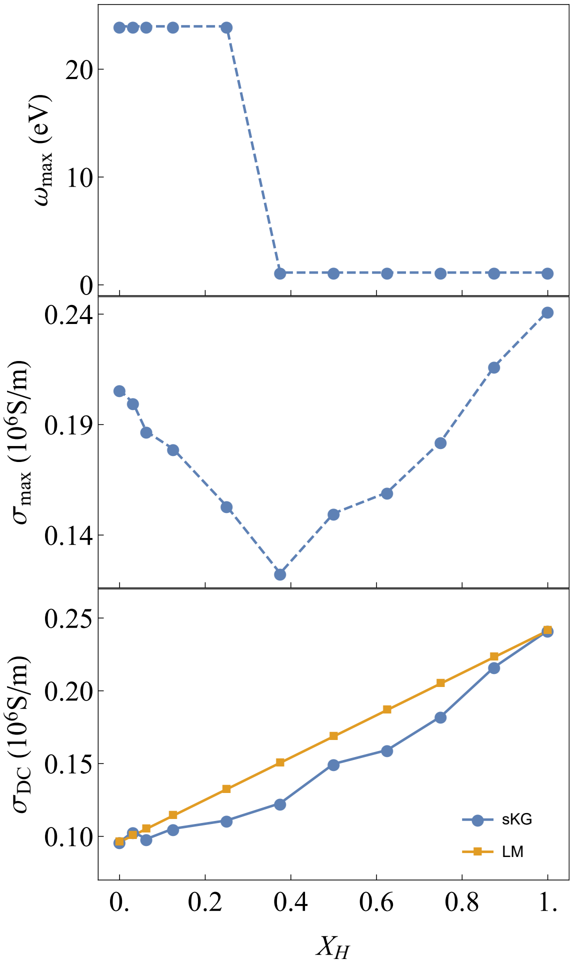

Figure 2.14. The maximal conductivity frequency ω_{max} (top panel), maximal conductivity σ_{max} (middle panel) and the DC conductivity of the actual (round blue markers) and the linear-mixing model σ_{LM} (square orange markers), as a function of the hydrogen ratio X_H in He-H mixtures.

function of X_H in the top panel of Fig. 2.14. This frequency displays an abrupt shift of ω_{max} from ~ 25eV to 0 (DC) as X_H passes through the critical value of $X_H^{crit} \sim 0.3$. This critical value, indicates an abrupt nonmetal-to-metal transition in the H-He system as reported in (Lorenzen 2011) for considerably lower temperatures. This critical hydrogen concentration is well withing the range of the Mott criterion for metallization in pure hydrogen, as seen in Lorenzen 2009 that shows it occurs at $n_H^{1/3} a_0 \approx 0.25$ for temperatures up to 15kK. In the present system, we find the metallization density at $n_H^{1/3} a_0 \approx 0.18$, which seems reasonable considering the fact that we're looking at a substantially higher temperature in which thermal effects promote the conductivity onset.

The finite ω_{max} is a results of the energy gap in what is generally an insulating system (He dominated) and the zero ω_{max} signifies its disappearance, allowing many of the energy transitions to occur at infinitesimal energy values. In the middle panel of Fig. 2.14 the transition through X_H^{crit} is seen as a qualitative change in the behavior of the maximal conductivity σ_{max}, which initially decreases as X_H approaches X_H^{crit}, and then increases as X_H grows further.

Finally, we compare the spectra in the different concentrations to a model of linear averaging

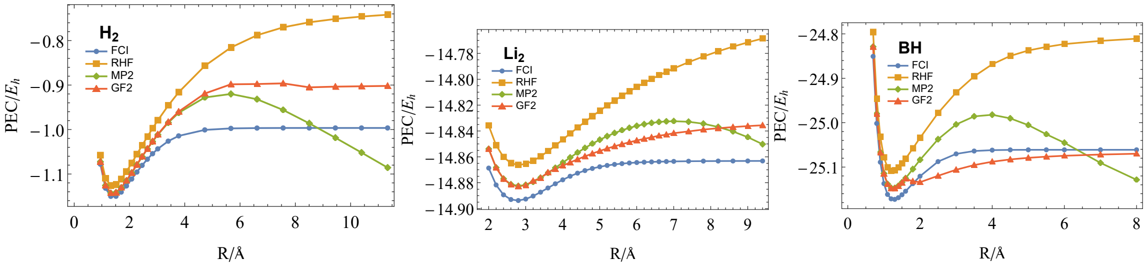

Figure 2.15. The Born-Oppenheimer potential curves for H_2, Li_2 and BH molecules in the 6-31G basis set as a function of the atomic distance R. Shown here the results obtained from FCI, RHF, MP2 (all computed by using GAMESS), and GF2 based on our code.

of pure helium and pure hydrogen spectra, defined as

$$\sigma_{\text{LM}}\left(X_{\text{H}};\omega\right)=X_{\text{H}}\sigma\left(1;\omega\right)+\left(1-X_{\text{H}}\right)\sigma\left(0;\omega\right)\ . \tag{2.2}$$

It can be seen in the lower panel of Fig. 2.14 that the DC conductivity $\sigma_{LM}\left(X_{\text{H}};0\right)$ based on the linear averaging model is typically greater than the corresponding value calculated using sKG. This is due to the fact that in the actual system the environment each atom experiences includes, on the average, a mixture of He and H atoms while in the linear averaging model each atom is surrounded by atoms of its own kind.

Matsubara Green's function approach for breaking chemical bonds

in collaboration with E. R. Haddad

Despite ingenious theoretical and computational advances over recent decades, we are still lacking in a generally applicable and usefully accurate approach for describing and predicting the energetic landscape of molecular bond breaking. As a result, we cannot offer reliable predictions of bond enthalpies, activation energies, and estimates of reaction rates for most molecular reactions of current interest. This situation occurs because the electronic structure at bond-breaking is a strongly-correlated electron system, which is notoriously complicated. Two general types of electron correlations are of importance in bond-breaking: dynamical correlations, due to the intricate motion of mutual electron collisions, and static correlations, which involve (near) energy degeneracy in the electronic ground state. The methods for addressing dynamical correlations are highly successful in the absence of static correlation but often break down catastrophically in its presence.

We aim to explore and develop a Green's function approach to molecular bond breaking. We started by creating a computer code implementing a second-order perturbative approximation to Dyson's self-energy in the formally-exact finite-temperature Matsubara Green's function framework. This approach has been dubbed GF2 and has sparked renewed interest in recent years through the works of D. Zgid and where the energy can be calculated using the Galitski-Migdal formula. The method is self-consistent and includes a mechanism to handle static correlations (as done in the MCSCF approaches). The approximation to the self-energy is based on similar formal developments as in MP2 theory and enables the treatment of dynamical correlations. The existence of mechanisms within the Matsubara-Dyson approach to handling both the static and dynamic correlations makes the framework attractive for treating bond breaking.

In Fig. 2.15 we show several approximations to the Born-Oppenheimer potential energy curves (PECs) for the molecules H_2, Li_2 and BH. The full-CI (FCI) PECs are the exact variational solutions of the many-body Schrodinger equation when the space of single-particle states is spanned by the 6-31G basis set. We see in all three molecules that the PEC based on the energy of the restricted

Hartree-Fock (RHF) method follows the FCI PEC closely in the "strongly bonded region" (near the minimum). However, for larger bond distances, it develops a strong spurious long-range attraction between the nuclei, rising way above the FCI PEC, a behavior stemming from the overly-ionic character of the RHF wave function. The MP2 PEC is based on a second-order perturbative correction to RHF theory. The correction is negative, and in the strongly-bonded region, it produces a PEC that is much closer to that of FCI. However, as the bond is stretched beyond a system-dependent critical distance, the MP2-based PEC generates an unphysical repulsive force between the nuclei as the PEC nose-dives indefinitely. This breakdown of MP2 a result of the energy gap between the RHF ground- and first-excited- states approaches zero (near-degeneracy in the RHF approximation).

The GF2 method involves a self-consistent calculation while also based on the second-order perturbation theory for the self-energy which is very similar formally to the MP2 approach. It is seen in Fig. 2.15 that in all three molecules the GF2 PEC is almost identical to that of MP2 in the strongly bonded region. As the bond is stretched further beyond the PEC minimum the GF2 energy strays from that of MP2. We see it does not take a nose-dive to negative paradise, a fact that happily shows that GF2 indeed can overcome the RHF degeneracy problem. Still, the second order approximation to the self energy is far from a success story. In Li_2 and BH, for example, there is still a significant force of attraction between the nuclei when in FCI it has died out. Furthermore, in BH we find a cusp in the PEC, which is difficult to understand.

Clearly, more work needs to be invested in order to understand the GF2 PECs. We plan to continue studying this with an eye for improving the self-energy.

Time-resolving the ultrafast H_2 roaming chemistry and H_3^+ formation using extreme-ultraviolet pulses

in collaboration with Ester Livshits and with Daniel Strasser and his group

The time-scales and formation mechanisms of tri-hydrogen cation products in organic-molecule-ionization processes are poorly understood, despite their cardinal role in the chemistry of the interstellar medium and in other chemical systems. Using an ultrafast extreme-ultraviolet pump and time-resolved near-IR probe, combined with high-level ab initio molecular dynamics calculations, we report unambiguously that H_3^+ formation in double-ionization of methanol occurs on a sub 100fs time-scale, settling previous conflicting findings of strong-field Coulomb explosion (CE) experiments. Our combined experimental-computational studies suggest that ultrafast competition, between proton- and long-range electron- transfer processes, determines whether the roaming neutral H_2 dynamics on the dication result in H_3^+ or H_2^+ fragments, respectively.

The left panel of Fig. (2.16) shows the potentials of the low- and the high-lying energy states of the methanol dication as a function of the CO stretch. The dynamics in the latter case typically results in rapid dissociation, accompanied by cleavage of the C-O bond as well as a three-body breakup. 16 In contrast, the dication formed in the low-lying states initially exhibits a potential charge imbalance that hinders direct CE due to the ∼3eV potential barrier indicated in Fig. (2.16). As a consequence dynamics on the low-lying states are prolonged and highly complex, involving the emergence of a roaming neutral H_2.

The right panel of Fig. (2.16) compares the simulated branching ratios for the H_3^+ product of roaming H_2, with the combined branching ratio for the three-body breakup channels, calculated for each initial excitation of the methanol dication. Over 1/3 of the ground-state trajectories produce H_3^+ , this compared with ∼4% obtained in previous ground-state simulations that did not include the 2nd order perturbation theory corrections. The high H_3^+ formation probability on the ground state, drops for the higher lying states and is completely quenched once the CO bond cleavage becomes possible above the third excited state. In contrast, the three-body breakup exhibits an opposite trend, which increases for higher-lying excited states.

These theoretical prediction provides a handle for the experimental time-resolved probing of the dynamics using a delayed nIR pulse, following excitation with the ultrafast EUV pulse. Where

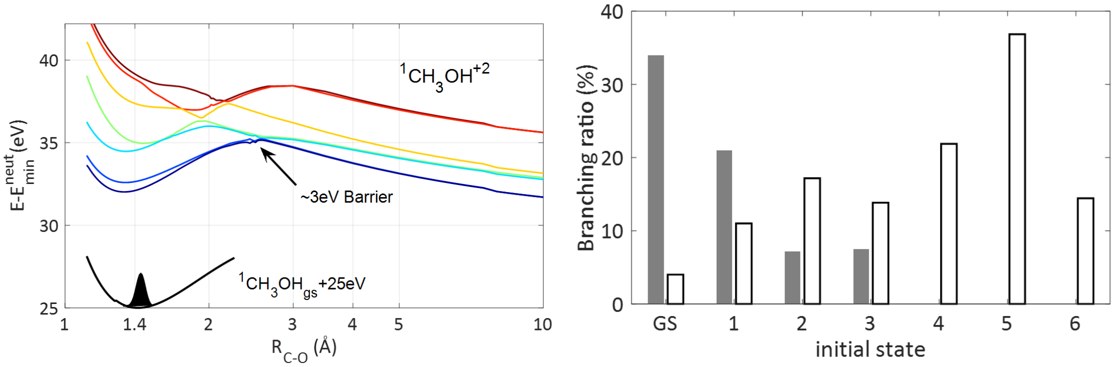

Figure 2.16. Left: The adiabatic potential curves for the C-O bond breaking channel of CH_3OH^{2+} using MS-CASPT2/(12e,10o)/aug-ccpVTZ.16 As the C-O strech coordinate is extended away from the Frank-Condon geometry of the neutral methanol ground state, shown by the black curve, the dication potentials exhibit a ~3eV barrier that prevents the C-O bond breaking on the low lying states. . The potentials are calculated while keeping all other coordinates at their neutral methanol ground state value. Right: AIMD simulated branching ratio as function of the initial dication state: full bars representing H_3^+ formation probability and empty bars representing the probability of three-body breakup.

the time delayed probe will excite the transient dication to higher-lying states, consequently quenching H_3^+ formation and enhancing three-body breakup. However, once the excess internal energy is released in a successful Coulomb explosion, the product branching is expected to be less affected by the probe pulse.

In designing the probe pulse, we ensure that its peak intensity is kept well below the threshold for strong-field CE, such that at long negative time delays the branching ratios are identical to the ratios measured with the EUV pulse alone. In particular, the H_3^+ formation branching ratio is 6% and the three-body to two-body ratio is 3 to 1. The effect of the nIR probe pulse delay (with respect to the EUV pulse) on the relative enhancement of the three:two body ratio is shown in Fig. 3a. The three:two body ratio increases by up to ~8% at positive time delays, as the nIR probe arrives shortly after the dication formation. This effect decays as the probe pulse arrives and positive time delays longer than ~70fs. For comparison, Fig. 3b shows the enhancement of doubly-ionized Ne^{2+} yield as a function of the nIR probe delay that reflects the instrumental response time. The full line in Fig. 3b represents a fit of the Ne^{2+} yield, assuming photoionization of high lying Ne^{+*} cations by the time delayed nIR pulse, which rise time reflects the cross-correlation of the EUV and nIR pulses. The dashed red line represents the corresponding Gaussian cross-correlation function, in agreement with the <35fs FWHM of our laser pulses. Fig. 3c shows the time correlated relative change in the $H_3^+ + COH^+$ branching ratio, which exhibits upto ~ 12% suppression. The full lines in Figs. 3b and 3c show a model trace including an exponential 70 ± 25fs lifetime, convoluted with the instrumental time response directly determined based on the Ne^{2+} data shown in Fig. 3b. While the three:two body ratio appears to return to its unperturbed value, the asymptotic H_3^+ formation remains suppressed by 2.5% even at long time delays. It should be mentioned that while the energy needed to dissociate the H_3^+ ground state is ~4.5eV32, nIR photodissociation of the highly vibrationally excited H_3^+ can still be expected. We therefore assign the residual H_3^+ depletion at long times to photodissociation of the vibrationally hot H_3^+ cations after the CE is completed.

Stochastic DFT in Gaussian basis-sets

in collaboration with M. Fabian and B. Shpiro et al. Wiley Interdisciplinary Reviews: Computational Molecular Science 2019, 10.1002/wcms.1412, e1412.

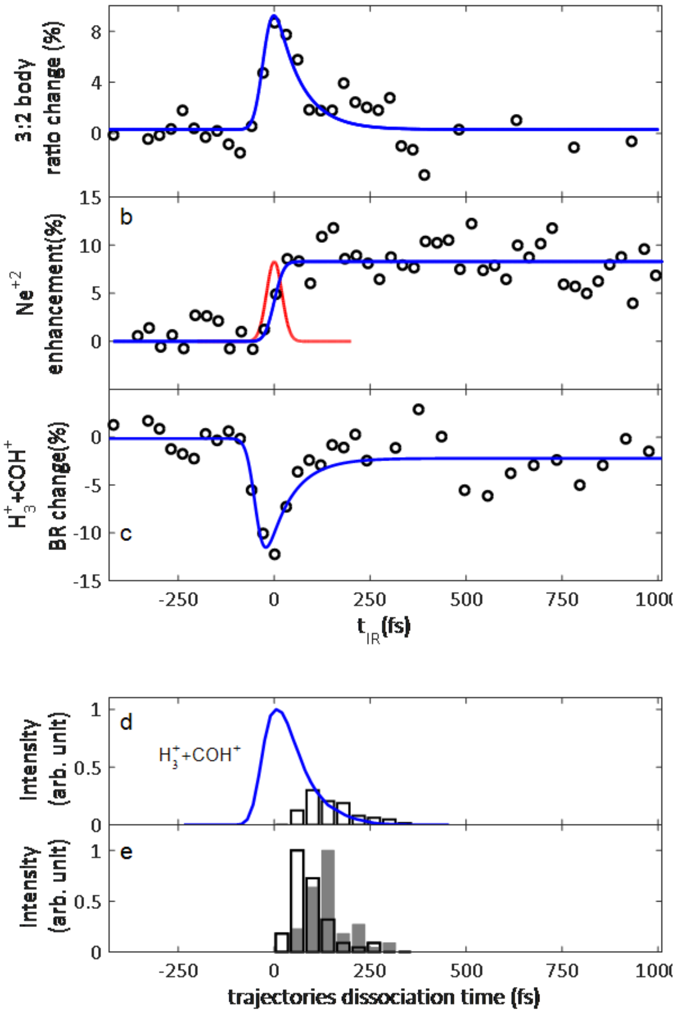

Figure 2.17. Time resolved experimental and theoretical data (a) measured enhancement of three:two body ratio, (b) measured transient Ne^{2+} cross correlation signal, which rise time is fitted to characterize the instrumental response function, shown by the dotted red line, (c) measured $H_3^+ + COH^+$ branching ratio transient depletion. All recorded as function of nIR probe delay with respect to the EUV pump pulse, with statistical error-bars are on the order of up to 5% (d) Simulated $H_3^+ + COH^+$ dissociation times distribution. Blue curve represents the corresponding experimental pump-probe response, convoluted with the measured instrumental response function. (e) Simulated neutral H_2 separation times distribution and the inverse harpooning times distribution in $H_2^+ + CHOH^+$ forming trajectories are shown by the empty and full gray bars respectively.

Linear-scaling implementations of density functional theory (DFT) reach their intended efficiency regime only when applied to systems having a physical size larger than the range of their Kohn-Sham reduced density matrix (RDM). This causes a problem since many types of large systems of interest have a rather broad RDM range and are therefore not amenable to analysis using DFT methods. For this reason, the recently proposed stochastic DFT (sDFT), avoiding exhaustive RDM evaluations, is emerging as an attractive alternative linear-scaling approach. This review develops a general formulation of sDFT in terms of a (non)orthogonal basis representation and offers an analysis of the statistical errors (SEs) involved in the calculation. Using a new Gaussian-type basis-set implementation of sDFT, applied to water clusters and silicon nanocrystals, it demonstrates and explains how the standard deviation and the bias depend on the sampling rate and the system size in various types of calculations. We also develop basis-set embedded-fragments theory, demonstrating its utility for reducing the SEs for energy, density of states and nuclear force calculations. Finally, we discuss the algorithmic complexity of sDFT, showing it has CPU wall-time linear-scaling. The method parallelizes well over distributed processors with good scalability and therefore may find use in the upcoming exascale computing architectures.

We consider a molecular system with a atomic basis-set of K basis functions $\phi_\alpha(\boldsymbol{r})$, with overlap matrix S and Fock matrix F. The basis functions are localized in space around their respective atoms. Thus S and F are very sparse matrices. The Roothan-Hall Equations produce the eigenfunction coefficient matrix C, with

$$C^T F C = E, \text{ and } C^T S C = I. \tag{2.3}$$

where E is the diagonal matrix of the energy eigenvalues. The complication, however, is that the C matrix is non-sparse and therefore should be circumvented. The first step in circumventing the calculation of the C matrix introduces the *reduced density matrix* (RDM) formally defined as

$$P = C f\left(E; T, \mu\right) C^T, \tag{2.4}$$

where $f\left(E; T, \mu\right)$ is the diagonal matrix obtained by plugging E instead of ε in the Fermi-Dirac distribution function:

$$f\left(\varepsilon; T, \mu\right) \equiv \frac{1}{1 + e^{(\varepsilon-\mu)/k_B T}}. \tag{2.5}$$

The diagonal matrix elements, $2f\left(\varepsilon_n\right)$ (we omit designating the temperature T and chemical μ in f when no confusion is expected) represent the level occupation of the MO $\psi_n(\boldsymbol{r}) = \phi_\alpha(\boldsymbol{r}) C_{\alpha n}$ (which typically holds a spin-up and a spin-down electron, hence the factor of 2). T can be a real finite temperature or a very low fictitious one. In the latter case, the $T \to 0$ limit of Eq. (2.5) yields $f\left(\varepsilon_n\right) = 1$ for $n \le N_{\text{occ}}$ and 0 otherwise, assuming that the chemical μ has been chosen such that $N_e = 2\sum_n f\left(\varepsilon_n\right)$.

In contrast to the formal definition in Eq. (2.3) of P as a matrix, in sDFT regards P as an *operator* expressed in terms of F and S through the relation

$$P = f\left(S^{-1}F; T, \mu\right) S^{-1}. \tag{2.6}$$

Here, $S^{-1}F$ is "plugged" in place of ε into the function f of Eq. (2.5) [1]. Just like P is an operator, our method also views S^{-1} as an *operator* which is applied to any vector u with linear-scaling cost using a preconditioned conjugate gradient method. The *operator* P, applied to an arbitrary vector u, uses a Chebyshev expansion of length N_C: $Pu = \sum_{l=0}^{N_C} a_l\left(T, \mu\right) u^l$ where a_l are the expansion coefficients and $u^0 = S^{-1}u$, $u^1 = Hu^0$ and then $u^{l+1} = 2Hu^l - u^{l-1}$, $l = 2, 3, \ldots$. In this expansion the operator H is a shifted-scaled version of the operator $S^{-1}F$ bringing its eigenvalue

---

[1] This relation can be proved by plugging $E = C^T F C$ from Eq. (2.3) into Eq. (2.4), giving $P = Cf\left(C^T F C; T, \mu\right) C^T$, then using the rule $Af\left(XA\right) = f\left(AX\right) A$ (valid for functions that can be represented as power series and square matrices) obtain $P = f\left(CC^T F; T, \mu\right) CC^T$ and finally using $CC^T = S^{-1}$ from from Eq. (2.3).

spectrum into the $[-1,1]$ interval. Every operation Pu, which involves repeated applications of H to various vectors is automatically linear-scaling due to the fact that F and S are sparse. Clearly, the numerical effort in the application of P to u depends on the length N_C of the expansion. When the calculation involves a finite physical temperature T, $N_C = 2\left(\frac{E_{max}-E_{min}}{k_B T}\right)$, where $E_{max}\,(E_{min})$ is the largest (smallest) eigenvalue of H. Since N_C is inversely proportional to T, the numerical effort of sDFT reduces as T^{-1} in contrast to deterministic KS-DFT approaches where it rises as T^3. For zero temperature calculations one still uses a finite temperature but chooses it according to the criterion $k_B T \ll \varepsilon_g$ where ε_g is the KS energy gap. For metals it is common to take a fictitious but low temperature.

The above analysis shows then, that the application of P to a vector can be performed in a linear-scaling cost without constructing P. We use this insight in combination with the fact that the expectation value of one-body observables $\hat{O} = \sum_{n=1}^{N_e} \hat{o}_n$ (where $\hat{o}$ is the underlying single electron operator and the sum is over all electrons) can be achieved as a matrix trace with P:

$$\left\langle \hat{O} \right\rangle = 2\mathrm{Tr}\left[PO\right], \tag{2.7}$$

where $O_{\alpha\alpha'} = \langle \phi_\alpha \left| \hat{o} \right| \phi_{\alpha'} \rangle$ is the matrix representation of the operator within the atomic basis. Eq. (2.7) can be used to express various expectation values, such as the electron number

$$N_e = 2\mathrm{Tr}\left[PS\right] = 2Tr\left[f\left(S^{-1}F;T,\mu\right)\right], \tag{2.8}$$

the orbital energy

$$E_{orb} = 2Tr\left[PF\right] = 2\mathrm{Tr}\left[e\left(S^{-1}F;T,\mu\right)\right], \tag{2.9}$$

where, $e\left(\varepsilon\right) = f\left(\varepsilon\right)\varepsilon$ and the fermionic entropy

$$\Sigma_F = -2k_B\mathrm{Tr}\left[PS\ln PS + \left(I-PS\right)\ln\left(I-PS\right)\right] = 2\mathrm{Tr}\left[\sigma_F\left(S^{-1}F;\beta,\mu\right)\right], \tag{2.10}$$

where $\sigma_F = -k_B\left(f\ln f + \left(1-f\right)\ln\left(1-f\right)\right)$. The expectation value of another observable, the density of states $\rho_s\left(E\right) = \sum_n \delta\left(E-\varepsilon_n\right)$ can also be written as a trace:

$$\rho_s\left(\varepsilon\right) = \pi^{-1}\lim_{\eta\to 0}\mathrm{Im}\,\mathrm{Tr}\left[\left(\varepsilon S - F - i\eta S\right)^{-1}S\right] = \pi^{-1}\mathrm{Im}\,\mathrm{Tr}\left[g\left(S^{-1}F;\varepsilon\right)\right], \tag{2.11}$$

where $g\left(\varepsilon';\varepsilon\right) = \lim_{\eta\to 0}\frac{1}{\varepsilon-\varepsilon'-i\eta}$.

Since the density matrix is an operator in the present approach, the trace in Eq. (2.7) can be evaluated by introducing the unit column vectors $u^{(\alpha')}$ ($\alpha' = 1,\ldots,K$) and operating with P on them, and the trace becomes:

$$\left\langle \hat{O} \right\rangle = 2\sum_{\alpha,\alpha'=1}^{K}\left(Pu^{(\alpha')}\right)_\alpha O_{\alpha\alpha'}. \tag{2.12}$$

Evaluating this equation requires *quadratic-scaling* computational complexity since it involves K applications of P to unit vectors $u^{(\alpha')}$. One important use of Eq. (2.7) is to compute the electron density at spatial point $\boldsymbol{r}$:

$$n\left(\boldsymbol{r}\right) = 2\mathrm{Tr}\left[PN\left(\boldsymbol{r}\right)\right], \tag{2.13}$$

where $N_{\alpha\alpha'}\left(\boldsymbol{r}\right) = \phi_\alpha\left(\boldsymbol{r}\right)\phi_{\alpha'}\left(\boldsymbol{r}\right)$ is the overlap distribution matrix, leading to the expression

$$n\left(\boldsymbol{r}\right) = 2\sum_{\alpha,\alpha'=1}^{K}\left(Pu^{(\alpha')}\right)_\alpha \phi_\alpha\left(\boldsymbol{r}\right)\phi_{\alpha'}\left(\boldsymbol{r}\right). \tag{2.14}$$

Here, given $\boldsymbol{r}$, only a finite (system-size independent) number of α and α' pairs must be summed over. Hence, the calculation of the density at just this point involves a linear-scaling effort because of the need to apply P to a finite number of $u^{(\alpha')}$'s. It follows, that the density function $n(\boldsymbol{r})$ on the entire grid can be obtained in quadratic scaling effort [2]. This allows us to formulate the SCF schema of:

$$\begin{aligned}\cdots \longrightarrow n(\boldsymbol{r}) \longrightarrow \{v_H[n](\boldsymbol{r}), v_{xc}[n](\boldsymbol{r})\} \longrightarrow \\ \longrightarrow F \xrightarrow{O(K^2)} n(\boldsymbol{r}) \longrightarrow \ldots,\end{aligned} \tag{2.15}$$

where the quadratic step is marked $O\left(K^2\right)$.

Summarizing, we have shown an alternative trace-based formulation of Kohn Sham theory which focuses on the ability to apply the DM to vectors in a linear-scaling way, without actually calculating the matrix P itself. This leads to a deterministic implementation of KS-DFT theory of quadratic scaling complexity.

Having described the quadratic scaling in the previous section, we are but a step away from understanding the way sDFT works. The basic idea is to evaluate the trace expressions (Eqs. (2.7)-(2.14)) using the *stochastic trace formula* :

$$\mathrm{Tr}[M] = \mathbf{E}\left\{\sum_{\alpha\alpha'}^{K} \chi_\alpha M_{\alpha\alpha'}\chi_{\alpha'}\right\} \equiv \mathbf{E}\,\left\{\chi^T M\chi\right\}, \tag{2.16}$$

where M is an arbitrary matrix, χ_α are K random variables taking the values ± 1 and $\mathbf{E}\,\left\{\chi^T M\chi\right\}$ symbolizes the statistical expected value of the functional $\chi^T M\chi$. One should notice that Eq. (2.16) is an identity, since we actually take the expected value. However, in practice we must take a finite sample of only I independent random vectors χ's. This gives an *approximate* practical way of calculating the trace of M:

$$\mathrm{Tr}[M] \approx \mathrm{Tr}_I[M] \equiv \frac{1}{I}\sum_{i=1}^{I}\left(\chi^i\right)^T M\chi^i. \tag{2.17}$$

From the central limit theorem, this trace evaluation introduces a fluctuation error equal to

$$\mathrm{Var}\left(\mathrm{Tr}_I[M]\right) = \frac{\Sigma_M^2}{I}, \tag{2.18}$$

where $\Sigma_M^2 = \mathbf{Var}\left(\mathrm{Tr}_1[M]\right)$ is the variance of $\sum_{\alpha\alpha'}^{K}\chi_\alpha M_{\alpha\alpha'}\chi_{\alpha'}$ (discussed in detail in below). This allows to balance between statistical fluctuations and numerical effort, a trade-off which we exploit in sDFT.

With this stochastic technique, the expectation value of an operator $\hat{O}$ becomes (c.f. Eq. (2.12)):

$$\left\langle\hat{O}\right\rangle = 2\mathbf{E}\,\left\{(P\chi)^T(O\chi)\right\}, \tag{2.19}$$

where the application of P to the random vector χ is performed in the same manner as described above for u (see the text immediately after Eq. (2.6)). This gives the electronic density (see Eq. (2.14)):

$$n(\boldsymbol{r}) = 2\mathbf{E}\left\{\psi_{P\chi}(\boldsymbol{r})\,\psi_\chi(\boldsymbol{r})\right\}, \tag{2.20}$$

yielding a vector (called a grid-vector) of density values $n(\boldsymbol{r})$ at each grid-point. This involves producing two grid-vectors, $\psi_\chi(\boldsymbol{r}) = \chi_\alpha\phi_\alpha(\boldsymbol{r})$ and $\psi_{P\chi}(\boldsymbol{r}) = (P\chi)_{\alpha'}\phi_{\alpha'}(\boldsymbol{r})$ and then multiplying them point by point and averaging on the I random vectors.

---

[2] Note that when the DM P is sparse, the evaluation of the density of Eq. 2.14 can be performed in linear-scaling complexity. The stochastic method (explained in Subsection **??**) does not exploit this sparsity explicitly.

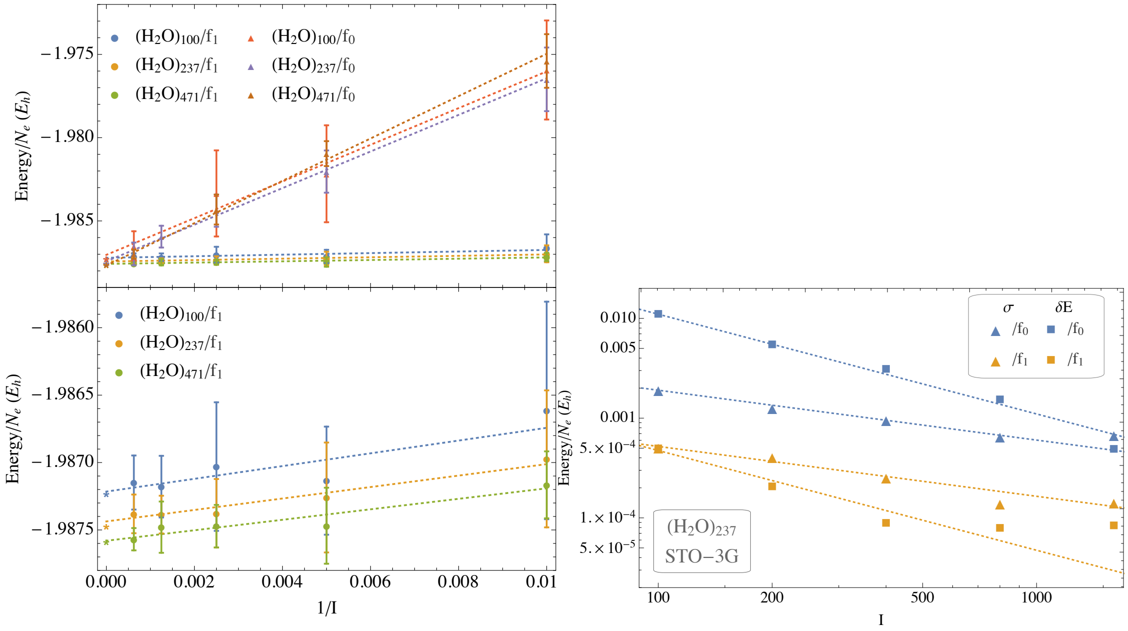

Figure 2.18. Left-Top panel: The estimate of energy per electron as a function of the inverse number of random vectors ($1/I$) for water molecule clusters of indicated sizes, without fragments ($/f_0$) and with fragments of single H_2O molecules ($/f_1$). The dotted lines are linear fit to the data (weighted by the inverse error bar length). The deterministic results are represented at $1/I = 0$ by star symbols. Left-Bottom panel: a zoomed view of the $/f_1$ results. These results were calculated using the STO-3G basis-set within the LDA. Right Panel: The standard deviation (σ,circles) and errors (δE, squares) of the stochastic estimate of the energy per electron as a function of the number of random vectors (I) in $(H_2O)_{237}$ without fragments ($/f_0$, blue) and with H_2O fragments ($/f_1$, yellow) . The dashed lines are best fit functions $\alpha I^{-n}$to the data, where $n = 1/2$ for fitting the standard deviations and $n = 1$ for the bias. These results were calculated using the STO-3G basis-set within the LDA.

Let us now turn our attention to demonstrating the validity of the sDFT calculation when comparing it to deterministic calculation under the same conditions. In Fig. 2.18 (left-top panel) where we plot, for water clusters of three indicated sizes, the energy per electron as a function of $1/I$, where I is the number of random vector $\chi's$ used for the stochastic trace formulas (Eq. (2.20)). As the the number of random vectors I grows (and $1/I$ drops) the results converge to the deterministic values (shown in the figure as stars at $1/I = 0$). We repeated the calculations 10 times with different random number generator seeds and used the scatter of results for estimating the standard deviation σ and the expected value μ (these are represented, respectively, as error bars and their midpoints in the figure). It is seen that the standard deviation in the energy per particle drops as I increases and in Fig. 2.18 right panel it is demonstrated that the standard deviation drops as $I^{-1/2}$, in accordance with the central limit theorem. The average values of the energy per particle in Fig. 2.18 left panels drop steadily towards the converged deterministic values (stars). The fact that the average is always larger than the exact energy, as opposed to fluctuating around it, is a manifestation of a bias δE in the method. When δE is larger than σ it drops in proportion to I^{-1}.

Scientific Activities

Roi Baer group members

Name	Project	Status	Period
Sayak Adhikari	Stochastic differential equations	MSc student	
Efrat Haddad	Bond breaking with Green functions	PhD student	
Ben Shpiro	sDFT with Gaussian basis - forces	PhD student	
Stanislav Zelner	Silicon etching	PhD student	
Eitam Arnon	sDFT and Langevin dynamics	PhD student	2020
Dr. Yael Cytter	sDFT of warm dense matter	PhD student	2019
Dr. Marcel Fabian	sDFT with Gaussian basis	PhD student	2019
Professor Vojtech Vlcek	sDFT and GW Electronic structure	PhD student	2018
Dr. Zhu Ruan	Dynamics of electrons in open systems	Postdoc	2016-2018
Dr. Helen Eisenberg	GW Electronic structure	Research Associate	

Roi Baer scientific collaborations

PI Name	Project	Institution
Eran Rabani	Stochastic electronic structure	UC Berkeley, USA
Daniel Neuhauser	Stochastic electronic structure	UCLA, USA
Ronald Redmer	Stochastic DFT	Rostock University, Germany
Leeor Kronik	TDDFT	Weizmann Institute, Israel
Sanford Ruhman	Electronic decay mechanisms in NCs	HUJI, Israel
Daniel Strasser	Coulomb explosion	HUJI, Israel

Roi Baer active grants

Project	Period	Foundation	Total grant in thousands
Dynamics of noninteracting Fermions in large open quantum systems	2019-2023	ISF	₪1000
Stochastic density functional theory for studying matter in extreme conditions	2020-2023	GIF	€105
Stochastic approaches to self-consistent second order Green function methods	2019-2023	BSF	$160
Stochastic electronic structure approaches to study low dimensional black phosphorene	2016-2019	NSF-BSF	$180

Conference organization (last 5 years)

2017 Dec 17-20	CECAM Workshop - Expeditious Methods in Electronic Structure
2018 Mar 12-15	Jerusalem Nonadiabatica 2018
2019	Co-organized with Dr. Snir Gazit and Dr. Eli Kraisler the Fritz Haber Winter Symposium, The Hebrew University of Jerusalem, Israel.
2019 May 22-27	Co-organized with Prof. E.K.U. Gross and Dr. Eli Kraisler, an International Workshop, “The exact factorization for electrons, nuclei, and photons”, The Hebrew University of Jerusalem, Israel.

Prizes, honors, editorial and review boards etc. (last 5 years)

2015	The Ratner Family Chair in Chemistry
2015-16	University of California Berkeley, Visiting Pitzer Professor
2015-16	Heising-Simons Fellow of the Kavli Energy Nanoscience Institute at UC Berkeley
2018	Hebrew University Rector’s Prize for Excellence in Research and Teaching

2.3 Snir Gazit

Research Activities

I am a condensed matter theorist. My main research interest lies in strongly correlated system, where interparticle interactions give rise to emergent collective behavior. More specifically, I am interested in parameter regimes, where quantum mechanical effects play a dominant role, such as low temperatures and high pressure. These intrinsically quantum mechanical phases include superconductors that conduct electrical current without dissipation and spin liquids defying magnetic ordering down to extremely low temperatures, well below the energy scale set by the magnetic exchange. This timely research line is motivated by experimental progress of recent years that allowed access to quantum states of matter by discovering novel strongly correlated materials and the introduction of highly accurate experimental probes. In a parallel effort, recent years’ breakthrough progress in quantum engineering, such as in cold atomic systems and superconducting qubits, is emerging as an experimental platform for highly tunable quantum simulations of many-body quantum phenomena. These systems are expected to become the basic building blocks for future quantum-based technologies.

Theoretical investigations of strongly correlated quantum systems require introducing novel concepts and tools beyond the standard methods of classical statistical mechanics. From the numerical perspective, the quantum Hilbert space’s rapid exponential growth poses strong limitations on exact numerical solutions of quantum mechanical problems using classical computers. Nevertheless, in recent years, we have witnessed significant advances in addressing these problems. These include identifying new classes of quantum Monte Carlo techniques that do not suffer from notorious numerical sign problem and tensor network based approaches that target low-entangled sates such as the density matrix normalization group (DMRG). More recently, ideas derived from the machine learning community are showing promising performance in representing highly entangled states. I am very actively involved in developing new numerical techniques to solve the quantum many body problem and apply them for the discovery of novel quantum phases and phase transition.

Below, I detail two of my recent research projects.

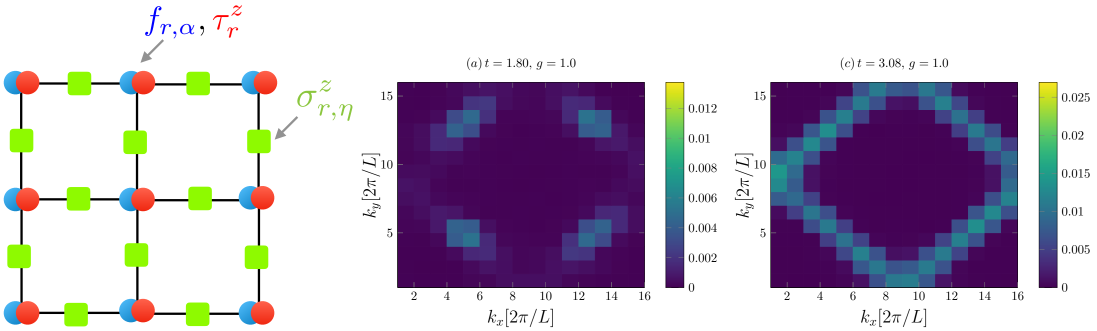

Figure 2.19. (a) A model of orthogonal fermions $f_{r,\alpha}$ coupled to an Ising gauge field $\sigma^z_{r,\eta}$ and Ising matter field τ^z_r (b) A reconstruction of the Fermi surface from (left) a small pockets about $k = \{\pm\pi/2, \pm\pi/2\}$ to (right) large diamond shaped Fermi surface.

Fermi-surface reconstruction without symmetry breaking

According to Pauli's principle, any quantum state can be occupied only by a *single* fermion. This simple rule has far reaching consequences. For free electrons in the presence of translational invariance, quantum states are labeled by momentum. Hence, at finite electron density the many-body ground state is simplify constructed by filling up momentum eigen-states. This naturally leads to the notion of a Fermi-surface, as contour in momentum space representing the highest in energy occupied state. By construction the volume, V_F enclosed inside the Fermi-surface is set the electronic density (modulo completely filled bands).

$$\frac{V_F}{(2\pi)^D} = n \bmod 1, \tag{2.21}$$

where n is the fermion density, and D is the spatial dimension. Remarkably, this relation is preserved in the presence of interaction as long as the system may be described by a Fermi-liquid, namely that at low energy excitation spectrum comprises well-defined electronic quasi-particles, characterized by a lifetime that is parametrically longer than their inverse energy. This fundamental result is the essence of the celebrated Luttinger's theorem (LT). In particular, LT states that for a fixed number of electrons, the only way to reduce V_F is by breaking translational symmetry, which enlarges the unit cell and reduces the density.

The experimental observation of transition between a small to large Fermi-surfaces, which does not necessarily involve breaking the translational symmetry in Cuprate materials and in Heavy fermion compounds, has challenged this long standing paradigm. From a theoretical perspective, it was realized that violating Luttinger's theorem entails electronic fractionalization and the introduction of an emergent gauge field degree of freedom. Analytic treatment of candidate theoretical models exhibiting such behavior is challenging, and many cases involve approximate techniques that do not allow making precise statements. Therefore, numerical approaches that may treat such systems in a numerically exact and unbiased manner are desirable.

In this project, we have introduced a numerically tractable model that allows investigating the violations of LT. More explicitly, our model realizes the simplest form of electronic fractionalization, where the physical fermion is decomposed into an 'orthogonal' fermion and an Ising matter fields, $c_\alpha = f_\alpha \tau^z$, where α denotes the spin index. The above decomposition introduces a gauge redundancy since the transformation $f_\alpha \to -f_\alpha$ and $\tau^z \to -\tau^z$ leaves physical degrees of freedom intact. This redundancy is compensated by the introduction of an Ising gauge field σ^z_b, on the lattice bonds. See Fig.2.19a for a graphical representation of the model. Using a sign problem free quantum Monte Carlo simulations, we have mapped the phase diagram of this model and identified a path in parameter space interpolating between a small and a large Fermi-surface without breaking translational symmetry. See Fig, 2.19b. Our findings resonate with ARPES measurements in the pseudogap phase of Cuprate materials, which, similarly to our model, exhibits a finite spectral weight only at the nodal points (k=$\{\pi/2,\pi/2\}$). Our results are a candidate theoretical model of this mysterious phase.

Magnon BEC transition in frustrated Kondo lattice

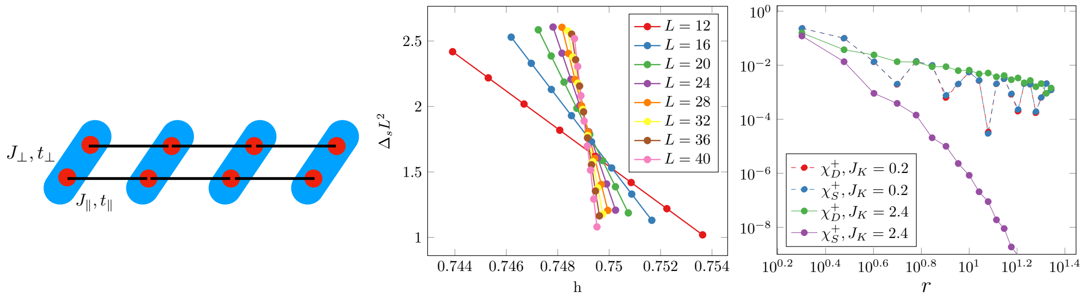

Figure 2.20. (a) Kondo Heisenberg ladder, with anisotropic fermion hopping and magnetic exchange. (b) Curve collapse analysis of the single particle gap, displaying a dynamical exponent $z = 2$. (c) Superconducting d-wave correlation in two-band model.

Heavy-fermion compounds are a paradigmatic instance of strongly correlated electronic systems. In such systems, charge fluctuations of localized f electrons are suppressed, and their spin remains the only dynamical degree of freedom. Further coupling to an itinerant band of electrons through a Heisenberg interaction leads to the famous Kondo-Heisenberg model,

$$\mathcal{H} = \sum_k \epsilon_k c_k^\dagger c_k + \sum_{i,j} J_{ij} S_i^f \cdot S_j^f + \sum_i J_K S_i^f \cdot S_j^c \tag{2.22}$$

Here, the first term describes a band of itinerant c electrons. The second term is a Heisenberg model of the localized f electron, and the last term is a Kondo coupling between spins of the c and f electrons. Typically, the above Hamiltonian represents a competition between anti-ferromagnetic ordering at small J_K mediated by RKKY interactions and a Heavy-fermion phase whose effective mass is greatly renormalized due to the flat f electron band at large J_K.

In recent years, several novel heavy fermion compounds have been discovered, where the the f electron reside on a geometrically frustrated lattices, e.g. the Shastry-Sutherland lattice in Yb_2Pt_2Pb, Ce_2Pt_2Pb, and Ce_2Ge_2Mg , a distorted triangular lattice in $YbAl_3C_3$, and a distorted Kagome lattice in CeRhSn and $CePd_{1-x}Ni_xAl$. The resulting magnetic correlations are expected to exhibit large quantum fluctuations. They may result in non-magnetic states such as a spin liquid or a valance bond solid (VBS) of singlet dimers. The focus on this work in the latter case, which is also expected to capture the magnetic properties of Yb_2Pt_2Pb.

In an insulating VBS state, the application of an external magnetic field reduces the energy splitting between the ground state singlet and one of the triplet states pointing along the field direction. For a sufficiently large field, a quantum phase transition occurs, where magnons (spin-one triplet excitations) condense in the so called magnon Bose-Einstein condensation (BEC). These transitions have been thoroughly investigated both theoretically and experimentally and are now considered to be well understood. Here, we reexamine this transition, in the case where localized moments are further Kondo coupled to a metal. This problem is potentially non-trivial since the gapless electrons can potentially destabilize the BEC transition.

Through a combination of analytic bosonization techniques and exact numerical DMRG calculations, we study a simplified one dimensional Toy model of Eq. 2.22, admitting a VBS ground sate at vanishing Kondo coupling, see Fig. 2.20a. Quite surprisingly, we find that the magnon BEC transition also survives at finite Kondo couplings, and critical properties such as the dynamical exponent $z = 2$ remain intact, see Fig. 2.20b. We also find that electronic correlations sensitively depend on the band structure. In cases where the chemical potential crosses two bands, we find evidence for d-wave superconductivity; see Fig. 2.20c. Based on scaling arguments, we generalize our results to higher dimensions. This allows us to interpret the logarithmic diverges of the specific heat found in Yb_2Pt_2Pb experiments as arising from a simple magnon BEC transition.

Scientific activities

Snir Gazit group members

Name	Project	Status	Period
Michal Zimmerman	Phases of dipolar excitons in a bilayer structure	PhD student	since October 2019
Gal Shkolnik	Bosonic realization of the orthogonal semi-metal	MSc student	since October 2019
Elyasaf Cohen	Frustrated magnets on the Lefschetz thimble	MSc student	since October 2019
Ayush Da	Quasiperiodic quantum critical points	MSc student	since since October 2020

Snir Gazit scientific collaborations

Name	Project	Institution
Subir Sachdev	Lattice gauge theories coupled to matter fields	Harvard University
Fakher Assaad	Lattice gauge theories coupled to matter fields	University of Würzburg
Jedediah H. Pixley	Frustrated heavy-fermions	Rutgers University

Snir Gazit active grants

Project	Period	Foundation	Total grant in thousands
Emergence and criticality in strongly interacting topological phases - a quantum Monte Carlo study	2018-2022	ISF	1000 NIS
Melting of a metallic valence bond solid in frustrated Kondo lattice model	2019-2021	BSF	$ 105

Conference organization (last 5 years)

2019	Co-organized with Dr. Eli Kraisler and Prof. Roi Baer the Fritz Haber Winter Symposium, The Hebrew University of Jerusalem, Israel.

Prizes, honors, editorial and review boards etc. (last 5 years)

2019	Alon Fellowship

2.4 Robert B. Gerber

The focus of our research group in theoretical and computational chemistry is on the following topics: (i) Development of new methods and algorithms for vibrational spectroscopy and dynamics of extended systems. (ii) Vibrational spectroscopy of conformers of peptides and sugars and their complexes with water. 3-D structure determination of biomolecules based on vibrational spectroscopy. (iii) Mechanisms and dynamics of reactions in liquid water surfaces. Photochemical atmospheric reactions in aerosols. (iv) Computational predictions of novel materials and their thermodynamic and chemical properties. Prediction of energetic materials, their structures and reactions.

Research Activities

Reaction Mechanisms of Atmospheric Molecules with Sea Water

Chemical reactions on sea water aerosols are known to play an extremely important role in the chemistry of the atmosphere. While the physical properties have been studied extensively, very little is known on the microscopic mechanisms of reactions wheresea water is involved. This is at present a frontier topic of atmospheric chemistry.

In the reported period, our group was able to unravel the microscopic mechanisms of the reactions of sea water aerosols with N_2O_5 from the gas phase. There is evidence that these rank among the most important processes in heterogenous atmospheric chemistry. I highlightbelow the main results obtained by our group on this topic in the reported period.

Small cluster model of hydrolysis and chloride ion substitution of N_2O_5 at sea water

The main products obtained for these reactions are HNO_3 and $ClNO_2$, the latter in the gas phase. The nature of the competition between the reactions involved was hitherto unknown. It is obviously very desirable to have a simple model for insights into this very complex system. We found a highly successful model for these processes, the three component cluster $(N_2O_5)(Cl^-)(H_2O)$. Our approach involved Ab Initio Molecular Dynamics (AIMD) simulations starting from intermediate transition states along the reaction pathways. Theresults lead to determination of the reactions paths, and to calculations of the dynamics in time in a number of key regions along the paths.

The energy along the minimum energy path is shown in Figure 2.21. The lowest energy structure on the energy landscape of the system are two HNO_3 molecules, complexed with the Cl^-. This corresponds to the hydrolysis reaction. However, this is not how the reactions proceed in time. First, an ultrafast reaction due to a low barrier involved, leads to formation of $ClNO_2$, the product of the substitution process ($NO_3{}^-$ is the other product in this channel). Only with the continuation of the process, is there a probability for the system to surmount much higher barriers, and ultimately after several other intermediate transition states lead to hydrolysis products.

The results establish that when Cl^- and H_2O are at the vicinity of N_2O_5, substitution is faster than hydrolysis. Only in those cases where the system "survives" substitution and formation of $ClNO_2$ as final product can hydrolysis occur, and the timescale for the latter is much longer. The results are in accord with experiments on clusters (By M. A. Johnson), and also provide explanations for bulk experiments. Insights gained are also useful for understanding other reactions of N_2O_5. The

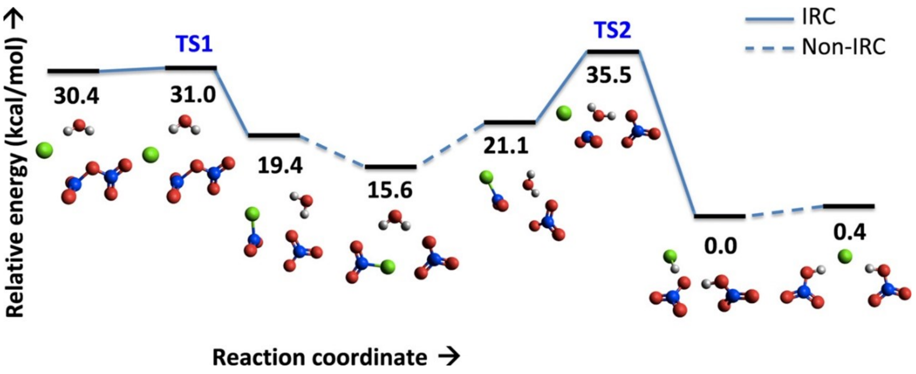

Figure 2.21. Potential energy landscape of $(N_2O_5)(Cl^-)(H_2O)$ along the minimum energy path. From Ref. [1].

work was published in Science Advances (McCaslin, Johnson, and R Benny Gerber 2019), with encouraging early interest of the atmospheric chemistry community.

Reactions of N_2O_5 with hydrated ions

Cl^- is present in sea water in much higher concentrations than other anions. However, other anions are also present in significant concentrations, enough to play a role in atmospheric chemistry. This is particularly the case for sea water aerosols, in which the concentrations of such ions can be much larger than in the sea.

We studied the mechanism of the reactions of several ions, to the point of characterizing in depth the properties of this large and important family of processes, which were hitherto unknown. Also, we collaborated with the groups of Gil Nathanson and of Tim Bertram, both of the University of Wisconsin at Madison, and were able to provide microscopic understanding of their interesting experimental results.

Model systems for our theoretical studies were hydrated anion of the type $(X)(H_2O)_{12}$,where X is a monovalent or divalent anion, in reaction with N_2O_5. For some of the ions, e.g. $SO_4{}^{-2}$, the 12 water molecules are, in the case of the isolated $(X)(H_2O)_{12}$,a nearly spherical hydration shell. In other cases the anion is a symmetrically located, e.g. at the surface of the water cluster. We used *ab initio* Molecular Dynamics simulations, with potentials from DFT/PBE0 + dispersion to describe the reactions. We also carried out transition state and reaction path calculations.

Very interesting insights were obtained, with in-depth understanding of experimental findings by Nathanson and Bertram (see below). The main results are:

(a) At room temperature, N_2O_5 and $(X)(H_2O)_{12}$ form first a pre-reaction complex, in all cases studied. In this complex, the solvation structure of the anion is strongly distorted compared with the isolated hydrated ion. However, direct reaction with the "adsorbed" N_2O_5 does not take place, as this requires the surmounting of a barrier, which causes a much-delayed process. The structure of the complexes $N_2O_5(X)(H_2O)_{12}$ is shown in Figure 2.22, for X= (Cl^-),$(SO_4{}^{-2})$, $(HCOO^-)$. This figure demonstrated clearly the very large distortion effect of the solvation structure upon complexation with N_2O_5, which plays a major role in promoting the subsequent reaction.

(b) Our studies of the reactions of the complexes determined the relative efficiencies of the different ions in attacking N_2O_5 in water media. Thus, $SO_4{}^{-2}$ and carboxylic ions $RCOO^-$,R- an alky; react much faster than Cl^-. This is of major importance in the analysis of these reactions for aerosols at atmospheric conditions.

(c) The Bertram-Nathanson experiments carried out in cooperation with Karimova and me found

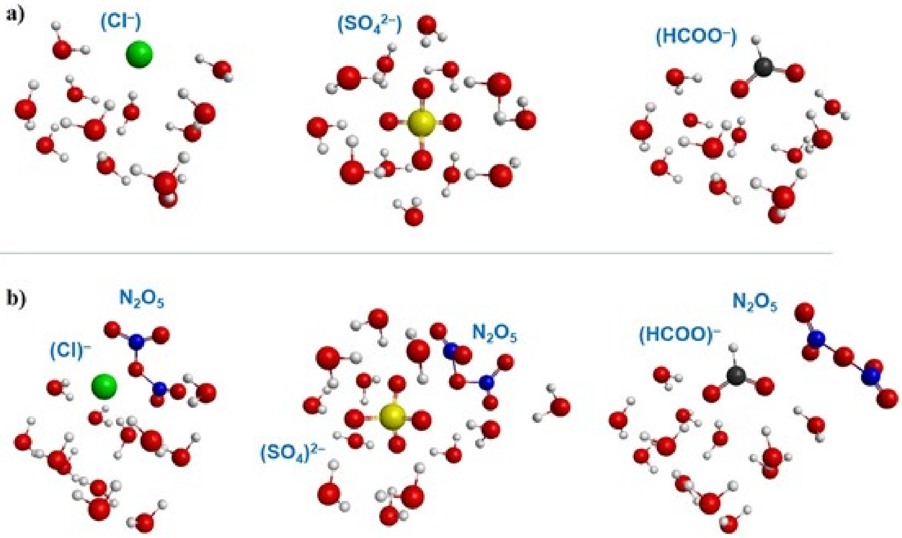

Figure 2.22. The structures of (a) Isolated hydrated ions $(X)(H_2O)_{12}$and of (b) The pre-reaction complexes $(N_2O_5)(X)(H_2O)_{12}$,for X=Cl^-,$SO_4{}^{-2}$,$HCOO^-$. The results are from Ref.[2] below, by Karimova et al.

that when $SO_4{}^{-2}$ and carboxylic ions are present in sea water, the formation of $ClNO_2$ from the reaction of Cl^- with N_2O_5 is suppressed. Our theoretical result (b) provides understanding of this (as well as predicting the effect for other ions).

(d) Our calculations predict the formation of intermediate species for some of the reactions. These new species may themselves play a role in atmospheric chemistry, which is potential importance.

The theoretical work in this project was led by Dr. Natalia Karimova, a postdoc in my group. She is the first author on Ref. (Karimova, Chen, et al. 2020), and the Bertram and Nathanson groups are our co-authors on this. Ref. (Staudt et al. 2019) focuses on the experimental results of the Bertram and Nathanson groups, and Karimova and me are co-authors. The study was carried out in the framework of CAICE, an NSF sponsored multi-PI center, which enables very fruitful collaborative research in atmospheric research.

Hydrolysis of N_2O_5 in pure water droplet

There is evidence that hydrolysis of N_2O_5 in liquid water media takes place also when no other dissolved species are present. Qualitative suggestions of the mechanism assumed that the first step of the process is penetration of adsorbed N_2O_5 into the bulk of the water, with the process then occurring following equilibration of the molecule in the bulk.

Dr. Estefania Rossich Molina, then a postdoc in our group, and myself showed computationally that hydrolysis of N_2O_5 can take place at the surface of liquid water. This drastically changes the previous paradigm of the hydrolysis mechanism.

The model used by Rossich Molina and myself considers an N_2O_5 molecule adsorbed on a cluster of 20 water molecules, a system of about one nanometer size. Searches guided by chemical intuition led to determination of an exit transition state (a transition state beyond which the system proceeds directly to hydrolysis products).The system has, of course, many other transition states, which are not exit states, on the pathways from the initial N_2O_5 adsorbed state to hydrolysis. We carried out *ab initio* Molecular Dynamics simulations starting from the exit transition state, and

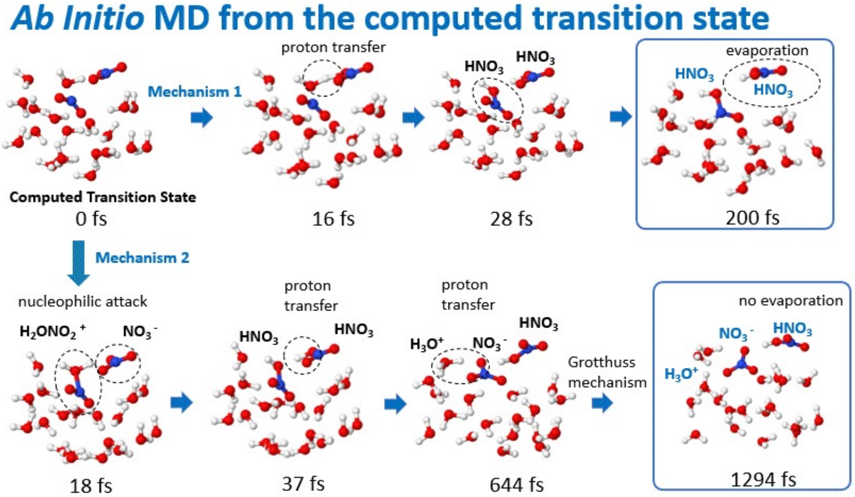

Figure 2.23. Snapshots from the dynamics of hydrolysis of N_2O_5, starting from the exit transition state. Two distinct mechanism are visible: a nucleophilic and an electrophilic one.

determined the properties of the hydrolysis reactions. Snapshots from the dynamics are shown in Figure 2.23, taken from Ref. (Rossich Molina and R. Benny Gerber 2020)

Note that the transition state consists of $NO_2(+)$, $NO_3(-)$ as a contact ion pair, with partial charges on the nitrogen oxides. Also, the ion pair is strongly coupled to a water molecule. A nucleophilic mechanism is possible, where the first step is attack by the O-end of the water on $NO_2(+)$. Also an electrophilic mechanism takes place, where the first step is attach by an H-atom of a water molecule on $NO_3(-)$. The ratio between the contributions of the two mechanisms is about 7(nucleophilic):3(electrophilic). The simulations also predict the ration between nascent formation of two HNO_3 molecules as products to formation of HNO_3 and ($NO_3{}^-$) with (H_3O^+). Finally, the simulations predict the fraction of HNO_3 molecules that evaporate upon hydrolysis.

The results of this study are important first in showing that surface hydrolysis does take place, and second in determining the detailed mechanism, that may be helpful in future understanding of hydrolysis of other molecules at surfaces. The results were published in J. Phys. Chem.

Photochemistry of Dissolved Organic Chromophores in Water: Absorption Spectra

Photochemistry at the water-air interface is in very many cases due to organic substances dissolved in the water. These can undergo reactions in the excited state, or act as photosensitizers by transferring electronic energy to other species and thus activate the latter. An essential step towards studying the photochemical reactions is to explore the absorption spectra. It is computational extremely difficult to simulate the real systems, as these are very complex. It is therefore necessary to develop models that correctly describe experiments on realistic systems, yet are computationally practical. Our work on this is a major first step forward on this frontier area of atmospheric chemistry. We carried out calculations of the optical absorption spectra of organic acid chromophores in water media, in collaboration with Professor V. H. Grassian and her group at the University of California at San Diego, who did corresponding experiments. This work was done in the framework of CAICE, an NSF-sponsored center of atmospheric chemistry.

Two systems were studied in the reported period. Dr. Dorit Shemesh, a Research Associate in my group carried out calculations for pyruvic acid in water. Dr. Natalia Karimova, a postdoc in our group pursued the spectra of benzoic acid dissolved in water. The approach taken in both of these studies was the following. The systems were modeled by small clusters of water, in which the chromophore species are embedded. To describe each acid HX, the spectrum was calculated for two speciated forms: the neutral, non-dissociated acid, and the corresponding anion, X^-, obtained upon deprotonation. The weight of each contribution to the spectra is estimated, and depends on the pH of the experimental system.

To compute the contribution to the spectrum from a given speciated form, *ab initio* Molecular Dynamics simulations are carried out for the ground state. At certain time intervals the system is promoted vertically to the excited state, in the spirit of the classical Franck- Condon model, which gives the excitation energy at that configuration. A sufficiently long simulation yield the full spectrum.

The following main conclusions were drawn from the calculations, and the comparisons with the experiments:

(a) Although the Grassian experiments were carried out for macroscopic solutions, our method led to very good agreement with experiment for fairly small clusters. 4 water molecules sufficed for pyruvic acid, while 8 water molecules gave good results for benzoic acid. Thus, the cluster model works well.

(b) The spectra of the anionic species is much more affected by the water molecules than is that of the neutral acid.

(c) The weight of the anionic relative contribution to the spectra depends on the pH of the real system. As expected, the higher the pH, the larger is the relative contribution of the anionic contribution compared with the neural form.

(d) A TD-DFT treatment of the excited states suffices for obtaining the main peaks. To obtain additional observed weak peaks, the higher level ADC(2) *ab initio* method had to be used.

These results open the way for applications to much larger chromophores. The project on pyruvic acid is described in Ref. (Karimova, Luo, et al. 2020) below, and the work on benzoic acid was published in Ref. (Shemesh et al. 2020)

Conformer Structure, Dynamics, Reactions and Spectroscopy of Protonated Sugars

It is very difficult to study sugar reactions in solution at a microscopic level, due the complexity if the systems. This motivates exploration of sugar processes in isolated, mass spectrometric conditions, in the hope that insights gained may prove relevant also for macroscopic media.

Michelle Dvores, a Ph.D. student of mine, carried out extensive computational studies of protonated sugar species, including conformer structures, dynamics of transitions between different structures, reactions and in particular intermediate species formed in the reactions. The work was carried in cooperation with Professor J. P. Simons (Oxford), Professor Philipp Maitre and Dr. Pierre Carcabal (Paris). Simons and Maitre are world class leader in mass spectrometry and spectroscopy of biomolecules.

In her research, Michelle Dvores carried out optimization of protonated sugar species, and pursued *ab initio* Molecular Dynamics simulations of conformational transitions and reaction processes. She identified and characterized intermediates and computed lifetimes. Finally to interact with experiments she carried out anharmonic calculations of vibrational spectroscopy, and provided insights and interpretations.

Highlight results obtained in the studies by Dvores include the following:

(a) The studies led to confirmation and to structure determination of the oxocarbenium ion, formed in a reaction of a protonated sugar species. The oxocarnenium ion was proposed years ago as an intermediate that plays a major role in many sugar reactions in solution. However, it proved difficult to establish the existence of this species and to determine its properties in experiments on processes in solution. Our simulation results combined with the mass spectrometric experiments of our collaborators, and the theoretical- experimental agreement on spectroscopy at the anharmonic level is the strongest evidence to date of the existence of the species, the mechanism of its formation, and its properties. Given the continuing debates on this species and its role, this is an important contribution to the field.

(b) Dvores computed the protonation sites, the structures involved and the migration time scales of protons between the different sites of methyl galactose. Such information is of major interest for sugar reactions, and is very rarely available. Dvores showed that some protonated sugar structures are very short lived, while other structures are stable. We explained this great diversity of lifetimes of different structures.

(c) The work of Dvores determined the conformations of the very reactive fucasyl cation, and the lifetimes of these structures, which are very short. The research established that a specific vibration of the species plays a crucial role in the structural changes. Finally, Dvores was able to show important differences between the alpha and beta anomers in these processes, a topic of much interest in sugar dynamics.

(d) This research demonstrated that it may be very advantageous to treat vibrational spectroscopy both by the quantum-mechanical VSCF method, and by classical MD simulations. For structures of very short lifetime, VSCF may fail. For stable, long-lived vibrations, the accuracy of VSCF can be much superior to that of classical MD. For systems having both short-lived and long-lived vibrational states, an approach using both methods may be the best way to go.

In summary, I believe that these studies have made an important contribution to the field of sugar structure and dynamics. Several of the findings are reported in Ref. (Dvores et al. 2020)

Decomposition Pathways and Dynamics of a Novel Polynitrogen Material

Polynitrogen materials are strictly the term for materials made only if nitrogen atoms. More flexibly, as we shall do here, this term is also used when referring to materials made mostly of nitrogen atoms. Extensive efforts are made now in several laboratories worldwide to discover and develop new such materials. Partly, this is in view of expected applications as energetic materials, e.g. explosives, propellants, and energy storage materials. A more fundamental motivation is just the interest in discovering new and interesting chemical behavior of nitrogen.

Recently, a new solid polynitrogen was prepared by Karl Christe of the University of Southern California. He established the chemical formula of the solid, $N_5^+[B(N_3)_4^-]$, where boron is the only non-nitrogen atom. Christe was able to determine that the N_5 group is a cation with $+1$ charge. The crystalline structure of the solid, and the thermodynamic and chemical properties of the material are as yet unknown.

Our group launched a project, led by Itai Zakai, to explore the chemical properties of these material computationally. The focus was on decomposition reactions of the molecular building blocks. The main objectives were to throw light on the chemistry of the polynitrogen, and also to investigate the likelihood of potential applications. Itai Zakai employed *ab initio* Molecular Dynamics simulations, with a potential from DFT as his main tool. As starting point of the project, the structure of the molecular building unit of the material. The structure is shown in Figure 2.24.

The calculation established that the molecule is indeed an ion pair, with the N_5^+ cation well separated from the rest of the molecular unit. The AIMD simulations show that fast decomposition of the molecule occurs for temperatures above 200K. Snapshots of the decomposition at that

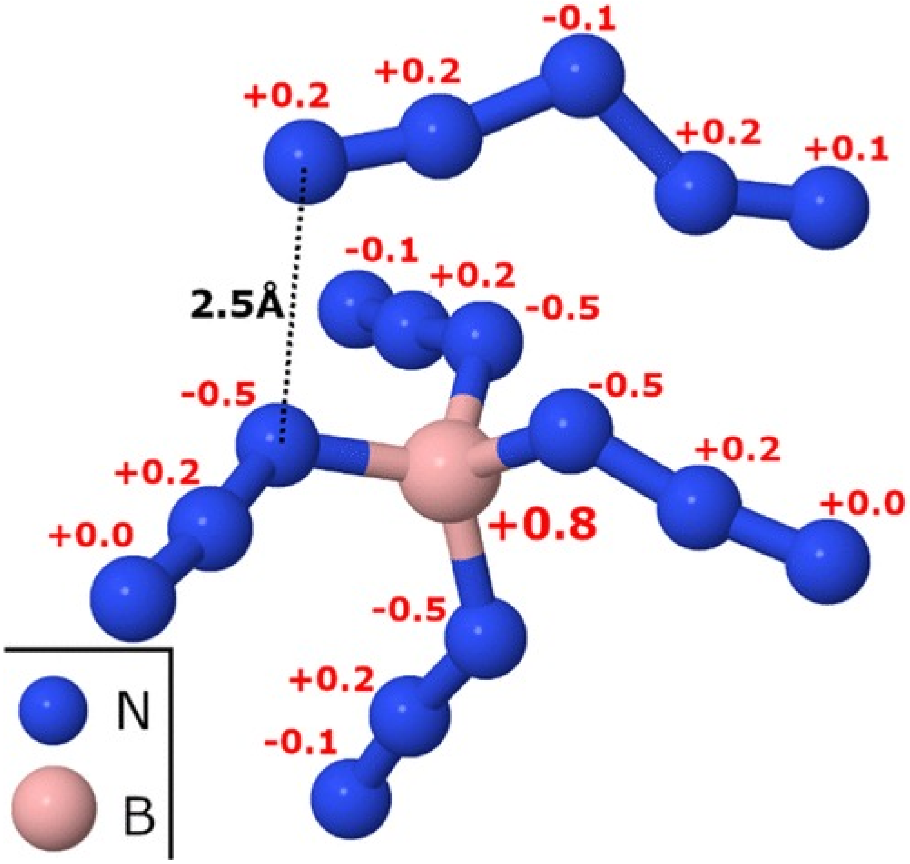

Figure 2.24. The computed structure of $(N_5{}^+)[B(N_3)_4{}^-]$. The results are from Ref. [8] below.

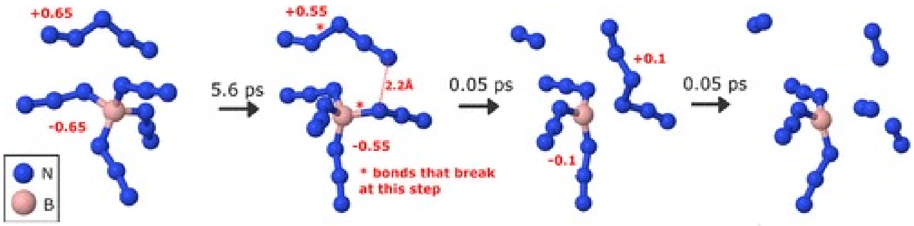

Figure 2.25. Snapshots from the decomposition dynamics of the $(N_5{}^+)[B(N_3)_4{}^-]$ at 200K. The results are from Ref. [8]

temperature are shown in Figure 2.25.

The first step in the process seems electron transfer to the N_5^+ cation. Detachment of a short nitrogen chain follows, with attack on an N_3 group bound to the boron atom. This leads to rapid ejection of N_2 molecules from the system. A total of four N_2 molecules are released on a picosecond time-scale from the beginning of the process. $B(N_3)_3$ is formed as a product, and does not undergo further decomposition even for much longer time. With the formation of the 4 N_2 molecules, much energy is released as kinetic energy of the products.

The results suggest that the system studied may prove a very effective propellant, as it releases a very large volume of gas per mol reagent, and does so on an extremely short timescale. The study confirms that the N_5 cation can be very useful in designing also other high energy density materials. The initial electron transfer which triggers the process is also suggestive for designing other polynitrogen energetic materials. The results of this work were published in Ref. (Zakai et al. 2019)

References

Dvores, M. P. et al. (2020). “Gas phase dynamics, conformational transitions and spectroscopy of charged saccharides: the oxocarbenium ion, protonated anhydrogalactose and protonated methyl galactopyranoside”. In: *Phys. Chem. Chem. Phys.* 22 (7), pp. 4144–4157. DOI: 10.1039/C9CP06572E.

Karimova, Natalia V., James Chen, et al. (2020). “SN2 Reactions of N2O5 with Ions in Water: Microscopic Mechanisms, Intermediates, and Products”. In: *The Journal of Physical Chemistry A* 124.4. PMID: 31880456, pp. 711–720. DOI: 10.1021/acs.jpca.9b09095.

Karimova, Natalia V., Man Luo, et al. (2020). “Absorption spectra of benzoic acid in water at different pH and in the presence of salts: insights from the integration of experimental data and theoretical cluster models”. In: *Phys. Chem. Chem. Phys.* 22 (9), pp. 5046–5056. DOI: 10.1039/C9CP06728K.

McCaslin, Laura M, Mark A Johnson, and R Benny Gerber (June 2019). “Mechanisms and competition of halide substitution and hydrolysis in reactions of N2O5 with seawater”. In: *Science Advances* 5.6, eaav6503. ISSN: 2375-2548. DOI: 10.1126/sciadv.aav6503.

Rossich Molina, Estefanía and R. Benny Gerber (2020). “Microscopic Mechanisms of N2O5 Hydrolysis on the Surface of Water Droplets”. In: *The Journal of Physical Chemistry A* 124.1. PMID: 31829595, pp. 224–228. DOI: 10.1021/acs.jpca.9b08900.

Shemesh, Dorit et al. (2020). “Absorption spectra of pyruvic acid in water: insights from calculations for small hydrates and comparison to experiment”. In: *Phys. Chem. Chem. Phys.* 22 (22), pp. 12658–12670. DOI: 10.1039/D0CP01810D.

Staudt, Sean et al. (2019). “Sulfate and Carboxylate Suppress the Formation of ClNO2 at Atmospheric Interfaces”. In: *ACS Earth and Space Chemistry* 3.9, pp. 1987–1997. DOI: 10.1021/acsearthspacechem.9b00177.

Zakai, Itai et al. (2019). “Structures, Stability, and Decomposition Dynamics of the Polynitrogen Molecule N5+B(N3)4– and Its Dimer [N5+]2[B(N3)4–]2”. In: *The Journal of Physical Chemistry A* 123.34. PMID: 31381345, pp. 7384–7393. DOI: 10.1021/acs.jpca.9b03704.

Scientific Activities

Robert B. Gerber group members

Name	Project	Status	Period
Dr. Dorit Shemesh	Photochemical reactions of atmospheric importance	Research Associate	Until September 2020
Dr. Laura M. McCaslin	Reactions of atmospheric oxidants with seawater droplets	PostDoc	January 2019-February 2020
Dr. Natalia V. Karimova	(1) Reactions of atmospheric molecules with ions in water (2) Photochemistry of dissolved organics in water	PostDoc	All reported period
Dr. Estefania Rossich Molina	Hydrolysis of atmospheric molecules at the air/water interface	PostDoc	2019
Michelle P. Dvores	Vibrational spectroscopy, structures, and dynamics of protonated sugars	PhD student	All reported period
Itai Zakai	(1) Reaction dynamics of polynitrogen molecules and materials (2) Reaction dynamics of HOCl at liquid water surfaces	PhD student	All reported period
Lior Sagiv	Time dependent mean-field method for vibrational dynamics and spectroscopy	PhD student	Until august 2020
Dr. Christopher Daub	Atmospheric bimolecular reactions of radicals	PostDoc	From September 2019

Robert B. Gerber scientific collaborations

Name	Project	Institution
Prof. B. J. Finlayson-Pitts	on atmospheric chemistry	UC Irvine, USA
Prof. S. A. Nizkorodov	on atmospheric photochemistry	UC Irvine, USA
Prof. Daniel Strasser	on multi-electron photoionization	Hebrew U., Israel
Prof. Mark Johnson	on chemical reactions in clusters	Yale U., USA
Prof. Gil Nathanson	Reactions at water surfaces	U. Wisconsin at Madison, USA
Prof. Tim Bertram	Reactions in atmospheric aerosols	U. Wisconsin at Madison, USA
Prof. V. H. Grassian	Photochemistry of organics in water	UC San Diego, USA
Prof. Juan Navea	Atmospheric photosensitizers	Skidmore college, NY, USA
Prof. J. P. Simons	Spectroscopy and structure of sugars and their hydrides	Oxford, UK
Prof. P. Maitre	Spectroscopy of sugars	U. Paris at Orsay, France
Prof. T. K. Roy	Vibrational spectroscopy of biomolecules	U. Jammu, India, USA
Dr. Theo Kurten	Bimolecular reactions of radicals	U. Helsinki, Finland
Prof. Lauri Halonen	Ionization of acids in water	U. Helsinki, Finland

Robert B. Gerber active grants

Project	Period	Foundation	Total grant in thousands
Relation of Reactivity to Structure	2018-2020	Ministry of Defense	₪100/year
Polynitramines	2018-2020	Ministry of Defense	₪150/year
Photochemistry of Aerosols	2020–	ISF	$ 55/year
Atmospheric reactions of radicals	2020–	A Finnish Science Agency	Postdoctoral Salary-Cannot state

Prizes, honors, editorial and review boards etc. (last 5 years)

2019	Invited Scientific Autobiography by the Annual Reviews of Physical Chemistry
2020	Gold Medal of the Israel Chemical Society

2.5 Eberhard K. U. Gross

Research Activities

Hardy Gross joined the faculty of the Hebrew University in July 2017 on the level of a 20% employment. In 2018 he was awarded an ERC Advanced Grant with HUJI being the host institution.

The ERC-funded group has started operation at the Fritz-Haber Center on September 1st, 2019. At that point, Prof. Gross' level of appointment with HUJI was raised to 100%.

At the moment, his principal research topics are the study of non-adiabatic effects within the framework of the exact factorization and the extension of density functional theory to describe the superconducting phase of matter. Another, overarching, research interest has been the development of algorithms which make the density-functional or many-body Green's function treatment possible for large and complex solid-state systems up to mesoscopic length scales, such as magnetic domains and their real-time dynamics.

Predicting Superconducting Transition Temperatures and Gap Functions

One of the great challenges of modern condensed-matter theory is the prediction of material-specific properties of superconductors, such as the critical temperature T_C and the gap at zero temperature Δ. The model of Bardeen, Cooper, and Schrieffer (BCS) accounts for the universal behavior of all conventional superconductors, but is not able to describe material dependent properties (Bardeen, Cooper, and Schrieffer 1957). A major step toward a first-principles approach to superconductivity was Eliashberg theory (Eliashberg 1960). Within the latter, all the relevant quantities that govern the superconducting properties of a material are calculated in the Nambu Green's function formalism using the analog of GW as approximation for the self-energy, where W refers to the screened Coulomb interaction, plus a renormalized phonon propagator. By virtue of Migdal's theorem (Migdal 1958), which implies that the neglected terms in the perturbation expansion of the self-energy are of the order of the square root of the electron to ion mass ratio, this method describes electron-phonon coupling effects very accurately. However, the treatment of Coulomb correlations is much harder, and, in practice, the electron-electron repulsion has mostly been modeled by an adjustable parameter μ^*, chosen as to reproduce the experimental T_C (Morel and Anderson 1962). In its common applications, thus, Eliashberg theory cannot be considered a genuine *ab initio* theory either.

Combining good accuracy with moderate numerical effort, density functional theory (DFT) is the method of choice for *ab initio* calculations of material-specific properties in the normal state. Following the discovery of high temperature superconductors, the formal framework of DFT was generalized to describe the superconducting phase of matter (Oliveira, Gross, and Kohn 1988). Compared to traditional many-body approaches, DFT for superconductors (SCDFT) has two major advantages: the computational simplicity of the equations and the absence of any empirical parameter, such as the μ^* of Eliashberg theory. In SCDFT, both the normal density $n(\mathbf{r})$ and the superconducting order parameter $\chi(\mathbf{r},\mathbf{r}')$ of the system are reproduced by a noninteracting Kohn-Sham (KS) system, where the exchange-correlation (xc) effects on superconductivity are included via the pairing potential $\Delta_s(\mathbf{r},\mathbf{r}')[n,\chi]$. The diagonal matrix elements of Δ_s with respect to the normal-state KS Bloch orbitals, $\Delta_{sk} = \langle\varphi_k|\Delta_s|\varphi_k\rangle$, play the role of a BCS gap function in the quasiparticle excitation spectrum, $E_k = \sqrt{\xi_k^2 + |\Delta_{sk}|^2}$, where ξ_k are the eigenvalues of the normal-state KS orbitals with index $k = (\mathbf{k}, n)$, i.e., Bloch vector $\mathbf{k}$ and band index n. The KS system is fully determined by solving the BCS-like gap equation,

$$\Delta_{sk} = -\mathcal{Z}_k \Delta_{sk} - \frac{1}{2} \sum_{k'} \mathcal{K}_{k,k'} \frac{tanh(\frac{\beta}{2} E_{k'})}{E_{k'}} \Delta_{sk'}, \tag{2.23}$$

where β is the inverse temperature. The kernel in this equation consists of two parts: a diagonal part $\mathcal{Z}_k$, which acts like the renormalization term in the Eliashberg equations, and a nondiagonal part, $\mathcal{K}_{k,k'} = \mathcal{K}^{ee}_{k,k'} + \mathcal{K}^{ph}_{k,k'}$, which can be interpreted as the interaction responsible for the formation of Cooper pairs. Once an approximation for the superconducting exchange-correlation functional is given, the kernels $\mathcal{Z}_k$ and $\mathcal{K}_{k,k'}$ follow from the second functional derivative of the exchange-correlation free energy with respect to the superconducting order parameter.

As for any DFT scheme, the success of the theory depends crucially on the availability of reliable exchange-correlation functionals. However, contrary to ordinary DFT, where a variety of functionals has appeared over the years, only two approximations have been proposed for the superconducting state. One of them is an LDA-type functional (Kurth et al. 1999), deduced from the superconducting electron gas, the other is an explicit orbital functional deduced from many-body theory (Lüders et al. 2005; Marques et al. 2005). For the latter, using the optimized effective potential method, the exchange-correlation kernels of Eq. 2.23 have been evaluated from the lowest order exchange diagram of the electron self-energy stemming from the Coulomb and phonon-mediated interactions. The functional thereby obtained, here referred to as LM2005, has opened up to fully *ab initio* calculations of T_C with relevant results (Profeta et al. 2006; Cudazzo et al. 2008; Akashi, Nakamura, et al. 2012; Akashi and Arita 2013; Akashi, Kawamura, et al. 2015; Floris, Profeta, et al. 2005; Arita et al. 2017). In particular, thanks to the low computational cost of the method, it has enabled the study of the full k-dependent anisotropy in the superconducting gap (Sanna, Profeta, et al. 2007; Gonnelli et al. 2008; Floris, Sanna, et al. 2007; Sanna, Franchini, et al. 2006; Linscheid et al. 2015; Floris, Profeta, et al. 2005; Kawamura, Akashi, and Tsuneyuki 2017). However, the LM2005 functional suffers from a major drawback: by construction it neglects higher order processes that in Eliashberg theory are included by the selfconsistent dressing of the electron Green's function in the self-energy diagram. In other words, some exchange-correlation contributions are neglected which, by Migdal's theorem, are of the same order in the electron-nuclear mass ratio. As consequence, the functional shows a systematic error, causing the predicted critical temperatures to be too low for materials with small electron-phonon coupling and too high for systems with strong electron-phonon coupling.

To overcome this limitation, we have developed, in the past two years, a novel exchange-correlation functional that retains the accuracy of Migdal´s approximation to the many-body electron-phonon self-energy, while having a simple analytic form. Our functional is based on a parametrization of the Eliashberg self-energy for a model superconductor with a simplified phonon system described by a single Einstein mode of frequency ω_{ph}. We assume that this model superconductor is isotropic, so that the pairing potential does not depend on the direction of **k**, but only on the energy, $\Delta_{sk} = \Delta_s(\xi_k)$. The electron-phonon matrix elements then reduce to $g_{k,k',\eta} = \sqrt{\lambda\omega_{ph}/(2N_F)}$, where λ is the (isotropic) coupling function and N_F is the density of states at the Fermi energy.

It should be emphasized that this simple model superconductor is only used for constructing the approximate exchange-correlation functional. Once this functional approximation is fixed, simulations of real materials still require the calculation of the full phonon spectrum and the complete electron-phonon coupling matrix. One could say that the construction is similar in spirit to the concept of the LDA: The latter also comes from a simple model system, the uniform electron gass, but LDA calculations of real materials still feature the full inhomogeneity of the system at hand. Ultimately, the approximate kernels in Eq. 2.23 take th form

$$\mathcal{Z}_k = -\frac{1}{tanh[(\beta/2)\xi_k]} \sum_{k',\eta} |g_{k,k',\eta}|^2 \times \frac{d}{d\xi_k}[I(\xi_k, \xi_{k'}, \omega_{q,\eta})], \tag{2.24}$$

$$\begin{aligned}\mathcal{K}^{ph}_{k,k'} &= \frac{\gamma_1\gamma_2}{tanh[(\beta/2)\xi_k]tanh[(\beta/2)E_{k'}]}\sum_{\eta}\omega_{q,\eta}|g_{k,k',\eta}|^2 \\ &\times \sum_{s_i=\pm} s_1 s_2 s_3 J\left(\xi_k, s_1\sqrt{\xi^2_{k'}+\gamma_3\Delta^2_{sk'}}, s_2\omega q, \eta, s_3\gamma_2\omega_{q,\eta}\right).\end{aligned} \tag{2.25}$$

Here, we have defined the functions

$$I(\xi,\xi',\omega) = f(\xi)f(\xi')n(\omega)\times\left[\frac{e^{\beta\xi}-e\beta(\xi'+\omega)}{\xi-\xi'-\omega}-\frac{e^{\beta\xi'}-e\beta(\xi+\omega)}{\xi-\xi'+\omega}\right], \tag{2.26}$$

$$\begin{aligned}J(\xi,E,\omega,\gamma) &= [f(\xi)+n(\omega)] \\ &\left[\frac{f(\xi-\omega)}{(\xi-\omega-E)(\xi-\omega-\gamma)}+\frac{f(E)}{(\gamma-E)(\xi-\omega-E)}-\frac{f(\gamma)}{(\gamma-E)(\xi-\omega-\gamma)}\right],\end{aligned} \tag{2.27}$$

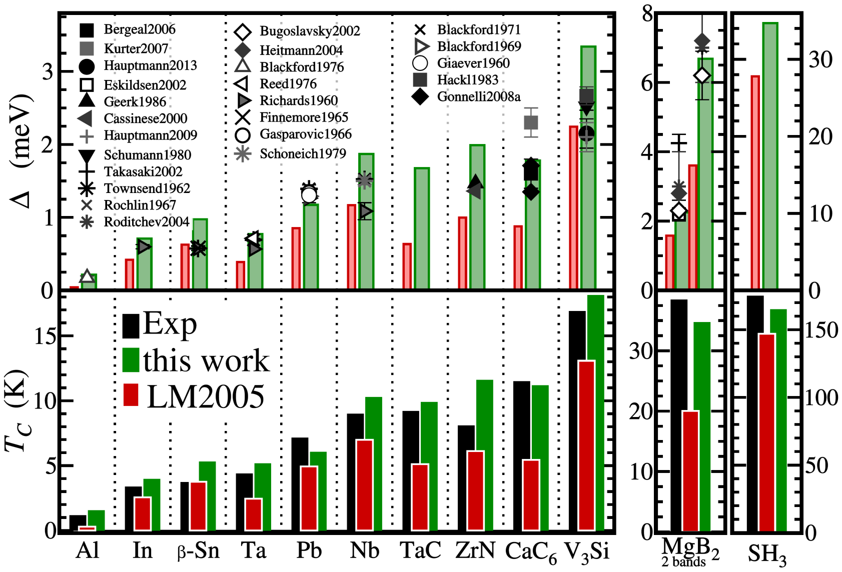

Figure 2.26. Comparison between theoretical and experimental superconducting transition temperatures (T_C) and gaps (Δ) showing that the present functional systematically improves over LM2005 (Lüders et al. 2005; Marques et al. 2005). All the materials are simulated at the calculated lattice within the PBE approximation (Perdew, Burke, and Ernzerhof 1996). Phonons are computed using density functional perturbation theory (Baroni et al. 2001); Coulomb scattering is calculated in static RPA.

where $f(\xi)$ and $n(\omega)$ are, respectively, the Fermi and Bose distributions. In addition, the Coulomb part of the kernel $\mathcal{K}^{ee}$ is simply given by the matrix elements of the static RPA screened potential.

In order to asses the accuracy of the proposed functional, we have calculated the gaps and the transition temperatures for a set of superconductors, including elemental systems from weak to strong coupling, and high-T$_C$ binary compounds. In Fig. 2.26 we show the calculated T$'_C$s and superconducting gaps, compared with the LM2005 and experimental results. As one can see, T$'_C$s and gaps predicted by the new functional are in excellent agreement with the experimental data for all the materials, improving significantly over the LM2005 approximation. By merging electronic structure methods and Eliashberg theory, the present approach sets a new standard in quality and computational feasibility for the prediction of superconducting properties. The publication of the work in (Sanna, Pellegrini, and Gross 2020) was an editor's choice and was featured on the APS platform "This Week in Physics" (https://doi.org/10.1103/Physics.13.s94).

Exact factorization-based density functional theory of electron-phonon systems

The standard picture of interacting electrons and phonons in solids is tied to the Born-Oppenheimer (BO) approximation. State-of-the-art first-principles calculations of electron-phonon-coupling effects start from a density functional theory (DFT) calculation for the electronic band structure with the nuclei being "clamped" at the equilibrium crystal structure. The normal modes of vibration (phonons) and first- and second-order electron-phonon coupling matrix elements are calculated from the response of the BO potential energy surface and Kohn-Sham (KS) orbitals to small displacements in the atomic positions. The electronic band structure, phonon modes and electron-phonon coupling terms define a BO reference state that contains enough information to evaluate several observables, such as the electron-phonon coupling constant λ and transition temperature T_c in conventional superconductors (see previous section) electronic band structure renormalization and electronic mass enhancement and specific heat. Nevertheless, there is growing interest in capturing nonadiabatic electron-phonon effects by *ab initio* approaches that go beyond this BO reference state.

Reliance on the BO approximation complicates subsequent many-body calculations. Since the electronic Hamiltonian is already included in the adiabatic potential energy surface from which the reference BO phonons are calculated, it is not straightforward to rigorously divide the original electron-nuclear Hamiltonian into electronic $\hat{H}_{elec}$, phononic $\hat{H}_{phon}$, and electron-phonon coupling $\hat{H}_{elec-phon}$ terms, as typically done in setting up many-body perturbation theory. The many-body formalisms that have been proposed (Antonius et al. 2015; Leeuwen 2004; Marini, Poncé, and Gonze 2015; Giustino 2017; Härkönen, Leeuwen, and Gross 2020) are vastly more complicated than the BO-based approach outlined above.

To avoid double-counting issues, it would be desirable to be able to calculate electronic and phononic observables within a formally-exact DFT-like framework. To this end we employ a recent generalization of density functional theory (Ryan Requist and Gross 2016; Li, R. Requist, and Gross 2018) based on the exact factorization (EF) of the electron-nuclear wavefunction into electronic and nuclear factors (Gidopoulos and Gross 2014; Abedi, Maitra, and Gross 2010). In contrast to multicomponent DFT, the basic variable is a conditional electronic density $n_R(\mathbf{r})$, a function which encodes the electronic density for each different set of nuclear coordinates $R = (\mathbf{R}_1, \mathbf{R}_2, \ldots)$. Working with $n_R(\mathbf{r})$ instead of the body-fixed-frame density $n(\mathbf{r})$ makes the exchange-correlation functionals in this theory closer to those of standard BO-based DFT.

Since EF-based DFT preserves the density-functional description of electronic structure that has made DFT so successful for solids, one can hope to obtain accurate approximations by building on the functionals of standard DFT. We follow an approximation strategy that consists in adding a nonadiabatic correction term to a standard DFT functional, such as a local density approximation (LDA) or a generalized gradient approximation (GGA). Analytical calculations for the Fröhlich model show that this approximation achieves the correct leading-order electron-phonon-coupling induced band structure renormalization, including the velocity renormalization near the Fermi energy.

The exact factorization method expresses the full electron-nuclear wavefunction as

$$\Psi(r,R)=\Phi_R(r)\chi(R), \tag{2.28}$$

where $r=\{\mathbf{r}_i\}$ denotes the set of electronic coordinates and $R=\{\mathbf{R}_\mu\}$ denotes the set of nuclear coordinates. The key variable in exact factorization-based DFT (Ryan Requist and Gross 2016; Li, R. Requist, and Gross 2018) is the conditional electronic density

$$\begin{aligned} n_R(\mathbf{r}) &= \frac{P(\mathbf{r},R)}{P(R)} = \frac{N\int|\Psi(\mathbf{r},\mathbf{r}_2,\ldots,\mathbf{r}_N,R)|^2 d\mathbf{r}_2\ldots d\mathbf{r}_N}{\int|\Psi(\mathbf{r}_1,\mathbf{r}_2,\ldots,\mathbf{r}_N,R)|^2 d\mathbf{r}_1\ldots d\mathbf{r}_N} \\ &= \langle\Phi_R|\hat{\psi}^\dagger(\mathbf{r})\hat{\psi}(\mathbf{r})|\Phi_R\rangle, \end{aligned} \tag{2.29}$$

where $P(\mathbf{r},R)$ is the joint probability to find an electron at position $\mathbf{r}$ and the nuclei at positions R and $P(R)$ is the marginal probability of finding the nuclei at R regardless of where the electrons are.

The electronic density $n(\mathbf{r})$ in a standard DFT calculation, which we hereafter denote as $n_R^{BO}(\mathbf{r})$, is also a conditional density depending parametrically on R. To see what beyond-BO contributions $n_R^{BO}(\mathbf{r})$ is missing, consider the Born-Huang expansion (Born and Huang 1954)

$$\Psi(r,R)=\sum_{J=0}^{\infty}\Phi_{JR}^{BO}(r)\chi_J^{BO}(R), \tag{2.30}$$

where $\Phi_{JR}^{BO}(r)$ is the J^{th} eigenstate of the BO Hamiltonian

$$\begin{aligned} \hat{H}^{BO} &= \sum_i \frac{\mathbf{p}_i^2}{2m_e} + \sum_{\mu<\nu}\frac{Z_\mu Z_\nu e^2}{4\pi\epsilon_0|\mathbf{R}_\mu-\mathbf{R}_\nu|} + \sum_{i<j}\frac{e^2}{4\pi\epsilon_0|\mathbf{r}_i-\mathbf{r}_j|} \\ &\quad -\sum_{i,\mu}\frac{Z_\mu e^2}{4\pi\epsilon_0|\mathbf{r}_i-\mathbf{R}_\mu|}. \end{aligned} \tag{2.31}$$

The exact conditional electronic density can be written in terms of the Born-Huang expansion as

$$n_R(\mathbf{r}) = \frac{\sum_{J=0}^{\infty}|\chi_J^{BO}(R)|^2\langle\Phi_{JR}^{BO}|\hat{\psi}^\dagger(\mathbf{r})\hat{\psi}(\mathbf{r})|\Phi_{JR}^{BO}\rangle}{\sum_{J=0}^{\infty}|\chi_J^{BO}(R)|^2}. \tag{2.32}$$

A standard DFT calculation gives only the single term

$$n_R^{BO}(\mathbf{r}) = \langle\Phi_{0R}^{BO}|\hat{\psi}^\dagger(\mathbf{r})\hat{\psi}(\mathbf{r})|\Phi_{0R}^{BO}\rangle. \tag{2.33}$$

In terms of the nuclear wavefunction $\chi(R)$ and conditional electronic wavefunction $\Phi_R(r)$, the total energy of the electron-nuclear system can be expressed as

$$E = T_{n,marg} + \int|\chi(R)|^2\big[\mathcal{E}^{BO}(R)+\mathcal{E}_{geo}(R)\big]dR, \tag{2.34}$$

where

$$
\begin{aligned}
T_{n,marg} &= \int \chi^*(R) \sum_\mu \frac{(\mathbf{P}_\mu + \mathbf{A}_\mu)^2}{2M_\mu} \chi(R) dR, \\
\mathcal{E}^{BO}(R) &= \langle \Phi_R | \hat{H}^{BO} | \Phi_R \rangle, \qquad (2.35) \\
\mathcal{E}_{geo}(R) &= \sum_\mu \frac{\hbar^2 \langle \nabla_{\mathbf{R}_\mu} \Phi_R \,| (1 - |\Phi_R\rangle\langle\Phi_R|) |\, \nabla_{\mathbf{R}_\mu} \Phi_R \rangle}{2M_\mu}
\end{aligned}
$$

and $\mathbf{A}_\mu \equiv \langle \Phi_R | - i\hbar \nabla_{\mathbf{R}_\mu} \Phi_R \rangle$. The kinetic energy of the marginal nuclear wave function, denoted $T_{n,marg}$, is related to the true nuclear kinetic energy by the identity $\langle \Psi | \hat{T}_n | \Psi \rangle = T_{n,marg} + \int |\chi(R)|^2 \mathcal{E}_{geo}(R) dR$. Making the energy stationary with respect to variations of $\chi(R)$ and $\Phi_R(r)$ subject to the partial normalization condition $\int |\Phi_R(r)|^2 dr = 1$ for all R leads to the following equations (Gidopoulos and Gross 2014; Abedi, Maitra, and Gross 2010):

$$\left[\hat{H}^{BO} + \hat{U}_{en} \right] |\Phi_R\rangle = \mathcal{E}(R) |\Phi_R\rangle \qquad (2.36)$$

$$\left[\sum_\mu \frac{\left(\mathbf{P}_\mu + \mathbf{A}_\mu\right)^2}{2M_\mu} + \mathcal{E}(R) \right] \chi(R) = E\chi(R), \qquad (2.37)$$

where $\hat{U}_{en}$ is a complicated operator that depends nonlinearly on χ and Φ_R. The nuclear equation has the form of a conventional Schrödinger equation with an exact potential energy surface $\mathcal{E} = \mathcal{E}^{BO} + \mathcal{E}_{geo}$ and an exact induced vector potential $\mathbf{A}_\mu$.

Exact factorization-based DFT (Ryan Requist and Gross 2016; Li, R. Requist, and Gross 2018) seeks to bypass the many-body electronic equation, Eq. (2.36), using in its place the conditional KS equation

$$\left[\frac{\mathbf{p}^2}{2m} + v_{en}(\mathbf{r}, R) + v^{EF}_{hxc}(\mathbf{r}, R) \right] \psi_{iR}(\mathbf{r}) = \epsilon_{iR} \psi_{iR}(\mathbf{r}), \qquad (2.38)$$

where $v_{en}(\mathbf{r}, R) = -\sum_\mu Z_\mu e^2 / 4\pi\epsilon_0 |\mathbf{r} - \mathbf{R}_\mu|$ and $v^{EF}_{hxc}(\mathbf{r})$ is a nonadiabatic Hartree-exchange-correlation potential. The latter can be written as

$$v^{EF}_{h_xc}(r, R) = v^{BO}_{h_{xc}}(r, R) + v_{geo}(r, R) \qquad (2.39)$$

$v^{BO}_{h_{xc}}(r, R)$ can be approximated as functional of $n_{\mathbf{R}}(\mathbf{r})$, using standard DFT approximations like LDA or GGAs. $v_{geo}(r, R)$ follows from the functional derivative of $\mathcal{E}_{geo}(R)$ with respect to $n_R(\mathbf{r})$. Studying the nonadiabatic electron transfer in LiF within a two-site Hubbard model (Li, R. Requist, and Gross 2018) suggests for $\mathcal{E}_{geo}(R)$ the simple approximation

$$\mathcal{E}_{geo}(R) = \int \frac{1}{2} y(n_R(\mathbf{r}) I_{\mu\nu} \nabla_\mu n_R(\mathbf{r}) \nabla_\nu n_R(\mathbf{r}) d\mathbf{r} \qquad (2.40)$$

$$y(n_R) = \frac{1}{4n_R} \qquad (2.41)$$

where $I_{\mu\nu}$ is an inverse inertia tensor. The performance of this approximate functional is demonstrated in Fig. 2.27 for the Hubbard dimer model. Comparing the exact density as function of R

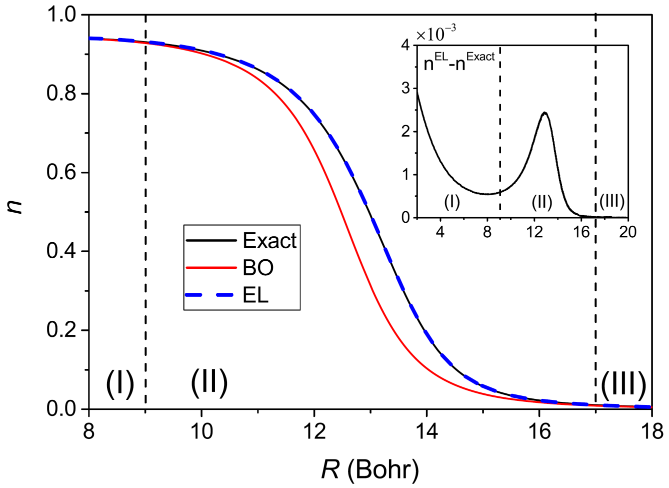

Figure 2.27. Comparison of the exact and the BO ground state densities. Also shown is the density obtained by solving the Euler-Lagrange (EL) equation with the approximate functional of Eqs. 2.40 and 2.41

with the density following from the above approximation, the agreement is excellent, while the mere BO result is far off, emphasizing the importance of non-adiabaticity for this case.

For electron-phonon systems, it is convinient to adopt Born von Kármán boundary conditions and work with the phonon normal mode coordinates $U = (U_{q\lambda})$. Along with this, we introduce the factorization (Ryan Requist, Proetto, and Gross 2019)

$$\psi(\mathbf{r}, U) = \Phi_U(\mathbf{r})\chi(U) \tag{2.42}$$

and rewrite all of the above equations replacing R by U. The phonon normal mode coordinates U are derived in the usual way by expanding to second order around the equilibrium positions and diagonalizing the resulting Hessian but, the crucial point is that we expand the exact potential energy surface, rather than the BO surface. Like before what we ultimately need is an approximation for $\mathcal{E}_{geo}(U)$ as functional of $n_U(\mathbf{r})$. Here we start from Eq. 2.35 and approximate the correlated conditional wave function by the Slater determinant of occupied Kohn-Sham orbitals. This defines an orbital-dependent functional for $\mathcal{E}_{geo}$ which can be viewed as an implicit functional of n_U. Once again, the crucial point is that nonadiabatic effects are described by a simple additive correction to an existing DFT functional. Fig. 2.28 shows that within this functional the well-known electronic band-structure renormalization (the phonon-induced "wiggle" near the Fermi energy of metals) is correctly reproduced.

Extending Solid-State Calculations to Ultra-Long-Range Length Scales

Density functional theory (DFT) has had a tremendous impact on solid-state physics and is, due to its computational efficiency, at the heart of modern computer based material research. In a typical calculation a single unit cell is solved with periodic boundary conditions. Effects extending far beyond the size of a single unit cell, such as magnetic domains and their current-driven dynamics, or the propagation of electromagnetic radiation through solids beyond the dipole approximation, are hard to capture. While it is, in principle, possible to use ever larger supercells, in practice one quickly reaches the limit of computational viability. This is mostly due to the poor scaling with the

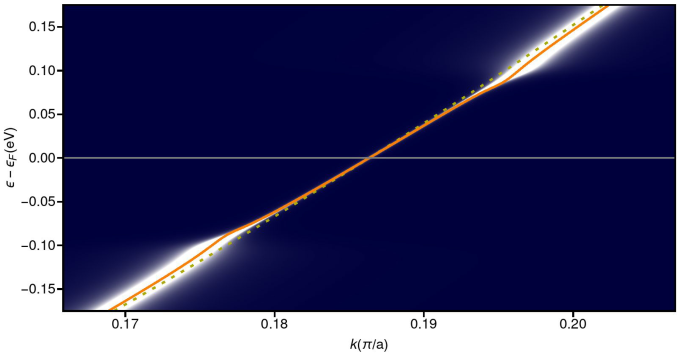

Figure 2.28. The Kohn-Sham band structure (orange) in exact factorization-based DFT captures the phonon-induced wiggle in the electronic spectral function (background blue-white color scale) of the Frohlich model with a parabolic electronic band (dashed yellow) linearly coupled to a single Einstein phonon with energy 0.1 eV.

number of atoms, $\mathcal{O}(N_{atom}^3)$, which plagues all computer programs with a systematic basis set. Recent progress based on linear scaling approaches (Goedecker 1999) was able to increase the computable system size considerably. Linear scaling approaches, however, require a "nearsightedness" of the system. While this might be fulfilled for effects strictly related to the charge density, this is certainly not fulfilled for large magnetic systems, such as magnetic domains.

To tackle this problem, we propose a fundamentally different approach to drastically extend the length scale of DFT calculations without significantly increasing the computational cost. Our approach relies on altered Bloch states and can be understood as a generalization of the spin-spiral ansatz (Sandratskii 1986) which emerges as a special case of our ansatz. In the spin-spiral ansatz, a momentum-dependent phase is added to the normal Bloch state. It then becomes possible to compute a large, extended spiraling magnetic moment with a single unit cell. While this is computationally very efficient, it is, at the same time, the biggest limitation of the spin-spiral ansatz: It allows only for a change in the direction of the magnetization while the magnitude of the magnetization and the charge density remain unaltered. We overcome this limitation by introducing an additional sum in the Bloch states over a finer grid in reciprocal space around each **k** point. The resulting densities then become a Fourier series with a controllable periodicity, which may extend far beyond the length scale of a single unit cell.

The systems we will focus on, are described by the Kohn-Sham (KS) Hamiltonian of spin-density functional theory:

$$\hat{H}_0 = -\frac{\nabla^2}{2} + v_s(\mathbf{r}) + \mathbf{B}_s(\mathbf{r}) \cdot \sigma \tag{2.43}$$

The KS potential $v_s = v_{ext}(\mathbf{r}) + v_H(\mathbf{r}) + v_{xc}(\mathbf{r})$ consists of an external potential v_{ext}, a Hartree potential v_H and an exchange-correlation (xc) potential v_{xc}. Similarly, the KS magnetic field $\mathbf{B}_s(\mathbf{r}) = (1/2c)\, \mathbf{B}_{ext}(\mathbf{r}) + \mathbf{B}_{xc}(\mathbf{r})$ can be decomposed into an external field $\mathbf{B}_{ext}$ and an xc field $\mathbf{B}_{xc}$.

Bloch states of the form $\varphi_{n\mathbf{k}}(\mathbf{r}) = u_{n\mathbf{k}}(\mathbf{r})e^{i\mathbf{k}\cdot\mathbf{r}}$, where $u_{n\mathbf{k}}$ is a lattice-periodic spinor function, are used in standard solid-state calculations. The central idea of our approach (Müller et al. 2020) is a generalization of this Bloch state to include long-range modulations. Our ultra-long-range ansatz employs, in addition to a momentum-dependent phase (Sandratskii 1986), momentum-dependent expansion coefficients which allow for changes in magnitude and direction of the spin and charge densities from cell to cell. For a fixed **k** vector our new Bloch-like state reads

$$\Phi_{\alpha}^{\mathbf{k}}(\mathbf{r}) = \frac{1}{\sqrt{N_u}} \sum_{n\kappa} c_{n\mathbf{k}+\kappa}^{\alpha} \begin{pmatrix} u_{n\mathbf{k}}^{\uparrow}(\mathbf{r}) \\ u_{n\mathbf{k}}^{\downarrow}(\mathbf{r}) \end{pmatrix} e^{i(\mathbf{k}+\kappa)\cdot\mathbf{r}} \tag{2.44}$$

where $u_{n\mathbf{k}}^{\uparrow\downarrow}$ are the normalized orbitals of a lattice-periodic system, *n* is a band index, and **k** a reciprocal space vector, $c_{n\mathbf{k}+\kappa}^{\alpha}$ are complex coefficients to be determined variationally and α labels a particular long-range state. The vectors κ live on a finer grid around each **k** point in reciprocal space, which we use to sample long-range effects. Finally, N_u is a normalization factor that is equal to the number of unit cells on which $\Phi_{\alpha}^{\mathbf{k}}$ is periodic.

From this wave function, we can construct the charge and magnetization density

$$\rho(\mathbf{r}) = \frac{1}{N_k} \sum_{\mathbf{k},\alpha} f_{\alpha}^{\mathbf{k}} \Phi_{\alpha}^{\mathbf{k}\dagger}(\mathbf{r}) \Phi_{\alpha}^{\mathbf{k}}(\mathbf{r}) \tag{2.45}$$

$$\mathbf{m}(\mathbf{r}) = \frac{1}{N_k} \sum_{\mathbf{k},\alpha} f_{\alpha}^{\mathbf{k}} \Phi_{\alpha}^{\mathbf{k}\dagger}(\mathbf{r}) \sigma \Phi_{\alpha}^{\mathbf{k}}(\mathbf{r}) \tag{2.46}$$

with the number of **k** points $N_{\mathbf{k}}$ and the ultra-long-range occupation numbers $f_{\alpha}^{\mathbf{k}}$ associated with the orbitals $\Phi_{\alpha}^{\mathbf{k}}$. The charge and magnetization density obtained from this wave function take the form

$$\rho(\mathbf{r}) = \sum_{Q} \rho_{Q}(\mathbf{r}) e^{i\mathbf{Q}\cdot\mathbf{r}} \tag{2.47}$$

and

$$\mathbf{m}(\mathbf{r}) = \sum_{Q} \mathbf{m}_{Q}(\mathbf{r}) e^{i\mathbf{Q}\cdot\mathbf{r}}, \tag{2.48}$$

with $\mathbf{Q} = \kappa - \kappa'$. These partial densities $\rho_{\mathbf{Q}}$ and $\mathbf{m}_{\mathbf{Q}}$ are complex in general and act as lattice-periodic Fourier coefficients. The resulting real-space densities $\rho(\mathbf{r})$ and $\mathbf{m}(\mathbf{r})$ are real functions, which, depending on the values of Q, will have a periodicity larger than the length scale of a unit cell. By adjusting the underlying κ lattice, it is therefore possible to change the **Q** vectors and hence allow for variations of arbitrary length in the system. We emphasize that there is no restriction on the magnitude of $\rho_{\mathbf{Q}}$, $\mathbf{m}_{\mathbf{Q}}$ and we are thus able to expand arbitrary modulations in the charge and magnetization densities. This is a key difference compared to the spin-spiral ansatz (Sandratskii 1986) or any down-folding technique.

With the densities at hand, we will now focus on generalizing the Hamiltonian such that meaningful, nontrivial values for the expansion coefficients $c_{n\mathbf{k}+\kappa}$ in Eq. 2.44 are obtained. The ultra-long-range Hamiltonian retains the full lattice periodic KS Hamiltonian $\hat{H}_0$ given in Eq. 2.43, but also has an additional "modulation" term

$$\hat{H} = \hat{H}_0 + \sum_{\mathbf{Q}} \hat{H}_{\mathbf{Q}}(\mathbf{r}) e^{i\mathbf{Q}\cdot\mathbf{r}} \tag{2.49}$$

The total Hamiltonian $\hat{H}$ is thus decomposed in the same way as the charge and magnetization densities. For a KS system like Eq.2.43, our modulation Hamiltonian reads

$$H_{\mathbf{Q}}(\mathbf{r}) = V_{\mathbf{Q}}(\mathbf{r}) + \mathbf{B}_{\mathbf{Q}}(\mathbf{r}) \cdot \sigma, \tag{2.50}$$

where $V_{\mathbf{Q}}(\mathbf{r})$ and $\mathbf{B}_{\mathbf{Q}}(\mathbf{r})$ are again complex, lattice periodic Fourier coefficients and contribute to long-ranged versions of the scalar potential and the magnetic field, respectively. The scalar potential can be decomposed into an external $V_{\mathbf{Q}}^{ext}(\mathbf{r})$, a Hartree potential $V_{\mathbf{Q}}^{H}(\mathbf{r})$, and an xc potential $V_{\mathbf{Q}}^{xc}(\mathbf{r})$. $V_{\mathbf{Q}}^{ext}(\mathbf{r})$ of an external, long-ranged potential can be freely chosen. The coefficients for the long-ranged Hartree potential $V_{\mathbf{Q}}^{H}(\mathbf{r})$ are obtained from the long-range density

$$V_{\mathbf{Q}}^{H}(\mathbf{r}) = \int d^3r' \frac{\rho_{\mathbf{Q}}(\mathbf{r}')}{|\mathbf{r}-\mathbf{r}'|} e^{-i\mathbf{Q}\cdot(\mathbf{r}-\mathbf{r}')} \tag{2.51}$$

Next we will determine the coefficients associated with the xc term. An important difference compared to the Hartree potential is that the xc potential is inherently a nonlinear functional of the densities, therefore the naive approach $V_{\mathbf{Q}}^{xc} = V_{xc}[\rho_{\mathbf{Q}}]$ may introduce a mixing of the real and imaginary part of $\rho_{\mathbf{Q}}$. Instead, we first Fourier transform the density to real space, $\rho_{\mathbf{R}}(\mathbf{r})$, and then evaluate the xc potential separately for each **R** vector. The inverse Fourier transform is then applied to obtain

$$V_{\mathbf{Q}}^{xc}(\mathbf{r}) = \frac{1}{N_{\mathbf{R}}} \sum_j V_{xc}[\rho_{\mathbf{R}_j}](\mathbf{r}) e^{-i\mathbf{Q}\cdot\mathbf{R}_j} \tag{2.52}$$

The coefficients of the magnetic field $\mathbf{B}_Q$ in Eq. 2.50 consist of an external field, an xc field, and a dipole-dipole field: $\mathbf{B}_{\mathbf{Q}}(\mathbf{r}) = (1/2c)\mathbf{B}_{\mathbf{Q}}{}^{ext}(\mathbf{r}) + \mathbf{B}_{\mathbf{Q}}{}^{xc}(\mathbf{r}) + (1/2c)\mathbf{B}_{\mathbf{Q}}{}^{D}(\mathbf{r})$. Again, the external magnetic field may be chosen arbitrarily and the xc field can be computed analogously to the xc potential

$$B_{\mathbf{Q}}^{xc}(\mathbf{r}) = \frac{1}{N_{\mathbf{R}}} \sum_j B_{xc}[\rho_{\mathbf{R}_j}, \mathbf{m}_{\mathbf{R}_j}](\mathbf{r}) e^{-i\mathbf{Q}\cdot\mathbf{R}_j} \tag{2.53}$$

The last term of $\mathbf{B}_{\mathbf{Q}}(\mathbf{r})$ corresponds to the magnetic field associated with the magnetostatic dipole-dipole interaction

$$B_{\mathbf{Q}}^{D}(\mathbf{r}) = \frac{1}{2c} \int d^3r' \frac{3\mathbf{e}_{\mathbf{r}-\mathbf{r}'}(\mathbf{m}_{\mathbf{Q}}(\mathbf{r}') \cdot \mathbf{e}_{\mathbf{r}-\mathbf{r}'}) - \mathbf{m}_{\mathbf{Q}}(\mathbf{r}')}{|\mathbf{r}-\mathbf{r}'|^3} e^{-i\mathbf{Q}\cdot(\mathbf{r}-\mathbf{r}')}, \tag{2.54}$$

where $\mathbf{e}_{\mathbf{r}-\mathbf{r}'}$ is the unit vector along the direction $\mathbf{r} - \mathbf{r}'$. The contribution of the dipole-dipole interaction is typically neglected in DFT calculations as it is usually small in comparison with $\mathbf{B}^{xc}$, which originates from the Coulomb exchange interaction. However, as the Coulomb exchange interaction is inherently short ranged, the magnetic dipole-dipole interaction is expected to have a significant contribution at larger length scales (Pellegrini et al. 2020). We therefore include this term in the modulation Hamiltonian.

We have implemented the ultra-long-range approach in the Elk electronic structure code (http://elk.sourceforge.net/), which is an all electron code using full-potential linearized augmented plane wave (FPLAPW) method, which is an all electron code using the full-potential linearized augmented plane wave (FPLAPW) method. The scaling of the method is linear in the number of **k** points and cubic in κ points.

To test our method, we performed a calculation for which the ultracell is small enough to be amenable to supercell calculations so that a detailed comparison is possible. The numerical test deals with the so-called γ phase of Fe. Previous calculations (Sjöstedt and Nordström 2002) have shown that the spin-spiral state has the lowest energy compared to several commensurate ferromagnetic and antiferromagnetic structures. The ultra-long-range method allows us to address the question whether the much larger variational freedom associated with the ultracell still yields the spin spiral as ground state. We perform both the traditional spin-spiral as well as the ultracell calculations for γ-Fe. Spin-orbit coupling cannot be used consistently with the spin-spiral ansatz but there is no such restriction with the long-range method. However, for the sake of comparison, spin-orbit coupling was not included in the ultracell calculations.

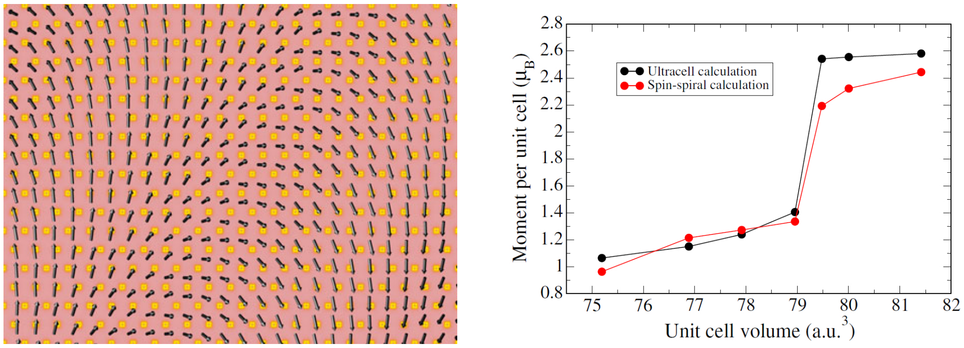

Figure 2.29. Ultra-long-range magnetization density of γ-Fe plotted in the plane perpendicular to [001]. The color indicates the magnitude of the magnetization and the arrows indicate the direction. The modulation encompasses 32 unit cells in the [100] direction (left). Plot of moment against unit cell volume for both the long-range and spin-spiral ansatz (right)

An initial magnetic field is required to break the spin symmetry. To ensure an unbiased calculation, we applied a random field to the ultracell calculation and subsequently reduced it to zero. Nevertheless, the magnetization converged to an ordered state where the magnitude was constant over the ultracell and only the direction varied (2.29 left). This corresponds precisely to the lattice parameter and undergoes a transition from $1\mu_B$ to $2.5\mu_B$ for this relatively small **Q** vector. As may be seen in Fig. (2.29 right), this behavior is observed for both the ultracell and spin-spiral calculations.

In another calculation, we tested the method with a long-range, external electrostatic field. This is in anticipation of future developments where ultra-long-range TDDFT calculations are performed in conjunction with Maxwell's equations. To demonstrate the power of our new method, we performed a calculation which is too large for a supercell. Rather than attempting to model a physical phenomenon at this stage, we simply apply an artificially chosen electrostatic potential to an insulator, in this case LiF.

The resultant change in density away from unit cell periodicity is plotted in Fig.2.30. As the potential is artificial, the important metric here is the computational effort expended in reaching the self-consistent solution. The rate of convergence is fairly slow because of the effect of the long-range Coulomb interaction, and thus we performed 170 iterations of the self-consistent loop. The calculation was performed on 480 CPU cores and each iteration took about 40 min. This level of performance for an all-electron calculation indicates that physical phenomena involving modulations of the electronic state over hundreds or thousands of unit cells are within reach of this approach.

The method presented here opens up exciting possibilities of future research: it paves the way

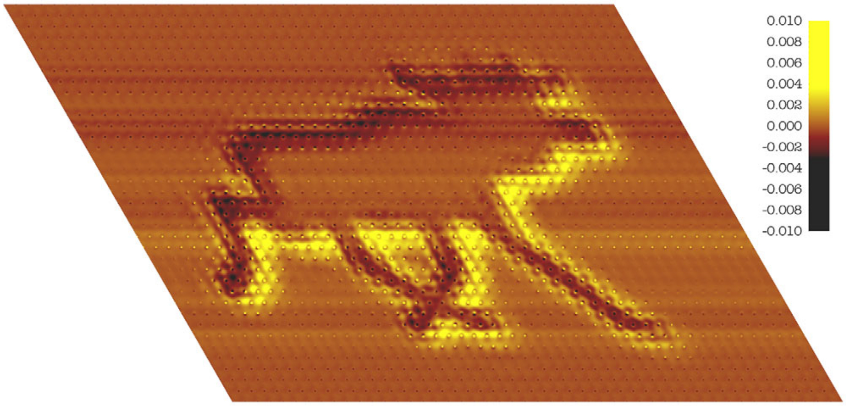

Figure 2.30. Self-consistent density without the $\rho_{\mathbf{Q}=0}(\mathbf{r})$ term for a 3456 atom ultracell of LiF with an artificial external potential. The plotting plane is perpendicular to [001] and contains 48 × 36 unit cells.

to calculations of mesoscopic systems, such as magnetic domain walls or skyrmions, which have so far been out of reach for *ab initio* methods like DFT. Furthermore, the novel technique is straightforwardly incorporated in real-time TDDFT calculations which, when combined with the solution of Maxwell's equations, will give access to the propagation of electromagnetic radiation through extended solids and to the dynamics of mesoscopic structures such as plasmonic microantennas within a genuine ab initio description.

This work (Müller et al. 2020) was featured in the APS platform "This week in Physics" (https://physics.aps.org/articles/v13/196) and Fig. 2.30 was chosen as the cover illustration of the PRL volume 125 issue 25.

References

Abedi, Ali, Neepa T. Maitra, and E. K. U. Gross (Sept. 2010). "Exact Factorization of the Time-Dependent Electron-Nuclear Wave Function". In: *Phys. Rev. Lett.* 105 (12), p. 123002. DOI: `10.1103/PhysRevLett.105.123002`. URL: `https://link.aps.org/doi/10.1103/PhysRevLett.105.123002`.

Akashi, R. and R. Arita (Aug. 2013). "Nonempirical study of superconductivity in alkali-doped fullerides based on density functional theory for superconductors". In: *Phys. Rev. B* 88 (5), p. 054510. DOI: `10.1103/PhysRevB.88.054510`. URL: `https://link.aps.org/doi/10.1103/PhysRevB.88.054510`.

Akashi, R., M. Kawamura, et al. (June 2015). "First-principles study of the pressure and crystal-structure dependences of the superconducting transition temperature in compressed sulfur hydrides". In: *Phys. Rev. B* 91 (22), p. 224513. DOI: `10.1103/PhysRevB.91.224513`. URL: `https://link.aps.org/doi/10.1103/PhysRevB.91.224513`.

Akashi, R., K. Nakamura, et al. (Aug. 2012). "High-temperature superconductivity in layered nitrides β-Li$_x M$NCl (M = Ti, Zr, Hf): Insights from density functional theory for superconductors". In: *Phys. Rev. B* 86 (5), p. 054513. DOI: `10.1103/PhysRevB.86.054513`. URL: `https://link.aps.org/doi/10.1103/PhysRevB.86.054513`.

Antonius, G. et al. (Aug. 2015). "Dynamical and anharmonic effects on the electron-phonon coupling and the zero-point renormalization of the electronic structure". In: *Phys. Rev. B* 92 (8), p. 085137. DOI: `10.1103/PhysRevB.92.085137`. URL: `https://link.aps.org/doi/10.1103/PhysRevB.92.085137`.

Arita, R. et al. (July 2017). “Nonempirical Calculation of Superconducting Transition Temperatures in Light-Element Superconductors”. In: *Adv. Mater.* 29.25. Special Issue: Materials Research at RIKEN CEMS, p. 1602421. DOI: 10.1002/adma.201602421. URL: http://tinyurl.sfx.mpg.de/vkoj.

Bardeen, J., L. N. Cooper, and J. R. Schrieffer (Dec. 1957). “Theory of Superconductivity”. In: *Phys. Rev.* 108 (5), pp. 1175–1204. DOI: 10.1103/PhysRev.108.1175. URL: https://link.aps.org/doi/10.1103/PhysRev.108.1175.

Baroni, S. et al. (July 2001). “Phonons and related crystal properties from density-functional perturbation theory”. In: *Rev. Mod. Phys.* 73 (2), pp. 515–562. DOI: 10.1103/RevModPhys.73.515. URL: https://link.aps.org/doi/10.1103/RevModPhys.73.515.

Born, M. and K. Huang (1954). *Dynamical theory of crystal lattices*. Oxford University Press, New York.

Cudazzo, P. et al. (June 2008). “Ab Initio Description of High-Temperature Superconductivity in Dense Molecular Hydrogen”. In: *Phys. Rev. Lett.* 100 (25), p. 257001. DOI: 10.1103/PhysRevLett.100.257001. URL: https://link.aps.org/doi/10.1103/PhysRevLett.100.257001.

Eliashberg, G. M. (Sept. 1960). “Interactions between Electrons and Lattice Vibrations in a Superconductor”. In: *Sov. Phys. JETP* 11 (3), pp. 696–702. URL: http://www.jetp.ac.ru/cgi-bin/e/index/e/11/3/p696?a=list.

Floris, A., G. Profeta, et al. (Jan. 2005). “Superconducting Properties of $\mathrm{MgB_2}$ from First Principles”. In: *Phys. Rev. Lett.* 94 (3), p. 037004. DOI: 10.1103/PhysRevLett.94.037004. URL: https://link.aps.org/doi/10.1103/PhysRevLett.94.037004.

Floris, A., A. Sanna, et al. (Feb. 2007). “Two-band superconductivity in Pb from ab initio calculations”. In: *Phys. Rev. B* 75 (5), p. 054508. DOI: 10.1103/PhysRevB.75.054508. URL: https://link.aps.org/doi/10.1103/PhysRevB.75.054508.

Gidopoulos, N. I. and E. K. U. Gross (2014). “Electronic non-adiabatic states: towards a density functional theory beyond the Born-Oppenheimer approximation”. In: *Philosophical Transactions of the Royal Society A: Mathematical, Physical and Engineering Sciences* 372.2011, p. 20130059. DOI: 10.1098/rsta.2013.0059. URL: https://royalsocietypublishing.org/doi/abs/10.1098/rsta.2013.0059.

Giustino, Feliciano (Feb. 2017). “Electron-phonon interactions from first principles”. In: *Rev. Mod. Phys.* 89 (1), p. 015003. DOI: 10.1103/RevModPhys.89.015003. URL: https://link.aps.org/doi/10.1103/RevModPhys.89.015003.

Goedecker, Stefan (July 1999). “Linear scaling electronic structure methods”. In: *Rev. Mod. Phys.* 71 (4), pp. 1085–1123. DOI: 10.1103/RevModPhys.71.1085. URL: https://link.aps.org/doi/10.1103/RevModPhys.71.1085.

Gonnelli, R. S. et al. (May 2008). “Evidence for Gap Anisotropy in $\mathrm{CaC_6}$ from Directional Point-Contact Spectroscopy”. In: *Phys. Rev. Lett.* 100 (20), p. 207004. DOI: 10.1103/PhysRevLett.100.207004. URL: https://link.aps.org/doi/10.1103/PhysRevLett.100.207004.

Härkönen, Ville J., Robert van Leeuwen, and E. K. U. Gross (June 2020). “Many-body Green’s function theory of electrons and nuclei beyond the Born-Oppenheimer approximation”. In: *Phys. Rev. B* 101 (23), p. 235153. DOI: 10.1103/PhysRevB.101.235153. URL: https://link.aps.org/doi/10.1103/PhysRevB.101.235153.

Kawamura, M., R. Akashi, and S. Tsuneyuki (Feb. 2017). “Anisotropic superconducting gaps in $\mathrm{YNi_2B_2C}$: A first-principles investigation”. In: *Phys. Rev. B* 95 (5), p. 054506. DOI: 10.1103/PhysRevB.95.054506. URL: https://link.aps.org/doi/10.1103/PhysRevB.95.054506.

Kurth, S. et al. (Sept. 1999). “Local Density Approximation for Superconductors”. In: *Phys. Rev. Lett.* 83 (13), pp. 2628–2631. DOI: 10.1103/PhysRevLett.83.2628. URL: https://link.aps.org/doi/10.1103/PhysRevLett.83.2628.

Leeuwen, Robert van (Mar. 2004). “First-principles approach to the electron-phonon interaction”. In: *Phys. Rev. B* 69 (11), p. 115110. DOI: `10.1103/PhysRevB.69.115110`. URL: `https://link.aps.org/doi/10.1103/PhysRevB.69.115110`.

Li, C., R. Requist, and E. K. U. Gross (2018). “Density functional theory of electron transfer beyond the Born-Oppenheimer approximation: Case study of LiF”. In: *The Journal of Chemical Physics* 148.8, p. 084110. DOI: `10.1063/1.5011663`. URL: `https://doi.org/10.1063/1.5011663`.

Linscheid, A. et al. (Aug. 2015). “First-Principles Calculation of the Real-Space Order Parameter and Condensation Energy Density in Phonon-Mediated Superconductors”. In: *Phys. Rev. Lett.* 115 (9), p. 097002. DOI: `10.1103/PhysRevLett.115.097002`. URL: `https://link.aps.org/doi/10.1103/PhysRevLett.115.097002`.

Lüders, M. et al. (July 2005). “Ab initio theory of superconductivity. I. Density functional formalism and approximate functionals”. In: *Phys. Rev. B* 72 (2), p. 024545. DOI: `10.1103/PhysRevB.72.024545`. URL: `https://link.aps.org/doi/10.1103/PhysRevB.72.024545`.

Marini, Andrea, S. Poncé, and X. Gonze (June 2015). “Many-body perturbation theory approach to the electron-phonon interaction with density-functional theory as a starting point”. In: *Phys. Rev. B* 91 (22), p. 224310. DOI: `10.1103/PhysRevB.91.224310`. URL: `https://link.aps.org/doi/10.1103/PhysRevB.91.224310`.

Marques, M. A. L. et al. (July 2005). “Ab initio theory of superconductivity. II. Application to elemental metals”. In: *Phys. Rev. B* 72 (2), p. 024546. DOI: `10.1103/PhysRevB.72.024546`. URL: `https://link.aps.org/doi/10.1103/PhysRevB.72.024546`.

Migdal, A. B. (Dec. 1958). “Interaction between Electrons and Lattice Vibrations in a Normal Metal”. In: *Sov. Phys. JETP* 7 (6), pp. 996–1001.

Morel, P. and P. W. Anderson (Feb. 1962). “Calculation of the Superconducting State Parameters with Retarded Electron-Phonon Interaction”. In: *Phys. Rev.* 125 (4), pp. 1263–1271. DOI: `10.1103/PhysRev.125.1263`. URL: `https://link.aps.org/doi/10.1103/PhysRev.125.1263`.

Müller, T. et al. (Dec. 2020). “Extending Solid-State Calculations to Ultra-Long-Range Length Scales”. In: *Phys. Rev. Lett.* 125 (25), p. 256402. DOI: `10.1103/PhysRevLett.125.256402`. URL: `https://link.aps.org/doi/10.1103/PhysRevLett.125.256402`.

Oliveira, L. N., E. K. U. Gross, and W. Kohn (June 1988). “Density-Functional Theory for Superconductors”. In: *Phys. Rev. Lett.* 60 (23), pp. 2430–2433. DOI: `10.1103/PhysRevLett.60.2430`. URL: `https://link.aps.org/doi/10.1103/PhysRevLett.60.2430`.

Pellegrini, C. et al. (Apr. 2020). “Density functional theory of magnetic dipolar interactions”. In: *Phys. Rev. B* 101 (14), p. 144401. DOI: `10.1103/PhysRevB.101.144401`. URL: `https://link.aps.org/doi/10.1103/PhysRevB.101.144401`.

Perdew, J. P., K. Burke, and M. Ernzerhof (Oct. 1996). “Generalized Gradient Approximation Made Simple”. In: *Phys. Rev. Lett.* 77 (18), pp. 3865–3868. DOI: `10.1103/PhysRevLett.77.3865`. URL: `https://link.aps.org/doi/10.1103/PhysRevLett.77.3865`.

Profeta, G. et al. (Feb. 2006). “Superconductivity in Lithium, Potassium, and Aluminum under Extreme Pressure: A First-Principles Study”. In: *Phys. Rev. Lett.* 96 (4), p. 047003. DOI: `10.1103/PhysRevLett.96.047003`. URL: `https://link.aps.org/doi/10.1103/PhysRevLett.96.047003`.

Requist, Ryan and E. K. U. Gross (Nov. 2016). “Exact Factorization-Based Density Functional Theory of Electrons and Nuclei”. In: *Phys. Rev. Lett.* 117 (19), p. 193001. DOI: `10.1103/PhysRevLett.117.193001`. URL: `https://link.aps.org/doi/10.1103/PhysRevLett.117.193001`.

Requist, Ryan, C. R. Proetto, and E. K. U. Gross (Apr. 2019). “Exact factorization-based density functional theory of electron-phonon systems”. In: *Phys. Rev. B* 99 (16), p. 165136. DOI: `10.1103/PhysRevB.99.165136`. URL: `https://link.aps.org/doi/10.1103/PhysRevB.99.165136`.

Sandratskii, LM (1986). “Energy Band Structure Calculations for Crystals with Spiral Magnetic Structure”. In: *Physica Status Solidi (B)* 136 (1), pp. 167–180. DOI: `10.1002/pssb.2221360119`. URL: `https://onlinelibrary.wiley.com/doi/abs/10.1002/pssb.2221360119`.

Sanna, A., C. Franchini, et al. (Apr. 2006). “Ab initio prediction of pressure-induced superconductivity in potassium”. In: *Phys. Rev. B* 73 (14), p. 144512. DOI: 10.1103/PhysRevB.73.144512. URL: https://link.aps.org/doi/10.1103/PhysRevB.73.144512.

Sanna, A., C. Pellegrini, and E. K. U. Gross (July 2020). “Combining Eliashberg Theory with Density Functional Theory for the Accurate Prediction of Superconducting Transition Temperatures and Gap Functions”. In: *Phys. Rev. Lett.* 125 (5), p. 057001. DOI: 10.1103/PhysRevLett.125.057001. URL: https://link.aps.org/doi/10.1103/PhysRevLett.125.057001.

Sanna, A., G. Profeta, et al. (Jan. 2007). “Anisotropic gap of superconducting CaC_6: A first-principles density functional calculation”. In: *Phys. Rev. B* 75 (2), p. 020511. DOI: 10.1103/PhysRevB.75.020511. URL: https://link.aps.org/doi/10.1103/PhysRevB.75.020511.

Sjöstedt, Elisabeth and Lars Nordström (July 2002). “Noncollinear full-potential studies of $\gamma - \mathrm{Fe}$”. In: *Phys. Rev. B* 66 (1), p. 014447. DOI: 10.1103/PhysRevB.66.014447. URL: https://link.aps.org/doi/10.1103/PhysRevB.66.014447.

Scientific activities

Eberhard K. U. Gross’s group members

Name	Project	Status	Period
Camilla Pellegrini	DFT for superconductors	PostDoc	10.2019-10.2020
Ryan Requist	Exact factorization	Research staff	since 01.2020
Chung-Yu Wang	Propagating coupled electrons and phonons in real time	PhD Student	since 09.2019
Andrea Muolo	Calculating the exact geometric phase for small molecules	PostDoc	since 10.2019
Chen Li	TDDFT beyond the Born-Oppenheimer approximation	PostDoc	09.2019-07.2020

Eberhard K. U. Gross’s Scientific Collaborations

Name	Project	Institution
Cesar Proetto	Electron-phonon interaction	Centro Atomico Bariloche, Argentina
Kieron Burke	DFT functional development	UCLA Irvine, USA
Nikitas Gidopoulos	Exact factorization	Durham University, UK
Federica Agostini	Mixed quantum-classical algorithms	University Paris-Saclay, France

Eberhard K. U. Gross's German Scientific Collaborations

Name	Project	Institution
Sangeeta Sharma	ELK code and ultrafast spin dynamics	Max-Born Institute Berlin
Kay Dewhurst	ELK code and electron-phonon coupling	MPI of Microstructure Physics Halle
Antonio Sanna	DFT for superconductors	MPI of Microstructure Physics Halle
Uwe Bovensiepen	Non-Equilibrium Dynamics of Condensed Matter in the Time Domain	University Duisburg-Essen

Eberhard K. U. Gross's active grants

Project	Period	Foundation	Total grant in thousands
Exact Factorization	2019-2024	ERC Advanced Grant	€2500

Conference Organization (last 5 years)

2019 May 22-27	Co-organized with Prof. Roi Baer and Dr. Eli Kraisler, an International Workshop, "The exact factorization for electrons, nuclei, and photons", The Hebrew University of Jerusalem, Israel.

Prizes, honors, editorial and review boards etc. (last 5 years)

2020	Mercator Fellow of the German Science Foundation at University Duisburg, Germany
2019	Isaiah Shavitt Lectureship Award, Technion, Haifa, Israel
2018	ERC Advanced Grant
2017	Fellow of the American Physical Society
2016	Berni Alder CECAM prize, Lausanne. Awarded every three years for outstanding contributions to the field of computer simulations in condensed matter physics, statistical physics and physical chemistry. It is the most prestigious European prize in this field and comes with a prize money of 5000 EUR.
2016	The 2016 Keneth S. Pitzer Memorial Lecture, UC Berkeley.
2016	Tsungming Tu Prize, Taipei. Awarded once a year, this is the highest academic honor granted by the Taiwanese Ministry of Science and Technology to international scholars. It comes with a prize money of 75,000 USD.
2015	The 2015 CECAM Lecture, EPFL, Lausanne
2015	Senior CMOA Medal for outstanding scientific achievements
2013-2017	Visiting Research Professorship at University of Hong Kong

2.6 Daniel Harries

Research Activities

The group's research focuses on how biologically complex solvation environments direct macromolecular association and determine the stability, physical properties, and association behavior of biological macromolecules. Specifically, in the currently reviewed period we have been following

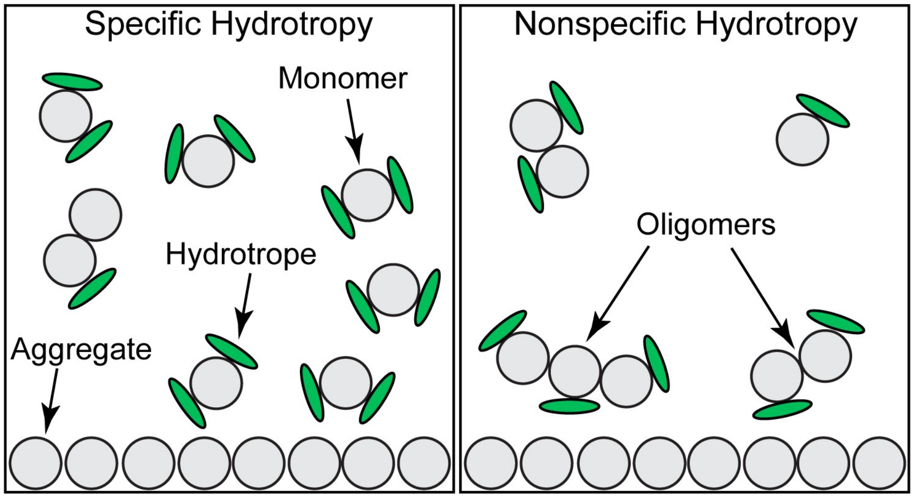

Figure 2.31. Caffeine molecules are found in an equilibrium of many different forms including aggregates and linear self-assembled oligomers. Sugars added to sultion can shift the equilibrium selectively, by interating differently with different surfaces of the oligomers. The origin of this selectivity has been mechanistically explained in our recent studies.

the effects of crowded and stressed environments on the folding of peptides and proteins and on the effect of solution on lipid interactions. Some highlights and developments from our endeavors in the past year two years are detailed in the following.

Solution effects on molecular association and self assembly

Based on recent publications in (Shumilin, Bogoslavsky, and Harries 2020) as well as media attention to our work, including Derek Lowe's In The Pipeline blog affiliated with Science Translational Medicine magazine. The study was led by Ilan Shumilin.

The aggregation of drugs and nutraceuticals in aqueous media is an outstanding problem for their efficacy and bioavailability. We have been looking at one of the ways that you can get poorly soluble molecules in at higher concentration, through the addition of "hydrotopes". Those are added molecular species that somehow stabilize other ones in water. It's known that these generally work by piling up around the less-soluble molecules and acting as a sort of bridge between them and the bulk watery phase. This may sound like the action of a surfactant, but hydrotropes are a bit different, since they do not on their own form mesophases in solution. So how do they perform their action? Knowing what's going on in more detail would be of great use in picking likely candidates and designing new ones. As a good model for hardly soluble hydrophobic molecules, we have been studying good old caffeine, which despite its ubiquity in coffee, tea, and soft drinks is actually not all that water-soluble. It has a tendency to form oligomers and aggregates in water, like many drug substances will, and that can give you a range of behaviors: precipitation, self-assembly into limited sized aggregates and also monomers, which are probably the most active form of the molecules. There are a range of hydrotopes known to affect caffeine's solubility, things like urea and thiocyanate which act in many such situations, but they affect the single molecules and the oligomers in the same way – they basically draw everything into solution. This work shows an interesting effect of sugar molecules, though: as others had noted, the addition of such species decreases the general solubility of caffeine, but on closer inspection, we found that the distribution changed: caffeine monomers were much more stabilized in solution than the oligomers. How is that possible? It seems that sugar interacts favorably with the tips of the caffeine piles, but not with the

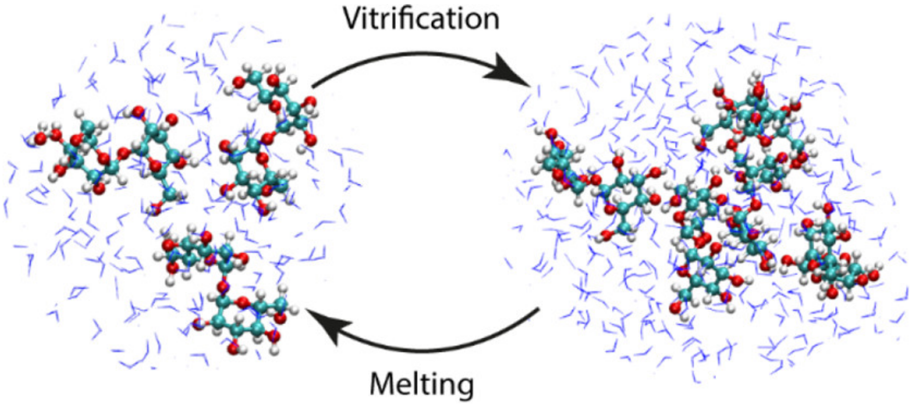

Figure 2.32. Transitions between solution conditions and the glassy state are echoed by a major change in corelated regions within the mixture that form upon cooling below the glass transition temperature. There changes can be precisely followed using a new methodology to gauge hydrogen bond strength (free energy, enthalpy, and entropy).

column sides. That means that they have a much greater effect on such species as they get shorter, and on the individual caffeine molecules most of all. Interestingly, sugars like glucose, sucrose, and fructose fall along a linear relationship for this effect (sucrose, for example, acts pretty much like glucose and fructose together, as it should), while trehalose is a definite outlier. That one's already been noted as an unusual stabilizer of macromolecules in solution (for reasons that are still being argued about), but in this case it seems that the trehalose is (compared to the others) much more excluded from the ”sides” of the oligomer stacks. This sort of ”selective hydrotopy” is a new thing, so the question is how common these effects are and whether they can be anticipated. But now that we know that it's possible, the search can commence for compounds that both associate with surfaces that are more exposed in solute monomers (such as the ”tips” of the caffeine oligomers here), and are also excluded from the surfaces that are formed by the oligomers. It'll be quite interesting to see how general this turns out to be: is it going to be mostly trehalose (which people already knew to try) or are there more things waiting out there to be found?

More dry than wet: Water-osmolyte mixtures in the concentrated and glassy state

Based on (Olgenblum, Sapir, and Harries 2020). Project led by Gil Olgenblum. Trehalose is a naturally occurring disaccharide known to remarkably stabilize biomacromolecules in the biologically active state. The stabilizing effect is typically observed over a large concentration range and affects many macromolecules including proteins, lipids, and DNA. Of special interest is the transition from aqueous solution to the dense and highly concentrated glassy state of trehalose that has been implicated in bioadaptation of different organisms toward desiccation stress. Although several mechanisms have been suggested to link the structure of the low water content glass with its action as an exceptional stabilizer, studies are ongoing to resolve which are most pertinent. Specifically, the role that hydrogen bonding plays in the formation of the glass is not well resolved. We have been modeling aqueous trehalose mixtures over a wide concentration range, using molecular dynamics simulations. We developed and emplied a methodology that allows us to analyze the thermodynamics of hydrogen bonds in simulations at different water contents and temperatures. Remarkably, this analysis is able to link the liquid to glass transition with changes in hydrogen bond characteristics. Most notably, the onset of the glassy state can be quantitatively related to the transition from weakly to strongly correlated hydrogen bonds. Our findings are a first step

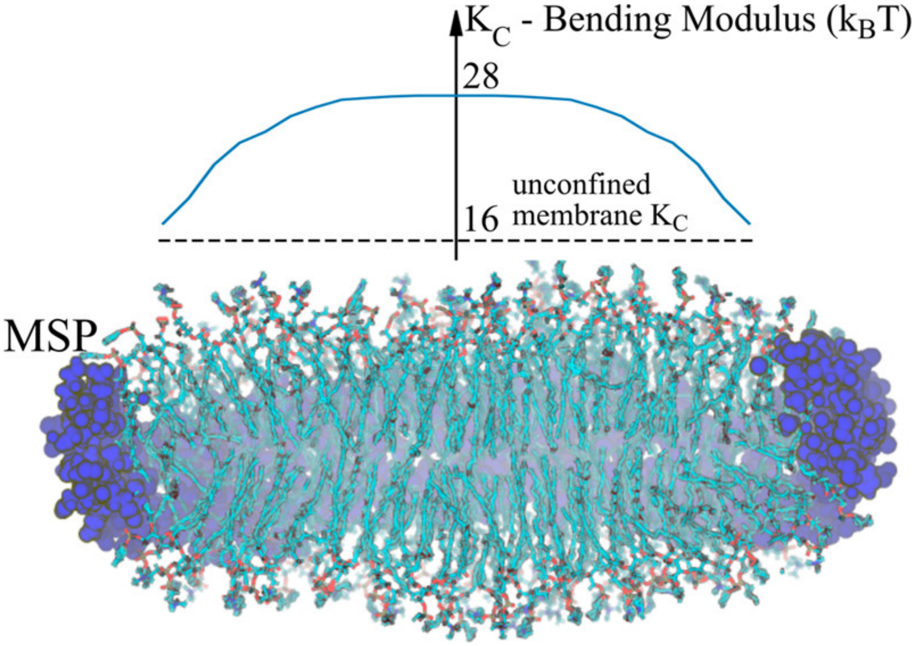

Figure 2.33. Lipid nanodiscs show spatially varying lipid ordering, that impacts the elastic properties within them. Lipid nanodiscs therefore show properties very different from those of large macroscopic membranes, highlighting the importance of nanoconfinement on the lipid material properties.

toward resolving the properties of the glass and the mechanisms of its formation in the presence of added macromolecules.

Elastic properties of lipids in nanodiscs are unisotropic and modulated by nanoconfinement

Based on the work (Schachter et al. 2020). This study was led by Itay Schachter.

Lipid nanodiscs are small synthetic lipid bilayer structures that are stabilized in solution by special circumscribing (or scaffolding) proteins or polymers. Because they create native-like environments for transmembrane proteins, lipid nanodiscs have become a powerful tool for structural determination of this class of systems when combined with cryo-electron microscopy or nuclear magnetic resonance. The elastic properties of lipid bilayers determine how the lipid environment responds to membrane protein perturbations, and how the lipid in turn modifies the conformational state of the embedded protein. However, despite the abundant use of nanodiscs in determining membrane protein structure, the elastic material properties of even pure lipid nanodiscs (i.e., without embedded proteins) have not yet been quantitatively investigated. A major hurdle is due to the inherently nonlocal treatment of the elastic properties of lipid systems implemented by most existing methods, both experimental and computational. In addition, these methods are best suited for very large ”infinite” size lipidic assemblies, or ones that contain periodicity, in the case of simulations. We have previously described a computational analysis of molecular dynamics simulations designed to overcome these limitations, so it allows quantification of the bending rigidity (K_c) and tilt modulus (k_t) on a local scale even for finite, nonperiodic systems, such as lipid nanodiscs. We have now applied this computational approach to extract values of K_c and k_t for a set of lipid nanodisc systems that vary in size and lipid composition. We find that the material properties of lipid nanodiscs are different from those of infinite bilayers of corresponding lipid composition, highlighting the effect of nanodisc confinement. Nanodiscs tend to show higher stiffness than their corresponding macroscopic bilayers, and moreover, their material properties vary spatially within them. The trends in moduli within the lipid nanodiscs correlate with spatially varying structural properties, including the area per lipid and the nanodisc thickness. The modulations of lipid elastic properties that we find should be carefully considered when making structural and functional inferences concerning embedded proteins.

References

Olgenblum, G.I., L. Sapir, and D. Harries (2020). "Properties of Aqueous Trehalose Mixtures: Glass Transition and Hydrogen Bonding". In: *Journal of Chemical Theory and Computation* 16.2, pp. 1249–1262. DOI: 10.1021/acs.jctc.9b01071.

Schachter, I. et al. (2020). "Confinement in Nanodiscs Anisotropically Modifies Lipid Bilayer Elastic Properties". In: *Journal of Physical Chemistry B* 124.33, pp. 7166–7175. DOI: 10.1021/acs.jpcb.0c03374.

Shumilin, I., B. Bogoslavsky, and D. Harries (2020). "Stressing crystals with solutes: Effects of added solutes on crystalline caffeine and their relevance to determining transfer free energies". In: *Colloids and Surfaces A: Physicochemical and Engineering Aspects* 599. DOI: 10.1016/j.colsurfa.2020.124889.

Scientific activities

Daniel Harries group members

Name	Project	Status	Period
Gil Olgenblum	Biomacromolecules in complex fluids	PhD student	since 2020
Itay Schachter	Membrane elasticity and protein-membrane interations	MS student	since 2019
Ilan Shumilin	Proteins in dense solvents	PhD student	since 2019
Yuri Shekhman	Membrane cosolute interactions	MS student	since 2018

Daniel Harries scientific collaborations

Name	Project	Institution
George Khelashvili and Harel Weinstein	Lipid membrane properties	Cornell U., USA
Pavel Jungwirth	Membrane elasticity and membrane interations	Czech Academy, Czech Republic
Dganit Danino	Self assembly of macromolecules	Technion, Israel
Uri Raviv	Membrane interactions	Hebrew U., Israel
Meir Lahav	Ice formation and electrofreezing	Weizmann Institute, Israel
Masha Niv	Taste sensing	Hebrew U., Israel
Gary Pielak	Proteins under crowding	UNC Chapel Hill, USA

Daniel Harries active grants

Project	Period	Foundation	Total grant in thousands
Modeling protein stabilization by osmolytes in concentrated or glassy media	2017-2021	ISF	$ 240
Impact of cosolutes on protein stability and folding kinetics in vitro and in cells	2018-2022	BSF	$ 200

Prizes, honors, editorial and review boards etc. (last 5 years)

2015-	Minerva fellowships committee
2015	Chemical Society of Japan Annual Asian lectureship award
2015	German Chemical Society (GDCh) Willstätter named-lectureship award
2016-19	ORNL review board member
2016-19	Associate editor Scientific Reports
2019	Dr. & Mrs. Philip Gotlieb Chair in Physical Chemistry

2.7 Ronnie Kosloff

Research Activities

Our research focuses on quantum phenomena: *Quantum Thermodynamics, Quantum Optimal Control Theory and Quantum Dynamics.*

Quantum Thermodynamics

Quantum Thermodynamics is a continuous dialogue between two independent theories: Thermodynamics and Quantum Mechanics. Whenever the two theories have addressed the same phenomena new insight has emerged. The dialogue has developed through the analysis of quantum engines and refrigerators.

We adopt the dogma that thermodynamics and quantum mechanics address the same subject matter, therefore have to be consistent (Alicki and Kosloff 2018). In this framework quantum mechanics provides the tools to describe the dynamics, while the strict laws of thermodynamics must be obeyed.

Engines have been an intrinsic part in the development of classical thermodynamics. Their analysis still serves as an integral part of current research in finite-time and quantum thermodynamics. These theories allow describing engines more realistically including non-ideal performance. It has been realized that any practical engine operates in a non-ideal irreversible mode. Typically, there are four sources of irreversible phenomena in engines:

1. Finite heat transport.

2. Friction.

3. Heat leaks.

4. Cost of switching contacts between subsystems.

The quantum Carnot engine

The trade-off between power and efficiency is well embedded in our everyday experience. It is witnessed in the performance of any realistic engine or refrigerator, from operation of large nuclear plants, through the internal combustion engines of our automobiles, and all the way to microscopic biological engines and the quantum regime. Despite the intuitive notion, a theoretical analysis requires a theoretical construction which encompasses both thermodynamics and quantum transient dynamics.

The limiting case was first treated by Carnot, who linked an engine's maximum attainable work production to reversible thermodynamic transformations, thereby obtaining the thermodynamic temperature scale and the universal optimal efficiency that depends only on the hot and cold bath temperatures. Unlike efficiency, power requires knowledge of the transient dynamics, which is outside the realm of classical thermodynamics. Finite-time thermodynamics (FFT) was developed to include the limitations the process duration places on the performance of an engine.

Our motivation was to model a quantum version of the Carnot engine. Eitan Geva at the time a graduate student developed a finite power model of the Carnot engine (Geva and Kosloff 1992). The model was first quantum model which was able to recover the Curzon Ahlborn efficiency at maximum power $\eta_{CA} = 1 - \sqrt{\frac{T_C}{T_h}}$. In this model the source of irreversibility was heat transport. To find a quantum source of friction we had to invoke coherence and nonadiabatic dynamics. This also led to abandoning the Carnot cycle and perform the analysis on the quantum Otto cycle. This was the work horse of quantum thermal machines for three decades.

Challenged by Peter Salamon we wanted to complete the investigation of the Carnot cycle. The obstacle was the dynamical description of isothermal stroke. The modeling of the thermalization process from first principles relies on a reduction from a closed composite system. The reduced description is achieved by tracing over the degrees of freedom of the surroundings, interacting with our system of interest. This description does not conserve entropy and allows exploration of thermodynamic processes in the quantum regime. Notably, the approach is based on the completely positive trace preserving (CPTP) dynamical map and the Markovian Gorini-Kossakowski-Lindblad-Sudarshan (GKLS) master equation.

In the case of a general driving, the adiabatic master equation was the only theory available. Our first step was to derived a GKLS master equation for simultaneous heat and work exchange (Dann, Levy, and Kosloff 2018). (Work of Amikam Levy and Roie Dann). This development was the enabler for the Carnot cycle study. In addition this study led to novel insight on quantum thermodynamics and quantum control. Four published papers are the current harvest of this effort (Kosloff 2019; Dann, Tobalina, and Kosloff 2019; Dann and Kosloff 2020; Dann, Roie, Tobalina, Ander, and Kosloff, Ronnie 2020). (Work by Roie Dann and Ander Tobalina).

Control of Thermlization We developed a control scheme for quantum systems coupled to a thermal bath. Our control target was state-to-state control between two Gibbs states. The scheme can be used to accelerate thermalization and cool the open system. Starting from a microscopic description, we derived the reduced system dynamics, leading to a non-adiabatic master equation. The equation contains non-trivial effects due to the non-adiabatic driving and bath interaction. These special features enable controlling the open system and accelerating the entropy changes. The control problem was then analyzed in the context of the theory of quantum control.

Speeding up the themalization rate comes with a thermodynamic cost, with a minimum work cost achieved in the adiabatic limit. Any additional cost is associated with the emergence of friction. When the Hamiltonian does not commute with itself at different times, driving at non-vanishing speed generates coherence and is manifested by additional work which is dissipated to the bath. Dissipated energy heats the bath and leads to positive entropy production and irreversibility. The first principle analysis conducted here demonstrated the quantum origin of friction (Dann, Tobalina, and Kosloff 2019; Dann, Roie, Tobalina, Ander, and Kosloff, Ronnie 2020). Work of Roie

Dann and Ander Tobalina.

Quantum signatures in the Carnot cycle The Carnot cycle combines reversible isothermal and adiabatic strokes to obtain optimal efficiency, at the expense of a vanishing power output. We constructed a quantum Carnot-analog cycles, operating irreversibly at non-vanishing power. Swift thermalization is obtained utilizing shortcut to equilibrium protocols and the isolated strokes employ frictionless shortcut to adiabaticity protocols. We solved the dynamics for a working medium composed of a particle in a driven Harmonic trap. A complete description of the state is obtained, incorporating both changes in energy and coherence. In the limit of finite cycle-time, coherence disappears and the efficiency converges to the ideal Carnot efficiency. Thus, demonstrating the trade-off between power and efficiency. At short cycle-times, generation of coherence is necessary to achieve power. To evaluate the importance of quantum coherence, we compared three types of cycles, Carnot-shortcut, Endo-shortcut and Endo-global. In the first two, the coherence is limited to the interior of the strokes, while for the last cycle the coherence never vanishes. This allows the Endo-global engine to operate at shorter cycle-times relative to the shortcut cycles. Introducing pure-dephasing to the Endo-global engine terminates the quantum coherence, and with it, the power output. This phenomena can be identified by evaluating the cycle performance, therefore indicating a quantum signature (Dann and Kosloff 2020). Work of Roie Dann.

Landauer's Principle in a Quantum Szilard Engine without a Maxwell's Demon Quantum Szilard engine constitutes an adequate interplay of thermodynamics, information theory and quantum mechanics. Szilard engines are in general operated by a Maxwell's Demon where Landauer's principle resolves the apparent paradoxes. We obtained a Szilard engine setup without featuring an explicit Maxwell's demon. In a demonless Szilard engine, the acquisition of which-side information is not required, but the erasure and related heat dissipation still take place implicitly. We explored a quantum Szilard engine considering quantum size effects. We see that insertion of the partition does not localize the particle to one side, instead creating a superposition state of the particle being in both sides. To be able to extract work from the system, particle has to be localized at one side. The localization occurs as a result of quantum measurement on the particle, which shows the importance of the measurement process regardless of whether one uses the acquired information or not. In accordance with Landauer's principle, localization by quantum measurement corresponds to a logically irreversible operation and for this reason it must be accompanied by the corresponding heat dissipation. This shows the validity of Landauer's principle even in quantum Szilard engines without Maxwell's demon (Aydin, Sisman, and Kosloff 2020) Work of Alhun Aydin, Altug Sisman.

Quantifying the unitary generation of coherence

Coherence is associated with transient quantum states; in contrast, equilibrium thermal quantum systems have no coherence. We investigated the quantum control task of generating maximum coherence from an initial thermal state employing an external field. A completely controllable Hamiltonian is assumed allowing the generation of all possible unitary transformations. Optimizing the unitary control to achieve maximum coherence leads to a micro-canonical energy distribution on the diagonal energy representation. We demonstrate such a control scenario starting from a given Hamiltonian applying an external field, reaching the control target. Such an optimization task is found to be trap-less. By constraining the amount of energy invested by the control, maximum coherence leads to a canonical energy population distribution. When the optimization procedure constrains the final energy too tightly, local suboptimal traps are found. The global optimum is obtained when a small Lagrange multiplier is employed to constrain the final energy (Kallush, Aroch, and Kosloff 2019). Work of Shimshon Kallush and Aviv Arochh.

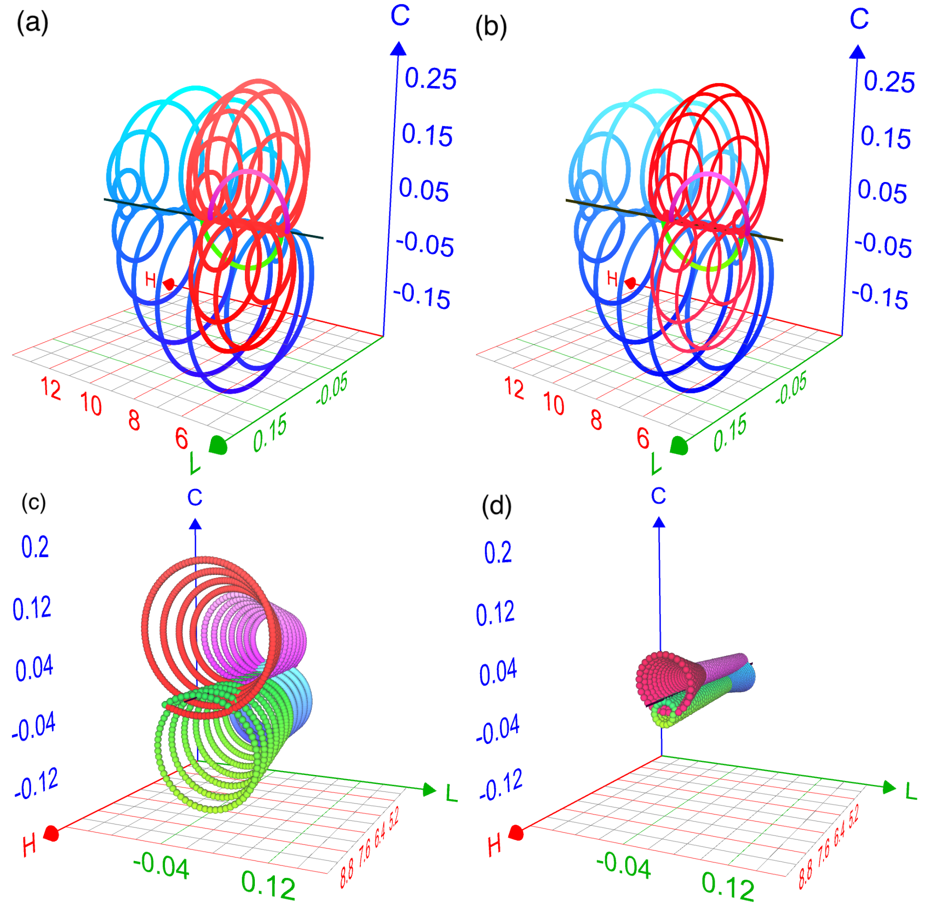

Figure 2.34. Carnot cycle trajectory in the $\{\langle\hat{H}\rangle, \langle\hat{L}\rangle, \langle\hat{C}\rangle\}$ observable vector space, where $\hat{L}$ is the Lagrangian, $\hat{C}$ is the position momentum correlation operator and $\hat{H}$ is the Hamiltonian. The red and blue lines display the open-expansion and compression strokes and the purple and green lines display the expansion and compression unitary strokes. Panel (a) shows the Shortcut cycle (b) Endo-shortcut cycle for a fast driving. The black line designates zero coherence $\langle\hat{L}\rangle = \langle\hat{C}\rangle = 0$. Note the change in scale for the coherence determining variables $\langle\hat{L}\rangle$ and $\langle\hat{C}\rangle$ for the upper and lower panels. Furthermore, in the shortcut trajectories coherence vanishes at the cycle's four corners.

Intertial Theorem

Closed-form solutions for the propagator are of utmost importance for quantum control. Generally, any Hamiltonian that allows control does not commute with itself at different times, leading to a time-ordering procedure in the evolution operator. Hence, the development of closed solutions, for control Hamiltonians, faces the formidable task of time-ordering. Moreover, one desires that such solutions are stable under variations in the driving protocol and external noise.

Our study was devoted to the construction of closed-form, stable solutions of driven quantum systems. Currently, the popular theoretical as well as experimental approach utilizes the adiabatic theorem, constrained to slow driving. Here, we propose approximate solutions for rapid processes based on the inertial theorem. In the appropriate limit these solutions incorporate the adiabatic approximation.

The inertial theorem utilizes a timescale separation between variables to generate the system's evolution for slow acceleration of the external driving. The derivation subsides in the Liouville space and requires the existence of a time-dependent operator basis. Formally, the theorem is

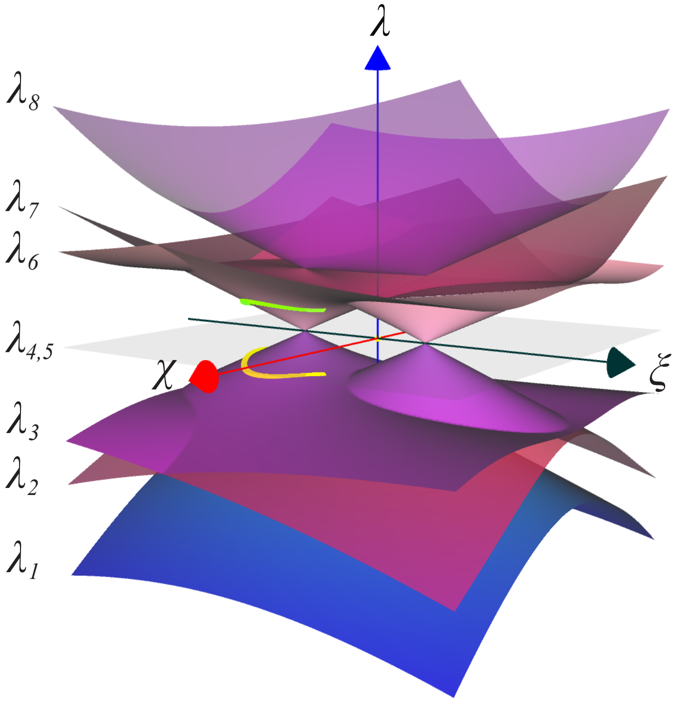

Figure 2.35. Landscape of the eigenvalues $\{\lambda\}$ of $\mathcal{M}$ of the Hamiltonian as a function of χ and ξ for $\gamma = 1/2$. The yellow and green streaks correspond to the studied inertial protocol.

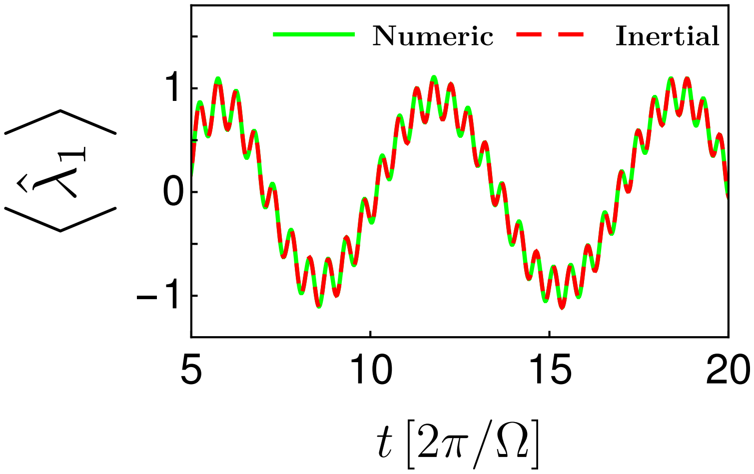

Figure 2.36. Expectation valued of the first Gell-Mann operator $\hat{\Lambda}_1$ (σ_x of 1 and 2 states) as a function of time, for a system represented by the Hamiltonian. The presented result is a typical behaviour of any system expectation values under the inertial protocol. The deviation between the numerical and inertial solutions is less than 0.015.

similar to the adiabatic theorem, where adiabatic states are replaced by the time-dependent eigenoperators of the generator of the propagator (Dann, Tobalina, and Kosloff 2019). The dynamics of eigenoperaters are characterized by geometric and dynamical phases. The inertial solutions remain precise for rapid driving of the system under the condition of slow acceleration relative to

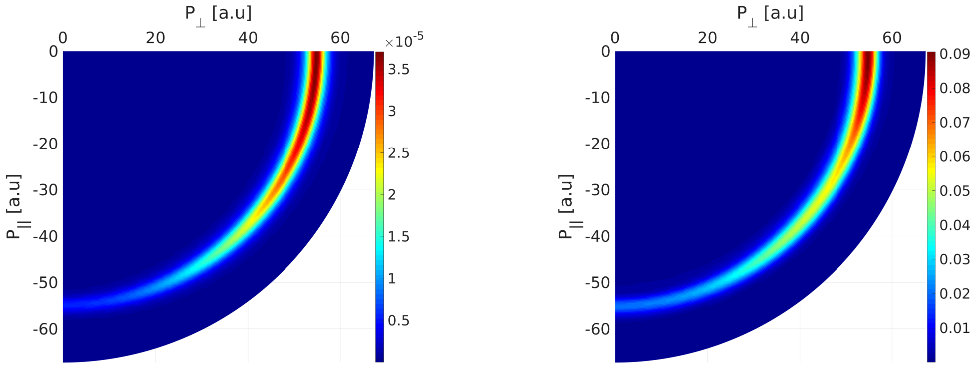

Figure 2.37. Angular distribution of the outgoing momentum shown as a density plot. The results are for fragments emitted from the transition between Σ and Π electronic surfaces with different intensity, (a) low intensity- $I = 10^{10}\frac{W}{cm^2}$, (b) high intensity - $I = 10^{16}\frac{W}{cm^2}$.

the system's dynamics.

Inertial protocols can generate a diverse family of solutions, as the fast degrees of freedom are arbitrary smooth functions while only the rate of change of the slow variables is restricted. These solutions identify new invariant operators, which are time-dependent constants of motion. Moreover, inertial solutions can be combined to generate an inertial Hamiltonian, extending the family of possible solutions.

Quantum control is an integral part of contemporary quantum science. Control is commonly achieved by engineering the Hamiltonian by means of external driving.

The inertial theorem can be a crucial element of the control tool box, generating rapid control protocols which go beyond the adiabatic driving regime. In addition, protocols based on time-dependent constants of motion, can replace adiabatic protocols, such as the STIRAP protocol for a three-level system.

Applications of the inertial theorem were tested on three physical models: a time-dependent harmonic oscillator, a driven two-level system, and a three-level system. These models are the building blocks of both experimental and theoretical studies performed in the quantum regime.

We also utilize the inertial solution to derive the equations of a motion for a driven open quantum system. We then analyse the geometric phase associated with the inertial solution. This phase differs in its physical role from the Berry phase of the adiabatic solution. In contrast to the Berry phase, the former phase directly influences observables and can be witnessed, for non-closed circuits in the driving parameter space. For systems interacting weakly with the environment, the geometric phase induces a shift in the decay rates. Work of Roie Dann.

Dissociation in strong field: a quantum analysis of the relation between angular momentum and angular distribution of fragments.

High-intensity time-domain spectroscopy can be modeled by explicitly solving the time-dependent Schrödinger equation, for which knowledge of the full Hamiltonian of the process is essential. Employing the Born–Oppenheimer approximation, the Hamiltonian is separated into electronic and nuclear terms. The nuclear degrees of freedom are represented by vibrational and rotational terms. Coupling the external electromagnetic field and the transition dipole moment, induces transitions between electronic states. Each electronic transition is accompanied by an angular momentum change of one unit of $\hbar$.

Our study had two main goals: first, to acquire a more fundamental comprehensive understanding of the high-field dissociation process on a quantum scale; and second, to simulate the angular distribution of the photo-fragments resulting from this process. The current simulation uses the physical parameters of F_2^-. The motivation to use the F_2^- molecule as a benchmark follows from a recent experimental study by Strasser *et al.*. Furthermore, its electronic structure is rather simple: there are only four low-lying states before reaching the detachment continuum. The photoelectron detachment channel is thus ignored, due to the $10\,eV$ energy gap to the closest electronic state.

We obtained a first principle model, which includes a numerically exact solution of the time-dependent Schrödinger equation. All of the nuclear rotational and vibrational states, and the couplings between them, are included. We simulate a finite temperature ensemble, and therefore the initial state is thermal. The option of the Floquet dressed picture is not employed here for the reason that it is limited to relative long pules. The angular distribution of the fragments, as well as other observables, are extracted directly from the calculated wavefunction (Ezra, Kallush, and Kosloff 2020). Work by Shimshon Kallush and Bar Ezra.

Optimization of high-order harmonic generation by optimal control theory: Ascending a functional landscape in extreme conditions

A theoretical optimization method of high-harmonic-generation (HHG) was developed in the framework of optimal-control-theory (OCT). The target of optimization is the emission radiation of a particular frequency. The OCT formulation includes restrictions on the frequency band of the driving pulse, the permanent ionization probability and the total energy of the driving pulse. The optimization task requires a highly accurate simulation of the dynamics. Absorbing boundary conditions are employed, where a complex-absorbing-potential is constructed by an optimization scheme for maximization of the absorption. A new highly accurate propagation scheme is employed, which can address explicit time dependence of the driving as well as a non-Hermitian Hamiltonian. The optimization process is performed by a second-order gradient scheme. The method is applied to a simple one-dimensional model system. The results demonstrate a significant enhancement of selected harmonics, with minimized total energy of the driving pulse and controlled permanent ionization probability. A successful enhancement of an even harmonic emission is also demonstrated (Schaefer and Kosloff 2020). Work by Ido Schaefer.

Novel search algorithm

Particle swarm optimization (PSO) is a powerful metaheuristic population-based global optimization algorithm. However, when it is applied to nonseparable objective functions, its performance on multimodal landscapes is significantly degraded. Here we show that a significant improvement in the search quality and efficiency on multimodal functions can be achieved by enhancing the basic rotation-invariant PSO algorithm with isotropic Gaussian mutation operators. The new algorithm demonstrates superior performance across several nonlinear, multimodal benchmark functions compared with the rotation-invariant PSO algorithm and the well-established simulated annealing and sequential one-parameter parabolic interpolation methods. A search for the optimal set of parameters for the dispersion interaction model in the ReaxFF-lg reactive force field was carried out with respect to accurate DFT-TS calculations. The resulting optimized force field accurately describes the equations of state of several high-energy molecular crystals where such interactions are of crucial importance. The improved algorithm also presents better performance compared to a genetic algorithm optimization method in the optimization of the parameters of a ReaxFF-lg correction model. The computational framework is implemented in a stand-alone C++ code that allows the straightforward development of ReaxFF reactive force fields (Furman et al. 2018).

Work of David Furman and Yehuda Zeiri.

Future directions

Our future research plans are focused on quantum control and quantum thermodynamics. We are currently studying a coherent control theory for open quantum systems where the influence of the control field on the dissipation is treated explicitly.

Our efforts in molecular physics will be in close contact with experimental groups. We will study control of the angular distribution in the photodissociation of F_2^-. This is a collaboration with the group of Daniel Strassers. We are studying Laser cooling of internal degrees of freedom of AlF. A molecule studied in the group of Gerard Meijer.

References

Alicki, Robert and Ronnie Kosloff (2018). “Introduction to Quantum Thermodynamics: History and Prospects”. In: *Thermodynamics in the quantum regime*. Ed. by Felix Binder et al. Fundamental Theories of Physics. Springer. DOI: `10.1007/978-3-319-99046-0_1`.

Aydin, Alhun, Altug Sisman, and Ronnie Kosloff (2020). “Landauer Principle in a Quantum Szilard Engine without Maxwell Demon”. In: *Entropy* 22.3, p. 294. ISSN: 1099-4300. DOI: `10.3390/e22030294`. URL: `https://www.mdpi.com/1099-4300/22/3/294`.

Dann, Roie and Ronnie Kosloff (2020). “Quantum Signatures in the Quantum Carnot Cycle”. In: *New Journal of Physics* 22.1, p. 013055.

Dann, Roie, Amikam Levy, and Ronnie Kosloff (2018). “Time-dependent Markovian quantum master equation”. In: *Phys. Rev. A* 98 (5), p. 052129. DOI: `10.1103/PhysRevA.98.052129`. URL: `https://link.aps.org/doi/10.1103/PhysRevA.98.052129`.

Dann, Roie, Ander Tobalina, and Ronnie Kosloff (2019). “Shortcut to Equilibration of an Open Quantum System”. In: *Phys. Rev. Lett.* 122 (25), p. 250402. DOI: `10.1103/PhysRevLett.122.250402`. URL: `https://link.aps.org/doi/10.1103/PhysRevLett.122.250402`.

Dann, Roie, Tobalina, Ander, and Kosloff, Ronnie (May 2020). “Fast route to equilibration”. In: *Phys. Rev. A* 101 (5), p. 052102. DOI: `10.1103/PhysRevA.101.052102`. URL: `https://link.aps.org/doi/10.1103/PhysRevA.101.052102`.

Ezra, Bar, Shimshon Kallush, and Ronnie Kosloff (2020). “Dissociation in strong field: a quantum analysis of the relation between angular momentum and angular distribution of fragments”. In: *Chemical Physics Letters* 756, p. 137845.

Furman, David et al. (2018). “Enhanced Particle Swarm Optimization Algorithm: Efficient Training of ReaxFF Reactive Force Fields”. In: *Journal of chemical theory and computation* 14.6, p. 3100.

Geva, Eitan and Ronnie Kosloff (1992). “A quantum-mechanical heat engine operating in finite time. A model consisting of spin-1/2 systems as the working fluid”. In: *The Journal of Chemical Physics* 96.4, pp. 3054–3067.

Kallush, Shimshon, Aviv Aroch, and Ronnie Kosloff (2019). “Quantifying the unitary generation of coherence from thermal quantum systems”. In: *Entropy* 21, p. 810.

Kosloff, Ronnie (2019). “Quantum thermodynamics and open-systems modeling”. In: *The Journal of Chemical Physics* 150.20, p. 204105. DOI: `10.1063/1.5096173`. eprint: `https://doi.org/10.1063/1.5096173`. URL: `https://doi.org/10.1063/1.5096173`.

Schaefer, Ido and Ronnie Kosloff (2020). “Optimization of high-harmonic generation by optimal control theory: Ascending a functional landscape in extreme conditions”. In: *Phys. Rev. A* 101 (0), p. 023407.

Scientific activities

Ronnie Kosloff group members

Name	Project	Status	Period
Aviv Aroch	Quantum Control	PhD student	since September 2017
Roie Dann	Quantum Thermodynamics	PhD student	since September 2018
Bar Ezra	Quantum Dynamics of Photodissociation	PhD student	since July 2020
Oren Lichtenstein	Quantum Dynamics of Photoisomerization	MSc student	since July 2018
Uriel Shafir	Quantum Open systems	MSc student	since July 2019

Ronnie Kosloff scientific collaborations

Name	Project	Institution
Shimshon Kallush	Quantum control	Hollon I.T., Israel
Zohar Amitay	Quantum control	Technion, Israel
Peter Salamon	Quantum thermodyanmics	UC San Diego, USA
Jimmie Oxeley	Explosives	U Rhode Island, USA
Christiane Koch	Quantum Control	FU Berlin, Germany

Ronnie Kosloff' active grants

Project	Period	Foundation	Total grant in thousands
Quantum thermodynamics	2014-2019	ISF	€100

Conference organization (last 5 years)

2018 Jul 07-26	Quantum Thermodynamics, KITP Santa Barbara

Prizes, honors, editorial and review boards etc. (last 5 years)

2018-19	Israel national committee on quantum science and technology

2.8 Eli Kraisler

Research Activities

Our group specializes in theoretical development and numerical implementation of new approximations and methods for electronic structure calculations. In particular, we focus on deriving new exchange-correlation approximations in density-functional theory (DFT), relying on satisfying exact constraints. We aim to improve the description of such important processes as dissociation, charge transfer, prediction of the fundamental and optical gaps in molecules and crystalline solids.

Non-analytic properties of the exchange-correlation potential and their relevance for excitations

Kohn-Sham density-functional theory (KS-DFT) is in principle an exact theoretical framework suitable to treat any many-electron system, be it a molecule, a nano-particle or a crystalline solid. In practice, however, one has to approximate the exchange-correlation (xc) energy for any practical calculation. The accuracy of the xc approximations is critical to the success of the whole approach. Common approximations yield sufficiently accurate predictions when the results are based on ground-state energies and when the system's atoms are close to their equilibrium positions. However, when dealing with excited states within KS-DFT, particularly those which induce ionization and charge transfer, or with dissociation of molecules, great challenges emerge: calculations with standard xc approximations can fail miserably in these situations.

In our recent works ((M. Hodgson et al. 2017) and (Eli Kraisler, M. J. P. Hodgson, and Gross 2020)) together with M. J. P. Hodgson (Durham University), Axel Schild (ETH Zürich) and E. K. U. Gross (Hebrew University), we revealed the fundamental reasons for these failures. In various regimes – electron addition, dissociation and charge transfer – the *exact* xc potential forms spatially sharp, non-analytic features, such as steps, plateaus and jumps. Maybe less important for ground-state properties, steps are crucial for describing dissociation, excitations, ionization and charge transfer. Unfortunately, many *approximate* xc potentials do not produce steps. We demonstrated, analytically and numerically, how many-electron excitation energies relate to KS energies via the step structures observed in the exact xc potential. In particular, we defined and numerically discovered the charge-transfer derivative discontinuity – a new feature of the xc potential that appears upon charge-transfer excitations (see Fig. 2.38).

We further showed that, contrary to common wisdom, steps can be obtained not only in the exact case, but also with common xc approximations, as simple as the LDA, but when addressed from the ensemble perspective. We considered a finite system with a varying number of electrons, N. By enforcing piecewise-linearity for the ensemble density, we showed that one obtains a plateau in the xc potential, even if the original densities come from an approximations as simple as the LDA (see Fig. 2.39).

Pauli potential: exact and approximate properties and use in orbital-free DFT, electron factorization and beyond

The Pauli potential is an essential quantity in orbital-free DFT and in the emergent method of exact electron factorization (EEF) for many-electron systems. Broadly speaking, the role of the Pauli potential is to account for the fact that we are describing a system of fermions (and not bosons), which are subject to Pauli's exclusion principle. Knowledge of the Pauli potential allows the description of a system within DFT relying on the density alone, without the need to calculate Kohn-Sham orbitals. This opens great possibilities, especially for very large systems of millions of atoms. However, accurate approximations for the Pauli potential are difficult to develop and few such approximations have been applied in materials research so far. This emphasizes the need to explore the properties of the Pauli potential. In a recent work by Axel Schild (ETH Zürich) and myself (Eli Kraisler and Schild 2020) we explored the behavior of the exact Pauli potential in finite systems, as a function of the number of electrons, N, employing the ensemble approach. Assuming the system is in contact with an electron reservoir, we allow the number of electrons to vary continuously and to obtain fractional as well as integer values. We derived an exact expression for the Pauli potential for a spin-polarized system with a fractional number of electrons and find that when the electron number surpasses an integer, the Pauli potential jumps by a spatially uniform

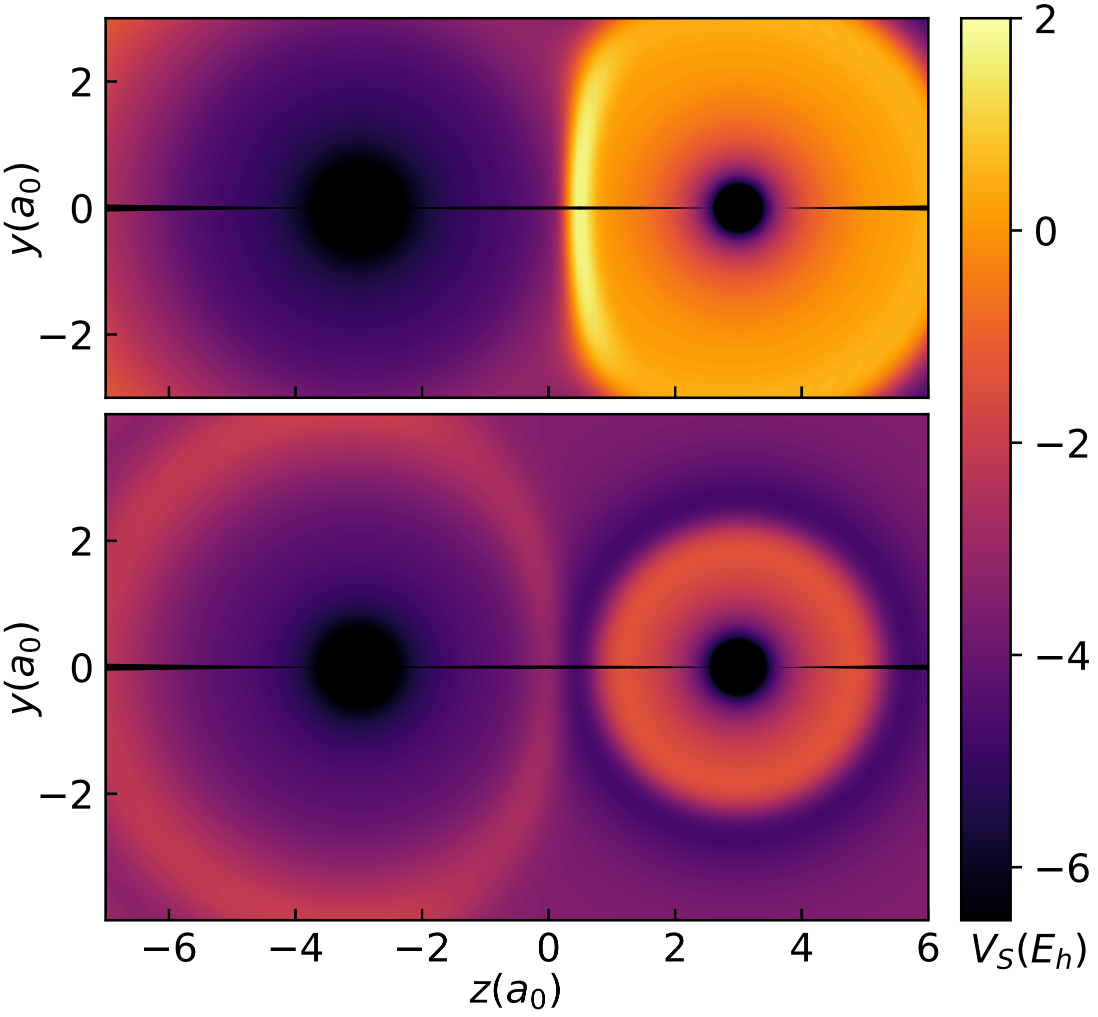

Figure 2.38. The exact KS potential for the Li$\cdots$Be molecule, $d = 6\,a_0$, with 4 electrons (top) and 4.001 electrons (bottom). The halo at $\sim 3\,a_0$ around Li$^+$ corresponds to the charge-transfer derivative discontinuity $\Delta_{\mathrm{Li}^+\,\mathrm{Be}^{++}}{}^{\mathrm{CT}}$

constant, similarly to the KS potential. The magnitude of the jump equals the KS (homo-lumo) gap (see Fig. 2.40). We illustrated our analytical findings by calculating the exact and approximate Pauli potentials for Li and Na atoms with fractional numbers of electrons.

The importance of the Pauli potential is not only for orbital-free DFT. It appears that one can use OF-DFT as a theoretical framework in order to produce fundamental, theoretical results in two directions: (i) detailed analytical description of the KS potential, particularly its step structure (see above); (ii) analytical results for the xc kernel – the functional derivative of the xc potential with respect to the density. This quantity is of extreme importance in Time-Dependent DFT (TDDFT). Both this directions will be pursued by our group in the near future.

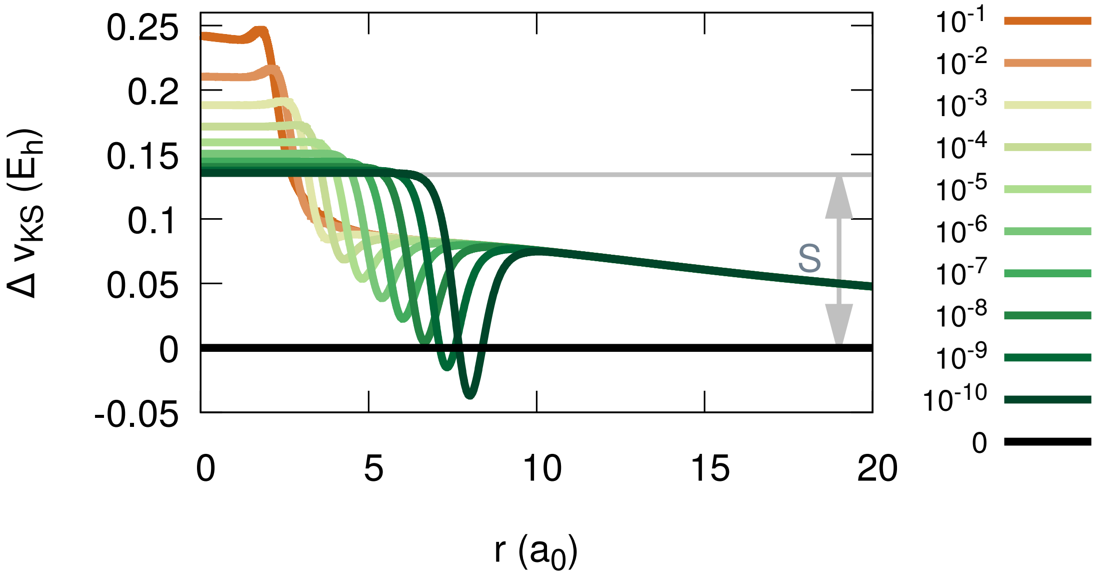

Figure 2.39. The plateau in the inverted LDA (invLDA) KS potential for Li with $2+\alpha$ electrons, for various values of α (see legend).

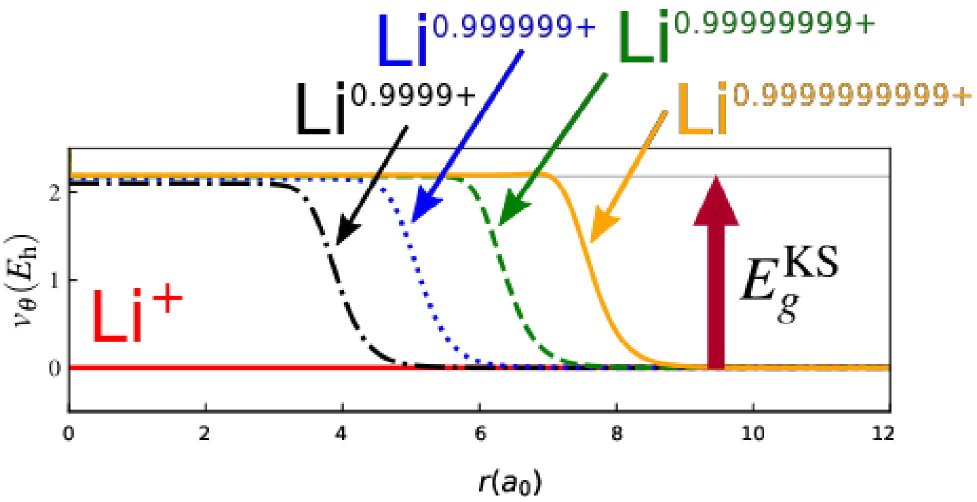

Figure 2.40. Exact Pauli potential, $v_\theta(r)$, for the Li atom with $2+\alpha$ electrons, for various values of α.

Exchange-correlation-hole-response function and a new strategy for approximating exchange and correlation

One approach to producing approximate xc functionals is via satisfying known properties of the exact functional. This yields approximations that are based on first principles, avoid usage of empirical input and promise to be widely applicable, for very different systems and chemical environments. In a recent work (E. Kraisler 2020) I reviewed two such exact properties: the asymptotic behavior of the xc energy density per particle and the asymptotic behavior of the Kohn-Sham potential, in finite many-electron systems. The derivation of the asymptotic forms for both quantities has been reviewed, employing the concepts of the adiabatic connection and of the xc hole with relation to the first quantity and the electron exact factorization (EEF) approach for the second one. It has been shown that the correct asymptotic behavior of one of the aforementioned quantities does not guarantee a correct behavior of the other. In this process, I explored in detail the xc hole response function $\eta_{\mathrm{xc}}(\vec{r};\vec{r''}|\vec{r'})$, which is the response of the xc hole $n_{\mathrm{xc}}(\vec{r''}|\vec{r'})$ to a perturbation in the density at $\vec{r}$. I outlined the role of this quantity in the construction of the xc potential, derived three of its properties and performed a detailed analytic derivation of its exchange part. The contributions that are most important to address in future approximation development were outlined. Finally, relying on the discussion on exact properties I suggested a new strategy for development of advanced approximations for exchange and correlation with a correct asymptotic behavior. It is schematically depicted in Fig. 2.41. This is a suggestion for classification of various xc functionals in rungs (or levels), as in the famous "Jacob's ladder". Figure 2.41 shows a drawing of a tree with branches on four different levels. On each level a different DFT quantity is meant to be approximated. Climbing the tree, one progresses from more simple and intuitive concepts, such as [focusing on the left part for the moment] the xc energy, E_{xc} (level 1), or the xc energy density per particle, $e_{\mathrm{xc}}(\vec{r})$ (level 2) to the more abstract concepts of the λ-averaged xc hole, $\bar{n}_{\mathrm{xc}}(\vec{r'}|\vec{r})$ (level 3) all the way to the top of the tree, with the λ-dependent hole, $n^{(\lambda)}_{\mathrm{xc}}(\vec{r'}|\vec{r})$. The number of coordinates each quantity has, as well as the difficulty to construct approximations, rises. Of course, descending is usually easier than ascending: once an approximation for a quantity is made, those below are immediately obtained, by integration. In addition, one can choose whether to climb the tree on the left, approximating exchange and correlation, or on the right, using the exact exchange and looking for a compatible correlation functional. The various known xc approximations can be located on one of the branches of this tree. It generally seems that the first two levels are rather congested, whereas the higher levels are only sparsely occupied. The strategy is to keep climbing the exchange-correlation tree, because the sweetest fruits are on the top (not shown in Fig. 2.41).

References

Hodgson, M.J.P. et al. (2017). "How Interatomic Steps in the Exact Kohn-Sham Potential Relate to Derivative Discontinuities of the Energy". In: *Journal of Physical Chemistry Letters* 8.24, pp. 5974–5980. DOI: `10.1021/acs.jpclett.7b02615`.

Kraisler, E. (2020). "Asymptotic Behavior of the Exchange-Correlation Energy Density and the Kohn-Sham Potential in Density Functional Theory: Exact Results and Strategy for Approximations". In: *Israel Journal of Chemistry* 60.8-9, pp. 805–822. DOI: `10.1002/ijch.201900103`.

Kraisler, Eli, M. J. P. Hodgson, and E. K. U. Gross (2020). "From Kohn-Sham to many-electron energies via step structures in the exchange-correlation potential". In: arXiv: `2008.12029`.

Kraisler, Eli and Axel Schild (2020). "Discontinuous behavior of the Pauli potential in density functional theory as a function of the electron number". In: *Phys. Rev. Research* 2 (1), p. 013159. DOI: `10.1103/PhysRevResearch.2.013159`.

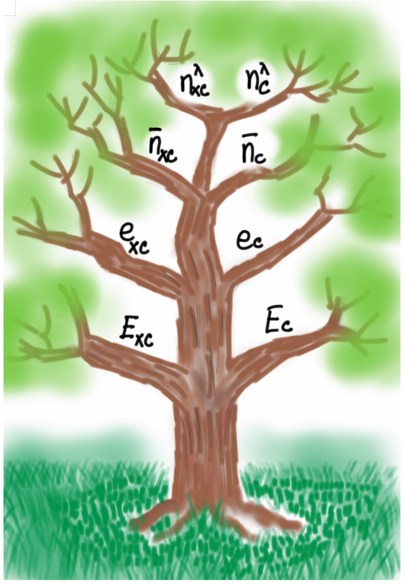

Figure 2.41. The exchange-correlation tree (details in text)

Scientific activities

Eli Kraisler group members

Name	Project	Status	Period
Sharon Lavie	Ionization potentials and fundamental gaps in atomic systems with the ensemble-DFT approach	MSc student	since March 2019
Eyal Tsvitman	New exchange - correlation approximations for dissociation with DFT	MSc student	since July 2020
Nathan E. Rahat	Exact solutions of the Schrödinger equation	BSc student – “Etgar” project	since September 2019

Eli Kraisler scientific collaborations

Name	Project	Institution
Dr. Axel Schild	Orbital-free DFT and Electron Exact Factorization	ETH Zürich, Switzerland
Dr. Linn Leppert	GW calculations in energy materials	University of Twente, Netherlands
Dr. M. J. P. Hodgson	Properties of the exact exchange-correlation potentials	University of Durham, UK
Dr. Tim Gould	The ensemble approach in DFT	Griffith University, Nathan, Australia
Dr. Attila Cangi	Approximations to exchange and correlation at high temperatures	Helmholtz-Zentrum Dresden-Rossendorf, Germany

Conference organization (last 5 years)

2020	Co-organized with Dr. Omer Yaffe (Weizmann Institute) the Materials Physics sessions at the Israel Physics Society (IPS-2020) Meeting.
2019	Co-organized with Dr. Snir Gazit and Prof. Roi Baer the Fritz Haber Winter Symposium, The Hebrew University of Jerusalem, Israel.
2019 May 22-27	Co-organized with Prof. Roi Baer and Prof. E. K. U. Gross, an International Workshop, “The exact factorization for electrons, nuclei, and photons”, The Hebrew University of Jerusalem, Israel.

Prizes, Honors, editorial and review boards etc. (last 5 years)

2020	Alexander von Humboldt visit grant to Germany (postponed due to COVID19)
2016-18	Alexander von Humboldt postdoctoral research fellowship
2016	John F. Kennedy Prize for academic excellence and scientific accomplishments

2.9 Raphael D. Levine

Research Activities

I am in charge of the theory work package of the EC FET Open project COPAC. The aim of COPAC is to demonstrate a concrete device that can process quantum information at room temperature. My research report for 2020 is a discussion of how the COPAC device, built by Prof. E Collini of Padua, satisfies the criterion of what a quantum computer can do. There have been several recent reports of quantum computations for chemical problems. What is new and unique is that we report on *dynamics*. The partners are my student Ksenia Komarova, Hugo Gattuso a coworker of Francoise Remacle and Francoise herself who is the coordinator of COPAC. Gattuso and Remacle dealt primarily with the electronic structure of the device while Komarova and myself worked primarily on the dynamics.

Quantum Device Emulates Dynamics of Two Coupled Oscillators

About forty years ago in a highly cited paper (Feynman 1982) Feynman reflected on simulating physics with computers. One of the two main options that Feynman discussed was using a new kind, a quantum computer, to simulate other quantum systems (section 4 of ref. (Feynman 1982)).

Feynman remarked that there can be a class of intersimulatable systems and possibly there can also be a universal machine. Here we discuss the former, more limited class with a specific application.

In the intervening years there was spectacular progress in the theory of quantum computing (Milburn 1999; Nielsen and Chuang 2010; Shapiro and Brumer 2012; Yuen-Zhou et al. 2014; Kais 2014; Lee et al. 2019; Albash and Lidar 2018; Gyongyosi and Imre 2019; National Academies of Sciences and Medicine 2019; Arute et al. 2019; Smith et al. 2019; Cao et al. 2019; Xia and Kais 2018; Arguello-Luengo et al. 2019) not all of which related to the vision of Feynman. An arguably concrete demonstration of quantum supremacy has been published by the Google team (Arute et al. 2019). Quantum computing algorithms also start to be applied to simulate quantum many body problems in physics and chemistry ((Smith et al. 2019; Cao et al. 2019; Xia and Kais 2018; Arguello-Luengo et al. 2019)) with special reference to eigensolvers. Quantum enhanced machine learning algorithms (Ciliberto et al. 2018) that take advantage of the new capabilities of quantum computers for linear algebra operations are being actively developed (Xia and Kais 2018; Rebentrost et al. 2018; Schuld, Sinayskiy, and Petruccione 2016). Such algorithms include Principal Component Analysis Canonical Correlation Analysis and other algebraic methods used for dimension reduction. Quantum algorithms are also being developed for sampling probability distributions (Gao, Zhang, and Duan 2018). The debate remains open on which physical hardware support is most suitable for quantum computing (*Hearing-the-quantum: Top 10 quantum experiments in 2019* 2019) and what will be the optimal quantum architecture, standalone computer or task dedicated module integrated in a hybrid quantum classical architecture (Pednault et al. 2019). Here we go back to classification of Feynman and describe a class of intersimulatable machines, where a member of the class has been realized experimentally on a solid state array of CdSe Quantum Dots (Collini, Gattuso, Bolzonello, et al. 2019; Collini, Gattuso, Kolodny, et al. 2020). The special point about the class is that we describe dynamics and not only energetics.

The hardware we consider is an array of semi conducting quantum dots, QDs. Each dot has lower lying electronically excited states with absorption in the visible within the coherence bandwidth of a fast laser. Addressing the device by a sequence of laser pulses and read-out is performed simultaneously on many dots (Collini, Gattuso, Bolzonello, et al. 2019; Collini, Gattuso, Kolodny, et al. 2020; Kambhampati 2011; Caram et al. 2014; Turner, Hassan, and Scholes 2012; Cassette, Dean, and Scholes 2016) as in 2D electronic spectroscopy (Cho 2009; Mukamel 1995). Reading concurrently many dots means that each value is read many times so that the observed mean value is the true average, similarly to NMR quantum computing (Warren 1997). Measuring over a classical ensemble of dots importantly means that practically there is no interference between measuring different observables that individually do not commute and so are not subject to a quantal uncertainty principle. There is however a negative side, the size variability of quantum dots means that the different dots are not quite identical and one must average the read-out over the distribution of sizes. This limits the frequency resolution or, equivalently, the time available for read-out (Gattuso, Levine, and Remacle 2020) to faster than the coupling to phonons and in that time scale the device operates on a purely electronic spectrum of an isolated system. We theoretically describe the device as an N state quantum system. At the moment it is the finite size dispersion of the dots as synthesized in the better experiments, say 5% or below, that limits the frequency resolution of the read-out by limiting the number of distinct states that can be resolved.

The physics of an N state quantum system, $|i\rangle, i = 1, 2, ..., N$, is fully described by N^2 real variables, that we chose as the N occupation probabilities, $N - 1$ if we impose normalization and $N(N - 1)$ real valued coherences. We think of these numbers as expectation values of N^2 Hermitian operators one of which is the identity operator, $\hat{\mathbb{I}}$. A carat superscript will be used to denote an operator. The N^2 operators induce transitions between quantum states and their *expectation values* are the logic variables. The operators are our analogues of the logic gates of quantum computing. It is sometimes simpler to use non-Hermitian operators, specifically $\hat{X}_{ij} = |i\rangle\langle j|$ where the Hermitian operators are $\left(\hat{X}_{ij} + \hat{X}_{ij}\right)/2$ and $\left(\hat{X}_{ij} - \hat{X}_{ij}\right)/2i$. We tend to think of $\hat{X}_{ij} = |i\rangle\langle j|$ as a coherence because its expectation value is the coherence between states $|i\rangle$ and $|j\rangle$. Figure 2.42 on the left shows the algebra for a system with a ground and two accessible excited levels, $i, j = 0, 1, 2$ or $N = 3$ that is a simple hardware. A quite different algebra for the two coupled oscillators we mean to emulate is shown on the right.

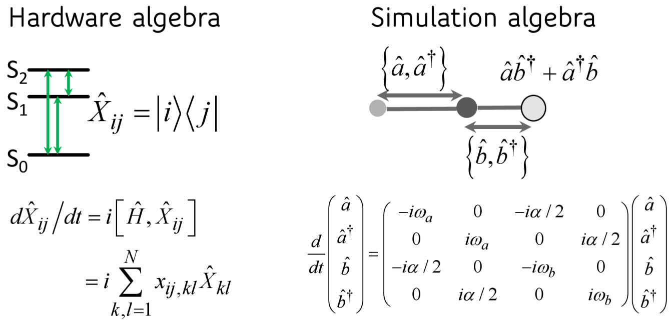

Figure 2.42. Operators and their evolution in the hardware (single QD) and in the physical system

The hardware as shown in Fig. 2.42 can simulate up to 9 variables. That turns out to be just enough for our needs. To have more flexibility we will recognize that in the CdSe quantum dots that we use each one of the two lowest excited levels is 12-fold degenerate. The strong spin-orbit coupling in Se will split each into two levels so that we will have 5^2 logic variables at our disposal.

In 2D electronic spectroscopy the laser pulses optically connect the different states of the systems which means (Alhassid and Levine 1978; Gilmore 2012) that the set of N^2 operators is closed under commutation with the Hamiltonian $\left[\hat{H}, \hat{X}_{ij}\right] = \sum_{k,l=1}^{N} x_{ij,kl}\hat{X}_{kl}$. The rate of change of the operators and thereby the rate of change of their mean values over the ensemble is therefore closed:

$$\left(\frac{\mathrm{d}\left\langle \hat{X}_{ij}\right\rangle}{\mathrm{d}t}\right) = i\left\langle\left[\hat{H}, \hat{X}_{ij}\right]\right\rangle = \sum_{k,l=1}^{N} x_{ij,kl}\left\langle \hat{X}_{kl}\right\rangle \tag{2.55}$$

The closure property defined on the operators means that equation (2.55) is valid for any density matrix $\hat{\rho}$ of the isolated system, pure or mixed, $\left\langle \hat{X}_{ij}\right\rangle = Tr(\hat{\rho}\hat{X}_{ij})$. Equation 2.55 allows our physical device (= the hardware) to emulate the time dependence of the N^2 values $\left\langle \hat{X}_{ij}\right\rangle$ starting from their value in the initial state and the parameters of the lasers and the transition dipoles. We have shown (Collini, Gattuso, Bolzonello, et al. 2019; Collini, Gattuso, Kolodny, et al. 2020) that the experimental response of our hardware is well reproduced by a numerical solution of equation (2.55) using quantum chemical computations of energy levels and transition dipoles. We will here use this numerical solution.

All quantal systems for which we can determine up to N^2 operators that are closed under commutation with the Hamiltonian are therefore intersimulatable by suitable arrangement of the addressing of the computing device by the laser pulses. One can exhibit the output for a particular input as a 3D map. By convention, one axis is the time interval T between the second and third laser pulses. So we show the tradeout from the device as a series of 2D maps each one is a cut of the 3D map at a particular value of T. Closure under commutation with the Hamiltonian is relevant only during the time when the evolution is unitary meaning the time when the system is effectively not coupled to its environment. This is only realistic for a short time so we limit attention to systems that can be read within that short time. A special but very common case of a system

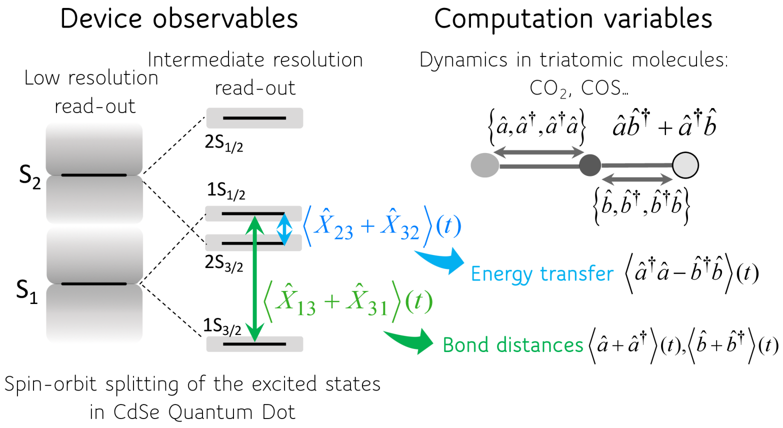

Figure 2.43. Realization of the concept. Left: the two lowest excited states of a single dot. At the lowest resolution each state is an unresolved band of 12 quantum states as mimicked by the shading. At an intermediate resolution that is achievable by experiments at room temperature each band is split by spin-orbit coupling into two bands of 4 and 8 states respectively. Right: the coupled oscillator system and two time dependent mean values, energy transfer and bond oscillation, that can be simulated. Intermediate resolution allows resolving up to 5^2 variables. The same number of variables can be simulated using a QD dimer read at a lowest spectroscopic resolution.

admitting an algebra of N^2 operators that are closed under commutation with the Hamiltonian is a quantum mechanical system of N states. But there are more general cases and in the example we discuss in the main text we demonstrate closed algebras of 5 and 9 operators. What is needed is that the expectation values of the operators in the algebra are sufficient to specify the initial state of the system we mean to simulate.

We discuss a linear molecule, e.g., COS, with two harmonic local stretches. Of course such a system is analytically soluble giving rise to a symmetric and anti-symmetric vibrational normal modes (Gerhard 1960). It is however physically rather different than the quantum device we use for the simulation, a device (= hardware) that is built on ultrafast dynamics of electronically excited states. In the main text we discuss a device using just one semi-conducting CdSe nanometric quantum dot with two electronically excited states, S_1 and S_2, see Fig. 2.42. At very high spectral resolution each one of the two excited states is split by spin orbit and crystal field couplings (Al. L. Efros and Rosen 2000; Sercel and Alexander L. Efros 2018; Norris and Bawendi 1996; Wong and Scholes 2011) to 12 fine structure states, so $1(S_0)+12(S_1)+12(S_2)=25$ states per dot (including the ground state) and 25^2 operators that require high resolution to be observable. (Recall that expectation values for these operators are logic variables). This high resolution is not achievable with currently available size dispersion of the dots. At an intermediate resolution that is already experimentally available (Collini, Gattuso, Bolzonello, et al. 2019) each band of 12 states is resolvable into two bands of 4 and 8 states respectively, see Fig. 2.43. For specific QD sizes and limited size dispersion, the four bands do not overlap and each band can be separately optically addressed, so for intermediate resolution two bands for each excited state or $(1(S_0)+2(S_1)+2(S_2))^2=5^2$ logic variables are already experimentally available using only the two lowest electronically excited states of a single dot. At a higher size dispersion one can have only 3 states or $(1(S_0)+1(S_1)+1(S_2))^2=9$ variables using a single dot.

For a quantum dot dimer, using two lowest excited states on each monomer at the lowest resolution gives $(1(S_0)+1(S_{1,A})+1(S_{2,A})+1(S_{1,B})+1(S_{2,B}))=5$ states or 5^2 variables. Accounting for the fine structure splittings in the quantum dot dimer provides 48 states at the highest resolution, a resolution that will not be achievable due to size dispersion of colloidal QD and thermal induced transition between states. We emphasize the question of frequency resolution because the inevitable size dispersion of quantum dots means that the different spectroscopic transitions have a finite width due to the size variation (Gattuso, Fresch, et al. 2020). Not all coherences can, in practice, be resolved. For example, we can emulate the dynamics of the two coupled harmonic oscillators, only for a limited number of vibrational periods, a time scale of about two hundred fs's, during which the set of operators that describe the electronic eigenstates of the computing device remain closed under commutation. At longer times, the coupling to the phonons and transfer of population between states due to the coupling to the environment leads to a loss of the closure property for the device.

The physical system we aim to simulate is the dynamics of two coupled oscillators. In the main text we use the simplest but realistic Hamiltonian that of two coupled harmonic oscillators. This Hamiltonian can be written as

$$\hat{H} = \omega_a \hat{a}^\dagger \hat{a} + \omega_b \hat{b}^\dagger \hat{b} + \alpha/2\left(\hat{a}^\dagger \hat{b} + \hat{a}\hat{b}^\dagger\right) \tag{2.56}$$

where $\hat{a}$ and $\hat{b}$ are the annihilation operators for the two bonds, $\hat{X} = \hat{a}^\dagger \hat{b} + \hat{a}\hat{b}^\dagger$ is the coupling between the two bonds as described in a force field model. It is a harmonic coupling in that it describes only a one quantum exchange between the two local bonds. we first consider the case when the two local harmonic oscillators are identical $\omega_a = \omega_b = \omega$, e.g., CO2, and an initial state that is not an equilibrium state but is stationary when there is no coupling, $\alpha = 0$. We compute a classical-like periodic quantity, the quantum mechanical energy transfer between the two oscillators. Then we discuss a state when initially the two bonds are displaced from their equilibrium distances. This more general case can also be simulated by a single quantum dot.

To compute the energy transfer, note that for the Hamiltonian eq. (2.56), the number of vibrational quanta $\hat{N} = \hat{a}^\dagger \hat{a} + \hat{b}^\dagger \hat{b}$ is a constant of the motion $\left[\hat{N}, \hat{H}\right] = 0$, while the difference $\hat{Z} = \hat{a}^\dagger \hat{a} - \hat{b}^\dagger \hat{b}$ is periodic in time $d\hat{Z}/dt = \alpha \hat{Y}$, $d\hat{Y}/dt = -\alpha \hat{Z}$ where $\hat{Y} = i\left(\hat{a}\hat{b}^\dagger - \hat{a}^\dagger \hat{b}\right)$. It follows that $\hat{Z}(t) = \hat{Z}(0)\cos\alpha t$ and the energy transfer at time t is:

$$\delta E = \omega\left(\left\langle \hat{Z} \right\rangle(t) - \left\langle \hat{Z} \right\rangle(0)\right) = \omega \left\langle \hat{Z} \right\rangle(0)(\cos\alpha t - 1) \tag{2.57}$$

where $\omega\left\langle \hat{Z} \right\rangle(0) = \omega\left\langle \hat{a}^\dagger \hat{a} - \hat{b}^\dagger \hat{b} \right\rangle(0)$ is the initial mismatch in energy of the two oscillators. See figure 2.44(a, b) for an example of a simulated energy transfer.

The energy transfer can be read from the time-dependent evolution of the mean values of the populations in the two lowest excited eigenstates 1 and 2 of a single dot and of the coherence between these two states, *after* a sequence of fs laser pulses that builds the electronic coherence between them:

$$\langle 1|\hat{\rho}(t)|2\rangle + \langle 2|\hat{\rho}(t)|1\rangle = 2\sqrt{\langle 1|\hat{\rho}(t)|1\rangle\langle 2|\hat{\rho}(t)|2\rangle}\cos\Delta E t \tag{2.58}$$

The density matrix of the device at the time t is $\hat{\rho}(t)$, $\hat{\rho}(t) = \sum_{i,j}^{N} x_{ij}(t)\hat{X}_{ij}$, and ΔE is the energy spacing between the two excited states. It is read by the oscillation of the coherence, which is the mean value of the projection operator $\hat{X}_{12} = |1\rangle\langle 2|$. The amplitude is read by the amplitude of the oscillation of the coherence, figure 2.44(b,d), or from the population of the two states, entries that appear along the diagonal in a coherence map representation of the output of 2D electronic spectroscopy (Cho 2009; Mukamel 1995).

To describe the energy of each local oscillator, their coupling and the resulting energy transfer we need the closed algebra of 5 operators,$\hat{I}, \hat{N}, \hat{X}, \hat{Y}, \hat{Z}$ where $\hat{N} \pm \hat{Z}$ specify the number of quanta

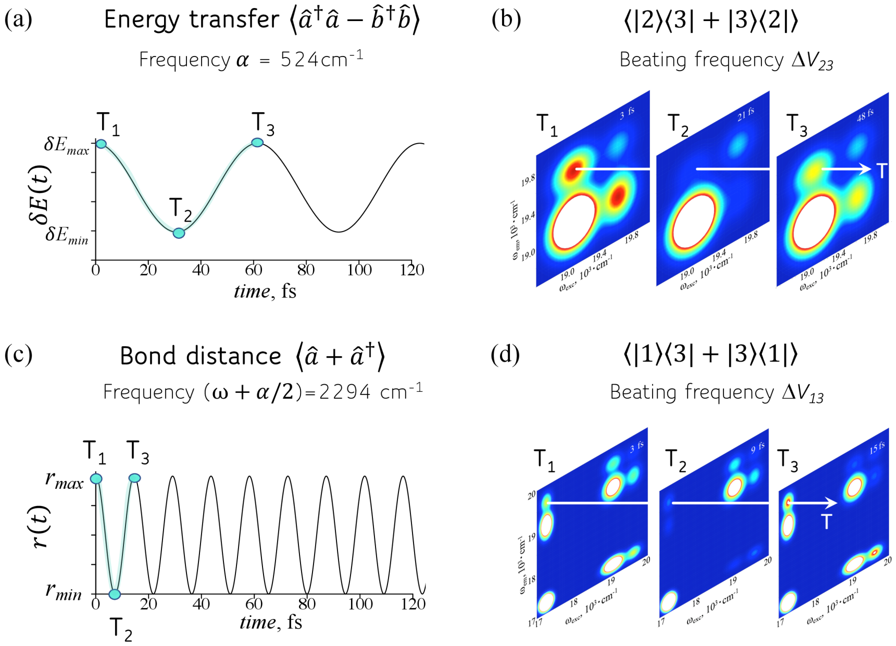

Figure 2.44. Emulation of vibrational dynamics. Left panels: Energy transfer $\delta E(t)$ from a hotter to a colder vibration, equation (2.57), and bond displacement $r(t)$ vs. time. Right panels: Evolution of the coherences in 2D frequency maps, computed for a 3% size dispersion, shown at different values of the delay time T between the first and second laser pulses as used in 2D electronic spectroscopy. These values of T are shown on the plots of the energy transfer and bond distance vs. time. Different regions on the 2D map are used to compute the low frequency oscillation of the energy transfer and high-frequency oscillations of the bond.

in each oscillator. To compute expectation values of quantum mechanical operators such as $\langle \hat{a} \rangle$ or $\left\langle \hat{b}^\dagger \right\rangle$ we need to enlarge the algebra. It turns out that adding the four operators $\left\{ \hat{a}, \hat{a}^\dagger, \hat{b}, \hat{b}^\dagger \right\}$ to the previous five provides a nine (Lie) operator algebra that is closed under commutation with the Hamiltonian, equation (2.59). The algebra is closed also for inequivalent local modes. Nine operators is the number of operators corresponding to the three lowest electronic states of a single QD. The full details are in the supplementary information and here we discuss the case of equivalent oscillators, when the two operators $\hat{a}, \hat{b}$ and separately $\hat{a}^\dagger, \hat{b}^\dagger$ form two closed sub-algebras. For example for the first pair:

$$\frac{\mathrm{d}}{\mathrm{d}t} \begin{pmatrix} \hat{a} \\ \hat{b} \end{pmatrix} = -i \begin{pmatrix} \omega & \alpha/2 \\ \alpha/2 & \omega \end{pmatrix} \begin{pmatrix} \hat{a} \\ \hat{b} \end{pmatrix} \tag{2.59}$$

with two eigenfrequencies $(\omega + \alpha/2)$ and $(\omega - \alpha/2)$ and eigenvectors $\hat{a} \pm \hat{b}$ and similarly for the second pair. For two identical local oscillators that are initially at rest and equally displaced from their equilibrium length $\langle \hat{a} \rangle (t) = \langle \hat{a} \rangle (0) exp\big(-i(\omega + \alpha/2)t\big)$ and similarly for its complex conjugate $\left\langle \hat{a}^\dagger \right\rangle (t)$. The bond length oscillates as $\langle \hat{r} \rangle (t) = \langle \hat{r} \rangle (0) \cos\left((\omega + \alpha/2)t\right)$ while the initial mean momentum is zero and it oscillates as $\sin\left((\omega + \alpha/2)t\right)$. To simulate the dynamics of the nine operators it is needed to compute three variables that oscillate with time at different frequencies. An example for the oscillation of the bond is shown in figure 2.44(c, d). These oscillations are resolvable even for the larger dispersion of the sizes of the QD. Variables changing with a low frequency, such as energy transfer, 524 cm^{-1}, are read closer to the diagonal, so the broadening due to size dispersion is more critical.

Last we comment that one can have quite realistic physical situations where one is unable to close an algebra of few operators. At the same time, it follows from the discussion in connection with equation (2.55) that in an isolated quantum mechanical system of N states there is always a (not unique) closed algebra of N^2 operators. The coherences $\hat{X}_{ij} = |i\rangle\langle j|\,, i,j = 1,2,...,N$ are a convenient set of such operators. When the quantum states $|i\rangle$ and $|j\rangle$ are connected by a transition dipole such coherences can be detected by optical means. For electronic states this could be pump-probe transient absorption spectroscopy or by non linear methods such as 2D electronic spectroscopy or four wave mixing.

In this report we used only the time dependence of the coherences of the quantum device to simulate the physical system. This is less of a restriction than one might think. To see the point consider the equations of motion of the observables of the physical system. Arrange the observables as components of a vector. The rate of change of this vector is described by a Liouvillian matrix. When we diagonalize this Liouvillian matrix we get a set of eigenfrequencies that fully characterize the characterization of the physical device by these variables. If we can describe such frequencies by the oscillation of the coherences of the quantum device and size dispersion is beneficial in this respect, we can do the time dependent part of the needed description.

References

Albash, Tameem and Daniel A. Lidar (Jan. 2018). “Adiabatic quantum computation”. In: *Reviews of Modern Physics* 90.1, p. 015002. DOI: `10.1103/revmodphys.90.015002`.

Alhassid, Y. and R. D. Levine (July 1978). “Connection between the maximal entropy and the scattering theoretic analyses of collision processes”. In: *Physical Review A* 18.1, pp. 89–116. DOI: `10.1103/physreva.18.89`.

Arguello-Luengo, Javier et al. (Oct. 2019). “Analogue quantum chemistry simulation”. In: *Nature* 574.7777, pp. 215–218. DOI: `10.1038/s41586-019-1614-4`.

Arute, Frank et al. (2019). “Quantum supremacy using a programmable superconducting processor”. In: *Nature* 574.7779, pp. 505–510. DOI: `10.1038/s41586-019-1666-5`. URL: `https://doi.org/10.1038/s41586-019-1666-5`.

Cao, Yudong et al. (Aug. 2019). “Quantum Chemistry in the Age of Quantum Computing”. In: *Chemical Reviews* 119.19, pp. 10856–10915. DOI: `10.1021/acs.chemrev.8b00803`.

Caram, Justin R. et al. (Feb. 2014). “Exploring size and state dynamics in CdSe quantum dots using two-dimensional electronic spectroscopy”. In: *The Journal of Chemical Physics* 140.8, p. 084701. DOI: `10.1063/1.4865832`.

Cassette, Elsa, Jacob C. Dean, and Gregory D. Scholes (Feb. 2016). “Two-Dimensional Visible Spectroscopy For Studying Colloidal Semiconductor Nanocrystals”. In: *Small* 12.16, pp. 2234–2244. DOI: `10.1002/smll.201502733`.

Cho, Minhaeng (June 2009). *Two-Dimensional Optical Spectroscopy*. Boca Raton: CRC Press. DOI: `10.1201/9781420084306`.

Ciliberto, Carlo et al. (Jan. 2018). “Quantum machine learning: a classical perspective”. In: *Proceedings of the Royal Society A: Mathematical, Physical and Engineering Sciences* 474.2209, p. 20170551. DOI: `10.1098/rspa.2017.0551`.

Collini, Elisabetta, Hugo Gattuso, Luca Bolzonello, et al. (Dec. 2019). “Quantum Phenomena in Nanomaterials: Coherent Superpositions of Fine Structure States in CdSe Nanocrystals at Room Temperature”. In: *The Journal of Physical Chemistry C* 123.51, pp. 31286–31293. DOI: `10.1021/acs.jpcc.9b11153`.

Collini, Elisabetta, Hugo Gattuso, Yuval Kolodny, et al. (June 2020). “Room-Temperature Inter-Dot Coherent Dynamics in Multilayer Quantum Dot Materials”. In: *The Journal of Physical Chemistry C* 124.29, pp. 16222–16231. DOI: 10.1021/acs.jpcc.0c05572.

Efros, Al. L. and M. Rosen (Aug. 2000). “The Electronic Structure of Semiconductor Nanocrystals”. In: *Annual Review of Materials Science* 30.1, pp. 475–521. DOI: 10.1146/annurev.matsci.30.1.475.

Feynman, Richard P. (June 1982). “Simulating physics with computers”. In: *International Journal of Theoretical Physics* 21.6-7, pp. 467–488. DOI: 10.1007/bf02650179.

Gao, X., Z.-Y. Zhang, and L.-M. Duan (Dec. 2018). “A quantum machine learning algorithm based on generative models”. In: *Science Advances* 4.12, eaat9004. DOI: 10.1126/sciadv.aat9004.

Gattuso, Hugo, Barbara Fresch, et al. (Feb. 2020). “Coherent Exciton Dynamics in Ensembles of Size-Dispersed CdSe Quantum Dot Dimers Probed via Ultrafast Spectroscopy: A Quantum Computational Study”. In: *Applied Sciences* 10.4, p. 1328. DOI: 10.3390/app10041328.

Gattuso, Hugo, R. D. Levine, and F. Remacle (Aug. 2020). “Massively parallel classical logic via coherent dynamics of an ensemble of quantum systems with dispersion in size”. In: *Proceedings of the National Academy of Sciences* 117.35, pp. 21022–21030. DOI: 10.1073/pnas.2008170117.

Gerhard, Herzberg (1960). *Infrared and Raman spectra of polyatomic molecules*. New York: Van Nostrand.

Gilmore, Robert (2012). *Lie Groups, Lie Algebras, and Some of Their Applications*. Mineola: Dover Books on Mathematics.

Gyongyosi, Laszlo and Sandor Imre (Feb. 2019). “A Survey on quantum computing technology”. In: *Computer Science Review* 31, pp. 51–71. DOI: 10.1016/j.cosrev.2018.11.002.

Hearing-the-quantum: Top 10 quantum experiments in 2019 (2019). URL: https://medium.com/swlh/top-quantum-computing-experiments-of-2019-1157db177611.

Kais, Sabre, ed. (2014). *Quantum Information and Computation for Chemistry*. Hoboken, NJ: John Wiley & Sons, Ltd. DOI: 10.1002/9781118742631.

Kambhampati, Patanjali (Jan. 2011). “Unraveling the Structure and Dynamics of Excitons in Semiconductor Quantum Dots”. In: *Accounts of Chemical Research* 44.1, pp. 1–13. DOI: 10.1021/ar1000428.

Lee, Joonho et al. (Nov. 2019). “Generalized Unitary Coupled Cluster Wave functions for Quantum Computation”. In: *Journal of Chemical Theory and Computation* 15.1, pp. 311–324. DOI: 10.1021/acs.jctc.8b01004.

Milburn, Gerard J. (1999). *The Feynman Processor: Quantum Entanglement and the Computing Revolution*. Reading, MA: Perseus Books.

Mukamel, Shaul (1995). *Principles of Nonlinear Optical Spectroscopy*. Oxford, NY: Oxford University Press.

National Academies of Sciences, Engineering and Medicine (2019). *Quantum Computing: Progress and Prospects*. Ed. by Emily Grumbling and Mark Horowitz. Washington, DC: The National Academies Press. ISBN: 978-0-309-47969-1. DOI: 10.17226/25196. URL: https://www.nap.edu/catalog/25196/quantum-computing-progress-and-prospects.

Nielsen, Michael A. and Isaac L. Chuang (2010). *Quantum Computation and Quantum Information*. Cambridge: Cambridge University Press. DOI: 10.1017/cbo9780511976667.

Norris, D. J. and M. G. Bawendi (June 1996). “Measurement and assignment of the size-dependent optical spectrum in CdSe quantum dots”. In: *Physical Review B* 53.24, pp. 16338–16346. DOI: 10.1103/physrevb.53.16338.

Pednault, Edwin et al. (2019). *On "Quantum Supremacy"*. URL: https://www.ibm.com/blogs/research/2019/10/on-quantum-supremacy.

Rebentrost, Patrick et al. (Jan. 2018). “Quantum singular-value decomposition of nonsparse low-rank matrices”. In: *Physical Review A* 97.1, p. 012327. DOI: 10.1103/physreva.97.012327.

Schuld, Maria, Ilya Sinayskiy, and Francesco Petruccione (Aug. 2016). “Prediction by linear regression on a quantum computer”. In: *Physical Review A* 94.2, p. 022342. DOI: `10.1103/physreva.94.022342`.

Sercel, Peter C. and Alexander L. Efros (June 2018). “Band-Edge Exciton in CdSe and Other II-VI and III-V Compound Semiconductor Nanocrystals - Revisited”. In: *Nano Letters* 18.7, pp. 4061–4068. DOI: `10.1021/acs.nanolett.8b01980`.

Shapiro, Moshe and Paul Brumer (2012). *Quantum Control of Molecular Processes*. Weinheim: John Wiley & Sons, Ltd. DOI: `10.1002/9783527639700`.

Smith, Adam et al. (Nov. 2019). “Simulating quantum many-body dynamics on a current digital quantum computer”. In: *Npj Quantum Information* 5.1, p. 106. DOI: `10.1038/s41534-019-0217-0`.

Turner, Daniel B., Yasser Hassan, and Gregory D. Scholes (Jan. 2012). “Exciton Superposition States in CdSe Nanocrystals Measured Using Broadband Two-Dimensional Electronic Spectroscopy”. In: *Nano Letters* 12.2, pp. 880–886. DOI: `10.1021/nl2039502`.

Warren, W. S. (Sept. 1997). “The Usefulness of NMR Quantum Computing”. In: *Science* 277.5332, pp. 1688–1690. DOI: `10.1126/science.277.5332.1688`.

Wong, Cathy Y. and Gregory D. Scholes (Mar. 2011). “Using two-dimensional photon echo spectroscopy to probe the fine structure of the ground state biexciton of CdSe nanocrystals”. In: *Journal of Luminescence* 131.3, pp. 366–374. DOI: `10.1016/j.jlumin.2010.09.015`.

Xia, Rongxin and Sabre Kais (Oct. 2018). “Quantum machine learning for electronic structure calculations”. In: *Nature Communications* 9.1, p. 4195. DOI: `10.1038/s41467-018-06598-z`.

Yuen-Zhou, Joel et al. (2014). *Ultrafast Spectroscopy*. Bristol: IOP Publishing. DOI: `10.1088/978-0-750-31062-8`.

Scientific activities

Raphael D. Levine group members

Name	Project	Status	Period
Swetha Vasudevan	Deciphering patient specific tumor network structures towards personalized diagnostics and treatments: by an an information-theoretical study	PhD student	since February 2017
Ksenia Komarova	Non-equilibrium electron dynamics in molecules and its coupling to nuclear motion	PhD student	since October 2017
Lisa Rachel George	Correlating transcription levels with epigenetic methylation in different cancer types	PhD student	since March 2018
Natalia Gelfand	Theoretical Investigation of Isotope effect in Vacuum Ultraviolet Photodissociation of Astronomically Relevant Molecules	PostDoctoral student	since October 2020

Raphael D. Levine scientific collaborations

Name	Project	Institution
Francoise Remacle	Coherent Optical Parallel Computing	FNRS Director of Research at Liege University, Belgium
James Heath and Wei Wei	Physical Characterization of Cancer	Institute for Systems Biology, Seattle, USA
Mark Thiemens	Experimental and Theoretical Investigation of Isotope effect in Vacuum Ultraviolet Photodissociation of Astronomically Relevant Molecules: Implications for the Early Solar System	University of California San Diegom USA

Raphael D. Levine active grants

Project	Period	Foundation	Total grant in thousands
Coherent Optical Parallel Computing	2018-2021	Horizon2020 FET Open EC program	€320
Physical Characterization of Cancer	2017-2021	NIH	$900
Experimental and Theoretical Investigation of Isotope effect in Vacuum Ultraviolet Photodissociation of Astronomically Relevant Molecules: Implications for the Early Solar System	2020-2023	NSF-BSF	$180

2.10 Masha Y. Niv

Research Activities

We study the chemical senses, mainly bitter and sweet taste, using a combination of computational homology modeling, docking, chemoinformatics, machine learning, sensory studies and cell-based assays.

Bitter taste receptors and their ligands

Bitter taste remains a major research direction in my lab for several years, including 2018-2020. (Dagan-Wiener et al. 2019; Dipizio2018 et al. 2018; Di Pizio, Ben Shoshan-Galeczki, et al. 2019; Di Pizio, Waterloo, et al. 2020; Nowak et al. 2018; Stoeger et al. 2020; Thawabteh et al. 2019; Xue, A. Y. et al. 2018). Recently, we have developed BitterIntense, a tool for predicting extreme bitterness of molecules (submitted and available on bioRxiv).Through the DFG-funded project with the Gmeiner lab in Erlangen, Germany we develop high-affinity synthetic ligands of bitter taste receptor T2R14, with the ultimate goal of determining the experimental (Xray or CryoEM) structure of a bitter taste receptor-ligand complex.(Di Pizio, Waterloo, et al. 2020)

Molecular recognition and signaling of sweet taste receptor

We are intrigued by the complex and unexpected signaling related to sweet taste. The possibility to discover novel natural compounds that may elicit sweet taste is of great interest for human health and nutrition. We have developed a structure-based protocol towards this end.(Ben Shoshan-Galeczki and Niv 2020) The stereoselectivity (or lack of it) in sweet taste recognition is an intriguing topic: it is known that not only D-glucose, but also L-glucose elicits sweet taste. We have shown the activity in functional cell-based assays, and are using molecular modeling, docking, and molecular dynamics to explain the basis of stereopromiscuity of the sweet taste receptor (submitted and available on bioRxiv).

Using sensory test and cell-based functional assays, we have shown that deuterated water (D_2O, “heavy water”) elicits sweet taste by activating the sweet taste heterodimer TAS1R/TAS1R3 (in revisions and available in bioRxiv). This work is an exciting cooperation of my lab (leading the sensory, cell-based and modeling aspects) with Prof. Pavel Jungwirth (who leads the force-field development and molecular dynamics direction), together with my long-standing collaborator and taste receptors expert Dr. Maik Behrens (TUM, Germany).

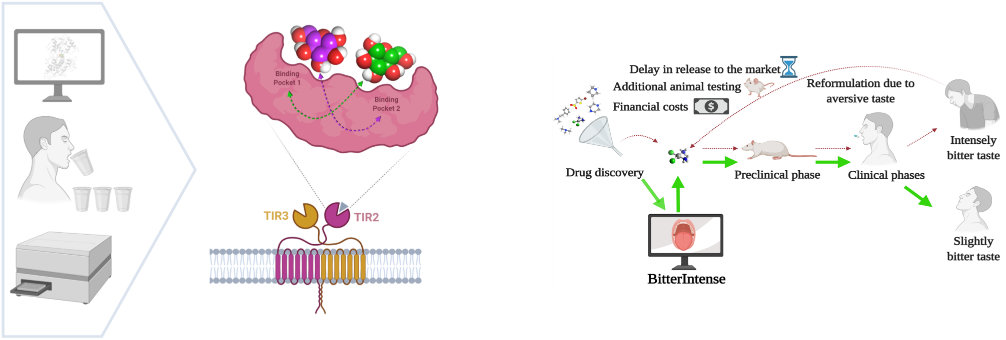

Figure 2.45. Schematic representation of some of the research topics in Niv lab 2018-2020

Smell and taste impairment in COVID19 patients

Soon after COVID19 pandemic broke out, anecdotal evidence that the SARS-CoV-2 virus may impair smell and taste function started to emerge. I have partnered with international colleagues early on to establish and co-lead the Global Consortium for Chemosensory Research, the GCCR. (Parma et al. 2020) In parallel, we are exploring chemosensory losses in Israeli patients, in order to improve screening for the disease (Karni et al. 2020), understand chemosensation and other symptoms recovery (Klein et al. 2020) and evaluate claims that taste and smell searches on Google can be used to monitor the pandemic. (Asseo et al. 2020)

References

Asseo, Kim et al. (2020). "Utility and limitations of Google searches for tracking disease: the case of taste and smell loss as markers for COVID-19". In: *medRxiv*. DOI: `10.1101/2020.05.07.20093955`.

Ben Shoshan-Galeczki, Y. and M. Y. Niv (2020). "Structure-based screening for discovery of sweet compounds". In: *Food Chem* 315, p. 126286. ISSN: 1873-7072 (Electronic) 0308-8146 (Linking). DOI: `10.1016/j.foodchem.2020.126286`.

Dagan-Wiener, A. et al. (2019). "BitterDB: taste ligands and receptors database in 2019". In: *Nucleic Acids Res* 47.D1, pp. D1179–D1185. ISSN: 1362-4962 (Electronic) 0305-1048 (Linking). DOI: `10.1093/nar/gky974`.

Di Pizio, A., Y. Ben Shoshan-Galeczki, et al. (2019). "Bitter and sweet tasting molecules: It's complicated". In: *Neurosci Lett* 700, pp. 56–63. ISSN: 1872-7972 (Electronic) 0304-3940 (Linking). DOI: `10.1016/j.neulet.2018.04.027`.

Di Pizio, A., L. A. W. Waterloo, et al. (2020). "Rational design of agonists for bitter taste receptor TAS2R14: from modeling to bench and back". In: *Cell Mol Life Sci* 77.3, pp. 531–542. ISSN: 1420-9071 (Electronic) 1420-682X (Linking). DOI: `10.1007/s00018-019-03194-2`.

Dipizio2018, A. et al. (2018). "Molecular Features Underlying Selectivity in Chicken Bitter Taste Receptors". In: *Front Mol Biosci* 5, p. 6. ISSN: 2296-889X (Print) 2296-889X (Linking). DOI: `10.3389/fmolb.2018.00006`.

Karni, Noam et al. (2020). "Self-rated smell ability enables highly specific predictors of COVID-19 status: a case control study in Israel". In: *medRxiv*. DOI: `10.1101/2020.07.30.20164327`.

Klein, Hadar et al. (2020). "Onset, duration, and persistence of taste and smell changes and other COVID-19 symptoms: longitudinal study in Israeli patients". In: *medRxiv*. DOI: `10.1101/2020.09.25.20201343`.

Nowak, S. et al. (2018). “Reengineering the ligand sensitivity of the broadly tuned human bitter taste receptor TAS2R14”. In: *Biochim Biophys Acta Gen Subj* 1862.10, pp. 2162–2173. ISSN: 0304-4165 (Print) 0304-4165 (Linking). DOI: `10.1016/j.bbagen.2018.07.009`.

Parma, V. et al. (2020). “More Than Smell-COVID-19 Is Associated With Severe Impairment of Smell, Taste, and Chemesthesis”. In: *Chem Senses* 45.7, pp. 609–622. ISSN: 1464-3553 (Electronic) 0379-864X (Linking). DOI: `10.1093/chemse/bjaa041`.

Stoeger, V. et al. (2020). “Bitter-Tasting Amino Acids l-Arginine and l-Isoleucine Differentially Regulate Proton Secretion via T2R1 Signaling in Human Parietal Cells in Culture”. In: *J Agric Food Chem* 68.11, pp. 3434–3444. ISSN: 1520-5118 (Electronic) 0021-8561 (Linking). DOI: `10.1021/acs.jafc.9b06285`.

Thawabteh, A. et al. (2019). “Bitterless guaifenesin prodrugs-design, synthesis, characterization, in vitro kinetics, and bitterness studies”. In: *Chem Biol Drug Des* 93.3, pp. 262–271. ISSN: 1747-0285 (Electronic) 1747-0277 (Linking). DOI: `10.1111/cbdd.13409`.

Xue, A. Y. et al. (2018). “Corrigendum: Independent Evolution of Strychnine Recognition by Bitter Taste Receptor Subtypes”. In: *Front Mol Biosci* 5, p. 84. ISSN: 2296-889X (Print) 2296-889X (Linking). DOI: `10.3389/fmolb.2018.00084`.

Scientific activities

Masha Y. Niv group members

Name	Project	Status	Period
Eitan Margulis	ML methods for bitter taste, CIDR data science fellowship	MSc student	2019-2020
Hadar Klein (nee Breen)	Taste and smell in health and disease: sensory tests and self-report studies	MSc student	2019-2020
Kim Asseo	Sensory nutrition: big data analysis of taste and smell responses	MSc student	since 2020
Dor Markus	Sweeteners from plants	MSc student	since 2020
Tomer Green	Chemical structure and perception of taste	MSc student	since 2020
Hodaya Karby	Modeling of chemosensory GPCRs-ligands interactions	MSc student	since 2020
Nitzan Dubovski	Molecular interactions of sweet compounds with their target receptors	PhD student	since 2016
Natalie Ben Abu	Sensory and cell-based study of non-sugar sweet tastants	PhD student	since 2017
Yaron Ben Shoshan Galeczki	Discovery of Sweet Compounds: computational and sensory approaches	PhD student	since 2017
Lior Peri	Cell-based research of bitter taste receptors	PhD student	since 2020
Eitan Margulis	Machine learning: expediting drug development and bitter taste research	PhD student	since 2020
Dr. Fabrizio Fierro	Modeling and MD of taste and metabolism GPCRs	PostDoc	since 2019

Masha Y. Niv active grants

Project	Period	Foundation	Total grant in thousands
Bitter molecules: chemical space, perceptual variation in humans and underlying 3D differences among TAS2Rvariants	2016-2019	ISF	₪650
Combining Biomimetic Micro/Nano Sensors with Chemoinformatics, Molecular Modeling and Sensory Studies Towards Better Understanding of Taste and Smell Sensation	2016-2019	ISF-NCSF	₪1100
Reduced calories sugar mixtures	2018-2019	HUGROW (via Yissum)	$ 10
Towards novel migraine drugs: activation of the pain receptor TRPA1 by cannabinoids	2018-2019	Integra (via Yissum)	₪84
Structure-guided discovery of high affinity TAS2R14 ligands	2019-2022	DFG	₪417
Neutralizing ochratoxin from grape juice and coffee	2019-2022	Ministry of Agriculture , Nitzan innovation	₪96
Sweetness recognition: studying mechanisms and identifying sweeteners	2019-2024	ISF	₪1450
Taste and smell loss symptoms in COVID-19 patients	2020-2021	COVID-19 Hebrew University	₪100

2.11 Igor Schapiro

Research Activities

The objective of our research is to apply and develop computational tools to understand chemical reactions in biomolecules and organic molecules. On the application side our focus is on light-induced reactions, in particular in chromophore-protein complexes and solvated molecules. For this purpose we employ the QM/MM methodology which allows an accurate and efficient treatment of large systems. On the development side we are interested in computational tools to support our research on photochemical/photobiological systems. In November 2020 Igor Schapiro received tenure and was promoted to the rank of Associate Professor.

The Origin of Extended Excited State Dynamics in the Phytochrome All2699g1

Phytochromes constitute a diverse family of bilin-binding photoreceptor proteins that regulate a wide range of physiological processes. Their photochemical properties make them attractive for applications in optogenetics and superresolution microscopy. Phytochromes undergo reversible photoconversion triggered by the *Z* - *E* photoisomerization about the double bond in the bilin chromophore. However, it is not fully understood at the molecular level how the protein framework facilitates the complex photoisomerization dynamics. We have studied a single-domain bilin-binding photoreceptor All2699g1 (Nostoc sp. PCC 7120) that exhibits photoconversion between the red light-absorbing (P_r) and far red-absorbing (P_{fr}) states just like canonical phytochromes. This study

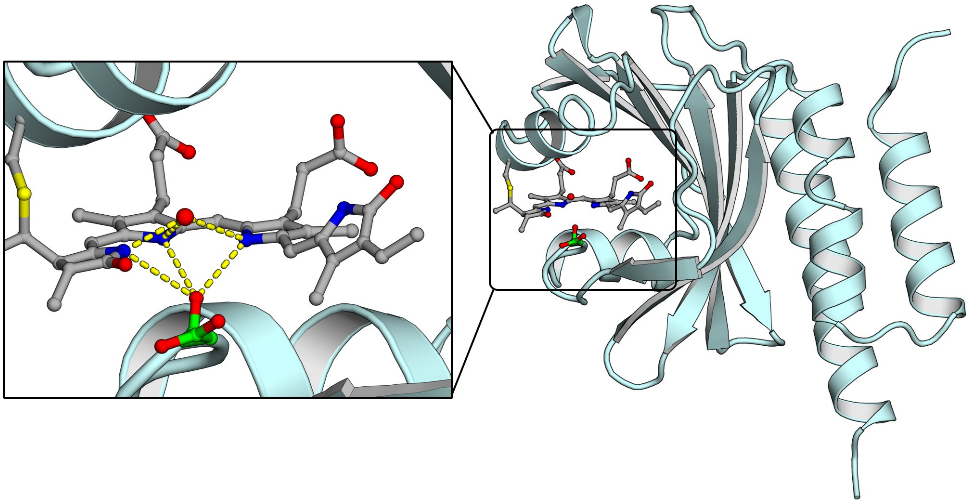

Figure 2.46. (A) All2699g1 protein structure in the Pr form. Zoom: The chromophore binding pocket. The PCB chromophore and the interactions with the pyrrole water as well as the Asp87.

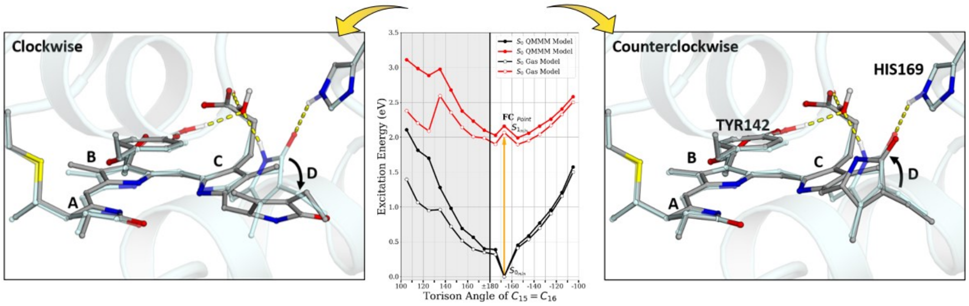

Figure 2.47. Relaxed scan along the torsion angle C14-C15=C16-C17 of the PCB chromophore in the phytochrome All2699g1. Evolution of the ground and excited state is shown in the middle panel. Clockwise (left panel) and counterclockwise (right panel) rotation of the ring D with the amino acids residues in the vicinity. The initial structure is shown in gray (solid structure), while the final point in each sense of rotation is shown in the transparent representation.

was performed in collaboration with Prof. Josef Wachtveitl (Uni Frankfurt, Germany) who performed the complementary time-resolved spectroscopy measurement. The experiment showed an unusually long excited state lifetime (broad lifetime distribution centered at 300 picoseconds). The excited state decay kinetics revealed a strongly distributed character which is imposed by the nonexponential protein dynamics.

Starting from a high-resolution crystal structure we have examined the photoisomerization mechanism of the P_r form by means of hybrid QM/MM simulations. which our simulation have attributed to the interactions between the isomerizing pyrrole ring D and an adjacent conserved Tyr142. Our findings offer a mechanistic insight into how the quantum efficiency of the bilin photoisomerization is tuned by the protein environment, thereby providing a structural framework for engineering bilin-based optical agents for imaging and optogenetics applications. (Figure 2.46B).

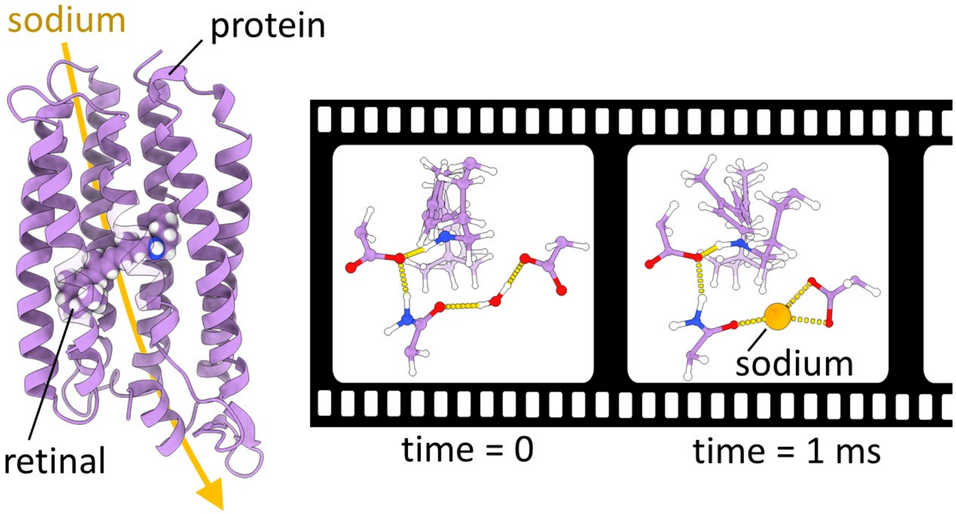

Figure 2.48. Left: The structure of the Krokinobacter eikastus rhodopsin 2. Right: The retinal protonated Schiff base and the counterion complex prior the photoexcitation (time = 0) and 1 ms after the excitation (1 ms).

Resolving the femtosecond to millisecond structural changes in a light-driven sodium pump

Light-driven sodium pumps actively transport small cations across cellular membranes. They are used by microbes to convert light into membrane potential and have become useful optogenetic tools with applications in neuroscience. To understand the mechanism of sodium pumping we studied the Krokinobacter eikastus rhodopsin 2 (KR2) as part of an interdisciplinary consortium that uses TR-SFX. The team of Dr. Jörg Standfuss (Paul Scherrer Institute, Switzerland) has obtained high-resolution snapshots throughout the KR2 photocycle, which visualized sodium translocation over time. The study was augmented by time-resolved spectroscopy in the visible and IR by the group of Prof. Joachim Heberle (FU Berlin). However, in the critical O intermediate, the binding site of the sodium in the vicinity of the retinal was not unambiguously resolved because it is isoelectronic to a water molecule. We have carried out QM/MM simulations to compute the excitation energies with either water or the sodium ion in the structure (Figure 2.48) and found that water would result in a blue shift of the absorption maximum, while the sodium ion will lead to a red shift. Experimental characterization of this intermediate showed a strong red shift, hence, confirming the binding of a sodium ion. These results provide a direct molecular insight into the dynamics of cation transport across biological membranes and the amino acids involved.

Scientific activities

Igor Schapiro's group members

Name	Project	Status	Period
Tal Dogon	Channelrhodopsin	BSc student	since 08.2020
Gil Amoyal	Proteorhodopsin	BSc student	08.2018 - 10.2020
Avishai Barnoy	Cyanobacteriochrome	MSc student	10.2018 - 09.2020
Qays Nesser-Edin	Retinal analogs	MSc student	since 08.2018
Ofer Filiba	Singlet-Triplet Crossing	PhD student	since 09.2019
Aditya Rao	Cyanobacteriochrome	PhD student	since 08.2016
Yigal Lahav	Chlorophyll proteins and spectral lineshapes	PhD student (co-supervised with Dr. Dror Noy)	since 01.2020
Efrat Pahima	Machine Learning for Photochemistry	PhD student	since 07.2020
Veniamin Borin	Bacteriorhodopsin	PostDoc	since 12.2016
Saumik Sen	Proteorhodopsin	PostDoc	since 12.2016
Rajiv K. Kar	Flavin and KR2	PostDoc	03.2017 - 06.2020
Suliman Adam	Membrane proteins	PostDoc	since 07.2018
Christian Wiebeler	Cyanobacteriochrome	PostDoc	02.2017 - 03.2019
Jonathan R. Church	QM/MM sampling	PostDoc	since 09.2019

Igor Schapiro's scientific collaborations

Name	Project	Institution
Wolfgang Gärtner	Cyanobacteriochrome	University of Leipzig, Germany
Josef Wachtveitl	Cyanobacteriochrome	Goethe University Frankfurt, Germany
Dror Noy	Chlorophyll proteins	Migal – Galilee Research Institute, Israel
Sandy Ruhman	Photochemistry	Hebrew University
Joachim Heberle	IR Spectroscopy	Freie Universitaet Berlin, Germany
Dima Gelman	Metal complexes	Hebrew University
Jörg Matysik	Flavin proteins	University of Leipzig, Germany
Jörg Standfuss	Retinal proteins	Paul Scherrer Institute, Switzerland

Igor Schapiro's active grants

Project	Period	Foundation	Total grant in thousands
PhotoMutant	2016-2021	ERC Starting Grant	€1400
Mercator Fellow at the SFB 1078	2017-2020	DFG	€80
Combined computational and experimental protein design for tuning the absorption and emission spectra of biological photoreceptors	2019-2021	Ministry of Science and Technology	₪650
Internationalization Grant	2020	Minerva Foundation	€30
Design Principles in Optogenetics: An Integrated Approach for Discovery, Analysis and Application of Novel Rhodopsins	2020-2023	ISF Center of Excellence	₪1000
Rational Design of peptidomimetics as inhibtors for the main protease of SARS-CoV2	2020-2021	Rothschild Foundation	₪100
Protonation depending photochemistry in rhodopsin and phytochrome photoreceptors	2021-2024	DFG SFB 1078	€120

Conference organization (last 5 years)

2018 Mar 12-15	Jerusalem Nonadiabatica (co-organized with Roi Baer)
2018 Oct 30-31	Joint Jerusalem-Vienna Workshop (co-organized with Roi Baer, E.K.U. Gross and Tamar Stein)
2019 Feb 12-13	Chairman of the Computational Chemistry Session, 84th ICS Meeting, Tel Aviv, Israel
2019 Sep 03-05	CECAM Workshop "Frontiers in Multiscale Modelling of Photoreceptor Proteins", Tel Aviv, Israel (co-organized with Maria-Andrea Mroginski, TU Berlin, Germany)

Prizes, honors, editorial and review boards etc. (last 5 years)

2015	ERC Starting Grant
2017	DFG Mercator Fellowship at the SFB 1078 Protonation Dynamics in Protein Function, FU Berlin, Germany
2018	Yoram Ben Porath President Prize for Excellence in Research
2019	ACS OpenEye Outstanding Junior Faculty Award in Computational Chemistry

2.12 Tamar Stein

Our research group is focused on developing new methods in quantum chemistry and applying them on various of systems.

Molecular formation in the Interstellar medium (ISM)

The presence and formation of a large variety of organic molecules in the interstellar medium is evident from both astronomical data of absorption and emission bands at different regions of the spectrum. Specifically, polycyclic aromatic hydrocarbons (PAHs) are ubiquitous in the interstellar medium (ISM). The mechanism for their formation in ISM's low temperature environment is, as of yet, a mystery nonetheless. Understanding the mechanism of formation of complex molecules such as PAHs and nitrogen–based PAHs (PANH) in the ISM is a long–standing challenge which has been drawing a growing attention for the past several decades. Quantum chemistry can play an essential role in the study of astrochemical reactions. Our calculations reveal the potential importance van der Waals clusters in the formation and growth of molecular species. The potential for different chemical reactions to occur within a cluster environment arises from the fact that such processes can take place at low temperatures after ionization process take place, as upon ionization the systems pose large amounts of energy. The process is demonstrated schematically on Fig. 2.49. Moreover, the spectator molecules in the cluster can provide a dissipation route for energy by detachment from the cluster, thus the system can stabilize efficiently even at low densities. The spectator molecules can also change the potential energy surface; by which it will pose a catalytic effect for certain reactions. *Ab initio* molecular dynamics (AIMD) simulations and density functional theory (DFT) computations the demonstrate the possibility of bond formation and molecular growth upon ionization of Van der Waals clusters of pure HCN clusters, and mixed clusters of HCN and HCCH, both of which are widespread in the interstellar medium. The results show, that upon ionization of the pure HCN clusters, strongly bound stable structures are formed that contain $N \cdots H$ bonds, and growth beyond pairwise HCN molecules is seen only in a small percentage of cases. In contrast, mixed clusters, where HCCH is preferentially ionized over HCN, can grow up to 3 or 4 units long with new carbon-carbon and carbon-nitrogen covalent bonds.

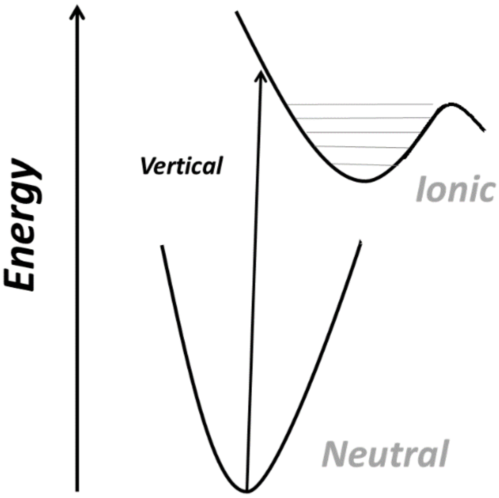

Figure 2.49. Schematic representation of the ionization process of the cluster. After the ionization, the cluster has large amount of energy to dissipate.

Moreover, cyclic molecules formed, such as the radical cation of pyridine, which is a prebiotic molecule. The results are significant as they provide a feasible pathway for molecular growth of small organic molecules containing both carbon and nitrogen in cold and relatively denser environments such as in dense molecular clouds but closer to the photo-dissociation regions, and protoplanetary disks. In the mechanism we propose, first, a neutral van der Waals cluster is formed. Once the cluster is formed it can undergo photoionization which leads to chemical reactivity without any reaction barrier.

Neural Network as a tool for studying larger clusters

To expand the AIMD simulation capabilities, we plan to develop Machine Learning (ML) algorithms based on neural networks (NN). Once set, the usage of potential energy surface based on NN will make the study of large clusters feasible. While maintaining the ab-initio accuracy, the computational cost of performing MD simulations will be considerably reduced, enabling us to thoroughly study the systems of interest, preforming large statistics and extending simulation time. The hard part, which is the bottle neck of the process, is training the model, a process which can last several months and require preforming a large amount of ab-initio calculations in order to adequately train the model. As our goal is to preform AIMD simulations, we will train the model

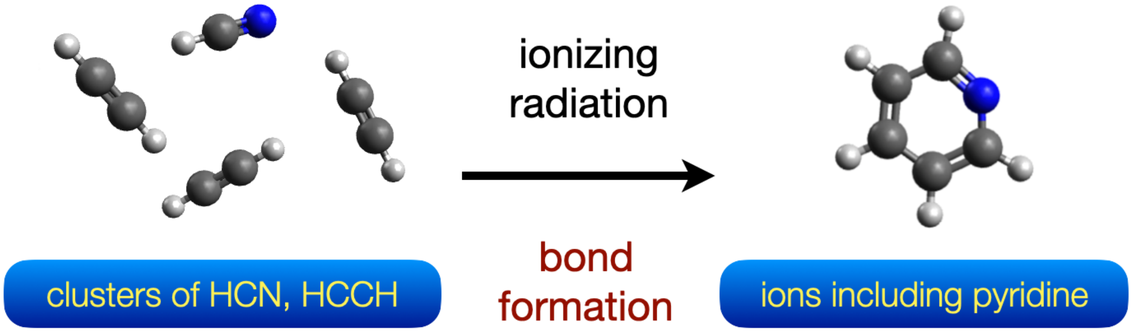

to accurately provide energies and forces, which are needed for the performance of AIMD. While training the model, one needs to use proper input coordinates in which the energy is rotationally and translationally invariant. Moreover, it should be invariant with respect to the indexing of the atoms, we are currently working on representation of the molecular systems so that it would be unique.

Scientific Activities

Tamar Stein group members

Name	Project	Status	Period
Dr. Estefania Rossich Molina	Machine Learning in Quantum Chemistry	PostDoc	since 09.2019
Alon Zamir	Quantum Chemistry	Undergraduate Student	since 07.2020
Aref Agbaria	Quantum Chemistry	Undergraduate Student	since 07.2020

Tamar Stein active grants

Project	Period	Foundation	Total grant in thousands
Molecular Formation upon Ionization of van der Waals Clusters and Implication to Astrochemistry	2020-2024	ISF	₪920
Development of machine learning methods for the field of quantum chemistry	2020	ISF Equipment	₪440

Conference organization (last 5 years

2020 Feb 18-19	The 85th Annual Meeting of the Israel Chemical Society, organized the Theoretical Chemistry session
2019 Oct 30-31	Co-organized joint workshop between the Hebrew University of Jerusalem and the University of Vienna. “Novel Approaches in Computational Photobiology”

Prizes, honors, editorial and review boards etc. (last 5 years)

2018-19	Golda Meir Fellowship

2.13 Raam Uzdin

My research combines foundation research of the interplay between thermodynamics and quantum theory with experiment and application to modern quantum setups such as cold atoms ion trap and superconducting circuits. Below are the three main branches in my research.

Exploiting thermodynamics for diagnostics of quantum circuits and quantum processors

Quantum computers and simulators aim to execute task that cannot be carried out on a classical computer. If the output of these devices is unknown how can we verify that it is working properly? One of the main problems in these devices is the fact that they are not perfectly isolated from the environment but this is very difficult to detect and quantify if the desired output is not known. We develop a novel approach based on repeating the operation or calculation many times sequentially. That is, take the output and feed it back to the device as input. Using thermodynamic tools we currently develop, we reach a good detection capability of interaction with some external environment. Our long-term goal is to develop this approach into a full fledged operational diagnostic tool that can also differentiate between different types of malfunctions. This research is a combination of foundation and practical aspects of realistic systems such as superconducting circuits, ion traps, Rydberg atoms and more.

High resolution quantum thermodynamics

Remarkably, under a few simple assumptions it can be shown that thermodynamics holds for the smallest conceivable systems - even just a few ions in trap that are well isolated from the rest of the world. The problem is that the second law of thermodynamics deals only with coarse-grained quantities such as entropy, average energy, and heat. In modern microscopic quantum setups (e.g. ion traps & superconducting circuits) it is possible to measure fine-grained (high resolution) quantities such as the population of a specific energy level in a specific particle. The tools I develop aim to find thermodynamic limitations on quantum processes involving fine-grained measurable quantities. The kinship between chemical reactions, and their rate equation to quantum dynamics of small system will be used to map my future findings on high resolution thermodynamics to chemistry.

Quantum effects in the thermodynamics of small systems

Although the underlying dynamics of any physical system is quantum (to the best of our knowledge), it turns out that even when very small number of particles are involved it is hard to find thermodynamic effects that cannot be explained with classical rate equations. My goal is to discover and understand such effect in various experimentally relevant setups. Some of my finding have already published and become standard reference in this research venue.

Research Activities

Completed projects:

Passivity deformation and the removal of thermodynamic obstacles in the microscopic realms

Shortly before joining HUJI, I have formulated a new approach to microscopic thermodynamics based on a new principle called “global passivity”(Uzdin, Levy, and Kosloff 2015). In the past, standard passivity was used in a rather limited way in thermodynamics. However, I discovered that by using passivity in a different way and applying it to new thermodynamic quantities (instead of work), remarkable results are obtained. As it turns out, the global passivity framework, inherits many of the limitations of the other existing frameworks. For example, thermodynamics produces trivial and useless predictions when one of the subsystems approaches zero temperature. In the last two years we have develop new framework called passivity deformation. Remarkably, it simultaneously resolves several issues that takes place in small microscopic systems. We have recently experimentally demonstrated (Henao, Uzdin, and Katz 2020) that this framework can assist improve heat leak detection in quantum circuits.

Catalytic quantum circuits

As in chemistry, in quantum information processing it is possible to use external object (a catalyst) that will enable to do tasks that are otherwise impossible. Crucially, this object returns to its initial state at the end of the process and therefore can be used again and perform as a catalyst. Although there are some theorems on the existence of catalytic transformations under certain assumptions, the actual protocol for carrying out these transformations is unknown. We develop a methodology (Henao and Uzdin 2020) for constructing them in a systematic way and understand the limitations in exploiting them. In particular we demonstrate catalytic cooling, i.e. cooling that cannot take place without the right catalyst. We also applied this approach to quantum metrology and showed that our catalytic protocols can enhance measurement sensitivity (e.g. sensitivity in temperature measurements).

Experimental Observation of quantum effects in microscopic heat machines

In (Uzdin, Levy, and Kosloff 2015) together with Amikam Levy and Ronnie Kosloff we predicted a several quantum effect in the operation microscopic heat engines. These effect arise due to superposition states in the engine’s energy levels (working fluid). I collaborated with Eilon Poem (then at Oxford) and other people from the Ian Walmsley group do design to an experiment in NV centers in diamonds. After intense two year we manage to come with a clean experimental observation of quantum effects in heat engines (Klatzow et al. 2019). This was the first observation of this kind.

Other completed project

In (Uzdin, Gasparinetti, et al. 2018) we showed how externally pumped decoherence can induce markovian dynamics when the environment is microscopic (e.g. just two spins). In (Perarnau-Llobet and Uzdin 2019) we shown that collective operations of work extraction units can help in work extraction and reduce the work fluctuation compared to using many smaller independent work extraction units.

References

Henao, Ivan and Raam Uzdin (2020). “Catalytic transformations with finite-size environments: applications to cooling and thermometry”. In: arXiv: `2010.09070 [quant-ph]`.

Henao, Ivan, Raam Uzdin, and Nadav Katz (2020). “Experimental detection of microscopic environments using thermodynamic observables”. In: arXiv: `1908.08968 [quant-ph]`.

Klatzow, James et al. (Mar. 2019). “Experimental Demonstration of Quantum Effects in the Operation of Microscopic Heat Engines”. In: *Physical Review Letters* 122.11. DOI: `10.1103/physrevlett.122.110601`.

Perarnau-Llobet, Martí and Raam Uzdin (Aug. 2019). “Collective operations can extremely reduce work fluctuations”. In: *New Journal of Physics* 21.8, p. 083023. DOI: `10.1088/1367-2630/ab36a9`.

Uzdin, Raam, Simone Gasparinetti, et al. (June 2018). “Markovian heat sources with the smallest heat capacity”. In: *New Journal of Physics* 20.6, p. 063030. DOI: `10.1088/1367-2630/aac932`.

Uzdin, Raam, Amikam Levy, and Ronnie Kosloff (Sept. 2015). “Equivalence of Quantum Heat Machines, and Quantum-Thermodynamic Signatures”. In: *Physical Review X* 5.3. DOI: `10.1103/physrevx.5.031044`.

Uzdin, Raam and Saar Rahav (2019). “The Passivity Deformation Approach for the Thermodynamics of Isolated Quantum Setups”. In: arXiv: `1912.07922 [quant-ph]`.

Scientific activities

Raam Uzdin group members

Name	Project	Status	Presently at
Tanmoy Pandit	Thermodynamic constraint on periodically driven system	PhD student	since October 2019
Ivan Henao	Catalytic quantum circuits	Postdoc	since July 2019

Raam Uzdin scientific collaborations

Name	Project	Institution
Prof. Nadav Katz	Heat leak detection in the IBM quantum processors	The Hebrew University of Jerusalem, Israel
Prof. Saar Rahav	Passivity deformation	Technion, Israel
Dr Simone Gasparinetti	Engineered environments in superconducting circuits	Chalmers University, Sweden
Prof. Roee Ozeri	Smallest markovian environments	Weizmann Institute, Israel
Prof. Ferdinand Schimdt Kaler and Dr. Ulrich Poschinger	Heat leak detection in ion trap	Mainz University, Germany
Dr. Marti Perarnau	Collective work extraction	Max Planck Institute of Quantum Optics, Germany

Raam Uzdin active grants

Project	Period	Foundation	Total grant in thousands
Boosting the thermodynamic predictive power in microscopic quantum devices	2020-2023	ISF	301€

Prizes, honors, editorial and review boards etc. (last 5 years)

Topical Editor in "Entropy" Journal

2.14 Assaf Zemel

Research Activities

Our laboratory is focused on understanding the mechanisms by which living cells sense and respond to physical properties of their environment. To sense local cues such as the rigidity and topography of the environment, cells exploit molecular motors to actively pull on their environment. In addition, molecular motor forces are used to organize the cells' cytoskeleton, to establish their morphology, and to drive growth. Below, I outline results from two studies that we've been concerned with in the past two years. One, published in (M. A. Jakobs, Franze, and Assaf Zemel 2020), pertains to the growth and maturation of neural cell processes, the other, not yet published and will be discussed briefly, to the role of cellular forces in cellular self-assembly.

Mechanical model of neuron polarization and growth

A fundamental question of neurobiology is how the distinctive polarity profile of the microtubule array in neuronal cell projections, axons and dendrites (often termed neurites), establishes. Axons and dendrites are the mature projections of neurons that transmit and receive information in the form of electrical signals. In contrast to dendrites, which remain short ($\approx 100\mu m$) and highly branched, axons may grow $mm - m$ long to reach their target site(s). Neurites comprise a densely packed microtubule (MT) cytoskeleton that functions as a substrate for the transport of proteins, organelles, and RNA by molecular motors (Kapitein and Hoogenraad 2015). The MTs are polar filaments and their polarity is recognized by distinct molecular motors that preferentially move along one direction on the filament. While in axons, most MTs orient uniformly with their plus-ends away from the cell body, in dendrites, this structural organization is not conserved and is often (e.g., in vertebrates) found to be locally mixed. Apart from serving as tracks for directed molecular transport, the MT cytoskeleton plays part in generating pushing forces that drive neurite outgrowth. This occurs via the interaction of the MTs with molecular motors (of the dynein and kinesin families), which slide the MTs along the membrane or past each other, to eventually extend the MT cytoskeleton forward (Rao et al. 2017). An important aspect of the molecular motors' directional gliding on the filaments, is that the forces they apply lead to filament sorting. The minus-end directed motor dynein, has been suggested to sort neuronal MTs by sliding plus-end-out MTs away from the cell body and minus-end-out MTs back into the cell body, thereby establishing the observed uniform MT polarity of the axon (Tanenbaum, Vale, and McKenney 2013; Castillo et al. 2015; Rao et al. 2017). In contrast, attenuated dynein activity, and/or enhanced kinesin activity have been proposed to explain the mixed MT polarity of vertebrate dendrites (Sharp, Yu, and Baas 1995; Castillo et al. 2015; Rao et al. 2017; Oelz et al. 2018). The molecular motor-generated forces that push the MTs towards the neurite tip are opposed by an actively generated load arising from the actomyosin cytoskeleton that envelops the MTs (see Fig.2.50) (Ahmad et al. 2000; Kapitein and Hoogenraad 2015).

We here studied the dynamics and mechanics of neural growth by simulating bundles of MTs that are cross-linked by ensembles of molecular motors and acted upon collectively by an opposing load (see Fig. 2.50); the algorithm is described in detail in (M. Jakobs, Franze, and Assaf Zemel 2015; M. A. Jakobs, Franze, and Assaf Zemel 2020). We identified two important factors that enter the force balance calculation and govern the structural and growth characteristics of the bundles: (i) the level of MT connectivity by motors (governed by χ below), and (ii) the load acting on the bundle as a whole (Fig. 2.50). The results are summarized in Fig. 2.51. Bundles subjected to

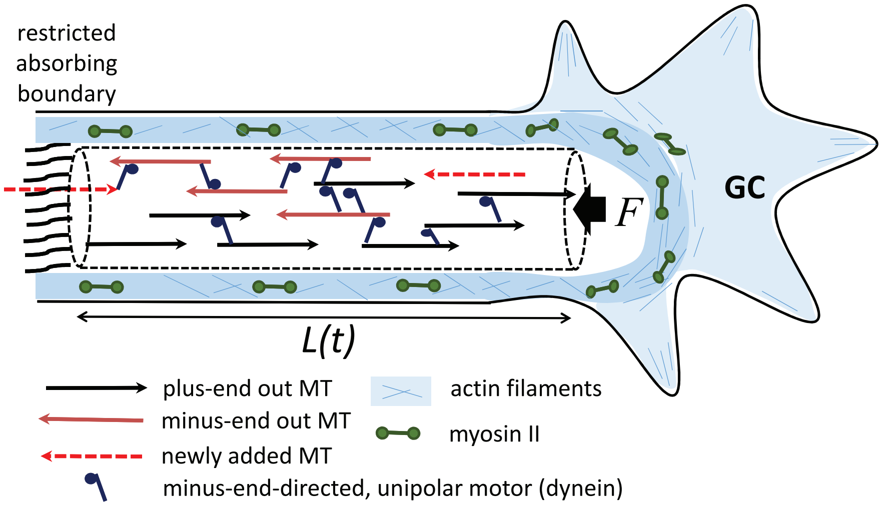

Figure 2.50. Schematic illustration of major elements considered in our model. On the left is the neurite shaft comprising the cross-linked MT bundle that expands as dynein molecular motors slide the filaments. MTs reaching the left boundary get absorbed into the cell body with some probability which accounts for the restricted permeability of the entangled meshwork of filaments at neurite entry. The MT bundle is subjected to a restoring load F on the right boundary arising from the actomyosin cytoskeleton enveloping the MTs (Mutalik et al. 2018). New MTs (dashed arrows) of either polarity enter (or polymerize at) arbitrary points in the bundle at a given frequency. Adjacent MTs may or may not be cross-linked by motors. The probability that an overlapping region between adjacent MTs be cross-linked by motors is given by χ.

stronger loads are shown to require more filaments in a cross-section to overcome the load and thus become wider and extend more slowly (panel 2A). With a higher level of motor connectivity between the filaments, the bundles narrow in cross-section (panel 2B) and grow more quickly (panel 2C) while the MTs efficiently sort to form extended, thin and uniformly-polarized bundles (panel 2E), as found in axons (Tanenbaum, Vale, and McKenney 2013; Castillo et al. 2015; Rao et al. 2017). In contrast, loosely connected bundles fail to organize and expand against a load (panel 2C, 2E), and result in short, wide and locally mixed bundles, as found in vertebrate dendrites (Baas, Black, and Banker 1989; Yau et al. 2016). We have also shown that the load may play a role in clearing the neurite entry from "ill" oriented minus-end-out MTs that accumulate in that region due to their retrograde transport along the neurite shaft (see the polarity at low x in panel 2D). These results shed important light on the mechanical mechanism that may underly the establishment of cytoskeleton polarity in emerging axons and dendrites during neuron development and regeneration.

Role of substrate rigidity in cellular self-assembly

Cell adhesion to the extracellular matrix is commonly accompanied by an active generation of elastic stresses in the cells' cytoskeleton. These stresses not only acquire the cells with a mechanism of sensing their mechanical environment, but, provided the environment is sufficiently soft, they may also affect other cells and thus give rise to elastic interactions among the cells (A. Zemel, De, and Safran 2011). Fig. 2.52, taken from Ref. (Califano and Reinhart-King 2008), illustrates the effect of substrate rigidity on the spontaneous distribution of endothelial cells. While on the more rigid substrates (lower panels) the cells are seen to uniformly disperse, on the soft substrates they self-assemble into premature network structures. A simple elastic calculation shows that the elastic interaction between two round cells that isotropically pull on the substrate is attractive (Bischofs and Schwarz 2003). Inspired by these results we hypothesized that the substrate mediates an attractive elastic interaction among the cells that drives cellular self-assembly on the substrates.

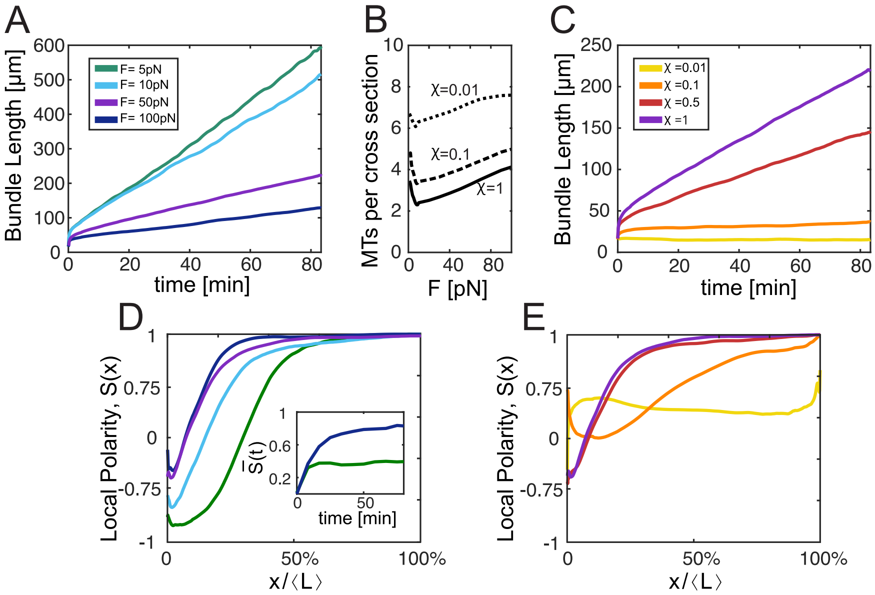

Figure 2.51. The effects of F and χ on bundle growth and polarity. (A) and (C) show the evolution of bundle length for varying levels of F and χ, respectively; green to blue correspond to $F = 5, 10, 50, 100$pN with $\chi = 1$; yellow to purple correspond to $\chi = 0.01, 0.1, 0.5, 1$ with $F = 50$pN. (B) shows the effect of the load on mean number of MTs per cross-section for varying levels of χ. The load on the bundle dictates its width and thereby its growth speed. (D) and (E) show the effects of F and χ on the scaled MT polarity profile $S(x) = (n_R(x) - n_L(x))/(n_R(x) + n_L(x))$ at $t = 80$ min, where n_R and n_L are the local number of MTs pointing with their plus-ends towards the neurite tip; color coding is as in (A) and (C); the inset in (D) shows that the length-averaged order parameter, $\bar{S}(t)$, stabilizes within ≈ 10 min. The load on the bundle restrains growth and biases the polarity profile at the neurite entry. Highly interconnected MT-bundles (large χ) more quickly expand (taper) and polarize under load, while loosely connected bundles fail to grow and remain short, wide, and mixed.

To examine this hypothesis quantitatively, we have developed a statistical mechanics mean-field theory to predict the phase behavior of cells as a function of the substrate rigidity and plating cell density. Fig. 2.53 shows a phase diagram in the substrate rigidity / cell density parameter space. The different curves are drawn for different values of an intrinsic cellular factor, ϵ_{cell}/T, which depends on the magnitude of cellular forces, the mean rigidity of the cells, their radius, and an effective temperature T which modulates the tendency of cells to disperse on the substrate. The region enclosed in each curve reflects a regime where the cells are predicted to phase separate into two coexisting, high and low density phases. For a given value of the interaction strength, ϵ_{cell}/T (which may correspond to a particular cell type), the theory predicts two critical substrate rigidities, E_s^c, below and beyond which the cells will undergo a first-order phase transition. Moreover, the theory predicts the minimum density (the lower half of the curves) required to drive cellular self-association. These and more detailed analysis of the theory will be published in a forthcoming paper.

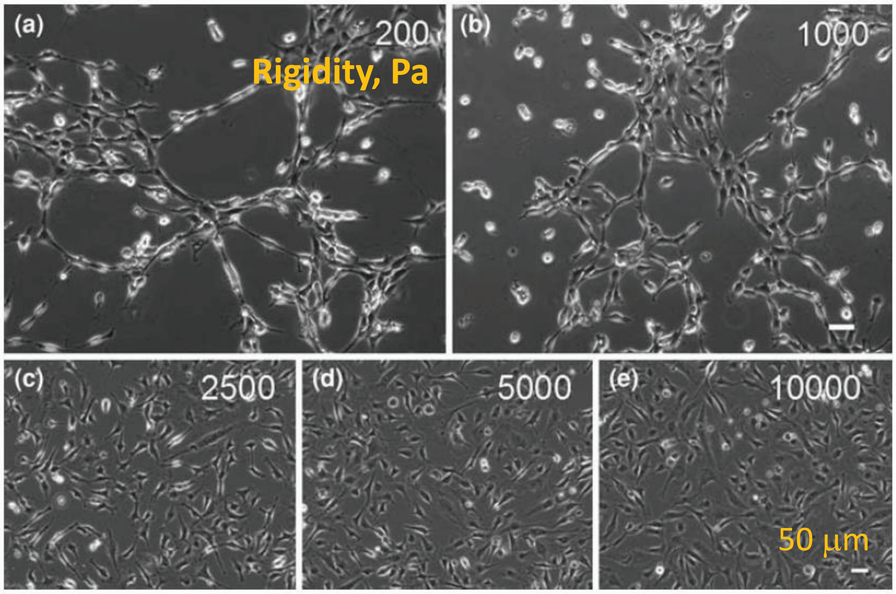

Figure 2.52. Effect of substrate rigidity on self-assembly of endothelial cells; the images are copied from Califano et al. (Califano and Reinhart-King 2008). The experiments were preformed on linearly elastic, fibronectin-coated polyacrylamid gels of varying rigidities. While on the more rigid substrates the cells uniformly disperse, on the softer ones they tend to cluster into small, premature network structures.

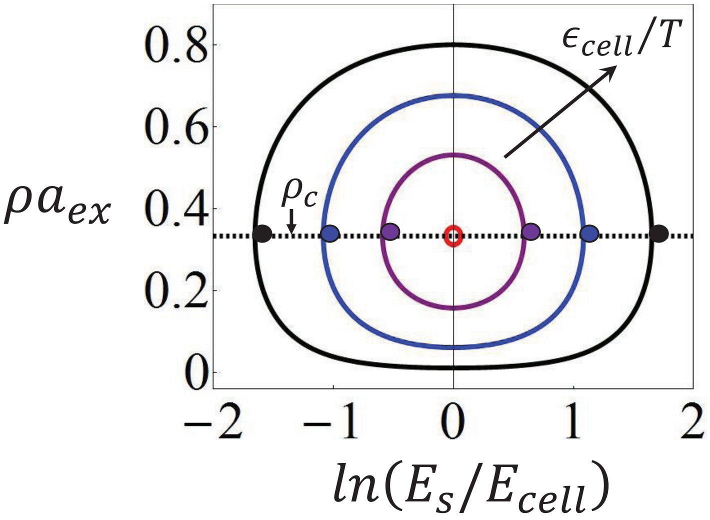

Figure 2.53. Calculated phase diagram illustrating how substrate rigidity E_s and mean cell density ρ may govern the tendency of cells to self-associate; a_{ex} is the excluded area per cell. The colored curves correspond to increasing values of the interaction strength parameter ϵ_{cell}/T, where $\epsilon_{cell} \sim P^2/(R^3_{cell}E_{cell})$ depends on the magnitude of cellular dipolar forces P, the cells' radius R_{cell} and their mean rigidity, E_{cell}; T signifies an effective temperature. The region enclosed by each curve corresponds to systems with coexisting high-density and low-density cell phases. The higher the interaction strength-parameter, ϵ_{cell}/T, the broader the interaction zone in parameter space.

References

Ahmad, Fridoon J et al. (2000). “Motor proteins regulate force interactions between microtubules and microfilaments in the axon”. In: *Nature cell biology* 2.5, pp. 276–280.

Baas, Peter W, Mark M Black, and Gary A Banker (1989). “Changes in microtubule polarity orientation during the development of hippocampal neurons in culture.” In: *The Journal of cell biology* 109.6, pp. 3085–3094.

Bischofs, I. B. and U. S. Schwarz (2003). “Cell organization in soft media due to active mechanosensing”. In: *Proc. Natl. Acad. Sci.* 100.16, pp. 9274–9279.

Califano, J.P. and C.A. Reinhart-King (2008). “A balance of substrate mechanics and matrix chemistry regulates endothelial cell network assembly”. In: *Cell. Mol. Bioengineering* 1.2, pp. 122–132.

Castillo, Urko del et al. (2015). “Interplay between kinesin-1 and cortical dynein during axonal outgrowth and microtubule organization in Drosophila neurons”. In: *eLife* 4, e10140.

Jakobs, Maximilian, Kristian Franze, and Assaf Zemel (2015). “Force Generation by Molecular-Motor-Powered Microtubule Bundles; Implications for Neuronal Polarization and Growth.” In: *Frontiers in cellular neuroscience* 9, p. 441.

Jakobs, Maximilian AH, Kristian Franze, and Assaf Zemel (2020). “Mechanical Regulation of Neurite Polarization and Growth: A Computational Study”. In: *Biophysical Journal* 118.8, pp. 1914–1920.

Kapitein, Lukas C and Casper C Hoogenraad (2015). “Building the Neuronal Microtubule Cytoskeleton”. In: *Neuron* 87.3, pp. 492–506.

Mutalik, Sampada P et al. (2018). “Cytoskeletal mechanisms of axonal contractility”. In: *Biophysical journal* 115.4, pp. 713–724.

Oelz, Dietmar B. et al. (2018). “Microtubule Dynamics, Kinesin-1 Sliding, and Dynein Action Drive Growth of Cell Processes”. In: *Biophysical Journal* 115.8, pp. 1614–1624.

Rao, Anand N et al. (2017). “Cytoplasmic dynein transports axonal microtubules in a polarity-sorting manner”. In: *Cell reports* 19.11, pp. 2210–2219.

Sharp, David J, Wenqian Yu, and Peter W Baas (1995). “Transport of dendritic microtubules establishes their nonuniform polarity orientation.” In: *The Journal of Cell Biology* 130.1, pp. 93–103.

Tanenbaum, Marvin E, Ronald D Vale, and Richard J McKenney (2013). “Cytoplasmic dynein crosslinks and slides anti-parallel microtubules using its two motor domains.” In: *eLife* 2, e00943.

Yau, Kah Wai et al. (2016). “Dendrites In Vitro and In Vivo Contain Microtubules of Opposite Polarity and Axon Formation Correlates with Uniform Plus-End-Out Microtubule Orientation.” In: *The Journal of neuroscience : the official journal of the Society for Neuroscience* 36.4, pp. 1071–1085.

Zemel, A., R. De, and S.A. Safran (2011). “Mechanical consequences of cellular force generation”. In: *Curr. Opin. Solid State Mat. Sci.*

Scientific activities

Assaf Zemel group members

Name	Project	Status	Presently at
Sravya Pamula	Cell shape and motility	PhD student	since October 2020

Assaf Zemel scientific collaborations

Name	Project	Institution
Maximilian Jakobs	Mechanics of neuron growth	Cambridge University UK
Kristian Franze	Mechanics of neuron growth, cell-cell elastic interactions	Friedrich-Alexander-Universität Erlangen-Nürnberg, Germany and Cambridge University, UK
Florian Rehfeldt	Cell polarization and shape acquisition	University of Bayreuth, Germany
Sarah Koester	Mechano-sensitivity and spreading of blood platelets	George-August-University, Göttingen, Germany
Thorsten Auth	Active shape acquisition of cells	Jülich, Germany

Conference organization (last 5 years)

2018 May 28	Symposium on Neuron Mechanics and Growth, Hebrew University
2021/22	EMBO Workshop Physics of cells: PhysCell2021

Chapter 3

Status of the center

3.1 Personnel

There are currently 14 groups in the center, headed by faculty members. In the reported time period 93 scientists have been active in the Center (see Table 3.1), including faculty members (14), non-faculty staff (6) long-term visitors (6), post-doctoral fellows (18) graduate students (M.Sc./Ph.D.) (44) and undergrads (6). Two systems managers Dr. Ester Livshits and Dr. Hadassah Elgavi are responsible for the maintenance and development of the diverse computing facilities of the Center and those of its members. Finally administrative and secretariat services help manage the workforce, budget, guests, and visits to the center.

Table 3.1: Personnel of the Fritz Haber center, 2019-2020

Role	Name
Members (14)	Prof. Noam Agmon, Prof. Roi Baer, Prof. Avinoam Ben–Shaul, Dr. Snir Gazit, Prof. Robert B. Gerber, Prof. Eberhard K. U. Gross, Prof. Daniel Harries, Prof. Ronnie Kosloff, Dr. Eli Kraisler, Prof. Raphael D. Levine, Prof. Masha Niv, Prof. Igor Schapiro, Dr. Tamar Stein, Dr. Raam Uzdin, Prof. Assaf Zemel
Non faculty research staff (6)	Dr. Faina Dubnikov, Dr. Helen Eisenberg, Dr. Hadassah Elgavi, Dr. Esther Livshits, Prof. Vladimir Nazarov, Dr. Ryan Requist
Long term visitors (6)	Prof. D. Neuhauser (UCLA), Prof. F. Remacle (Liege), Prof. A.Dell –Hammerich (Illinois), Dr. G. Katz, Dr. S. Kallush (Ort Braude), Dr. N. Rom (Rafael)
Postdocs (18)	Dr. Veniamin A. Borin, Dr. Saumik Sen, Dr. Florian Habecker , Dr. Rajiv Kumar Kar, Dr. Laura McCaslin , Dr. Estefania Rossich Molina, Dr. Suliman Adam, Dr. Ido schaefer, Dr. Ivan Henao, Dr. Martina Costa Reis, Dr. Chen Li, Dr. Camilla Pellegrini , Dr. Andrea Muolo , Dr. Jonathan Richard Church , Dr. Marcel Fabian , Dr. Yael Cytter , Dr. Fabrizio Fierro

Role	Name
Graduate Student (MSc/PhD) (44)	Michelle Dvoris, Lior Sagiv, Eitam Arnon, Lisa Moses George, Ofer Filiba, Ilan Shumilin, Roy Noff, Ben Shpiro, Itay Zackay, Efrat Hadad, Aditya G. Rao, Swetha Vasudevan, Aviv Aroch, Roi Dan, ksenia Komarova, Stanislav Zelner, Bar Ezra, Tanmoy Pandit , Chung-Yu Wang, Efrat Pahima , Michal Zimmerman, Nitzan Dubovski, Natalie Ben Abu, Yaron Ben Shoshan Galeczki, Lior Peri, Eitan Margulis, Itay Schachter, Sharon Lavie, Yuri Shakhman, Gal Shkolnik, Elyasaf Cohen, Ayush De, Yigal Lahav, Kays Nassereddin, Avishai Bar-Noy, Oren Lichtenstien, Sayak Adhhikari, Uriel Shafir, Gil Olgenblum, Hadar Klein, Kim Asseo, Dor Markus, Tomer Green, Hodaya Karby
Undergrad Students (BSc) (6)	Nathan Rahat, Shai Kauffman, Gil Amoyal, Alon Zamir, Amon Himmelman, Tal Dogon
Administrative personnel	Ms. Geula Levy
Computing services and consulting (2)	Dr. Ester Livhshits, Dr. Hadassah Elgavi

3.2 Computer center resources

The computer facility of the Center is the principal research tool of all scientists in the center. Most of the computers are purchased by the different researchers from their personal grants. The center offers to the researchers the services of System Managers Drs. Ester Livshits and Hadassah Elgavi, responsible for the maintenance and development of our computer services, which include both equipment of the center, and machines used by individual groups.

An overview of the compute nodes is listed in Table 3.2 according to the type of processor. The servers of the FHRC computer center are physically located in two server rooms. The main room is in the Ross Building 201 while the second is in Aronberg 18.

Table 3.2: High-performance computing cluster.

Processor Type	Number of nodes
Intel	390
AMD	70
Nvidia GPU	6

3.3 Fiscal report and proposed budget

Last year's expenses used ca 2% more funds than planned for salaries and ca 20% more for equipment. Since the sums are small such fluctuations are not unusual. The funds were taken from the exchange of scientists budget, which was not used due to the pandemic.

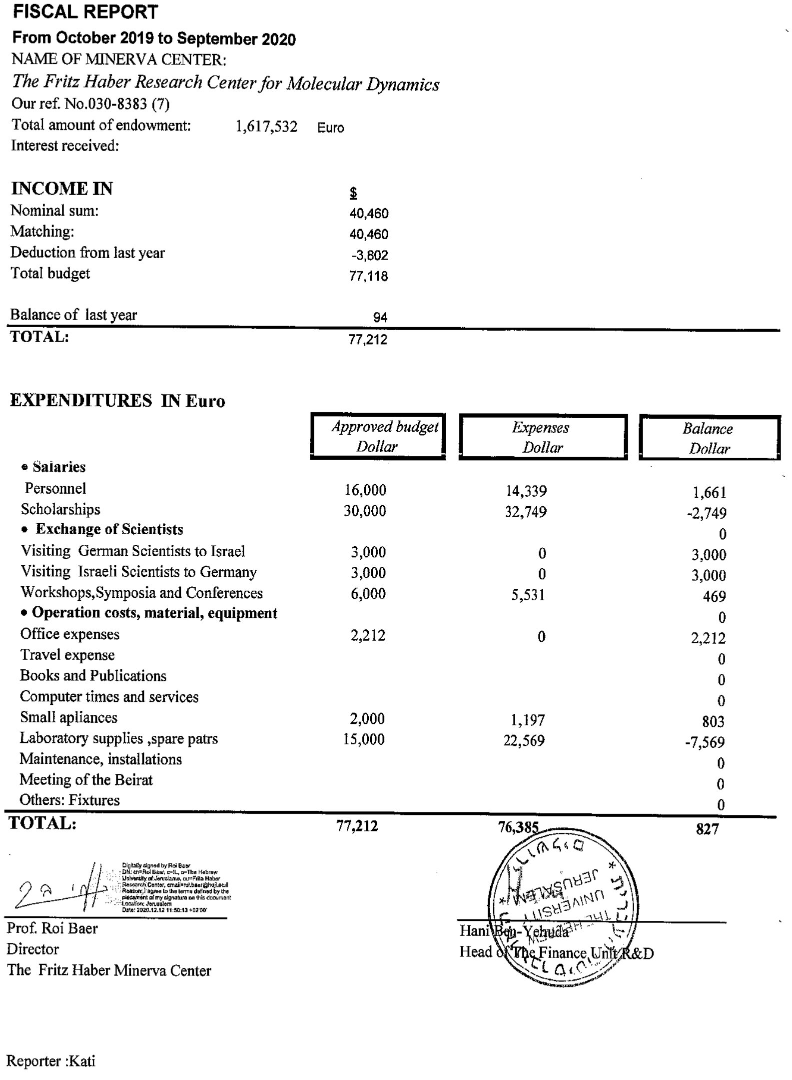

FISCAL REPORT

From October 2019 to September 2020

NAME OF MINERVA CENTER:

The Fritz Haber Research Center for Molecular Dynamics

Our ref. No.030-8383 (7)

Total amount of endowment: 1,617,532 Euro

Interest received:

INCOME IN	**$**
Nominal sum:	40,460
Matching:	40,460
Deduction from last year	-3,802
Total budget	77,118
Balance of last year	94
TOTAL:	77,212

EXPENDITURES IN Euro

	Approved budget Dollar	*Expenses Dollar*	*Balance Dollar*
• **Salaries**			
Personnel	16,000	14,339	1,661
Scholarships	30,000	32,749	-2,749
• **Exchange of Scientists**			0
Visiting German Scientists to Israel	3,000	0	3,000
Visiting Israeli Scientists to Germany	3,000	0	3,000
Workshops,Symposia and Conferences	6,000	5,531	469
• **Operation costs, material, equipment**			0
Office expenses	2,212	0	2,212
Travel expense			0
Books and Publications			0
Computer times and services			0
Small apliances	2,000	1,197	803
Laboratory supplies ,spare patrs	15,000	22,569	-7,569
Maintenance, installations			0
Meeting of the Beirat			0
Others: Fixtures			0
TOTAL:	**77,212**	**76,385**	**827**

Digitally signed by Roi Baer
DN: cn=Roi Baer, c=IL, o=The Hebrew University of Jerusalame, ou=Fritz Haber Research Center, email=roi.baer@huji.ac.il
Reason: I agree to the terms defined by the placement of my signature on this document
Location: Jerusalem
Date: 2020.12.12 11:50:13 +02'00'

Prof. Roi Baer
Director
The Fritz Haber Minerva Center

Hani Ben-Yehuda
Head of The Finance Unit R&D

Reporter :Kati

3.4 Proposed Budget for 2020-21

The proposed budget is similar to the from the last reporting period. The main expense is salaries and scholarships while less is devoted to exchange of scientists. A sum of 15,000 Euros will fund laboratory supplies and spare parts.

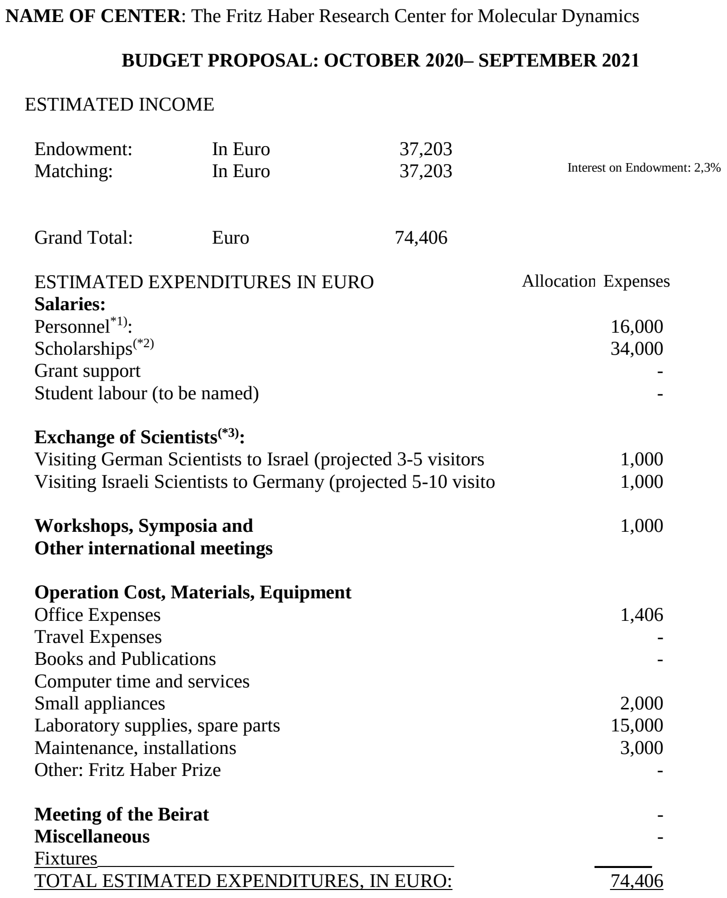

NAME OF CENTER: The Fritz Haber Research Center for Molecular Dynamics

BUDGET PROPOSAL: OCTOBER 2020– SEPTEMBER 2021

ESTIMATED INCOME

Endowment:	In Euro	37,203	
Matching:	In Euro	37,203	Interest on Endowment: 2,3%
Grand Total:	Euro	74,406	

ESTIMATED EXPENDITURES IN EURO	Allocation	Expenses
Salaries:		
Personnel[*1)]:		16,000
Scholarships(*2)		34,000
Grant support		-
Student labour (to be named)		-
Exchange of Scientists(*3):		
Visiting German Scientists to Israel (projected 3-5 visitors		1,000
Visiting Israeli Scientists to Germany (projected 5-10 visito		1,000
Workshops, Symposia and Other international meetings		1,000
Operation Cost, Materials, Equipment		
Office Expenses		1,406
Travel Expenses		-
Books and Publications		-
Computer time and services		
Small appliances		2,000
Laboratory supplies, spare parts		15,000
Maintenance, installations		3,000
Other: Fritz Haber Prize		-
Meeting of the Beirat		-
Miscellaneous		-
Fixtures		
TOTAL ESTIMATED EXPENDITURES, IN EURO:		74,406

Appendix A

List of publications during 2019-2020

A.1 Noam Agmon

1. Temperature and Nuclear Quantum Effects on the Stretching Modes of the Water Hexamer , NR Samala, N Agmon, *Journal of Physical Chemistry A*, 124(40), 8201-8208 (2020)
2. Thermally Induced Hydrogen-Bond Rearrangements in Small Water Clusters and the Persistent Water Tetramer , NR Samala, N Agmon, *ACS Omega*, 4(27), 22581-22590 (2019)
3. Temperature Dependence of Intramolecular Vibrational Bands in Small Water Clusters , NR Samala, N Agmon, *Journal of Physical Chemistry B*, 123(44), 9428-9442 (2019)
4. Ionic radii of hydrated sodium cation from QTAIM , JJ Fifen, N Agmon, *Journal of Chemical Physics*, 150(3) (2019)

A.2 Roi Baer

1. Time-resolving the ultrafast H2 roaming chemistry and H3 + formation using extreme-ultraviolet pulses, E Livshits, I Luzon, K Gope, R Baer, D Strasser, *Communications Chemistry*, 3(1) (2020)
2. Absence of Triplets in Single-Photon Double Ionization of Methanol, K Gope, E Livshits, DM Bittner, R Baer, D Strasser, *Journal of Physical Chemistry Letters*, 11(19), 8108-8113 (2020)
3. Range-separated stochastic resolution of identity: Formulation and application to second-order Green"s function theory, W Dou, M Chen, TY Takeshita, R Baer, D Neuhauser, E Rabani, *Journal of Chemical Physics*, 153(7) (2020)
4. Dopant levels in large nanocrystals using stochastic optimally tuned range-separated hybrid density functional theory, AJ Lee, M Chen, W Li, D Neuhauser, R Baer, E Rabani, *Physical Review B*, 102(3) (2020)
5. Linear–Response Time-Dependent Density Functional Theory with Stochastic Range-Separated Hybrids, X Zhang, G Lu, R Baer, E Rabani, D Neuhauser, *Journal of Chemical Theory and Computation*, 16(2), 1064-1072 (2020)
6. Stochastic Resolution of Identity for Real-Time Second-Order Green"s Function: Ionization Potential and Quasi-Particle Spectrum, W Dou, TY Takeshita, M Chen, R Baer, D Neuhauser, E Rabani, *Journal of Chemical Theory and Computation*, 15(12), 6703-6711 (2019)

7. Stochastic embedding DFT: Theory and application to p–nitroaniline in water, W Li, M Chen, E Rabani, R Baer, D Neuhauser, *Journal of Chemical Physics*, 151(17) (2019)
8. Stochastic density functional theory, MD Fabian, B Shpiro, E Rabani, D Neuhauser, R Baer, *Wiley Interdisciplinary Reviews: Computational Molecular Science*, 9(6) (2019)
9. Transition to metallization in warm dense helium-hydrogen mixtures using stochastic density functional theory within the Kubo-Greenwood formalism, Y Cytter, E Rabani, D Neuhauser, M Preising, R Redmer, R Baer, *Physical Review B*, 100(19) (2019)
10. Energy window stochastic density functional theory, M Chen, R Baer, D Neuhauser, E Rabani, *Journal of Chemical Physics*, 151(11) (2019)
11. Quantum Monte Carlo assessment of density functionals for π-electron molecules: ethylene and bifuran, E Ospadov, SM Rothstein, R Baer, *Molecular Physics*, 117(17), 2241-2250 (2019)
12. Stochastic resolution of identity second-order Matsubara Green"s function theory, TY Takeshita, W Dou, DGA Smith, WA De Jong, R Baer, D Neuhauser, E Rabani, *Journal of Chemical Physics*, 151(4) (2019)
13. Nonmonotonic band gap evolution in bent phosphorene nanosheets, V Vlček, E Rabani, R Baer, D Neuhauser, *Physical Review Materials*, 3(6) (2019)
14. Spin Blockades to Relaxation of Hot Multiexcitons in Nanocrystals, T Ghosh, J Dehnel, M Fabian, E Lifshitz, R Baer, S Ruhman, *Journal of Physical Chemistry Letters*, 10(10), 2341-2348 (2019)
15. Stochastic time-dependent DFT with optimally tuned range-separated hybrids: Application to excitonic effects in large phosphorene sheets, V Vlček, R Baer, D Neuhauser, *Journal of Chemical Physics*, 150(18) (2019)
16. Making Sense of Coulomb Explosion Imaging, I Luzon, E Livshits, K Gope, R Baer, D Strasser, *Journal of Physical Chemistry Letters*, 10(6), 1361-1367 (2019)
17. Overlapped embedded fragment stochastic density functional theory for covalently-bonded materials, M Chen, R Baer, D Neuhauser, E Rabani, *Journal of Chemical Physics*, 150(3) (2019)

A.3 Avinoam Ben Shaul

1. Sizes of long RNA molecules are determined by the branching patterns of their secondary structures, Alexander Borodavka, Surendra W Singaram, Peter G Stockley, William M Gelbart, Avinoam Ben-Shaul, Roman Tuma, Biophysical journal 111 (10), 2077-2085 (2016).
2. Biography of William M. Gelbart, A Ben-Shaul, CM Knobler, AJ Liu, The Journal of Physical Chemistry B 120 (26), 5789-5793 (2016).
3. William M. Gelbart: An Appreciation, A Ben-Shaul, CM Knobler, AJ Liu, The Journal of Physical Chemistry B 120 (26), 5787-5788 (2016).
4. A Prüfer-Sequence Based Algorithm for Calculating the Size of Ideal Randomly Branched Polymers, SW Singaram, A Gopal, A Ben-Shaul, The Journal of Physical Chemistry B 120 (26), 6231-6237 (2016).
5. A short history of membrane physics, E Sackmann, A Ben-Shaul, Handbook of Lipid Membranes: Molecular, Functional, and Materials Aspects ... (2016)

A.4 Snir Gazit

1. Performance of the rigorous renormalization group for first order phase transitions and topological phases, M. Block, J. Motruk, **S. Gazit**, M. P. Zaletel, Z. Landau, U. Vazirani, N. Y. Yao, arXiv:2010.15851, under review in *Phys. Rev. B.* (2020)

2. Quasiperiodic Floquet-Thouless energy pump, F. Nathan, R. Ge, **S. Gazit**, M. S. Rudner, M. Kolodrubetz, arXiv:2010.11485, under review in *Phys. Rev. Lett.* (2020)

3. Evidence for deconfined U(1) gauge theory at the transition between toric code and double semion, M. Dupont, **S. Gazit**, T. Scaffidi, arXiv:2008.06509, under review in *Phys. Rev. Lett.* (2020)

4. From trivial to topological paramagnets: The case of $\mathbb{Z}_2$ and $\mathbb{Z}_2^3$ symmetries in two dimensions, M. Dupont, **S. Gazit**, T. Scaffidi, arXiv:2008.11206, accepted to *Phys. Rev. B.* (2020)

5. Superuniversality from disorder at two-dimensional topological phase transitions, B. Kang, S. A. Parameswaran, A. C. Potter, R. Vasseur, **S. Gazit**, arXiv:2008.09617 accepted to *Phys. Rev. B* (2020)

6. Fermi-surface reconstruction without symmetry breaking, **S. Gazit**, F. F. Assaad, S. Sachdev, arXiv:1906.11250 accepted to *Phys. Rev. X.* (2020)

7. Quantum phase transitions of tri-layer excitons in atomically thin heterostructures, Y. Slobodkin, Y. Mazuz-Harpaz, S. Refaely-Abramson, **S. Gazit**, H. Steinberg, and R. Rapaport, arXiv:2004.06687, accepted to *Phys. Rev. Lett.* (2020)

8. Adiabatic ground state preparation in an expanding lattice, C, T. Olund, M, Block, **S. Gazit**, J, McGreevy, and N. Y. Yao, *Phys. Rev. B* 101, 155152 (2020)

9. Magnon Bose-Einstein Condensation and Superconductivity in a Frustrated Kondo Lattice, P. A. Volkov, **S. Gazit**, and J. H. Pixley, *PNAS* August 25, (2020) 117 (34)

10. Multiparticle interactions for ultracold atoms in optical tweezers: Cyclic ring-exchange terms, A. Bohrdt, A. Omran, E. Demler, **S. Gazit**, F. Grusdt, Phys. Rev. Lett. 124, 073601 (2020)

11. Floquet Hopf Insulators, T. Schuster, **S. Gazit**, J. E. Moore, N. Y. Yao, *Phys. Rev. Lett.* 123, 266803 (2019)

12. Improving techniques for diagnostics of laser pulses by compact representations, P. Sidorenko, A. Dikopoltsev, T. Zahavy, O. Lahav, **S. Gazit**, Y. Shechtman, A. Szameit, D. J. Tannor, Y. C. Eldar, M. Segev, and O. Cohen, *Opt. Express 27, 8920-8934* (2019)

A.5 Robert B. Gerber

1. Impact of pH and NaCl and $CaCl_2$ Salts on the Speciation and Photochemistry of Pyruvic Acid in the Aqueous Phase, M Luo, D Shemesh, MN Sullivan, MR Alves, M Song, RB Gerber, VH Grassian, *Journal of Physical Chemistry A*, 124(25), 5071-5080 (2020)

2. Absorption spectra of pyruvic acid in water: insights from calculations for small hydrates and comparison to experiment, D Shemesh, M Luo, VH Grassian, RB Gerber, *Physical Chemistry Chemical Physics*, 22(22), 12658-12670 (2020)

3. Absorption spectra of benzoic acid in water at different pH and in the presence of salts: Insights from the integration of experimental data and theoretical cluster models, NV Karimova, M Luo, VH Grassian, R Benny Gerber, *Physical Chemistry Chemical Physics*, 22(9), 5046-5056 (2020)
4. Isomer-specific cryogenic ion vibrational spectroscopy of the D_2 tagged $Cs^+(HNO_3)(H_2O)$: N =0-2 complexes: Ion-driven enhancement of the acidic H-bond to water, S Mitra, CH Duong, LM McCaslin, RB Gerber, MA Johnson, *Physical Chemistry Chemical Physics*, 22(8), 4501-4507 (2020)
5. Gas phase dynamics, conformational transitions and spectroscopy of charged saccharides: The oxocarbenium ion, protonated anhydrogalactose and protonated methyl galactopyranoside, MP Dvores, P Çarçabal, P Maître, JP Simons, RB Gerber, *Physical Chemistry Chemical Physics*, 22(7), 4144-4157 (2020)
6. Integrated experimental and theoretical approach to probe the synergistic effect of ammonia in methanesulfonic acid reactions with small alkylamines, V Perraud, J Xu, RB Gerber, BJ Finlayson-Pitts, *Environmental Science: Processes and Impacts*, 22(2), 305-328 (2020)
7. SN2 Reactions of N_2O_5 with Ions in Water: Microscopic Mechanisms, Intermediates, and Products, NV Karimova, J Chen, JR Gord, S Staudt, TH Bertram, GM Nathanson, RB Gerber, *Journal of Physical Chemistry A*, 124(4), 711-720 (2020)
8. Microscopic Mechanisms of N_2O_5 Hydrolysis on the Surface of Water Droplets, E Rossich Molina, RB Gerber, *Journal of Physical Chemistry A*, 124(1), 224-228 (2020)
9. Hydrogenic Stretch Spectroscopy of Glycine-Water Complexes: Anharmonic Ab Initio Classical Separable Potential Calculations, L Sagiv, B Hirshberg, RB Gerber, *Journal of Physical Chemistry A*, 123(39), 8377-8384 (2019)
10. Experimental and Theoretical Studies of the Environmental Sensitivity of the Absorption Spectra and Photochemistry of Nitenpyram and Analogs, MJ Ezell, W Wang, D Shemesh, A Ni, RB Gerber, BJ Finlayson-Pitts, *ACS Earth and Space Chemistry*, 3(9), 2063-2075 (2019)
11. Sulfate and Carboxylate Suppress the Formation of $ClNO_2$ at Atmospheric Interfaces, S Staudt, JR Gord, NV Karimova, EE McDuffie, SS Brown, RB Gerber, GM Nathanson, TH Bertram, *ACS Earth and Space Chemistry*, 3(9), 1987-1997 (2019)
12. Structures, Stability, and Decomposition Dynamics of the Polynitrogen Molecule $N_5^+B(N_3)_4^-$ And Its Dimer $[N_5^+]_2[B(N_3)_4^-]_2$, I Zakai, D Grinstein, S Welner, RB Gerber, *Journal of Physical Chemistry A*, 123(34), 7384-7393 (2019)
13. Conformers of Ubiquitin 6+ for Different Charge Distributions: Atomistic Structures and Ion Mobility Cross Sections, T Gantman, M Goldstein, E Segev, RB Gerber, *Journal of Physical Chemistry B*, 123(30), 6401-6409 (2019)
14. Ion reactions in atmospherically-relevant clusters: Mechanisms, dynamics and spectroscopic signatures, NV Karimova, LM McCaslin, RB Gerber, *Faraday Discussions*, 217, 342-360 (2019)
15. Mechanisms and competition of halide substitution and hydrolysis in reactions of N2O5 with seawater, LM McCaslin, MA Johnson, R Benny Gerber, *Science Advances*, 5(6) (2019)
16. Exotic systems: General discussion, C Dessent, M Johnson, B Gerber, R Wester, K Asmis, I Avdonin, E Bieske, M Gatchell, J Bull, P Sarre, M-P Gaigeot, C-W Chou, R Mabbs, K Jordan, MK Beyer, L McCaslin, A Krylov, S Schlemmer, AB McCoy, J Verlet, Z Meir, J Simons, V Gabelica, S Willitsch, *Faraday Discussions*, 217, 601-622 (2019)

17. Pushing resolution in frequency and time: General discussion, J Simons, M Johnson, K Asmis, AB McCoy, S Daly, R Wester, A Rijs, P Sarre, M-P Gaigeot, R Mabbs, K Jordan, C Dessent, D Neumark, C-W Chou, B Gerber, O Dopfer, J Oomens, A Krylov, S Schlemmer, S Willitsch, J Verlet, R Wild, M Gatchell, M Stockett, J Roithová, MK Beyer, S Xantheas, J Gibbard, P Dohnal, *Faraday Discussions*, 217, 290-321 (2019)
18. Going large(r): General discussion, M Ahmed, S Daly, C Dessent, O Dopfer, V Gabelica, M-P Gaigeot, M Gatchell, B Gerber, J Gibbard, C Johnson, M Johnson, K Jordan, A Krylov, K Lovelock, M Mayer, L McCaslin, AB McCoy, D Neumark, SB Nielsen, J Oomens, A Rijs, T Rizzo, J Roithová, J Simons, M Stockett, A Trevitt, J Verlet, X-B Wang, R Wester, S Xantheas, *Faraday Discussions*, 217, 476-513 (2019)
19. Controlling internal degrees: General discussion, M Ahmed, K Asmis, I Avdonin, MK Beyer, E Bieske, S Bougueroua, C-W Chou, S Daly, O Dopfer, L Ellis-Gibbings, V Gabelica, M-P Gaigeot, M Gatchell, B Gerber, C Johnson, M Johnson, K Jordan, A Krylov, M Mayer, L McCaslin, AB McCoy, D Neumark, M Ončák, J Oomens, A Rijs, T Rizzo, J Roithová, P Sarre, S Schlemmer, J Simons, M Stockett, A Trevitt, J Verlet, X-B Wang, R Wester, S Willitsch, S Xantheas, *Faraday Discussions*, 217, 138-171 (2019)

A.6 Eberhard K. U. Gross

1. Combining Eliashberg Theory with Density Functional Theory for the Accurate Prediction of Superconducting Transition Temperatures and Gap Functions, A Sanna, C Pellegrini, EKU Gross, *Physical Review Letters*, **125**(5), 057001 (2020)
2. Ab-Initio Real-Time Magnon Dynamics in Ferromagnetic and Ferrimagnetic Systems, N Singh, P Elliott, JK Dewhurst, EKU Gross, S Sharma, *Physica Status Solidi (B) Basic Research*, **257**(7), 1900654 (2020)
3. Many-body Green's function theory of electrons and nuclei beyond the Born-Oppenheimer approximation, VJ Härkönen, R Van Leeuwen, EKU Gross, *Physical Review B*, **101**(23), 235153 (2020)
4. Extending solid-state calculations to ultra-long-range length scales, T Müller, S Sharma, EKU Gross, K Dewhurst, *Phys. Rev. Lett.*, **125**, 256402 (2020)
5. Exact factorization of the electron-nuclear wavefunction: Theory and Applications, F Agostini, EKU Gross, in: *Quantum Chemistry and Dynamics of Excited States: Methods and Applications*, eds. L Gonzalez, R Lindh, (Wiley 2020), p. 531-562
6. Time-Dependent Density Functional Theory for Spin Dynamics, P Elliott, M Stamenova, J Simoni, S Sharma, S Sanvito, EKU Gross, in: *Handbook of Materials Modeling*, W Andreoni, S Yip ed(s), (Springer 2020), p. 841-866
7. TDDFT and Quantum-Classical Dynamics: A Universal Tool Describing the Dynamics of Matter, F Agostini, BFE Curchod, R Vuilleumier, I Tavernelli, EKU Gross, in: *Handbook of Materials Modeling*, W Andreoni, S Yip ed(s), (Springer 2020), p. 75-121
8. The microscopic origin of spin-orbit mediated spin-flips, P Elliott, N Singh, K Krieger, EKU Gross, S Sharma, JK Dewhurst, *Journal of Magnetism and Magnetic Materials*, **502**, 166473 (2020)
9. Density functional theory of magnetic dipolar interactions, C Pellegrini, T Müller, JK Dewhurst, S Sharma, A Sanna, EKU Gross, *Physical Review B*, **101**(14), 144401 (2020)

10. Generation of magnetic skyrmions by focused vortex laser pulses, OP Polyakov, IA Gonoskov, VS Stepanyuk, EKU Gross, *Journal of Applied Physics*, **127**(7), 073904 (2020)
11. Complete description of the magnetic ground state in spinel vanadates, J Krishna, N Singh, S Shallcross, JK Dewhurst, EKU Gross, T Maitra, S Sharma, *Physical Review B*, **100**(8), 081102 (2019)
12. Exact factorization-based density functional theory of electron-phonon systems, R Requist, CR Proetto, EKU Gross, *Physical Review B*, **99**(16), 165136 (2019)
13. Model Hamiltonian for strongly correlated systems: Systematic, self-consistent, and unique construction, R Requist, EKU Gross, *Physical Review B*, **99**(12), 125114 (2019)
14. Electron-nuclear entanglement in the time-dependent molecular wavefunction, F Agostini, EKU Gross, BFE Curchod, *Computational and Theoretical Chemistry*, **1151**, 99-106 (2019)
15. Competing Spin Transfer and Dissipation at Co/Cu (001) Interfaces on Femtosecond Timescales, J Chen, U Bovensiepen, A Eschenlohr, T MÃŒller, P Elliott, EKU Gross, JK Dewhurst, S Sharma, *Physical Review Letters*, **122**(6), 067202 (2019)
16. Direct evaluation of the isotope effect within the framework of density functional theory for superconductors, M Lüders, P Cudazzo, G Profeta, A Continenza, S Massidda, A Sanna, EKU Gross, *Journal of Physics Condensed Matter*, **31**(33), 334001 (2019)

A.7 Daniel Harries

1. Bridges of Calcium Bicarbonate Tightly Couple Dipolar Lipid Membranes, L Fink, C Allolio, J Feitelson, C Tamburu, D Harries, U Raviv, *Langmuir*, 36(36), 10715-10724 (2020)
2. Heterogeneous Electrofreezing of Super-Cooled Water on Surfaces of Pyroelectric Crystals is Triggered by Trigonal Planar Ions, S Curland, C Allolio, L Javitt, S Dishon Ben-Ami, I Weissbuch, D Ehre, D Harries, M Lahav, I Lubomirsky, *Angewandte Chemie - International Edition*, 59(36), 15575-15579 (2020)
3. Stressing crystals with solutes: Effects of added solutes on crystalline caffeine and their relevance to determining transfer free energies, I Shumilin, B Bogoslavsky, D Harries, *Colloids and Surfaces A: Physicochemical and Engineering Aspects*, 599 (2020)
4. Confinement in Nanodiscs Anisotropically Modifies Lipid Bilayer Elastic Properties, I Schachter, C Allolio, G Khelashvili, D Harries, *Journal of Physical Chemistry B*, 124(33), 7166-7175 (2020)
5. Restructuring a Deep Eutectic Solvent by Water: The Nanostructure of Hydrated Choline Chloride/Urea, L Sapir, D Harries, *Journal of Chemical Theory and Computation*, 16(5), 3335-3342 (2020)
6. Properties of Aqueous Trehalose Mixtures: Glass Transition and Hydrogen Bonding, GI Olgenblum, L Sapir, D Harries, *Journal of Chemical Theory and Computation*, 16(2), 1249-1262 (2020)
7. How Sugars Modify Caffeine Self-Association and Solubility: Resolving a Mechanism of Selective Hydrotropy, I Shumilin, C Allolio, D Harries, *Journal of the American Chemical Society*, 141(45), 18056-18063 (2019)

A.8 Ronnie Kosloff

1. Quantum finite-time thermodynamics: Insight from a single qubit engine, R Dann, R Kosloff, P Salamon, *Entropy*, 22(11), 1-47 (2020)
2. Dissociation in strong field: A quantum analysis of the relation between angular momentum and angular distribution of fragments, B Ezra, S Kallush, R Kosloff, *Chemical Physics Letters*, 756 (2020)
3. Branching ratio coherent control in ultrafast bond making, Z Amitay, L Liat, DM Reich, R Kosloff, CP Koch, *Chemical Physics Letters*, 1412(9) (2020)
4. Fast route to equilibration, R Dann, A Tobalina, R Kosloff, *Physical Review A*, 101(5) (2020)
5. Landauer's principle in a quantum szilard engine without Maxwell"s Demon, A Aydin, A Sisman, R Kosloff, *Entropy*, 22(3) (2020)
6. Optimization of high-order harmonic generation by optimal control theory: Ascending a functional landscape in extreme conditions, I Schaefer, R Kosloff, *Physical Review A*, 101(2) (2020)
7. Quantum signatures in the quantum Carnot cycle, R Dann, R Kosloff, *New Journal of Physics*, 22(1) (2020)
8. Imaging Recoil Ions from Optical Collisions between Ultracold, Metastable Neon Isotopes, B Ohayon, H Rahangdale, J Chocron, Y Mishnayot, R Kosloff, O Heber, G Ron, *Physical Review Letters*, 123(6) (2019)
9. Shortcut to Equilibration of an Open Quantum System, R Dann, A Tobalina, R Kosloff, *Physical Review Letters*, 122(25) (2019)
10. Quantum thermodynamics and open-systems modeling, R Kosloff, *Journal of Chemical Physics*, 150(20) (2019)
11. Quantum control in ultrafast coherent bond making, Z Amitay, L Levin, DM Reich, R Kosloff, CP Koch, *Journal of Chemical Physics*, Part F165-QIM (2019)

A.9 Eli Kraisler

1. Asymptotic Behavior of the Exchange-Correlation Energy Density and the Kohn-Sham Potential in Density Functional Theory: Exact Results and Strategy for Approximations, E Kraisler, *Israel Journal of Chemistry*, 60(8-9), 805-822 (2020)
2. Asymptotic behavior of the Hartree-exchange and correlation potentials in ensemble density functional theory, T Gould, S Pittalis, J Toulouse, E Kraisler, L Kronik, *Physical Chemistry Chemical Physics*, 21(36), 19805-19815 (2019)
3. Discontinuous behavior of the Pauli potential in density functional theory as a function of the electron number, E Kraisler, A Schild, *Physical Review Research*, 2(1), 013159, (2020)

A.10 Raphael D. Levine

1. Raman-guided subcellular pharmaco-metabolomics for metastatic melanoma cells, J Du, Y Su, C Qian, D Yuan, K Miao, D Lee, AHC Ng, RS Wijker, A Ribas, RD Levine, JR Heath, L Wei, *Nature Communications*, 11(1) (2020)

2. Multi-omic single-cell snapshots reveal multiple independent trajectories to drug tolerance in a melanoma cell line, Y Su, ME Ko, H Cheng, R Zhu, M Xue, J Wang, JW Lee, L Frankiw, A Xu, S Wong, L Robert, K Takata, D Yuan, Y Lu, S Huang, A Ribas, R Levine, GP Nolan, W Wei, SK Plevritis, G Li, D Baltimore, JR Heath, *Nature Communications*, 11(1) (2020)

3. Parallel Quantum Computation of Vibrational Dynamics, K Komarova, H Gattuso, RD Levine, F Remacle, *Frontiers in Physics*, 8 (2020)

4. Quantum Device Emulates the Dynamics of Two Coupled Oscillators, K Komarova, H Gattuso, RD Levine, F Remacle, *Journal of Physical Chemistry Letters*, 11(17), 6990-6995 (2020)

5. Massively parallel classical logic via coherent dynamics of an ensemble of quantum systems with dispersion in size, H Gattuso, RD Levine, F Remacle, *Proceedings of the National Academy of Sciences of the United States of America*, 117(35) (2020)

6. Thermodynamic energetics underlying genomic instability and whole-genome doubling in cancer, F Remacle, TG Graeber, RD Levine, *Proceedings of the National Academy of Sciences of the United States of America*, 117(31), 18880-18890 (2020)

7. Room-Temperature Inter-Dot Coherent Dynamics in Multilayer Quantum Dot Materials, E Collini, H Gattuso, Y Kolodny, L Bolzonello, A Volpato, HT Fridman, S Yochelis, M Mor, J Dehnel, E Lifshitz, Y Paltiel, RD Levine, F Remacle, *Journal of Physical Chemistry C*, 124(29), 16222-16231 (2020)

8. Correlated electron-nuclear motion during non-Adiabatic transitions in LiH and its isotopomers, KG Komarova, S Van Den Wildenberg, F Remacle, RD Levine, *Journal of Physics B: Atomic, Molecular and Optical Physics*, 53(13) (2020)

9. Coherent exciton dynamics in ensembles of size-dispersed cdse quantum dot dimers probed via ultrafast spectroscopy: A quantum computational study, H Gattuso, B Fresch, RD Levine, F Remacle, *Applied Sciences (Switzerland)*, 10(4) (2020)

10. Metabolic, Physiological, and Transcriptomics Analysis of Batch Cultures of the Green Microalga Chlamydomonas Grown on Different Acetate Concentrations, KA Bogaert, E Perez, J Rumin, A Giltay, M Carone, N Coosemans, M Radoux, G Eppe, RD Levine, F Remacle, C Remacle, *Cells*, 8(11) (2019)

11. Temporal and spatially resolved imaging of the correlated nuclear-electronic dynamics and of the ionized photoelectron in a coherently electronically highly excited vibrating LiH molecule, S Van Den Wildenberg, B Mignolet, RD Levine, F Remacle, *Journal of Chemical Physics*, 151(13) (2019)

12. Intracellular redox potential is correlated with miRNA expression in MCF7 cells under hypoxic conditions, H Johnston, P Dickinson, A Ivens, AH Buck, RD Levine, F Remacle, CJ Campbell, *Proceedings of the National Academy of Sciences of the United States of America*, 116(39), 19753-19759 (2019)

13. Time resolved mechanism of the isotope selectivity in the ultrafast light induced dissociation in N2, KG Komarova, F Remacle, RD Levine, *Journal of Chemical Physics*, 151(11) (2019)

14. Consecutive feedback-driven constitutional dynamic networks, L Yue, S Wang, V Wulf, S Lilienthal, F Remacle, RD Levine, I Willner, *Proceedings of the National Academy of Sciences of the United States of America*, 116(8), 2843-2848 (2019)

A.11 Masha Y. Niv

1. Tracking COVID-19 using taste and smell loss Google searches is not a reliable strategy, K Asseo, F Fierro, Y Slavutsky, J Frasnelli, MY Niv, *Scientific Reports*, 10(1) (2020)
2. More Than Smell-COVID-19 Is Associated With Severe Impairment of Smell, Taste, and Chemesthesis, V Parma, K Ohla, MG Veldhuizen, MY Niv, CE Kelly, AJ Bakke, KW Cooper, C Bouysset, N Pirastu, M Dibattista, R Kaur, MT Liuzza, MY Pepino, V Schöpf, V Pereda-Loth, SB Olsson, RC Gerkin, P Rohlfs DomÃnguez, J Albayay, MC Farruggia, S Bhutani, AW Fjaeldstad, R Kumar, A Menini, M Bensafi, M Sandell, I Konstantinidis, A Di Pizio, F Genovese, L Öztürk, T Thomas-Danguin, J Frasnelli, S Boesveldt, Ö Saatci, LR Saraiva, C Lin, J Golebiowski, L-D Hwang, MH Ozdener, MD Guàrdia, C Laudamiel, M Ritchie, J Havlícek, D Pierron, E Roura, M Navarro, AA Nolden, J Lim, KL Whitcroft, LR Colquitt, C Ferdenzi, EV Brindha, A Altundag, A Macchi, A Nunez-Parra, ZM Patel, S Fiorucci, CM Philpott, BC Smith, JN Lundström, C Mucignat, JK Parker, M van den Brink, M Schmuker, FPS Fischmeister, T Heinbockel, VDC Shields, F Faraji, E SantamarÃa, WEA Fredborg, G Morini, JK Olofsson, M Jalessi, N Karni, A D"Errico, R Alizadeh, R Pellegrino, P Meyer, C Huart, B Chen, GM Soler, MK Alwashahi, A Welge-Lüssen, J Freiherr, JHB de Groot, H Klein, M Okamoto, PB Singh, JW Hsieh, DR Reed, T Hummel, SD Munger, JE Hayes, *Chemical senses*, 45(7), 609-622 (2020)
3. Structure-based screening for discovery of sweet compounds, Y Ben Shoshan-Galeczki, MY Niv, *Food Chemistry*, 315 (2020)
4. Functions of Opsins in Drosophila Taste, NY Leung, DP Thakur, AS Gurav, SH Kim, A Di Pizio, MY Niv, C Montell, *Current Biology*, 30(8), 1367-1379.e6 (2020)
5. Bitter-Tasting Amino Acids l-Arginine and l -Isoleucine Differentially Regulate Proton Secretion via T2R1 Signaling in Human Parietal Cells in Culture, V Stoeger, A-K Holik, K Hölz, T Dingjan, J Hans, JP Ley, GE Krammer, MY Niv, MM Somoza, V Somoza, *Journal of Agricultural and Food Chemistry*, 68(11), 3434-3444 (2020)
6. Rational design of agonists for bitter taste receptor TAS2R14: from modeling to bench and back, A Di Pizio, LAW Waterloo, R Brox, S Löber, D Weikert, M Behrens, P Gmeiner, MY Niv, *Cellular and Molecular Life Sciences*, 77(3), 531-542 (2020)
7. A bioinspired in vitro bioelectronic tongue with human T2R38 receptor for high-specificity detection of N-C=S-containing compounds, C Qin, Z Qin, D Zhao, Y Pan, L Zhuang, H Wan, A Di Pizio, E Malach, MY Niv, L Huang, N Hu, P Wang, *Talanta*, 199, 131-139 (2019)
8. Bitter and sweet tasting molecules: It's complicated, A Di Pizio, Y Ben Shoshan-Galeczki, JE Hayes, MY Niv, *Neuroscience Letters*, 700, 56-63 (2019)
9. Allostery in Its Many Disguises: From Theory to Applications, SJ Wodak, E Paci, NV Dokholyan, IN Berezovsky, A Horovitz, J Li, VJ Hilser, I Bahar, J Karanicolas, G Stock, P Hamm, RH Stote, J Eberhardt, Y Chebaro, A Dejaegere, M Cecchini, J-P Changeux, PG Bolhuis, J Vreede, P Faccioli, S Orioli, R Ravasio, L Yan, C Brito, M Wyart, P Gkeka, I Rivalta, G Palermo, JA McCammon, J Panecka-Hofman, RC Wade, A Di Pizio, MY Niv, R Nussinov, C-J Tsai, H Jang, D Padhorny, D Kozakov, T McLeish, *Structure*, 27(4), 566-578 (2019)

10. RASA2 and NF1; two-negative regulators of Ras with complementary functions in melanoma, R Arafeh, A Di Pizio, AG Elkahloun, O Dym, MY Niv, Y Samuels, *Oncogene*, 38(13), 2432-2434 (2019)
11. Bitterless guaifenesin prodrugs–design, synthesis, characterization, in vitro kinetics, and bitterness studies, A Thawabteh, F Lelario, L Scrano, SA Bufo, S Nowak, M Behrens, A Di Pizio, MY Niv, R Karaman, *Chemical Biology and Drug Design*, 93(3), 262-271 (2019)
12. Correction to: Recombinant ostreolysin induces brown fat–like phenotype in HIB–1B cells (Molecular Nutrition & Food Research, (2017), 61, 9, (1700057), 10.1002/mnfr.201700057), T Oren, L Nimri, E Yehuda–Shnaidman, K Staikin, Y Hadar, A Friedler, H Amartely, M Slutzki, AD Pizio, MY Niv, I Peri, L Graeve, B Schwartz, *Molecular Nutrition and Food Research*, 63(5) (2019)
13. Bitterdb: Taste ligands and receptors database in 2019, A Dagan-Wiener, A Di Pizio, I Nissim, MS Bahia, N Dubovski, E Margulis, MY Niv, *Nucleic Acids Research*, 47(D1), D1179-D1185 (2019)

A.12 Igor Schapiro

1. Structures of the archaerhodopsin-3 transporter reveal that disordering of internal water networks underpins receptor sensitization, JF Bada Juarez, P Judge, S Adam, D Axford, J Vinals, J Birch, T Kwan, K Hoi, HY Yen, A Vial, PE Milhiet, C Robinson, I Schapiro, I Moraes, A Watts *Nature Communications*, in press
2. Computational Studies of Photochemistry in Phytochrome Proteins, JR Church, AG Rao, A Barnoy, C Wiebeler, I Schapiro, *Challenges and Advances in Computational Chemistry and Physics*, 31, 197-226 (2021)
3. NeoR, a near-infrared absorbing rhodopsin, M Broser, A Spreen, PE Konold, E Peter, S Adam, V Borin, I Schapiro, R Seifert, JTM Kennis, YA Bernal Sierra, P Hegemann, *Nature Communications*, 11(1) (2020)
4. Modulation of Light Energy Transfer from Chromophore to Protein in the Channelrhodopsin ReaChR, JCD Kaufmann, BS Krause, S Adam, E Ritter, I Schapiro, P Hegemann, FJ Bartl, *Biophysical Journal*, 119(3), 705-716 (2020)
5. Tuning Quantum Dots Coupling Using Organic Linkers with Different Vibrational Modes, Y Kolodny, S Fererra, V Borin, S Yochelis, CN Dibenedetto, M Mor, J Dehnel, S Remmenik, E Fanizza, M Striccoli, I Schapiro, E Lifshitz, Y Paltiel, *Journal of Physical Chemistry C*, 124(29), 16159-16165 (2020)
6. The interplay between chromophore and protein determines the extended excited state dynamics in a single-domain phytochrome, C Slavov, T Fischer, A Barnoy, H Shin, AG Rao, C Wiebeler, X Zeng, Y Sun, Q Xu, A Gutt, K-H Zhao, W Gärtner, X Yang, I Schapiro, J Wachtveitl, *Proceedings of the National Academy of Sciences of the United States of America*, 117(28), 16356-16362 (2020)
7. Femtosecond-to-millisecond structural changes in a light-driven sodium pump, P Skopintsev, D Ehrenberg, T Weinert, D James, RK Kar, PJM Johnson, D Ozerov, A Furrer, I Martiel, F Dworkowski, K Nass, G Knopp, C Cirelli, C Arrell, D Gashi, S Mous, M Wranik, T Gruhl, D Kekilli, S Brünle, X Deupi, GFX Schertler, RM Benoit, V Panneels, P Nogly, I Schapiro, C Milne, J Heberle, J Standfuss, *Nature*, 583(7815), 314-318 (2020)

8. Spin-chemical effects on intramolecular photoinduced charge transfer reactions in bisphenanthroline copper(I)-viologen dyad assemblies, MS Lazorski, I Schapiro, RS Gaddie, AP Lehnig, M Atanasov, F Neese, UE Steiner, CM Elliott, *Chemical Science*, 11(21), 5511-5525 (2020)
9. Carbohydrate-Binding Capability and Functional Conformational Changes of AbnE, an Arabino-oligosaccharide Binding Protein, S Lansky, R Salama, S Shulami, N Lavid, S Sen, I Schapiro, Y Shoham, G Shoham, *Journal of Molecular Biology*, 432(7), 2099-2120 (2020)
10. Intramolecular Proton Transfer Controls Protein Structural Changes in Phytochrome, A Kraskov, AD Nguyen, J Goerling, D Buhrke, F Velazquez Escobar, M Fernandez Lopez, N Michael, L Sauthof, A Schmidt, P Piwowarski, Y Yang, T Stensitzki, S Adam, F Bartl, I Schapiro, K Heyne, F Siebert, P Scheerer, MA Mroginski, P Hildebrandt, *Biochemistry*, 59(9), 1023-1037 (2020)
11. Dynamic Properties of the Photosensory Domain of Deinococcus radiodurans Bacteriophytochrome, G Battocchio, R González, AG Rao, I Schapiro, MA Mroginski, *Journal of Physical Chemistry B*, 124(9), 1740-1750 (2020)
12. Ultrafast Backbone Protonation in Channelrhodopsin-1 Captured by Polarization Resolved Fs Vis-pump–IR-Probe Spectroscopy and Computational Methods, T Stensitzki, S Adam, R Schlesinger, I Schapiro, K Heyne, *Molecules*, 25(4) (2020)
13. Structural elements regulating the photochromicity in a cyanobacteriochrome, X Xu, A Port, C Wiebeler, K-H Zhao, I Schapiro, W Gärtner, *Proceedings of the National Academy of Sciences of the United States of America*, 117(5), 2432-2440 (2020)
14. Nuclear spin-hyperpolarization generated in a flavoprotein under illumination: experimental field-dependence and theoretical level crossing analysis, Y Ding, AS Kiryutin, AV Yurkovskaya, DV Sosnovsky, RZ Sagdeev, S Bannister, T Kottke, RK Kar, I Schapiro, KL Ivanov, J Matysik, *Scientific Reports*, 9(1) (2019)
15. OpenMolcas: From Source Code to Insight, I Fdez Galván, M Vacher, A Alavi, C Angeli, F Aquilante, J Autschbach, JJ Bao, SI Bokarev, NA Bogdanov, RK Carlson, LF Chibotaru, J Creutzberg, N Dattani, MG Delcey, SS Dong, A Dreuw, L Freitag, LM Frutos, L Gagliardi, F Gendron, A Giussani, L González, G Grell, M Guo, CE Hoyer, M Johansson, S Keller, S Knecht, G Kovačević, E Källman, G Li Manni, M Lundberg, Y Ma, S Mai, JP Malhado, PÅ Malmqvist, P Marquetand, SA Mewes, J Norell, M Olivucci, M Oppel, QM Phung, K Pierloot, F Plasser, M Reiher, AM Sand, I Schapiro, P Sharma, CJ Stein, LK Sørensen, DG Truhlar, M Ugandi, L Ungur, A Valentini, S Vancoillie, V Veryazov, O Weser, TA Wesołowski, P-O Widmark, S Wouters, A Zech, JP Zobel, R Lindh, *Journal of Chemical Theory and Computation*, 15(11), 5925-5964 (2019)
16. Atomistic insight into the role of threonine 127 in the functional mechanism of channelrhodopsin-2, D Ehrenberg, N Krause, M Saita, C Bamann, RK Kar, K Hoffmann, D Heinrich, I Schapiro, J Heberle, R Schlesinger, *Applied Sciences (Switzerland)*, 9(22) (2019)
17. Spectroscopic Properties of Lumiflavin: A Quantum Chemical Study, RK Kar, VA Borin, Y Ding, J Matysik, I Schapiro, *Photochemistry and Photobiology*, 95(2), 662-674 (2019)
18. The Effective Conjugation Length Is Responsible for the Red/Green Spectral Tuning in the Cyanobacteriochrome Slr1393g3, C Wiebeler, AG Rao, W Gärtner, I Schapiro, *Angewandte Chemie - International Edition*, 58(7), 1934-1938 (2019)
19. QM/MM benchmarking of cyanobacteriochrome Slr1393g3 absorption spectra, C Wiebeler, I Schapiro, *Molecules*, 24(9) (2019)

20. Synthesis, spectroscopy and QM/MM simulations of a biomimetic ultrafast light-driven molecular motor, I Schapiro, M Gueye, M Paolino, S Fusi, G Marchand, S Haacke, ME Martin, M Huntress, VP Vysotskiy, V Veryazov, J Léonard, M Olivucci, *Photochemical and Photobiological Sciences*, 18(9), 2259-2269 (2019)

A.13 Tamar Stein

1. Electrochemical deposition of N-heterocyclic carbene monolayers on metal surfaces, E Amit, L Dery, S Dery, S Kim, A Roy, Q Hu, V Gutkin, H Eisenberg, T Stein, D Mandler, F Dean Toste, E Gross, *Nature Communications*, 11(1) (2020)
2. Molecular growth upon ionization of van der Waals clusters containing HCCH and HCN is a pathway to prebiotic molecules, T Stein, PP Bera, TJ Lee, M Head-Gordon, *Physical Chemistry Chemical Physics*, 22(36), 20337-20348 (2020)
3. Molecular Formation upon Ionization of van der Waals Clusters and Implication to Astrochemistry, T Stein, J Jose, *Israel Journal of Chemistry*, 60(8-9), 842-849 (2020)
4. Photoredox-Mediated Reaction of gem–Diborylalkenes: Reactivity Toward Diverse 1,1–Bisborylalkanes, N Kumar, N Eghbarieh, T Stein, AI Shames, A Masarwa, *Chemistry – A European Journal*, 26(24), 5360-5364 (2020)
5. Probing solvation and reactivity in ionized polycyclic aromatic hydrocarbon-water clusters with photoionization mass spectrometry and electronic structure calculations, B Xu, T Stein, U Ablikim, L Jiang, J Hendrix, M Head-Gordon, M Ahmed, *Faraday Discussions*, 217, 414-433 (2019)

A.14 Assaf Zemel

1. Mechanical Regulation of Neurite Polarization and Growth: A Computational Study, MAH Jakobs, K Franze, A Zemel, *Biophysical Journal*, 118(8), 1914-1920 (2020)

A.15 Raam Uzdin

1. The second law and beyond in microscopic quantum setups. Thermodynamics in the Quantum Regime., R. Uzdin, Springer, Cham. 681-712 (2018)
2. Heat sources with the smallest heat capacity, R. Uzdin, S. Gasparinetti, and R. Ozeri, Markovian New Journal of Physics 20, 063030 (2018)
3. Global passivity in microscopic thermodynamics, R. Uzdin, and S. Rahav. Physical Review X 8, 021064 (2018).
4. Collective operations can extremely reduce work fluctuations, M. Perarnau-Llobet, and R. Uzdin. New Journal of Physics 21, 083023 (2019)
5. Experimental demonstration of quantum effects in the operation of microscopic heat engines, J. Klatzow, et al. Physical Review Letters 122, 110601 (2019).

6. Experimental detection of microscopic environments using thermodynamic observables , I. Henao and N. Katz, and R. Uzdin, arXiv: 1908.08968, under review in Phys. Rev. lett.
7. The Passivity Deformation Approach for the Thermodynamics of Isolated Quantum Setups , R. Uzdin and S. Rahav, arXiv: 1912.07922, under review in Phys. Rev. X quantum.
8. Catalytic transformations with finite-size environments: applications to cooling and thermometry, I. Henao, and R. Uzdin, arXiv: 2010.09070, under review in New Journal of Physics.

Appendix B

Foreign relations

B.1 Scientific visitors during 2018-2020

Dates	Name	Affiliation
6-8/10/2018	Dr. Olexandr Isayev	Carnegie Mellon University, USA
25/10-21/11/18	Prof. Joachim Heberle	Freie Universität Berlin
30/10-2/11/18	Mr. Shishir Khandelwal	ETH Zürich, Switzerland
10-11/11/18	Prof. Kevin Jung	Sogang University, Korea
22-24/11/18	Prof. Klemen Bohinc	University of Ljubljana, Slovenia
16-19/12/18	Prof. Gerard Meijer	Fritz Haber Institute of the Max Planck Society, Germany
16-19/12/18	Prof. Helmut Grubmüller	Max Planck Institute for Biophysical Chemistry, Germany
16-19/12/18	Prof. Eberhard K.U. Gross	Hebrew University, Israel
28/12/18 – 21/1/19	Prof. Francoise Remacle	University of Liège, Belgium
19-22/01/19	Dr. Theo Kurten	University of Helsinki, Finland
25/1/19-1/2/19	Prof. Garry Joseph Pielak	University of North Carolina at Chapel Hill, USA
3-9/2/2019	Prof. Ernst-Walter Knapp	Freie Universität Berlin, Germany
3-9/2/2019	Jovan Dragelj	Freie Universität Berlin, Germany
11-18/02/19	Prof. Phillip Gould	University of Cennecticut, USA
17-19/2/19	Prof. Heather Kulik	MIT, USA
17-18/2/19	Aditya Nandy	MIT, USA
17-18/2/19	Jon Paul Janet	MIT, USA
17-18/2/19	Nick Yang	MIT, USA
23/2 – 16/3/19	Prof. Francoise Remacle	University of Liège, Belgium
15/5-26/9/19	Prof. Daniel Neuhauser	University of California, Los Angeles, USA
15/3-30/5/19	Prof. Horia Petrache	Indiana University, USA

Dates	Name	Affiliation
18-24/03/19	Prof. Phillip Gould	University of Cennecticut, USA
23/3-8/4/2019	Dr. Gilbert Grell	Universidad Autónoma de Madrid, Spain
26-31/03/19	Dr. Ivan Gonoskov	Friedrich Schiller University Jena, Germany
28/4-9/5/2019	Prof. Vladimir U. Nazarov	Academia Sinica, Taiwan
15/5-1/7/19	Dr. Paramita Halder	Birla Institute of Technology and Science, India
22-28/05/19	Prof. William M. Gelbart	University of California, Los Angeles, USA
26/5-19/6/19	Prof. Brian Burrows	Staffordshire University, England
26-30/05/19	Dr. Jogvan Magnus Haugaard Olsen	Aarhus University, Denmark
19-26/6/19	Prof. Francoise Remacle	University of Liège, Belgium
7-10/07/19	Prof. Sabre Kais	Purdue University, USA
20/7-18/8/19	Prof. Francoise Remacle	University of Liège, Belgium
20-28/07/19	Dr. Hugo Gattuso	University of Liège, Belgium
3-13/8/2019	Dr. Stephan Van Den Wildenberg	University of California, San Diego, USA
31/8-1/9/2019	Prof. Gerrit Groenhof	University of Jyväskylä, Finland
1-6/9/2019	Prof. Kazuhiro Fujimoto	Nagoya University, Japan
2-6/9/2019	Dr. Christian Wiebeler	Universität Paderborn, Germany
5-8/09/19	Prof. Maria-Andrea Mroginski	TU Berlin, Germany
3-12/9/2019	Dr. Florian Habecker	Carl von Ossietzky Universität Oldenburg, Germany
5-19/9/2019	Prof. Francoise Remacle	University of Liège, Belgium
29/10-2/11/2019	Prof. Leticia Gonzalez	Universität Wien, Austria
29/10-2/11/2019	Prof. Markus Oppel	Universität Wien, Austria
29/10-2/11/2019	Prof. Pedro A. Sanchez Murcia	Medical University of Graz, Austria
29/10-2/11/2019	Prof. Boris Maryasin	Universität Wien, Austria
30/10-4/11/2019	Prof. Jose Palao	Universidad de La Laguna, Spain
2-8/11/2019	Prof. Lajos Diosi	Wigner Research Centre for Physics, Hungary
3/11/2019	Dr. Amikam Levy	Bar-Ilan University, Israel
5-10/11/2019	Dr. Cristina Gonzalez Espinoza	University of Geneva, Switzerland
5-10/11/2019	Niccolo Ricardi	University of Geneva, Switzerland
21-24/11/19	Prof. Barry Honig	Columbia University, USA
5/12/2019 – 05/01/2020	Prof. Daniel Neuhauser	University of California, Los Angeles, USA

Dates	Name	Affiliation
27/12/2019 – 25/01/2020	Prof. Francoise Remacle	University of Liège, Belgium
14-16/02/20	Prof. Stuart Rice	University of Chicago, USA
19-22/02/2020	Carrie Ann Weidner	Aarhus University, Denmark
23-27/02/2020	Dr. Linn Leppert	University of Twente, Netherlands
27/2-18/3/2020	Claire Joleen Stewart	University of North Carolina at Chapel Hill, USA

B.2 Seminars given at the center during 2018-2020

Date	Speaker	Title of talk
1.11.18	Roi Dann (Kosloff Group) Aditya Rao (Schapiro Group)	Time Dependent non-Adiabatic Makovian Master Equation The Protonation State of A Histidine Determines the Conformational Diversity in the Cyanobacteriochrome AnPixJg2
5.11.18	Prof. Rob Bisseling, Utrecht University	Parallel Linear Algebra on High-Performance Computers
11.11.18	Dr. Viktor Chikan, Kansas State University	Manipulating NanoparticlesMolecules with Intense Electric & Magnetic Fields
22.11.18	Dr. Klemen Bohinc, Univ. of Ljubljana	Charge Properties of Nanoparticles
13.12.18	Prof. Christiane Koch, University of Kassel	Quantum Control of Photoelectron Circular Dichroism
30.12.18	Ido Schaefer (Kosloff Group)	Optimal Control Theory of High Harmonic Generation
17.1.19	Dr. Florian Habecker, Oldenburg University	Dissipative Quantum Dynamics Using the Stochastic Surrogate Hamiltonian Approach
20.1.19	Dr. Theo Kurten, University of Helsinki, Finland	Computational Insights Into Atmospheric Auto-Oxidation Mechanisms Forming Low-Volatility Vapors
31.1.19	Prof. Gary J. Pielak, University of North Carolina at Chapel Hill	Ned for New Theory and Simulations to Understand Protein Behavior in Cells
17.2.19	Drs. J.P. Janet, A. Nandy & Y. Tang, MIT	Workshop: Introduction to Machine Learning in the Chemical Sciences
20.3.19	Alhun Aydin	Quantum Shape Effects and Novel Thermodynamic Behaviors aat Nanoscale
26.3.19	Prof. Manabu Shiraiwa, UC Irvine CA	Multiphase Chemistry of Organic Aerosols and Reactive Oxygen Species
8.4.19	Dr. Or Szekely, Weizmann Institute	Hyperpolarized Water to Visualize Disordered, Well-Folded and Lowly Populated States in Proteins
15.4.19	Prof. Horia I. Petrache, Purdue University	Electronic Static Charging of Lipid Membranes
30.4.19	Dr. Diana Qiu, Lawrence Berkeley National Lab	Excitons in Flatland: Exploring and Manipulating Many-body Effects on the Optical Excitations in Quasi-2D Materials
29.5.19	Dr. J.M. Haugaard Olsen, University of Tromso, Norway	Development of Multiscale Methods for Computational Biomolecular Spectroscopy
4.6.19	Marcel Fabian (Baer Group)	Gaussian Basis Set Approach to Stochastic Density Functional Theory
6..6.19	Prof. A. Dybala-Defratyka, Lodz U. of Technology, Poland	Isotope Effects as Analytical Probes – A Computational Perspective
17.6.19	Eitam Arnon (Baer Group)	Langevin Sampling of Thermal Nanocrystal configurations on stochastic density functional theory

Date	Speaker	Title of talk
17.6.19	Michelle Dvores (Gerber Group)	Unravelling the Mechanisms and Dynamics of Sugar Reactions
20.6.19	Yael Cytter (Baer Group)	A Stochastic Approach to Thermal Density Functional Theory
1.9.19	Prof. Gerrit Groenhof, Univ. of Jyvaskyla, Finland	Manipulating Molecules with Mirrors
23.10.19	Prof. V. Mandelstam, Irvine, CA	Sampling General Distributions with Quasi-Regular Grids: Application to the Vibrational Spectra Calculations; Nuclear Quantum Effects in Atomic and Molecular Clusters
31.10.19	Prof. Ali Hasanali, Int”l Center for Theoretical Physics, Italy	The Many Faces of Water:An Atomistic Approach
23.10.19	Prof. V. Mandelshtam, University of California Irvine, USA	Sampling general distributions with quasi-regular grids: Application to the vibrational spectra calculations
29.10.19	Dr. Lauren J. Webb, The University of Texas at Austin, USA	Investigating Electrostatic Mechanisms of Biomolecular Organization and Function
31.10.19	Prof. Ali Hassanali, The International Center for Theoretical Physics, Italy	The Many Faces of Water: An Atomistic Approach
21.11.19	Dr. Suliman Adam (Schapiro Group)	Structural Factors Determining the Absorption Spectrum of Channelrhodopsins: A Case Study of the Chimaera C1C2
21.11.19	Dr. Jonathan R. Church (Schapiro Group)	Gas-Phase Reaction Kinetics of Pyruvic Acid with OH-Radicals
5.12.19	Prof. Dan T. Major, Bar-Ilan University	Enzyme catalysis: Both different and better
10.12.19	Prof. Guy Makov, Ben Gurion University	Discovering a novel nanometric cubin phase in monochalcogenide semiconductors- theory meets experiment
16.1.20	Ofer Filiba (Schapiro Group), HUJI	Involvement of triplet state in isomerization of retinal analogs
16.1.20	Ksenia Komarova (Levine Group)	Chirality of the rhodamine heterodimer tethered on DNA scaffold
30.01.20	Dr. Barak Hirshberg, ETH Zurich	Path integral molecular dynamics for bosons and fermions: From ultracold atoms to quantum dots

B.3 Workshops/conferences organized/supported by center 2018-2020

Year	Activity	Organizer
2018	Thermodynamics of quantum systems: measurement, engines, and control, June 25-29	Ronnie Kosloff, in Kavli Inst. for Theoretical Physics, UCSB, USA
	Mini Symposium on Neuron Mechanics and Growth, May 28	Assaf Zemel (HUJI), Eran Perlson (TAU)
	Jerusalem Nonadiabatica 2018: Nonadiabatic processes, March 12-15	Roi Baer, Igor Schapiro, Ronnie Kosloff, Eberhard K. U. Gross, Daniel Neuhauser
	"Information Theory and Dynamics: From Elementary Processes to System Chemistry, In Honor of Raphael D. Levine's 80th Birthday", ACS 256th National Meeting in Boston, MA, August 19-23	Sabre Kais (Purdue), Todd Martinez (Stanford)
2019	Computational Chemistry session, The 84th Annual Meeting of the Israel Chemical Society, February 12-13	Igor Schapiro (HUJI)
	International Workshop "The exact factorization for electrons, nuclei, and photons", May 22-27	Prof. E.K.U. Gross (HUJI), Prof. Roi Baer (HUJI), Dr. Eli Kraisler (HUJI)
	CECAM Workshop - Frontiers in Multiscale Modelling of Photoreceptor Proteins, September 3-5	Igor Schapiro (HUJI), Maria-Andrea Mroginski (TU Berlin)
	Fritz Haber Winter Symposium, The Hebrew University of Jerusalem	Dr. Eli Kraisler (HUJI), Dr. Snir Gazit (HUJI), Prof. Roi Baer (HUJI)
	Novel Approaches in Computational Photobiology, October 31 - November 1	Tamar Stein (HUJI), Igor Schapiro (HUJI), Roi Baer (HUJI), E.K.U. Gross (HUJI), Leticia Gonzalez (Vienna)
	Dr. Tova Feldman Seminar, November 3	Ronnie Kosloff (HUJI)
2020	Theoretical Chemistry session, The 85th Annual Meeting of the Israel Chemical Society, February 18-19	Tamar Stein (HUJI)
2021	EMBO Workshop Physics of cells: PhysCell2021	Assaf Zemel (HUJI)